Zonal Winds Between 25 and 120 KM Retrieved from Solar Occultation Spectra

John H. Shaw
Department of Physics

Garrett W. van Cleef
Graduate Research Associate

National Aeronautics and Space Administration
Washington, D.C. 20546

Grant No. NAGW-1129
Final Report
RF Project 766291/719915

July 1989

ZONAL WINDS BETWEEN 25 AND 120 KM RETRIEVED FROM SOLAR OCCULTATION SPECTRA

DISSERTATION

Presented in Partial Fulfilment of the Requirements for the Degree Doctor of Philosophy in the Graduate School of The Ohio State University

By

Garrett Warren van Cleef II, B.Sc.

The Ohio State University

1989

DISSERTATION COMMITTEE:

J. H. Shaw

C. D. Andereck

R. D. Knight

C. V. Heer

Approved by

_____

Adviser

Department of Physics

ZONAL WINDS BETWEEN 25 AND 120 KM RETRIEVED FROM SOLAR OCCULTATION SPECTRA

By

Garrett W. van Cleef II, B.S.

The Ohio State University, 1989

Professor John H. Shaw, Adviser

ABSTRACT

Atmospheric winds at heights between 25 and 120 km have been retrieved with precisions of 5/ms^{-1} from the Doppler shifts of atmospheric absorption lines measured from a satellite-borne instrument. Lines of the ν_3 CO_2 and ν_2 H_2O rotation-vibration bands caused by gases in the instrument allowed the instrumental frequency scale to be absolutely calibrated so that accurate relative speeds could be obtained. By comparing the positions of both sets of instrumental lines the calibration of the frequency scale was determined to be stable to a precision of $< 2 \times 10^{-5}$/cm^{-1} during the course of each occultation. It was found that the instrumental resolution of 0.015/cm^{-1} after apodization, the signal to noise ratio of about 100 and stable calibration allowed relative speeds to be determined to a precision of 5/ms^{-1} or better by using small numbers of absorption lines between 1600 and 3200/cm^{-1}. Absolute absorption line positions were simultaneously recovered to precisions of 5×10^{-5} cm^{-1} or better.

The wind speed profiles determined from four sunset occultations and one sunrise occultation show remarkable similarities in the magnitudes and directions of the zonal wind velocities as functions of height. These wind profiles appear to be manifestations of atmospheric tides. The periodic heating of the atmosphere primarily by ozone absorption and water insolation can force global

circulation of the upper atmosphere as described by Lindzen and Chapman (1970). The diurnal and semidiurnal Fourier components of the heating rates as predicted by Groves (1983) were shown to be significant in driving the tidal circulation. The linear or "classical" tidal theory [Lindzen, Chapman, 1970], however, predicts wind speeds which grow exponentially with height due to the exponential decrease in the hydrostatic background pressure. The growth was found to lead to wind speeds much larger in amplitude than revealed by the spectroscopic measurements. The classical theory must break down in a nonlinear way and the consequences of nonlinear and adiabatic instabilities present in such growth in amplitude is discussed.

VITA

[redacted] [redacted]

1983	B.S., Stevens Institute of Technology, Hoboken, New Jersey
1983–1989	Department of Physics, Ohio State University, Columbus, Ohio

PUBLICATIONS

van Cleef, G. W., J. H. Shaw, C. B. Farmer, Zonal winds between 25 and 120 km obtained from solar occultation spectra, *Geophys. Res. Lett.*, 14, 1266-1268, 1987.

RESEARCH AREA

Infrared spectroscopy and atmospheric physics.

TABLE OF CONTENTS

LIST OF FIGURES

Figures

LIST OF TABLES

Tables

INTRODUCTION

Mission Objectives

The Atmospheric Trace Molecule Spectroscopy experiment (ATMOS) was designed to obtain high resolution infrared absorption spectra from an orbiting platform in space. The instrument was managed for the National Aeronautics and Space Administration (NASA) by the Jet Propulsion Laboratory (JPL) under the direction of C. B. Farmer and was first flown in the spring of 1985 as a payload of the shuttle Spacelab-3 mission. This project has also become a part of NASA's Upper Atmospheric Research program (UAR). The major goal of the UAR is to obtain quantitative data pertaining to the state of the upper atmosphere over a long period of time to determine the effects of natural and perhaps man-made changes of the atmosphere's physical state. Information has been obtained from the Spacelab-3 experiment by the ATMOS experimental team concerning the volume mixing ratios (VMRs) and concentrations of a number of minor and trace gases in the atmosphere. Temperature and pressure variations with height were also obtained by analyzing the strengths and equivalent widths of the absorption lines and these measurements are related to upper atmosphere dynamics. The purpose of the research described here was to determine if accurate wind speeds along the line of sight can be obtained to high precision. This was achieved. In addition the influence of the diurnal and semi-diurnal Fourier components of

the heating of the lower atmosphere on the upper atmospheric circulation is discussed in this report.

The ATMOS instrument is a fast Fourier-transform (FFT) interferometer which covers a wide spectral range from 600 to 5000 cm^{-1}. This spectral range is further divided into smaller regions by the use of specialized filters to increase the signal to noise ratio of the processed spectra. With a scan time of about 2 s the spectra have an unapodized resolution of about 0.01 cm^{-1}, a digital frequency spacing of 0.0075 cm^{-1} and a vertical resolution of about 4 km. A variety of programs is available on a Prime 955 computer at the ATMOS data analysis center to study the spectra.

The mission's strategy was that, by using the sun as the source of radiation, absorption spectra of about 40 molecular species in the earth's atmosphere could be observed in successive spectra during sunset and sunrise solar "occultations". An occultation, or more precisely a limb observation, is defined as when the earth's atmosphere intersects a line between the orbiter and the sun during an orbit. From these spectra the properties of the atmospheric constituents and the dynamical state of the atmosphere in regions near the tangent points of observation were studied. A tangent point is defined as the point above the earth's surface where a light ray from the sun to the orbiter is closest to the earth's surface. This distance above the earth's surface is referred to as the *tangent height.* A description of the optical filters used to define several spectral regions and a list of some molecules whose infrared transitions occur in these regions are given in Table 1 [Farmer, 1987].

During the course of the mission two latitude bands were sampled. Mid-

latitude sunsets occurred near 30° N and sunrises near 50° S. Since the orbital period of the platform was about 90 minutes a wide range of longitudes was available for study in the two latitude bands. The Spacelab-3 Mission (SL-3) was launched on board the shuttle Challenger on April 29, 1985 at 21:00:30 EST and Table 2 lists the geographical locations, times, and filter region for each occultation. For each occultation a set of spectra was obtained in a period of a few minutes and hence a cross section of the atmospheric state could be sampled as a function of altitude for the latitude and longitude about the tangent points. A total of 19 such occultations accumulated almost 1200 atmospheric spectra. In addition, more than 1000 solar spectra were obtained at altitudes far above those where infrared absorption by telluric gases is significant.

Overview of Thesis Research

After the completion of the mission in May 1985 the raw data were processed and soon afterwards the first transformed spectra were available for analysis. It was decided to study the possibility of measuring winds from the spectra and to estimate the accuracy which can be expected. Due to the relative motion of the shuttle orbiter with respect to the atmosphere as well as possible motions caused by atmospheric circulations the absorption line positions were expected to change significantly from spectrum to spectrum. It was determined that the relative speeds between the observer and the atmosphere surrounding the tangent points could be determined by measuring the Doppler shifts of groups of absorption lines and the relative speeds

associated with these shifts.

To measure the Doppler shift of a moving absorber, the frequencies of two lines must be compared, the rest frame position and the position in the moving frame. If c is the speed of light, v is the relative speed of the absorber to the orbiter, and ς is the wavenumber (in cm^{-1}) of the line in the rest frame, then the new wavenumber in the moving frame is shifted from the rest frame position by the amount

$$\Delta\varsigma = \frac{v}{c}\varsigma. \tag{1}$$

The relative speed v can be determined by this shifts in frequency by

$$v = \frac{\Delta\varsigma}{\varsigma}c. \tag{2}$$

The accuracy of v is limited by how well known the rest frame position ς is relative to the instrument's "true" rest frame position for that transition. It was determined that even if the instrumental calibration is not "absolute", and hence line positions determined using it were not absolute, accurate wind speeds could, nonetheless, still be determined. This is true since v depends not on the Doppler shift $\Delta\varsigma$ alone, but on the *ratio* $\Delta\varsigma/\varsigma$. Average calibration offsets will cancel in the determination of v and this is discussed in §II.4. This technique was found to require that for at least one telluric absorption band, a set of corresponding lines due to gases inside the instrument needed to be present in the spectra. The accuracy was then transferred to other spectral regions by a "bootstrapping" technique which utilized the wind speeds determined from bands in which instrumental lines were available to determine the positions of new absorption lines relative to the instrument's calibration.

It was determined that a sufficient number of spectral lines was available

in the spectra ($\sim$ 20-40 lines/spectrum) to obtain precisions of 5 ms^{-1} or better by measuring the Doppler shifts of telluric absorption lines [Shaw, 1985] using realistic estimates of the noise level. It was also determined that upper limits of fluctuations in the calibration stability of the instrument were needed since the precisions of the wind speeds would be ultimately limited by these. Such uncertainties were determined to be extremely small and did not contribute more than 1-2 ms^{-1} errors.

Accurate relative speed profiles were estimated from spectra with tangent heights between 25 and 120 km and were found to have precisions from 3 to 5 ms^{-1} throughout this range. In order to obtain wind speeds relative to the rotating frame of the earth the orbital motion of the shuttle and the rotational motion of the tangent points were estimated from telemetry data provided by Goddard Space Flight Center. This motion was subtracted from the relative speeds between the orbiter and the atmosphere estimated from the Doppler shifts to obtain wind speeds relative to the earth's surface. Uncertainties due to errors in estimating the line of sight velocity components were found to be less than 2 or 3 ms^{-1}. The residual wind speed profiles were found to indicate essentially the zonal component of the atmospheric flow.

Similarities of the wind speeds with height were found in all four sunset occultations analyzed. These profiles were found to have wavelike characteristics and further investigation of this phenomenon was done. (Since only one sunrise occultation was available in the filter used for wind speeds such comparisons with other sunrise measurements are unavailable at the current time.) Such variations in altitude can be described by the theory of atmospheric tides [Siebert, 1961; Chapman, Lindzen, 1970]. The source of the

excitations and their "wavelike" nature can be explained by the periodic absorption of solar radiation by the atmosphere, particularly by ozone between 20 and 90 km and water vapor below 10 km altitude. Since this happens on a global scale the response of the atmosphere is also on this scale. The notion of tidal eigenfunctions and accompanying vertical structure equations were derived and solutions to these mathematical models were computed. There were similarities of the phases predicted between the theory and the ATMOS results. The "classical" theory of tides, however, was found to be inadequate in describing the magnitudes of the waves at heights above about 85 km since it ignores the contributions due to non-linearities and adiabatic instabilities. The wind speeds measured do contain information of the geometric distribution of global heating rates regarding the absorption of solar radiation in the atmosphere. This can be attributed to the global scale of the atmospheric response to tidal forcing. Further study into the non-linearities in the fluid dynamics as well as future measurements of winds in a manner similar to the ATMOS project may yield important data about the geographical distribution of the gaseous absorbers.

Table 1 Frequency transition ranges of the ATMOS optical filters together with the principal molecular species that can be analyzed in these regions [Farmer, 1987].

Filter 1 600-1200 cm^{-1}	Filter 2 1100-2000 cm^{-1}	Filter 3 1580-3400 cm^{-1}	Filter 4 3100-4700 cm^{-1}
CO_2	CO_2	CO_2	CO_2
H_2O	H_2O	H_2O	H_2O
O_3		O_3	
	CH_4	CH_4	
		CO	
		N_2O	
NH_3	H_2O_2	NO	HF
HNO_2	HO_2	(NO_2)	(HCN)
(HNO_3)			
HNO_4			
CCl_3F	(NO)	HDO	
CCL_2F_2	NO_2	(H_2O_2)	
CHCClF2	N_2O_5	H_2CO	
CH_3Cl	HNO_3		
CCl_4		HCl	
COF_2	HOCl	(CH_3Cl)	
COClF	CF_4	OCS	
ClO	SO_2	HCN	
$ClONO_2$			

Table 2 Summary of occultation spectra obtained during the Spacelab-3 mission. Latitudes and Longitudes refer to both high ($\sim$ 120 km) and low ($\sim$ 0 km) tangent heights. MET - Mission Elapsed Time, GMT - Greenwich Mean Time.

Occ Type	Opt Fil	MET Start	GMT 60 km	Lat Low/High	Long (E) Low/High
SR01	3	0/07:13	119/23:17	49.9/48.5 S	118.0/117.0
SS01	1	0/08:08	120/00:12	34.5/35.9 N	276.3/277.1
SS02	1	0/18:52	120/10:54	32.6/34.1 N	115.3/116.1
SR02	3	0/19:27	120/11:20	49.1/47.5 S	294.6/293.3
SS03	2	0/21:55	120/13:57	33.6/31.9 S	70.2/69.3
SS04	4	1/00:55	120/17:00	33.0/31.3 N	24.2/23.3
SR03	6	1/01:34	120/17:36	48.6/46.9 S	202.7/201.4
SS05	1	1/02:28	120/18:32	32.8/31.1 N	1.2/0.3
SS06	3	1/07:01	120/23:07	31.9/30.1 N	292.1/291.2
SS07	2	1/08:33	121/00:38	31.7/36.0 N	269.2/268.2
SS08	1	1/10:05	121/02:10	31.4/29.6 N	246.2/245.2
SR04	4	1/15:18	121/07:21	47.4/45.6 S	356.0/354.7
SR05	2	1/16:49	121/08:53	47.3/45.5 S	332.6/331.8
SR06	1	1/18:21	121/10:24	47.2/45.4 S	310.1/308.8
SR07	5	1/19:53	121/11:56	47.1/45.1 S	287.2/285.8
SS09	3	2/01:22	121/17:26	28.5/26.6 N	16.1/15.2
SS10	4	2/02:53	121/18:58	28.1/26.2 N	353.1/352.2
SS11	3	2/04:25	121/20:30	27.8/25.9 N	330.1/329.2
SS12	2	2/05:51	121/22:01	27.3/25.3 N	284.1/283.2
SS13	3	2/07:27	121/23:33	27.3/25.3 N	284.1/283.2

CHAPTER I

SPECTROSCOPIC THEORY

I.1 The Michelson Interferometer and Fourier Transform Spectroscopy

In the classical Michelson interferometer Figure 1.1.1 light from the source ∞ is collimated at C into a beam which is incident on a half-silvered beam splitter B. The reflected ray travels to a stationary mirror S and it is reflected back to the beam splitter. The partially transmitted ray travels to a movable mirror M and is reflected back to the beam splitter. The two split beams recombine at O and are sent to the detector D. Since M is movable, the two beams interfere both constructively and destructively as the path difference x changes.

For simplicity we consider an incident beam with frequency f. The wavenumber ς is related to the frequency f and the speed of light c by

$$\varsigma \equiv \frac{f}{c}. \tag{1.1}$$

If we assume the amplitude A of this monochromatic incident beam is split evenly between both arms M and S with path difference x and if we neglect

losses in intensity in the beam due to dispersion then the complex amplitude of the beam at the detector is

$$A_D = \frac{1}{2}A(1 + e^{i\delta}), \tag{1.2}$$

where the phase difference is

$$\delta = 2\pi\varsigma x. \tag{1.3}$$

The intensity at the detector D is

$$I(\varsigma, x) = |A_D|^2 = \frac{1}{2}(1 + \cos\delta)A^2 = \frac{1}{2}(1 + \cos\delta)I_0(\varsigma). \tag{1.4}$$

Suppose that $I(\varsigma)$ represents the spectral radiance (power/cm^{-1}) then total signal $I_0(x)$ received at the detector D is the sum of all contributions at all frequencies

$$\begin{aligned} I_0(x) &= \int_0^\infty d\varsigma\, \frac{1}{2}(1 + \cos\delta)\, I(\varsigma), \\ &= \frac{1}{2}\int_0^\infty d\varsigma\, I_0(\varsigma) + \frac{1}{2}\int_0^\infty d\varsigma\, \cos\delta\, I(\varsigma), \\ &\equiv \frac{1}{2}\left[\bar{I} + I(x)\right]. \end{aligned} \tag{1.5}$$

The first term $\bar{I}$ is the total incident intensity while the second term $I(x)$ is the modulated part and is given by

$$I(x) = 2I_0(x) - \bar{I}. \tag{1.6}$$

In Fourier spectroscopy the interference pattern $I(x)$, also known as an *interferogram*, is measured and from it the the spectral radiance $I(\varsigma)$ is determined. From the theory of Fourier transforms we have the relationship

$$I(x) \propto \int_{-\infty}^{\infty} d\varsigma'\, \cos 2\pi\varsigma x\, I(\varsigma'), \tag{1.7}$$

where it is assumed that $I(\varsigma) = 0$ for $\varsigma < 0$. This can be inverted [Mathews, Walker, 1970] to give

$$I(\varsigma) \propto \int_{-\infty}^{\infty} dx \, \cos 2\pi\varsigma x \, I(x) \tag{1.8}$$

and the pair of equations (1.7-8) are a Fourier-cosine pair. This technique of spectroscopy has the multiplex advantage which improves the signal to noise since all spectral features are simultaneously recorded in the interferograms [Thorne, 1988].

In practice the maximum path difference is not infinite but is usually confined to a limited region say, $-L < x < L$. Then $I(x)$ is zero outside this range and the spectrum (1.8) is

$$I'(\varsigma) \propto \int_{-L}^{L} dx \, \cos 2\pi\varsigma x \, I(x). \tag{1.9}$$

Some spectral information is lost due to the finite path length with a subsequent degradation of the instrumental resolution. If we consider the case of a monochromatic input signal I_0 at wavenumber ς'

$$I(\varsigma) = I_0 \, \delta(\varsigma - \varsigma'), \tag{1.10}$$

then the output interferogram is a cosine function

$$I(x) = I_0 \, \cos 2\pi\varsigma' x. \tag{1.11}$$

Since data are only available for $-L < x < L$ the computed spectrum $I'(\varsigma)$ is

$$\begin{aligned} I'(\varsigma) &\propto I_0 \int_{-L}^{L} dx \, \cos 2\pi\varsigma x \, \cos 2\pi\varsigma' x \\ &\propto I_0 L \, [\operatorname{sinc} 2\pi(\varsigma' + \varsigma)L + \operatorname{sinc} 2\pi(\varsigma' - \varsigma)L] \end{aligned} \tag{1.12}$$

where the sinc function is defined as

$$\operatorname{sinc} y = \frac{\sin y}{y}. \tag{1.13}$$

Since the first term on the right hand side of (1.12) in negligible compared to the second the output interferogram for the monochromatic wave is

$$I'(\varsigma) \propto I_0 L \operatorname{sinc} 2\pi(\varsigma' - \varsigma)L. \tag{1.14}$$

Figure 1.1.2 shows the first two zeros of the sinc function $\pm 1/2L$. The resolution of the spectra is approximately $1/2L$ and corresponds to the region of maximum instrumental response to a spectral feature. Outside this region the sinusoidal variation of the instrumental response is due to the finite path difference. As $L \to \infty$ the sinc function approaches a δ-function. and we retrieve all spectral information.

Now consider the case where the radiation is described by a spectral density $I(\varsigma)$

$$I(\varsigma) = \int_{-\infty}^{\infty} d\varsigma'\, \delta(\varsigma - \varsigma') I(\varsigma'). \tag{1.15}$$

Then, from (1.7), the interferogram is

$$\begin{aligned} I(x) &\propto \int_{-\infty}^{\infty} d\varsigma\, \cos 2\pi\varsigma x \int_{-\infty}^{\infty} d\varsigma'\, I(\varsigma')\, \delta(\varsigma - \varsigma'), \\ &= \int_{-\infty}^{\infty} d\varsigma'\, \cos 2\pi\varsigma' x\, I(\varsigma'). \end{aligned} \tag{1.16}$$

Since data are only gathered for $-L < x < L$ the resolved spectrum is, from (1.9)

$$\begin{aligned} I'(\varsigma) &\propto \int_{-L}^{L} dx\, \cos 2\pi\varsigma x\, I(x), \\ &= \int_{-\infty}^{\infty} d\varsigma' \int_{-L}^{L} dx\, \cos 2\pi\varsigma x\, \cos 2\pi\varsigma' x\, I(\varsigma'). \end{aligned} \tag{1.17}$$

We see that (1.17) can be written

$$I'(\varsigma) = \int_{-\infty}^{\infty} d\varsigma'\, i(\varsigma,\varsigma')\, I(\varsigma'), \tag{1.18}$$

if we define the normalized *instrument function*

$$\begin{aligned} i(\varsigma,\varsigma') &\equiv \int_{-L}^{L} dx\, \cos 2\pi\varsigma' x\, \cos 2\pi\varsigma x, \\ &= L\left[\operatorname{sinc} 2\pi(\varsigma+\varsigma')L + \operatorname{sinc} 2\pi(\varsigma-\varsigma')L\right]. \end{aligned} \tag{1.19}$$

It can be shown [Thorne, 1988] that this form is normalized

$$\int_{-\infty}^{\infty} d\varsigma\, i(\varsigma,\varsigma') = 1. \tag{1.20}$$

We see that (1.19) represents a response centered around $\varsigma = \pm\varsigma'$. This is true since Fourier transforms of functions in the x domain always have mirror images about zero in the ς domain. If we define

$$i_{\pm}(\varsigma,\varsigma') \equiv L \operatorname{sinc} 2\pi L(\varsigma \pm \varsigma'), \tag{1.21}$$

then the instrument function (1.19) is

$$i(\varsigma,\varsigma') = i_{+}(\varsigma,\varsigma') + i_{-}(\varsigma,\varsigma'). \tag{1.22}$$

Usually we refer to the region $\varsigma > 0$ so that the contribution of i_{+} is usually negligible for $\varsigma \gg 1/2L$. We can then say the instrument function is approximately

$$i(\varsigma,\varsigma') \doteq i(\varsigma-\varsigma') \equiv 2i_{-}(\varsigma,\varsigma') = 2L \operatorname{sinc} 2\pi L(\varsigma-\varsigma'). \tag{1.23}$$

The convolution between two functions $A(\varsigma)$ and $B(\varsigma)$ is defined as

$$A(\varsigma) * B(\varsigma) \equiv \int_{-\infty}^{\infty} d\varsigma'\, A(\varsigma - \varsigma')B(\varsigma) \tag{1.24}$$

so then (1.18) can be expressed

$$I'(\varsigma) = i(\varsigma) * I(\varsigma). \tag{1.25}$$

The resolved spectrum $I'(\varsigma)$ is the convolution of the true spectrum $I(\varsigma)$ with the instrumental function i.

The resolution $\delta\varsigma = 1/2L$ caused by the finite path length allows information from nearby wavenumbers ς' to contribute to the partially resolved spectrum at ς which is given by (1.25). The sinc function has a "ringing" at wavenumbers not centered near the maximum of the instrument function which can contribute significant interferences between different wavenumbers in the spectra. Figure 1.1.3 shows the ringing caused by this instrument function about an absorption line taken from the ATMOS spectra. The deep central spike is the instrumental response at the spectral line center while the side lobes are artifacts of the finite path difference and not real spectral features. This ringing can be mathematically filtered out through a process called *apodization* - literally meaning "cutting of the feet" [Thorne, 1988] - but with a complementary loss of spectral resolution . From the property of Fourier transforms it can be shown that the transform of a product of functions is the convolution of their transforms

$$[AB](\varsigma) = A(\varsigma) * B(\varsigma). \tag{1.26}$$

We can now imagine multiplying the interferograms $I(x)$ by an "apodizing function" $a(x)$. An apodized spectrum can be retrieved from this apodized interferogram $a(x)\,I(x)$ using (1.25)

$$I'(\varsigma) = i(\varsigma) * [aI](\varsigma) = i(\varsigma) * [a(\varsigma) * I(\varsigma)]. \tag{1.27}$$

If we define the apodized instrument function

$$i_a(\varsigma,\varsigma') = \int_{-\infty}^{\infty} d\varsigma''\, i(\varsigma-\varsigma'')\, a(\varsigma''-\varsigma') \tag{1.28}$$

then by using (1.25) the apodized spectrum (1.27) can be shown to be

$$I'(\varsigma) = \int_{-\infty}^{\infty} d\varsigma'\, i_a(\varsigma,\varsigma')\, I(\varsigma'). \tag{1.29}$$

The apodizing function $a(x)$ can be freely chosen to achieve whatever mathematical filtering is desired but always at the cost of spectral resolution. There are several apodizing functions available to the user when computing the ATMOS spectra and they are described in detail by Norton and Beer (1976). Figure 1.1.4 shows the absorption line used in Figure 1.1.3 after convolution with three different apodization functions available on the ATMOS computer and described by Norton and Beer [1976] were used. These apodizing functions give more smoothing of the spectral while degrading the resolution from 0.0125 cm^{-1} to about 0.015 cm^{-1} between the several functions. The apodizing functions widen the spectral features and cause the peak absorptances of the lines in the spectra to decrease. The apodizing function chosen in this study eliminated false spectral features greater than the noise level and had a resulting resolution of about 0.015 cm^{-1}. This was found to be acceptable within the measurement requirements §I.12.

If an interferogram $I(x)$ is sampled at intervals Δx features at other wavenumbers may be superimposed on real features unless the value of Δx is properly chosen. This "aliasing" is due to the periodicity of the Fourier transform and is described by Thorne (1988). Thorne shows that the inter-

ferogram must be sampled at least every

$$\Delta x = \frac{1}{2\varsigma_{\min}} \tag{1.30}$$

if the minimum wavenumber is $\varsigma_{\min}$ to avoid this sort of overlapping. Special optical filters must also be used to prevent false lines from appearing in the spectra. The ATMOS filters were carefully chosen to avoid aliasing [Farmer, 1987].

Absolute line positions, are ultimately limited by the accuracy of the He-Ne laser wavelength used to calibrate the instrument. If the recorded value of the path difference x^* is related to the true path difference x by

$$x^* = (1+\alpha)x \tag{1.31}$$

where $|\alpha| \ll 1$ then the interferogram (1.7) is

$$I(x) = I\left(\frac{x^*}{1+\alpha}\right) = \int_{-\infty}^{\infty} d\varsigma' \cos 2\pi\varsigma' \left(\frac{x^*}{1+\alpha}\right) I(\varsigma'). \tag{1.32}$$

This shows how the interferogram is related to the path difference recorded by the instrument. These interferograms are then processed by (1.9). However, since the path difference is uncertain, we obtain a spectrum

$$\begin{aligned} I'(\varsigma) &= \int_{-L}^{L} dx^* \cos 2\pi\varsigma x^* \, I(x) \\ &= \int_{-\infty}^{\infty} d\varsigma' \, I(\varsigma') \int_{-L}^{L} dx^* \cos 2\pi\varsigma x^* \cos 2\pi\varsigma' \frac{x^*}{1+\alpha}. \end{aligned} \tag{1.33}$$

The instrument function is then

$$i_\alpha(\varsigma,\varsigma') = L\left[\operatorname{sinc} 2\pi\left(\varsigma + (1+\alpha)\varsigma'\right)L + \operatorname{sinc} 2\pi\left(\varsigma - (1+\alpha)\varsigma'\right)L\right]. \tag{1.34}$$

From this result the uncertainty in the laser frequency causes the path lengths to be in error which causes features at frequency ς in the convolved spectra to

be shifted by $-\alpha\varsigma$. Typical errors in the He-Ne frequency are given by $\varsigma(\alpha) \sim \mathcal{O}(10^{-8})$ [Norton, 1989] and line positions determined from the spectra should be uncertain to this degree. It is shown in §II.4 that these uncertainties do not affect the accuracy of the winds from Doppler shifts provided that a set of instrumental lines with atmospheric counterparts can be measured in the spectra.

Due to the digital nature of the interferogram data and the presence of noise in the detector signals the location of zero path difference (ZPD) in the interferogram can be in error. The point of zero path difference is defined as that value of x for which all frequencies interfere constructively. For an ideal interferogram this point is taken as the origin of x. Errors in locating ZPD can introduce apparent asymmetries in the interferograms which may cause frequency dependent calibration errors in the resolved spectra $I'(\varsigma)$. To see this, suppose that an estimate of ZPD is in error by an amount ξ. Then the measured interferogram (1.7) is

$$I(x) \propto \int_{-\infty}^{\infty} d\varsigma' \cos 2\pi\varsigma'(x+\xi)\, I(\varsigma'). \tag{1.35}$$

Using the form of this interferogram which is sampled from $-L < x < L$ we have

$$\begin{aligned} I'(\varsigma) &\propto \int_{-L}^{L} dx \cos 2\pi\varsigma x\, I(x) \\ &= \int_{-\infty}^{\infty} d\varsigma'\, I(\varsigma') \int_{-L}^{L} dx \cos 2\pi\varsigma x \cos 2\pi\varsigma'(x+\xi) \\ &= \int_{-\infty}^{\infty} d\varsigma'\, i(\varsigma,\varsigma')\, I(\varsigma'). \end{aligned} \tag{1.36}$$

The instrument function contains the phase error and can be evaluated using

standard integration

$$\begin{aligned} i(\varsigma,\varsigma') &= \int_{-L}^{L} dx\, \cos 2\pi\varsigma x\, \cos 2\pi\varsigma'(x+\xi) \\ &= L\,[\operatorname{sinc} 2\pi(\varsigma-\varsigma')L + \operatorname{sinc} 2\pi(\varsigma+\varsigma')L]\cos 2\pi\varsigma'\xi \\ &\simeq L \operatorname{sinc} 2\pi(\varsigma-\varsigma')L \cdot \cos 2\pi\varsigma'\xi. \end{aligned} \tag{1.37}$$

The instrument response function $i(\varsigma,\varsigma')$ is modulated by the term $\cos\varsigma'\xi$. For values of $\varsigma'\xi \ll 1$ the interferogram will peak when $\varsigma' = \varsigma$ and should produce symmetric line shapes. For large frequencies where $\varsigma'\xi \sim 1$ the instrument function will not peak at ς and the phase errors can produce significant distortions in the line shapes which may cause systematic errors in the positions of spectral features.

An estimate of the magnitudes of these systematic fluctuations in line positions set a limit of the accuracy of the relative speed measurements. The sampling interval Δx of two fringes of the He-Ne laser used for calibration was used to obtain the interferograms [Norton, 1989]. The wavelength of the laser is about 633 nm which corresponds to $\Delta x \simeq 1.27 \times 10^{-4}$ cm. The precision of determining ZPD was estimated to be 1000 times better than this value [Norton, 1989] which corresponds to $\varsigma(\xi) \sim \mathcal{O}(10^{-7})$ cm. For typical infrared transitions the distortions in the instrument function are negligible. With this degree of precision distortions the phase errors are negligible and we can therefore expect the calibration of the instrument to be extremely stable.

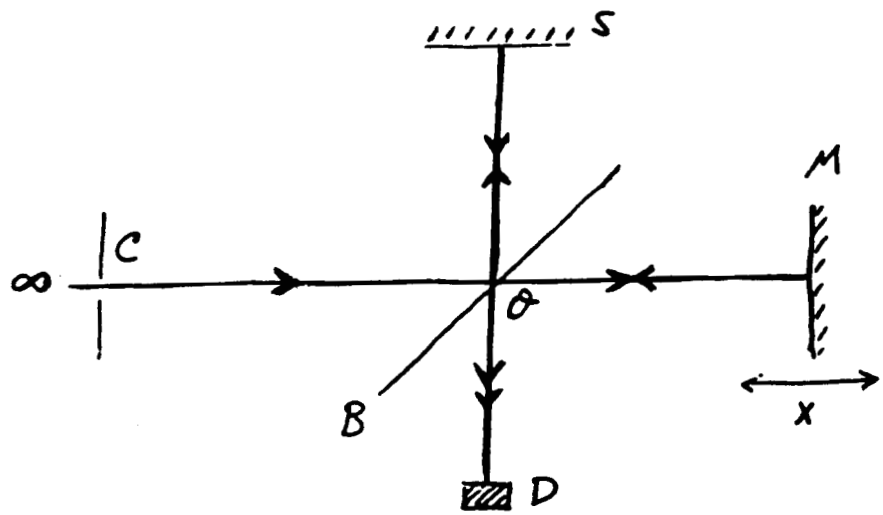

Figure 1.1.1 Simple Michelson interferometer. The ATMOS interferometer has a much more complex optical arangement [Farmer, 1987], however, the basic interferometric principles are the same as in this simple design.

Figure 1.1.2 Instrumental response function $\operatorname{sinc} x$. The amplitude of the oscillation decreases as $|x|$ increases.

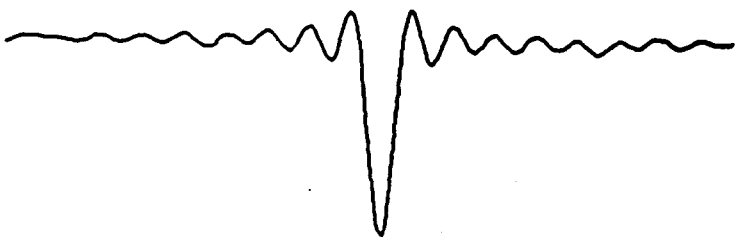

Figure 1.1.3 Absorption line from ATMOS spectra without apodization. Notice the sinc function behavior of the instrumental response function away the line center where it is a maximum.

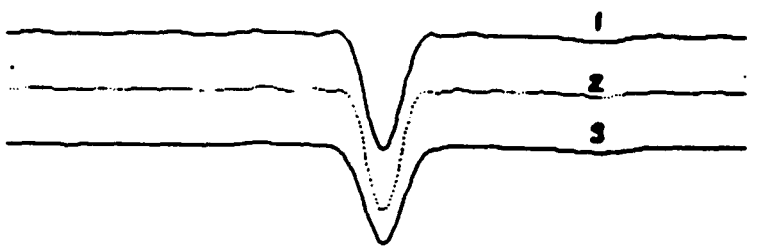

Figure 1.1.4 Same absorption above with apodizing functions 1, 2 and 3 [Norton, Beer, 1976]. The figures have been displaced vertically for clarity. Notice that the 'ringing' in Figure 1.1.3 has been eliminated at the expense of instrumental resolution. The peak absorptance of the line is also smaller. Apodization '2' was used in this study.

I.2 Measuring Doppler Shifts from ATMOS Spectra

Due to the geometry of the experiment the measurements are confined to the components of atmospheric motion along the line of sight. In order to determine the components we need to measure to total relative motion between the gas near the tangent points and the orbiter and then subtract from these results motion due to the shuttle's orbit and the earth's rotation. The residual speed is then the component of wind relative to the earth's rotating frame along the tangent ray path. In order to obtain the relative speed it is useful to observe the actual positions of absorption lines in the ATMOS spectra and compute the Doppler shifts of their wavenumbers from a rest frame position. The observed position ς_j of a feature in the moving frame is related to its position $\hat{\varsigma}_j$ in the rest (non-moving) frame by the non-relativistic Doppler shift

$$\varsigma_j = \left(1 + \frac{v}{c}\right) \hat{\varsigma}_j \equiv (1 + \beta)\hat{\varsigma}_j. \tag{1.38}$$

Here v is the relative speed between the orbiter and the absorber, c is the speed of light, and $\beta \equiv v/c$ which is $\mathcal{O}(10^{-5})$ for orbital speeds. In order to obtain winds to 5 ms^{-1} we need to be able to determine ς to about 0.00005 cm^{-1}. Equivalent precisions can be obtained by using many absorption lines.

I.3 Quantum Mechanics of Infrared Spectroscopy

The ATMOS interferometer is designed to measure the absorption of solar radiation in the infrared. In this section we examine the physical processes involved and describe the quantum mechanical basis for the spectra.

The energy of a molecule depends on the locations and motions of its nuclei, center of mass, orientation, and electronic state. Let the locations of all the nuclei relative to the molecule's center of mass $\mathbf{R}^{cm}$ be described by the vector $\mathbf{R}$. The electronic energy of the molecule is then described by $E(\mathbf{R})$. This energy is evaluated with stationary nuclei. However, due to the uncertainty principle

$$\sigma(R^i_{x,y,z})\,\sigma(P^i_{x,y,z}) \geq \frac{\hbar}{2} \tag{1.39}$$

no real molecule can have fixed nuclei i since the more accurately their positions $\mathbf{R}^i$ are determined the larger is the uncertainty in their momenta $\mathbf{P}^i$. The nuclei therefore "oscillate" about an equilibrium configuration $\mathbf{R}^{eq}$ in accordance with the uncertainty principle. Also, the molecule cannot be considered to have a fixed center of mass $\mathbf{R}^{cm}$ and from the uncertainty principle it has some translational momentum. The molecule also cannot have a fixed orientation since the uncertainty in its angular momentum would then be infinite. All these three types of motion must be considered as part of the wave function.

The nuclear motions can be treated within the context of the Born-Oppenheimer approximation [Berry, Rice, Ross, 1980]. The lighter electrons are considered to move much more rapidly than the heavier nuclei. For every

configuration of the nuclei during their slower scale motions, the electrons are considered to attain an "equilibrium" state. The Hamiltonian $\hat{\mathcal{H}}$ of the molecule can be assumed to be the sum of the nuclear kinetic energy $\hat{\mathcal{H}}_{\mathrm{n}}$ and the energy of the electronic state $\hat{\mathcal{H}}_{\mathrm{e}}$

$$\hat{\mathcal{H}} = \hat{\mathcal{H}}_{\mathrm{n}} + \hat{\mathcal{H}}_{\mathrm{e}}. \tag{1.40}$$

Let the positions of all the electrons relative to the center of mass $\mathbf{R}^{\mathrm{cm}}$ be given by the vector $\mathbf{r}$. Then Born-Oppenheimer approximation states that the wave function $\psi(\mathbf{r}, \mathbf{R})$ of the molecule is separable into a nuclear and electronic wave function

$$\psi(\mathbf{r}, \mathbf{R}) \doteq \psi_{\mathrm{n}}(\mathbf{R})\psi_{\mathrm{e}}(\mathbf{r}, \mathbf{R}). \tag{1.41}$$

The electronic part satisfies the relation

$$\hat{\mathcal{H}}_{\mathrm{e}}\psi_{\mathrm{e}}(\mathbf{r}, \mathbf{R}) = E(\mathbf{R})\psi_{\mathrm{e}}(\mathbf{r}, \mathbf{R}). \tag{1.42}$$

By using the Schrödinger equation

$$\hat{\mathcal{H}}\psi = E\psi \tag{1.43}$$

it can be shown [Berry, Rice, Ross, 1980] from (1.41-3) that

$$\psi_{\mathrm{e}}(\mathbf{r}, \mathbf{R})\hat{\mathcal{H}}_{\mathrm{n}}\psi_{\mathrm{n}}(\mathbf{R}) + \psi_{\mathrm{n}}(\mathbf{R})\hat{\mathcal{H}}_{\mathrm{n}}\psi_{\mathrm{e}}(\mathbf{r}, \mathbf{R}) = \psi_{\mathrm{e}}(\mathbf{r}, \mathbf{R})\left[E - E(\mathbf{R})\right]\psi_{\mathrm{n}}(\mathbf{R}). \tag{1.44}$$

The second term on the left hand side is neglected since there are only small interactions between electronic and nuclear motions. This is the Born-Oppenheimer approximation and (1.44) can then be expressed as

$$\left[\hat{\mathcal{H}}_{\mathrm{n}} + E(\mathbf{R})\right]\psi_{\mathrm{n}}(\mathbf{R}) = E\psi_{\mathrm{n}}(\mathbf{R}). \tag{1.45}$$

The quantity $E(\mathbf{R})$ is the effective potential energy field caused by the electrons in which the nuclei move.

Now assume at that the energy is separable into three parts, translation of the center of mass, internal vibration, and rotation of the molecule's orientation. (Even though this is not quite accurate and there are corrections to this assumption, it will suffice for the following discussion). Then the nuclear Hamiltonian can be written as

$$\hat{\mathcal{H}}_{\mathbf{n}} = \hat{\mathcal{H}}_{\mathbf{trans}} + \hat{\mathcal{H}}_{\mathbf{vib}} + \hat{\mathcal{H}}_{\mathbf{rot}}. \tag{1.46}$$

Let the total mass of the molecule be M, the individual nuclear masses be m_i, the center of mass momentum operator be $\hat{\mathbf{P}}^{\mathbf{cm}}$, the nuclear momenta relative to the center of mass operator in the "molecular coordinate frame" be $\hat{\mathbf{P}}_i$, the angular momentum of the molecular coordinate frame relative to the observer's frame operator be $\hat{\mathbf{L}}$, the molecular moment of inertia be $\mathbf{I}$, and the set of angles Ω needed to specify the orientation of the molecular coordinate system in the observer's frame. The moments of inertia are evaluated by

$$\begin{aligned} I_x &= \sum_i m_i(y_i^2 + z_i^2), \\ I_y &= \sum_i m_i(z_i^2 + x_i^2), \\ I_z &= \sum_i m_i(x_i^2 + y_i^2). \end{aligned} \tag{1.47}$$

The the Hamiltonians in (1.41) can be expressed as

$$\begin{aligned} \hat{\mathcal{H}}_{\mathbf{trans}} &= \frac{(\hat{\mathbf{P}}^{\mathbf{cm}})^2}{2M}, \\ \hat{\mathcal{H}}_{\mathbf{vib}} &= \sum_i \frac{\hat{\mathbf{P}}_i^2}{2m_i} + E(\mathbf{R}), \end{aligned} \tag{1.48}$$

$$\hat{\mathcal{H}}_{\rm rot} = \frac{\hat{L}_x^2}{2I_x} + \frac{\hat{L}_y^2}{2I_y} + \frac{\hat{L}_z^2}{2I_z}.$$

The wave function is

$$\psi_{\rm n} = \psi_{\rm trans}\psi_{\rm int}\psi_{\rm rot} \tag{1.49}$$

and the energy becomes

$$E = E_{\rm trans} + E_{\rm vib} + E_{\rm rot}. \tag{1.50}$$

The three eigenvalue equations for the translational, vibrational and rotational energy levels are

$$\begin{aligned}
\hat{\mathcal{H}}_{\rm trans}\psi_{\rm trans}(\mathbf{R}_{\rm cm}) &= \frac{(\hat{\mathbf{P}}^{\rm cm})^2}{2M}\psi_{\rm trans}(\mathbf{R}_{\rm cm}) \\
&= E_{\rm trans}\psi_{\rm trans}(\mathbf{R}_{\rm cm}), \\
\hat{\mathcal{H}}_{\rm vib}\psi_{\rm vib}(\mathbf{R}) &= \left[\sum_i \frac{\hat{\mathbf{P}}_i^2}{2m_i} + E(\mathbf{R})\right]\psi_{\rm vib}(\mathbf{R}) \\
&= E_{\rm vib}\psi_{\rm vib}(\mathbf{R}), \\
\hat{\mathcal{H}}_{\rm rot}\psi_{\rm rot}(\Omega) &= \left[\frac{\hat{L}_x^2}{2I_x} + \frac{\hat{L}_y^2}{2I_y} + \frac{\hat{L}_z^2}{2I_z}\right]\psi_{\rm rot}(\Omega) \\
&= E_{\rm rot}\psi_{\rm rot}(\Omega).
\end{aligned} \tag{1.51}$$

The translational energy levels form a continuum when the length scale of the motion is large. The occupation of translational energy levels is related to the temperature of the gas and, as we shall see, the Doppler shifts due to these thermal motions cause the absorption lines to have a width characteristic of their average motion. The vibrational energy levels are discrete and are well approximated by the harmonic oscillator model near the minima of their vibrational potential wells. Infrared transitions between vibrational

and rotational levels are observed in the ATMOS spectra for many atmospheric gases. The rotational levels have quantized angular momentum due to the azimuthal periodicity of the wave function and accompany vibrational transitions.

I.4 Normal Coordinates and Vibrational Energy for Triatomic Molecules

There were about 40 molecular species whose spectra were measured with the ATMOS interferometer. In this study CO_2, H_2O and N_2O were used to obtain wind speeds. We will therefore concentrate on the quantum mechanics of vibration of triatomic molecules which describe the spectra of these three molecules.

A molecule with N atoms has $3N$ independent nuclear coordinates in general. However, not all of these coordinates are required in describing the internal molecular energy E_{vib}. In the absence of external fields the center of mass coordinates $\mathbf{R}^{\text{cm}}$ and the orientation Ω do not affect the vibrational energy. For linear molecules such as CO_2 and N_2O, two angles (spherical coordinates) are needed to specify the orientation of the symmetry axis, while for non-linear molecules such as H_2O three angles (Euler angles) are needed to specify the complete orientation. Thus there are $n = 3N - 5$ or $3N - 6$ vibrational degrees of freedom. For linear triatomic molecules this

corresponds to $n = 4$ degrees of freedom while for non-linear molecules we have $n = 3$ degrees of freedom.

In a triatomic molecule the vibrational energy is a function of three or four independent generalized coordinates q_σ, $\sigma = 1,..,n$ [Herzberg, 1945]. The cartesian coordinates $\mathbf{R}_i$ of each nucleus i are related to the generalized coordinates by

$$\mathbf{R}_i = \mathbf{R}_i(\mathbf{q}). \tag{1.52}$$

There is a preferred set of these coordinates $\mathbf{q}$ in terms of which the vibrational motion can be expressed as simply as possible, the normal coordinates [Herzberg, 1945]. In this approach we assume a well-defined equilibrium geometry about which the nuclei perform small oscillations. This equilibrium geometry is called a molecular frame. The nuclei are assumed to perform oscillations in a potential energy field $V(\mathbf{q}) \equiv E(\mathbf{R}(\mathbf{q}))$ about an equilibrium position given by $\mathbf{q}^{eq}$. Since this equilibrium position is defined to be a potential energy minimum in the context of the Born-Oppenheimer approximation, then $(\partial V/\partial q_\sigma)_{\mathbf{q}^{eq}} = 0$. If we define our normal coordinates to have a zero value at equilibrium, $\mathbf{q}^{eq} \equiv \mathbf{0}$, then the potential energy function can expressed as

$$V(\mathbf{q}) = V(\mathbf{0}) + \frac{1}{2}\sum_{\sigma\sigma'}\left(\frac{\partial^2 V}{\partial q_\sigma \partial q_{\sigma'}}\right)_0 q_\sigma q_{\sigma'} + \cdots. \tag{1.53}$$

from a Taylor series expansion about the equilibrium point. For sufficiently small oscillations all of the extra terms in the expansion (1.53) can be dropped as well as $V(\mathbf{0})$ since it is a constant for the equilibrium geometry. This harmonic approximation is only useful for the states near the bottom of the potential well and additional anharmonic terms need to be included for a

more accurate solution elsewhere [Herzberg, 1945].

If we define the force constants [Berry, Rice, Ross, 1980]

$$k_{\sigma\sigma'} \equiv \left(\frac{\partial^2 V}{\partial q_\sigma \partial q_{\sigma'}}\right)_0 \tag{1.54}$$

then the potential energy in the harmonic approximation is

$$V(\mathbf{q}) = \frac{1}{2}\sum_{\sigma\sigma'} k_{\sigma\sigma'} q_\sigma q_{\sigma'}. \tag{1.55}$$

The kinetic energy of the molecule is

$$T = \frac{1}{2}\sum_i m_i \left|\dot{\mathbf{R}}_i\right|^2. \tag{1.56}$$

It can be shown [Fetter, Walecka, 1980] that, in terms of the normal coordinates,

$$T = \frac{1}{2}\sum_{\sigma\sigma'} m_{\sigma\sigma'} \dot{q}_\sigma \dot{q}_{\sigma'} \tag{1.57}$$

where the reduced mass matrix is defined by

$$m_{\sigma\sigma'} = \sum_i m_i \left(\frac{\partial \mathbf{R}_i}{\partial q_\sigma} \cdot \frac{\partial \mathbf{R}_i}{\partial q_{\sigma'}}\right)_0 \tag{1.58}$$

which becomes a real, symmetric, constant matrix for the equilibrium geometry.

The Hamiltonian operator $\hat{H}_{\text{vib}}$ could be obtained from (1.48) and (1.55), however the Schrödinger equation would be very difficult to solve due to the coupling $k_{\sigma\sigma'}$ between terms. It can be shown [Fetter, Walecka, 1980] that a set of normal coordinates can always be determined so that the matrices k and m are diagonalized. In this case the potential energy is given by

$$V = \frac{1}{2}\sum_\sigma k_\sigma q_\sigma^2 \tag{1.59}$$

and the kinetic energy is

$$T = \frac{1}{2}\sum_{\sigma} m_\sigma \dot{q}_\sigma^2 = \sum_{\sigma} \frac{p_\sigma^2}{2m_\sigma} \tag{1.60}$$

where we use $p_\sigma \equiv m_\sigma \dot{q}_\sigma$. Then the Hamiltonian operator becomes

$$\hat{\mathcal{H}}_{\text{vib}} = \sum_{\sigma} \hat{\mathcal{H}}_{\text{vib},\sigma} \tag{1.61}$$

where

$$\hat{\mathcal{H}}_{\text{vib},\sigma} = \frac{\hat{p}_\sigma^2}{2m_\sigma} + \frac{1}{2}k_\sigma q_\sigma^2. \tag{1.62}$$

The vibrational Hamiltonian can be written as a sum of noninteracting harmonic oscillators and the wave function can be written as the product

$$\psi_{\text{vib}}(\mathbf{q}) = \prod_{\sigma} \psi_{\text{vib},\sigma}(q_\sigma). \tag{1.63}$$

The energy is then given by the sum

$$E_{\text{vib}} = \sum_{\sigma} E_{\text{vib},\sigma} \tag{1.64}$$

where

$$\hat{\mathcal{H}}_{\text{vib},\sigma}\psi_{\text{vib},\sigma} = E_{\text{vib},\sigma}\psi_{\text{vib},\sigma}. \tag{1.65}$$

The operator (1.62) is the Hamiltonian of a simple quantum mechanical harmonic oscillator and the eigenfunctions $\psi_{\text{vib},\sigma}(q_\sigma)$ are well known. The energy eigenvalues are given by

$$E_{\text{vib},\sigma} = (\nu_\sigma + \frac{1}{2})\hbar\omega_\sigma \tag{1.66}$$

where

$$\omega_\sigma = \sqrt{\frac{k_\sigma}{m_\sigma}} \tag{1.67}$$

and

$$\nu_\sigma = 0, 1, 2, \cdots; \quad \sigma = 1, \cdots, n. \tag{1.68}$$

For small displacements the oscillations about the equilibrium configurations reduce to those of a set of independent harmonic oscillators of frequency ω_σ. Any small amplitude motion is then a linear combination of the harmonic oscillators.

The determination of the types of motion corresponding to each normal mode can, in general, be determined from the masses of the nuclei and the equilibrium configuration. One method [Berry, Rice, Ross, 1980] for determining the normal mode motions is to examine the molecule in the molecular frame. Here the sum of the momenta of the nuclei is zero

$$\sum_i \mathbf{P}_i = \mathbf{0}. \tag{1.69}$$

Since the coordinate system rotates with the molecule the total angular momentum must also vanish

$$\sum_i \mathbf{L}_i = \mathbf{0}. \tag{1.70}$$

Since the particles are in simple harmonic motion the momentum components are a quarter of a cycle ahead of the displacements

$$\mathbf{P}_i = \frac{d\mathbf{R}_i}{dt} = i\omega_\sigma \mathbf{R}_i \tag{1.71}$$

so that (1.69) becomes

$$\sum_i m_i \mathbf{R}_i = \mathbf{0}. \tag{1.72}$$

Since each nucleus i oscillates about an equilibrium position $\mathbf{R}_i^{eq}$ each angular momentum is

$$\mathbf{L}_i = m_i \mathbf{R}_i^{eq} \times \dot{\mathbf{R}}_i \tag{1.73}$$

so that

$$\sum_i m_i \mathbf{R}_i^{eq} \times \mathbf{R}_i = \mathbf{0}. \tag{1.74}$$

Combining (1.72) and (1.74) a set of relative coordinate displacements can be determined for each type of molecular configuration. Figure 1.4.1 and 1.4.2 show the various vibration modes for the CO_2 and H_2O molecule respectively.

To evaluate the relative vibrational frequencies of the various modes requires a knowledge of the potential energy surface $E(\mathbf{R})$ and this is not always available. However the relative magnitudes of the frequencies can occasionally be established. Consider the CO_2 molecule in the following example. This molecule has four modes, an asymmetric stretching (ν_3), symmetric stretching (ν_1), and two degenerate bending modes (ν_2). For a given displacement, the bending modes require less stretching of the bonds and hence smaller changes in the bond energy than the stretching modes. Therefore the bending modes should have lower frequencies. Also since the C atom is lighter than the O atom, and since the asymmetric mode requires larger bond stretching than the symmetric mode, the asymmetric stretching mode should have a higher frequency. Thus the frequencies should be ordered as

$$\varsigma(\text{asymm stretch}) > \varsigma(\text{symm stretch}) > \varsigma(\text{bending}). \tag{1.75}$$

This is in fact true for the CO_2 molecule where it is found spectroscopically that $\varsigma(\text{asymm stretch}) = 2349\text{cm}^{-1}$, $\varsigma(\text{symm stretch}) = 1388\text{cm}^{-1}$, and $\varsigma(\text{bending}) = 667\text{cm}^{-1}$. These are referred to as the ν_3, ν_1, and ν_2 vibration modes respectively.

Each vibrational mode can be excited to many energy levels. In the harmonic oscillator an infinite set of energy eigenvalues are spaced at inter-

vals of $\hbar\omega$. In real molecules, the higher vibrational energy levels stretch the molecule. At farther separations the molecule breaks apart because the quantum mechanical binding energy of the electron cloud becomes weaker than nuclear repulsion [Berry, Rice, Ross, 1980]. The bound energy levels become more closely spaced as the ibational quantum number increases since the average curvature of the potential well represented by the k_σ well is reduced. This due to deviations of the binding energy from a pure parabolic potential and is shown in Figure 1.4.3.

Each mode of oscillation may have more than one quantum of vibrational energy. In fact, different modes of oscillation may be present simultaneously. The modes are classified by the number of vibrational quanta associated with the state [see Herzberg, 1945]. As an example, the first excited asymmetric vibrational mode of CO_2 is labeled the 'ν_3' which stands for one quantum of the $n = 3$ vibrational state. Two quanta of the symmetric stretching mode is labeled '$2\nu_1$'. Combinations are designated by a sum. For the vibrational state with one quantum in the symmetric stretching $n = 1$ and two quanta in the bending $n = 2$ modes is labeled $\nu_1 + 2\nu_2$. Further elaboration on rotational-vibrational states and nomenclature for many molecules is given by Herzberg (1945).

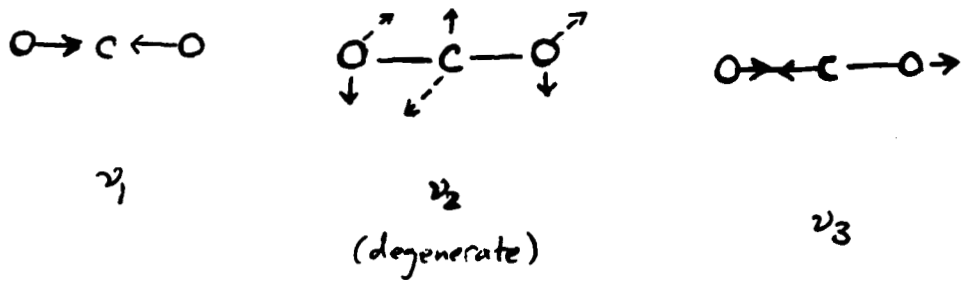

Figure 1.4.1 Normal mode vibrations for the CO_2 molecule.

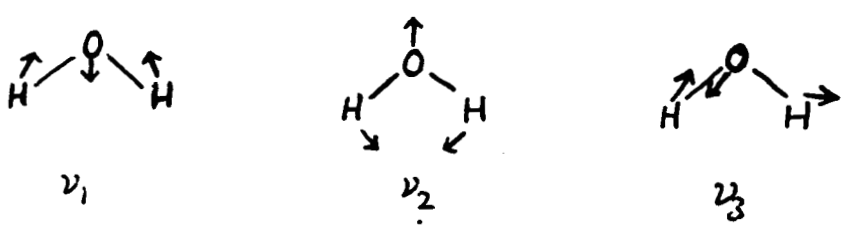

Figure 1.4.2 Normal mode vibrations for the H_2O molecule.

I.5 Rotational Energy Levels

In the case of diatomic molecules (such as CO) and linear triatomic molecules (such as CO_2 and N_2O) the rotational energy can be approximated reasonably well by the rigid symmetric top model

$$I_0 \equiv I_x = I_y \neq I_z \tag{1.76}$$

where the z axis is defined to be the bonding axis. Then the rotational Hamiltonian can be expressed as

$$\hat{\mathcal{H}}_{\text{rot}} = \frac{\hat{\mathbf{L}}^2}{2I_0} + \frac{1}{2}\left(\frac{1}{I_z} - \frac{1}{I_0}\right)\hat{L}_z^2, \tag{1.77}$$

where $\hat{\mathbf{L}}^2$ is the total angular momentum operator (squared) and the z component of the angular momentum operator is $\hat{L}_z$ whose eigenfunctions are the spherical harmonics $Y_{lm}(\theta,\phi)$ [Berry, Rice, Ross, 1980],

$$\hat{\mathbf{L}}^2 Y_{lm}(\theta,\phi) = l(l+1)\hbar^2 Y_{lm}(\theta,\phi), \tag{1.78}$$

$$\hat{L}_z Y_{lm}(\theta,\phi) = m\hbar Y_{lm}(\theta,\phi). \tag{1.79}$$

In the case of the rigid rotor the energy levels are

$$E_{\text{rot}} = \frac{\hbar^2}{2}\left[\frac{l(l+1)}{I_0} + m^2\left(\frac{1}{I_z} - \frac{1}{I_0}\right)\right] \tag{1.80}$$

for $l = 0, 1, 2, \ldots$ and $m = -l, \ldots, l$.

If the atoms are considered as mass points then there is no z component of the angular momentum and the levels are $2l+1$ degenerate. However, in a linear molecule the contributions to I_z from the electrons and the non-zero

nuclear radii are both very small, $I_z \ll I_0$, and the coefficient of $\hat{L}_z^2$ in (1.80) is much larger than that of $\hat{\mathbf{L}}^2$. For example, the energy associated with $\hat{L}_z^2$ is very large when $L_z \neq 0$ in all states except the ground states when it vanishes [Goody, 1964; Berry, Rice, Ross, 1980]. In any case, this second term can be included into the electronic energy since it is a constant and the rotational energy can be described by

$$E_{\text{rot}} = \frac{J(J+1)\hbar^2}{2I_0} \tag{1.81}$$

for $J = 0, 1, 2, \cdots$. The quantum number J is used instead of l in describing molecular angular momentum and in the case of linear molecules $\Lambda\hbar$ is identified as the z component of angular momentum where Λ is an integer. For a linear molecule $\Lambda = 0, 1, 2, \cdots$ and therefore the total angular momentum must be equal to or greater than Λ, $J = \Lambda, \Lambda+1, \Lambda+2, \cdots$. Most of the infrared rotational-vibrational spectra described in this study are associated with molecules that are in the electronic ground state which corresponds to $\Lambda = 0$. In the case of the asymmetric top where all moments of inertia are unequal such as the case for H_2O there is no axis about which the angular momentum is conserved and the solutions cannot be described by spherical harmonics. The solutions still have $2l+1$ levels for each value of l, but they are complex and there are no degeneracies [Herzberg, 1945; Goody, 1964].

I.6 Rotation-Vibration Spectra

The moment of inertia I_0 is related to the bond lengths between atoms. When a molecule undergoes vibrational oscillation, the anharmonicity in the potential well forces the average equilibrium bond length for each vibrational state to increase. This increases the moment of inertia and decreases the energies of the rotational levels (1.81). The modified rotational energy levels are described by [Berry, Rice, Ross, 1980]

$$\begin{aligned} E_{\text{vib-rot}} &= E_{\text{vib}} + E_{\text{rot}} \\ &= E_{\text{vib}} + J(J+1)hcB_\nu \qquad (1.82) \\ &= J(J+1)hc\left[B_e - \alpha_e(\nu + \frac{1}{2}) + \cdots\right] \qquad (1.83) \end{aligned}$$

where B_ν is the rotational constant for the vibration level ν, α_e is a constant, and $B_e = \hbar/4\pi cI_0$ is the constant which characterizes the energy of the rigid rotator. The energy levels (1.83) describe linear molecules such as CO, CO_2 and N_2O. The energy levels are much more complicated for nonlinear molecules such as H_2O and CH_4 and cannot be described by (1.82-3).

If the energy of the incoming photon is equal to the difference between two energy levels of a molecule, a transition between the two states may be induced provided the molecule can interact with field as a whole. The probability of a transition between two states is proportional to $|\mu_{n,n'}|^2$ where $\mu_{n,n'}$ is the dipole between the two states n and n'

$$\mu_{n,n'} = \langle n'|\mu|n\rangle. \qquad (1.84)$$

The dipole operator μ is usually given by $e\mathbf{r}$, e being the charge of the electron and $\mathbf{r}$ the position vector. There are additional terms to the transition probability involving quadrupole moments, magnetic dipole moments, and so on, however rates of these types of transitions are usually of an order of magnitude or more smaller than those for electric dipole transitions [Steinfeld, 1985]. For the rigid rotator it can be shown [Goody, 1964; Berry, Rice, Ross, 1980] that the probability for a dipole transition is non-zero if $\Delta J = \pm 1$. For the harmonic oscillator the dipole selection rule is $\Delta\nu = \pm 1$. A molecule can undergo transitions in which both the vibrational and rotational quantum numbers change according to the selection rules. I will be concerned here with rotation-vibration transitions in the ground state since these are the dominant type of transitions observed in the ATMOS spectra.

In (1.82-3) we see that the rotation-vibration energy is proportional to the constant hc. We can define a new quantity which describes the rotational part of the energy

$$\epsilon_{\text{rot}} \equiv \frac{E_{\text{rot}}}{hc} \tag{1.85}$$

$$= J(J+1)\left[B_e - \alpha_e\left(\nu + \frac{1}{2}\right) + \cdots\right]. \tag{1.86}$$

The unit of measurement of this quantity is cm^{-1}. The differences between energy levels $\Delta\epsilon$ described in the manner of (1.85-6) is in terms of wavenumbers ς which is the number of wavelengths of radiation within a centimeter of length in a vacuum. If λ is the wavelength in vacuum then the frequency f is related to it by

$$f = \frac{c}{\lambda}. \tag{1.87}$$

For a transition of energy difference ΔE the corresponding frequency of radiation is

$$f = \frac{\Delta E}{h} = c\,\Delta\varepsilon \equiv c\,\varsigma. \tag{1.88}$$

Explicitly,

$$f \propto \varsigma = 1/\lambda. \tag{1.89}$$

Therefore frequency and wavenumbers are proportional to each other.

In an absorption or emission process the energy of each photon involved must equal the difference between the energy levels. For linear molecules, if the lower energy level of the vibrational mode is given by the quantum numbers ν, J and that of the upper energy level by ν', J' then the energy difference, in wavenumbers, is

$$\varsigma = (\nu' - \nu)\varsigma_e + J'(J'+1)B_{\nu'} - J(J+1)B_\nu \tag{1.90}$$

where

$$\varsigma_e = \frac{\hbar\omega_e}{hc} \tag{1.91}$$

for the vibrational mode. For absorption processes in which $\Delta\nu = +1$ there are two sets of rotation lines, those with $\Delta J = +1$ and those with $\Delta J = -1$. $\Delta J = 0$ is prohibited in dipole transitions in the ground electronic state since there is no net dipole moment between the states. The set of transitions where $\Delta J = +1$ is called the R branch and is given by $J' = J + 1$. The line positions for this branch can be written in the form

$$\varsigma_R = \varsigma_e + (J+1)(B_{\nu+1} + B_\nu) + (J+1)^2(B_{\nu+1} - B_\nu). \tag{1.92}$$

The case where $\Delta J = -1$ is called the P branch and is given by $J' = J - 1$. The line positions are

$$\varsigma_P = \varsigma_e - J(B_{\nu+1} + B_\nu) + J^2(B_{\nu+1} - B_\nu). \tag{1.93}$$

The quadratic terms involve the differences due to vibrational stretching between the rotational constants. In an infrared transition where the electronic states remain the same for reasons explained earlier the rotational constant decreases with increasing the vibrational quantum number ν. From (1.92) it can be seen that a value for J is eventually reached where the frequencies begin to decrease with increasing J. This causes a band head - such as the solar CO band heads observed in the ATMOS spectra §II.3 - and occurs in the R branch in rotation-vibration spectra since $B_{\nu+1} < B_\nu$ [Berry, Rice, Ross, 1980]. The B_ν values, however, are usually very close to one another and it is difficult to observe band heads in spectra taken at ordinary temperatures. Typical values for the rotational constants is of the order of several cm^{-1} for atmospheric gases such as CO_2 and N_2O. The lines are spaced far enough apart that lines of the same vibration band do not interfere with each other.

I.7 Radiative Transfer

The energy of a molecule in the ground electronic state consists of translational, vibrational and rotational energy. The vibrational and rotational energy are associated with internal degrees of freedom while the translational motion is related to the center of mass coordinates. The molecules can transfer energy among themselves via collisional and radiative processes. Molecules can lose or gain translational energy due to elastic collisions with other molecules. The internal and translational energy can also be exchanged in inelastic collisions. When a gas is subjected to radiation of frequencies comparable to differences in energy levels of its molecules energy can be absorbed and emitted. The populations of the various energy levels is therefore related to the balance between collisional and radiative processes.

In the lower atmosphere below 70 km the collision rates are larger than the radiative rates due to the higher molecular density [Gao, 1988]. The populations of the the rotational-vibrational levels are then dominated by molecular collisions and are described by the Boltzmann distribution [Thorne, 1988]. A quantity called the temperature T can be defined which specifies the mean kinetic energy $\frac{3}{2}kT$ of the colliding particles and the particles follow a Maxwellian velocity distribution. This is called local thermodynamic equilibrium (LTE) since the molecules cannot be considered to be in complete thermodynamic equilibrium due to radiative processes between themselves, the rest of the atmosphere, space and solar radiation. The molecules can be considered to be in local thermodynamic equilibrium with the total radiation

of the atmosphere which is described by the Planck blackbody distribution at the kinetic temperature temperature T [Thorne, 1988]. In the following derivations we assume that the condition of LTE is adequate and this was found to be approximately true by Gao (1988) for the ν_3 rotation-vibration transitions of CO_2 at altitudes between 70 and 130 km.

SPONTANEOUS EMISSION

Spontaneous emission at a frequency f_0 occurs naturally from an excited state s to a lower energy state s' . It is induced by zero point oscillations in the radiation field [Cohen-Tannoudji, 1977]. The rate of this process $A_{s\to s'}$ is related to the electric dipole matrix element $\mu_{ss'} = \langle s|\mu|s'\rangle$ between the states by

$$A_{s\to s'} = \frac{16\pi^3 f_0^3}{3\epsilon_0 hc^3}|\mu_{ss'}|^2 \tag{1.94}$$

[Thorne, 1988]. The mean lifetime between the states is then given by

$$\tau_{ss'} = A^{-1}_{s\to s'}. \tag{1.95}$$

STIMULATED EMISSION AND ABSORPTION

Besides the spontaneous emission of radiation from an excited state to a lower energy state there can also induced transitions in the presence of external fields. Suppose a lower energy state has the energy $hf_{s'}$ and the upper state has the energy hf_s. An electromagnetic wave with frequency

$f_0 = f_s - f_{s'}$ can be described by an electric field

$$\begin{aligned} \mathcal{E} &= \mathcal{E}_0 \cos(2\pi f_0 t) = \mathcal{E}_0 \cos(2\pi f_s t - 2\pi f_{s'} t) \\ &= \mathcal{E}_0 \left[\cos(2\pi f_{s'} t)\cos(2\pi f_s t) + \sin(2\pi f_{s'} t)\sin(2\pi f_s t)\right]. \end{aligned} \quad (1.96)$$

Each element of the sum (1.96) has a component that oscillates with the frequency of each state. It is these resonances with the dipole moment of each state that eventually induces transitions between the two states [Aller, 1963]. The photon of frequency f_0 can drive a transition between the two states, with an efficiency which depends on the strength of the dipole between the states. The electric field can induce both absorption and emission of a photon and the rates of both of these processes are proportional to the average photon intensity $\bar{I}$ near the transition frequency ν_0 [Thorne, 1988]

$$\tau_{\text{abs}} = B_{s' \to s} \bar{I}, \quad (1.97)$$

$$\tau_{\text{ems}} = B_{s \to s'} \bar{I} \quad (1.98)$$

respectively. The coefficients $A_{s \to s'}$, $B_{s' \to s}$ and $B_{s \to s'}$ are commonly referred to as *Einstein coefficients* and are used to describe the rates of the various emission and absorption processes.

RADIATIVE BALANCE

If $n_{s'}$ and n_s are the density of molecules in the lower and upper state respectively then the relationship between the absorption and emission processes in radiative equilibrium is given by the relation

$$n_{s'} B_{s' \to s} \bar{I} = n_s A_{s \to s'} + n_s B_{s \to s'} \bar{I} \quad (1.99)$$

since in equilibrium the rate of photons emitted is equal to the rate of photons being absorbed. Then the photon intensity can be solved for

$$\bar{I} = \frac{A_{s\to s'}/B_{s\to s'}}{(n_{s'}B_{s'\to s}/n_s B_{s\to s'}) - 1}. \tag{1.100}$$

The ratio of the populations n'_s/n_s is undetermined. In local thermodynamic equilibrium at temperature T the ratio of the populations in each state is given by Boltzmann's equation [Steinfeld, 1985; Thorne, 1988]

$$\frac{n_{s'}}{n_s} = \frac{g_{s'}}{g_s} e^{hf_0/kT} \tag{1.101}$$

where g_i are the degeneracies of each state. Then

$$\bar{I} = \frac{A_{s\to s'}/B_{s\to s'}}{(g_{s'}B_{s'\to s}/g_s B_{s\to s'})\, e^{hf_0/kT} - 1}. \tag{1.102}$$

However from Planck's Law [Aller, 1963]

$$I_f = \frac{2hf^3/c^2}{e^{hf/kT} - 1} \tag{1.103}$$

for a blackbody radiator at the temperature T. Since I_f varies slowly over the width $\Delta\nu$ of the line, $\bar{I}$ can be replaced with I_{f_0}

$$\frac{2hf_0^3/c^2}{e^{hf_0/kT} - 1} = \frac{A_{s\to s'}/B_{s\to s'}}{(g_{s'}B_{s'\to s}/g_s B_{s\to s'})\, e^{hf_0/kT} - 1}. \tag{1.104}$$

Since this must hold for all T it can be shown that the Einstein coefficients are then related to each other by

$$A_{s\to s'} = \frac{2hf_0^3}{c^2} B_{s\to s'}, \tag{1.105}$$

$$g_{s'}B_{s'\to s} = g_s B_{s\to s'}. \tag{1.106}$$

and depend only on the electric dipole matrix element and the energy difference between the states.

The case where LTE is not valid is discussed by Gao (1988) and Thorne (1988). At altitudes in the atmosphere high enough where molecular collisions are less frequent than radiative processes, the populations of rotational-vibrational energy levels are dominated by absorption and emission processes. The kinetic temperature T is then not adequate to describe the populations of the states. The lower atmosphere is the main source of photons present for absorption and the blackbody radiation distribution which describes them may not correspond to the local kinetic temperature of the gas [Gao, 1988]. The atmosphere is then considered to be in a state of non-LTE (NLTE). The grand effect of NLTE is to alter the populations of the various occupied states. It was found by Gao (1988) that between 70 and 130 km the deviations of the atmosphere from LTE do not affect the populations of rotational levels significantly from the Boltzmann distribution at a kinetic temperature corresponding to the temperature of the lower atmosphere. Although LTE/NLTE is important for determining the populations of various states, it is not important for obtaining wind speeds §§II.

I.8 Line Shapes

The shapes of spectral lines depends on the molecules and their physical conditions. In this section we examine some of the most important physical

processes which describe spectral line shapes. Due to the uncertainty principle the finite life times of excited molecular states causes the lines to have a natural width (in photon energy) and shape. This width is a characteristic fundamental to the molecule and depends only on the frequency of the transition and the dipole matrix elements between the states (1.94). The thermal motions of the molecules also causes the frequencies of radiation involved in the absorption/emission processes to be Doppler shifted from the natural line shape as described by (I.1). The distribution of velocities and hence Doppler shifts are governed by the Maxwell velocity distribution. Finally, a molecule may also undergo collisions with other molecules in the gas. A molecule can interact with the radiation field during the period of time between collisions. A sum of all frequencies over that period of time can appear to the molecule as the correct driving frequency due to the properties of the Fourier transform. Frequencies well away from the transition frequency may drive the transition. All of these mechanisms as well as combinations of them can be described by a line profile $\phi(\varsigma)$ which describes the normalized distribution of the photon energies which induce transitions.

The width ΔE of an energy level s is implied by the uncertainty relation

$$\Delta E_s \, \tau_s \geq \frac{\hbar}{2} \tag{1.107}$$

where τ_s is the mean lifetime of the state. If the lower state has an infinite lifetime, which is the case for transitions to the ground state, then width of the transition, in wavenumbers (1.85), is

$$\Delta\varsigma_s \geq \frac{1}{4\pi c \tau_s}. \tag{1.108}$$

In general, each transition has a natural lifetime given by

$$\tau_s^{-1} = \sum_{s'} A_{s \to s'} \tag{1.109}$$

where s' denotes all lower energy states and $A_{s \to s'}$ is given by (1.94), the coefficient of the wave function of the state s is then of the form

$$\psi \propto \tau_s^{-1/2} e^{-t/2\tau_s} \tag{1.110}$$

since the square modulus of the wave function represents the probability of finding the state and $\tau_s^{-1} e^{-t/\tau_s}$ is the probability density of a decay between times t and $t + dt$. Consider a transition at frequency f_0. The decay causes the emission of photons about the frequency f_0. The electric field $\mathcal{E}$ due to this transition caused by emission decays as [Thorne, 1988]

$$\mathcal{E}(t) \propto e^{-t/2\tau_s} e^{-i\omega_0 t}. \tag{1.111}$$

where $\omega_0 = 2\pi f_0 = 2\pi c \varsigma_0$. The strength of the electric field decays with increasing time and has an oscillating part due to the transition frequency. This electric field has a Fourier transform

$$\mathcal{E}(\omega) = (2\pi)^{-1} \int_{-\infty}^{\infty} dt\, \mathcal{E}(t) e^{i\omega t}. \tag{1.112}$$

Since $\mathcal{E}(t)$ is only defined for $t \geq 0$,

$$\mathcal{E}(\omega) \propto \left[\frac{1}{2\tau} - i(\omega - \omega_0) \right]^{-1}. \tag{1.113}$$

The line intensity is proportional to the square of the electric field [Jackson, 1975] $I_\omega = |\mathcal{E}(\omega)|^2$ and it can be shown by integration that

$$I(\varsigma) = I_0 \frac{1}{\pi} \frac{\Delta\varsigma_N}{(\varsigma - \varsigma_0)^2 + (\Delta\varsigma_N)^2}. \tag{1.114}$$

where $\Delta\varsigma_N = (4\pi c\tau_s)^{-1}$ is the natural line width in wavenumbers which is in agreement with the width predicted by the uncertainty principle (1.108). The total line intensity integrated over all wavenumbers is defined as

$$I_0 \equiv \int_{-\infty}^{+\infty} I(\varsigma)\, d\varsigma. \tag{1.115}$$

The line profile for natural broadening is

$$\phi_N(\varsigma) \equiv \frac{1}{\pi}\frac{\Delta\varsigma}{(\varsigma-\varsigma_0)^2+(\Delta\varsigma)^2} \tag{1.116}$$

and this is normalized as $\int_{-\infty}^{\infty}\phi_N(\varsigma)\,d\varsigma = 1$.

As an example, for an infrared transition to the ground state $\tau_s = A_{2\to1}$. Since $f_0 = c\,\varsigma_0$ then (1.94) becomes

$$A_{2\to1} = \frac{16\pi^3\varsigma_0^3}{3\epsilon_0 h}\,|\mu_{21}|^2 \tag{1.117}$$

For a typical ν_3 CO_2 transition we can choose, for exampleoul-m, $\varsigma_0 = 2330$ cm^{-1} and $\mu_{12} \sim 10^{-29}$ Cm as typical values. Then $A_{2\to1} \sim 3.6 \times 10^4$ Hz. This gives $\Delta\varsigma_N \sim 7 \times 10^{-9} cm^{-1}$ as the natural width which indicates that these lines are very narrow, about six to seven orders of magnitude smaller than the resolution of the ATMOS interferometer.

The thermal motions of the molecules in a gas cause the frequencies of the absorbed or emitted photons to be Doppler shifted

$$\frac{\varsigma_0' - \varsigma_0}{\varsigma_0} = \frac{v}{c} \tag{1.118}$$

where ς_0' is the wavenumber in the observer's frame, ς_0 is the frequency in the molecule's rest frame and v is the relative speed between the molecule and the observer along the line of sight. The fraction of molecules moving with

speed v and $v + dv$ along the line of sight is given by a normalized Maxwell distribution [Thorne, 1988]

$$\frac{dn}{n} = \sqrt{\frac{2kT}{\pi m}} \exp\left[-\frac{mv^2}{2kT}\right] dv \tag{1.119}$$

$$= \frac{c}{\varsigma_0}\sqrt{\frac{2kT}{\pi m}} \exp\left[-\frac{mc^2(\varsigma - \varsigma_0)^2}{2kT\varsigma_0^2}\right] d\varsigma. \tag{1.120}$$

From this result the Doppler line profile is given by

$$\phi_D(\varsigma) = \frac{1}{\Delta\varsigma_D\sqrt{\pi}} \exp\left[-\left(\frac{\varsigma - \varsigma_0}{\Delta\varsigma_D}\right)^2\right] \tag{1.121}$$

The Doppler width is

$$\Delta\varsigma_D = \varsigma_0\sqrt{\frac{2kT}{mc^2}}. \tag{1.122}$$

As an example, for a temperature of 300 K, $\varsigma_0 = 2300$ cm^{-1}, and a CO_2 mass of 44 gm/mole, $\Delta\varsigma_D = 2.6 \times 10^{-3}$cm^{-1}. Note that the Doppler broadening is much larger than natural broadening

$$\Delta\varsigma_D \gg \Delta\varsigma_N. \tag{1.123}$$

in the infrared regions but is still about 5 times smaller than the resolution of the ATMOS interferometer.

A molecule can also have collisions with other molecules. Let the mean time between collisions be τ_C. For simplicity consider a gas with a density such that the time between collisions is much greater that the interaction time τ_I, the time for the collision processes. If the time between collisions is t^* the radiation affecting the molecule will subject to random phase interruptions caused by collisions [Rybicki, Lightman, 1979]. Specifically, between collisions, the component of the electric field which affects the molecule is

$$\mathcal{E}'(t) \propto e^{-i\omega_0 t} \tag{1.124}$$

for $0 \leq t \leq t^*$ where again $\omega_0 = 2\pi f_0 = 2\pi c\varsigma_0$. By using (1.112) the Fourier transform of this field is

$$\mathcal{E}'(\omega, t^*) \propto \exp\left[i(\omega - \omega_0)t^*/2\right] \frac{\sin\left[(\omega - \omega_0)t^*/2\right]}{(\omega - \omega_0)/2}. \tag{1.125}$$

Again since $I'(\omega, t^*) = |\mathcal{E}'(\omega, t^*)|^2$ then

$$I'(\omega, t^*) \propto \left(\frac{\sin[(\omega - \omega_0)t^*/2]}{(\omega - \omega_0)/2}\right)^2. \tag{1.126}$$

The probability $d\mathcal{P}(t^*)$ that the molecule has a collision between time t^* and $t^* + dt^*$ is

$$d\mathcal{P}(t^*) = \tau_C^{-1} e^{-t^*/\tau_C} dt^*. \tag{1.127}$$

The final intensity distribution is given by the average of the individual intensity distributions (1.126) over the probability function (1.127)

$$I(\omega) = \tau_C^{-1} \int_0^\infty I'(\omega, t^*) e^{-t^*/\tau_C} dt^*. \tag{1.128}$$

This integral can integrated by standard methods to be

$$I(\varsigma) = I_0 \frac{1}{\pi} \frac{\Delta\varsigma_C}{(\varsigma - \varsigma_0)^2 + (\Delta\varsigma_C)^2} \tag{1.129}$$

where the collisional width, also called the Lorentz width, is given by

$$\Delta\varsigma_C = (2\pi c\tau_C)^{-1} \tag{1.130}$$

and I_0 is the total line intensity (1.115). The profile for pressure broadening is also a Lorentzian like natural broadening

$$\phi_C(\varsigma) \equiv \frac{1}{\pi} \frac{\Delta\varsigma_C}{(\varsigma - \varsigma_0)^2 + (\Delta\varsigma_C)^2}. \tag{1.131}$$

The mean time between collisions can be estimated by

$$\tau_C = (\text{mean free path})/(\text{thermal speed}) = \frac{1}{n\Sigma}/\sqrt{\frac{3kT}{m}} \qquad (1.132)$$

where n is the density of molecules, Σ is an average collision cross section, m is the molecular mass. From (1.130)

$$\Delta\varsigma_C = \frac{1}{c}P\Sigma\sqrt{\frac{3}{4\pi^2 mkT}} \qquad (1.133)$$

by using the ideal gas equation $P = nkT$. Since atmospheric densities decrease with height exponentially we expect that collision broadening to be important primarily near the surface. As height increases the collisional frequencies decrease in a like manner and we expect that the lines are governed by the Doppler shape. Above about 50 km the primary line shapes are Doppler with small Lorentz contributions. Below about 20 km pressure broadening is important.

In the regions between 20 and 60 km altitudes the atmospheric absorption lines can show both Doppler and Lorentz (pressure) broadening. The observed line shape is actually a set of Lorentz profiles averaged over the Maxwell velocity distribution [Rybicki, Lightman, 1979]. The line shape is a convolution of the Doppler and Lorentz profiles and is called the Voigt profile

$$\phi_V(\varsigma) = \phi_D(\varsigma) * \phi_L(\varsigma) = \int_{-\infty}^{\infty} d\varsigma'\, \phi_D(\varsigma' - \varsigma)\, \phi_C(\varsigma'). \qquad (1.134)$$

This profile is normalized since the Doppler and Lorentz profiles are normalized and this can be seen by integration

$$\begin{aligned} \int_{-\infty}^{\infty} d\varsigma\, \phi_V(\varsigma) &= \int_{-\infty}^{\infty} d\varsigma'\, \phi_L(\varsigma') \int_{-\infty}^{\infty} d\varsigma'\, \phi(\varsigma' - \varsigma) \\ &= 1. \end{aligned} \qquad (1.135)$$

The Voigt line shape is governed by two widths, the Doppler width $\Delta\varsigma_D$ and Lorentz width $\Delta\varsigma_C$. When pressure broadening becomes dominant $\Delta\varsigma_C \gg \Delta\varsigma_D$ and the line shape becomes a pure Lorentzian. In the upper atmosphere where pressure broadening is negligible compared to Doppler broadening $\Delta\varsigma_D \gg \Delta\varsigma_L$ the line center has a Doppler shape while the 'wings' - the absorption outside of the Doppler width - have the Lorentz shape.

I.9 Absorption and Emission Coefficients

The ATMOS spectra show the absorption of the atmospheric gases along the line of sight between the observer and the sun. The ray path passes through all altitudes above the tangent point of observation. In this section we discuss how the transmitted intensity depends on the amount of absorber along the line of sight. We use this information to examine how important the contributions of the absorber in regions far away from the tangent point contribute the the observed line positions in §II.13.

The line shapes discussed in the previous section apply to large ensembles of molecules undergoing radiative and collisional transitions. Large amounts of gas along the line of sight between the radiation source and the instrument enable the molecules to absorb significant amounts of the incoming radiation due to cumulative effects of absorption. The absorption coefficient α_ς is defined to describe the loss of beam intensity dI_ς at wavenumber ς as it travels over a distance ds of the medium by

$$dI_\varsigma = -\alpha_\varsigma I_\varsigma \, ds. \tag{1.136}$$

A spontaneous emission coefficient j_ς is also defined as the power emitted per unit volume. This can be assumed to be isotropically distributed since there is no preferred direction of radiation in an emission. If an incident beam with parallel rays such as solar rays in the ATMOS experiment is used, then the spontaneous emission term j_ς can be neglected since most of the emitted radiation goes out of the field of view.

Let s be the upper energy state of a transition, s' the lower energy state and n the number of active molecules per unit volume. Then $hc\varsigma\, n_s A_{s\to s'}\phi(\varsigma)$ is the power emitted by spontaneous emission per unit volume per unit wavenumber where $hc\varsigma$ is the photon energy and $n_s A_{s\to s'}\phi(\varsigma)$ is the rate of photons emitted per unit wavenumber per unit volume. This radiation caused by this term is isotropically distributed and can be neglected relative to the beam absorption.

The power absorbed per unit wavenumber per unit volume is the difference between absorption and stimulated emission since the stimulated emission will be polarized with respect to the incoming radiation [Steinfeld, 1976] and can be thought of as "negative absorption"

$$hc\varsigma\,(n_{s'}B_{s'\to s} - n_s B_{s\to s'})I_\varsigma\,\phi(\varsigma).$$

Since the intensity I_ς is the power per unit wavenumber per unit area the power absorbed per unit wavenumber per unit volume is the change in intensity per unit length along the beam

$$\frac{dI_\varsigma}{ds} = hc\varsigma\,(n_{s'}B_{s'\to s} - n_s B_{s\to s'}). \tag{1.137}$$

Then the absorption coefficient can be determined from (1.136)

$$\alpha_\varsigma = hc\varsigma\,(n_s B_{s\to s'} - n_{s'}B_{s'\to s})\phi(\varsigma). \tag{1.138}$$

If the system is in thermodynamic equilibrium with itself, which is the case with of an atmosphere in LTE and will be assumed to be approximately true for NLTE [Gao, 1988] then from (1.101)

$$\frac{n_{s'}}{n_s} = \frac{g_{s'}}{g_s}e^{hc\varsigma/kT}. \tag{1.139}$$

By using this in (1.138) and using the Einstein relation (1.106)

$$\alpha_\nu = hc\varsigma\, n_{s'} B_{s'\to s}(1 - e^{-hc\varsigma/kT})\phi(\varsigma). \tag{1.140}$$

The transmitted intensity neglecting the spontaneous emission term is the solution of (1.136)

$$\frac{dI_\varsigma}{ds} = -\alpha_\varsigma I_\varsigma \tag{1.141}$$

which can be solved

$$I_\varsigma = I_\varsigma(0)e^{-\int_0^L \alpha_\varsigma ds} \tag{1.142}$$

where L is the total path length the radiation travels through the absorber and $I_\varsigma(0)$ is the radiation intensity in the absence of any absorption.

It was shown §I.8 that the line widths are much smaller than the central wavenumber ς_0. Also, at infrared wavenumbers and at typical atmospheric temperatures the exponential factor in (1.140) is much less than unity and the absorption coefficient can be well approximated by

$$\alpha_\varsigma \doteq n_{s'} hc\varsigma_0 B_{s'\to s}\phi(\varsigma). \tag{1.143}$$

Then the transmitted intensity (1.142) can be written as

$$I_\varsigma = I_\varsigma(0)e^{-k_\varsigma u}. \tag{1.144}$$

The number of molecules per unit area in the lower state is defined by

$$u = \int_0^L ds\, n_{s'} \tag{1.145}$$

where it is should be recalled that $n_{s'}$ is the density of molecules in the lower state. The absorption cross section per molecule k_ς is given by

$$k_\varsigma = S\phi(\varsigma). \tag{1.146}$$

and the *line strength* is defined as

$$S = hc\varsigma_0 B_{s' \to s}. \tag{1.147}$$

The line strength is also equal to the integrated absorption coefficient k_ς since the line profile is normalized and this can be shown by integrating (1.146)

$$S = \int_{-\infty}^{\infty} d\varsigma \, k_\varsigma. \tag{1.148}$$

I.10 Optical Depth, Equivalent Widths, and Curve of Growth

The optical depth τ_ς at a given wavenumber ς is related to the mean free path of a photon [Thorne, 1988]. We define

$$\tau_\varsigma = k_\varsigma u \tag{1.149}$$

so that (1.144) is

$$I_\varsigma(\tau_\varsigma) = I_\varsigma(0)\, e^{-\tau_\varsigma}. \tag{1.150}$$

For $\tau_\varsigma \ll 1$ the medium is "optically thin" while for $\tau_\varsigma \gg 1$ it is "optically thick". For the case of optically thin layers we can expand (1.150)

$$I_\varsigma(\tau_\varsigma) = I_\varsigma(0)\,(1 - \tau_\varsigma + \cdots). \tag{1.151}$$

In this case the transmitted intensity I_ς decreases linearly with an increase in the amount of absorber u. As the amount of absorber u increases this linear behavior no longer holds true and saturation is reached. The absorption line initially saturates at the line center and then outwards towards the "wings". Figure 1.10.1 shows this saturation as the amount of absorber increases.

The total loss of incident radiation due to absorption by the line is

$$\int_{\text{line}} d\varsigma\, [I_\varsigma(0) - I_\varsigma(\tau_\varsigma)] = \text{Power Loss/Area}. \tag{1.152}$$

The ratio of this quantity to the incident intensity per unit wavenumber defines the equivalent width

$$W = \int_{\text{line}} d\varsigma \left[1 - \frac{I_\varsigma(\tau_\varsigma)}{I_\varsigma(0)}\right]. \tag{1.153}$$

From (1.150) we have

$$W = \int_{\text{line}} d\varsigma \, (1 - e^{-\tau_\varsigma}). \tag{1.154}$$

The equivalent width is independent of the instrumental resolution [Thorne, 1988]. Although a decrease in resolution will cause the observed line to "spread out" over a greater spectral region, the equivalent width remains the same as the 'true' line. Thus measurements of the equivalent widths of absorption lines can be used to obtain information regarding the total absorption of the line and properties associated with it such as temperature, pressure, and absorption cross sections u [Gao, 1988]. If the instrumental resolution becomes larger and hence the resolved width of the line at, say, half maximum absorption increases, the peak absorptances must decrease since the equivalent width with remains the same.

A typical characteristic of an absorption feature is its width $\Delta\varsigma$ as described in §I.9. This is characteristic of Doppler and Lorentz lines, as well as the convolution of the two which is called a Voigt line. If we change variables

$$x = \frac{\varsigma - \varsigma_0}{\Delta\varsigma} \tag{1.155}$$

(1.154) can be written as

$$\frac{W}{\Delta\varsigma} = \int_{\text{line}} dx \, (1 - e^{-\tau_x}). \tag{1.156}$$

For the Doppler line (1.121)

$$\tau_x = Su \, \phi_{\text{D}}(\varsigma) = \frac{Su}{\Delta\varsigma_{\text{D}}} \frac{1}{\sqrt{\pi}} e^{-x^2}. \tag{1.157}$$

For the Lorentzian (1.131)

$$\tau_x = Su \, \phi_{\text{L}}(\varsigma) = \frac{Su}{\pi\Delta\varsigma_{\text{C}}} \frac{1}{1 + x^2}. \tag{1.158}$$

We see that in both cases the fraction of the equivalent width (EW) to the line width $W/\Delta\varsigma$ is a function of $Su/\Delta\varsigma$. If we define

$$\alpha = \frac{Su}{\Delta\varsigma} \tag{1.159}$$

then (1.157-8) can be written

$$\tau_x(\text{Doppler}) = \frac{1}{\sqrt{\pi}} e^{-x^2}\,\alpha, \tag{1.160}$$

$$\tau_x(\text{Lorentz}) = \frac{1}{\pi}\frac{1}{1+x^2}\,\alpha. \tag{1.161}$$

For the two cases I computed the integrals (1.150) as a function of α and are plotted in Figure 1.10.2. Both curves have the same slope in the region where $\alpha < 1$. This linear region is predicted by (1.156). For small τ_x we have

$$\frac{W}{\Delta\varsigma} \simeq \int_{\text{line}} dx\,\tau_x. \tag{1.162}$$

For the Doppler and Lorentz lines we have

$$\left(\frac{W}{\Delta\nu}\right)_{\text{Doppler}} \simeq \alpha\sqrt{\frac{1}{\pi}}\int_{-\infty}^{\infty} dx\, e^{-x^2} = \alpha, \tag{1.163}$$

$$\left(\frac{W}{\Delta\nu}\right)_{\text{Lorents}} \simeq \alpha\frac{1}{\pi}\int_{-\infty}^{\infty} dx\,\frac{1}{1+x^2} = \alpha. \tag{1.164}$$

The growth rate is the same for both type of lines in the linear regions. The equivalent width is then directly proportional to the amount of absorber. The linear growth for both Doppler and Lorentz lines continue until $\log Su/\Delta\varsigma \sim 1/2$ which can be seen in Figure 1.10.2.

As the amount of absorber continues to increase the equivalent width of a Doppler line W_D approaches almost ten times the line width $\Delta\varsigma_D$ and increasing the amount of absorber u does not increase the equivalent width significantly beyond this which can be seen in Figure 1.10.2. Since the Doppler

width $\Delta\varsigma_D$ depends primarily on the temperature T and not the pressure the equivalent width W_D will not change significantly with height.

For a pressure broadened line, the curve in Figure 1.10.2 shows that the equivalent width of a Lorentz line W_C increases indefinitely relative to the line width $\Delta\varsigma_C$. Since the line width depends directly on the pressure P (1.133), as the altitude decreases and the amount of absorber along the line of sight remains significant, the increasing pressure causes the equivalent width W_C of the lines to grow without limit. In the case of strong absorption lines such as the ν_3 CO_2 band, large spectral regions can become opaque due to strong pressure broadened saturation.

The increasing equivalent width limits the altitude ranges where pressure broadened lines may be useful for measuring wind speeds since the lines as observed by the instrument must not be distorted §I.12. If the equivalent width of the line is much smaller than the instrumental resolution, the line will yield approximately the same shape as an infinitesimally thin absorption line with the same equivalent width. "Flattening" of the line shape near the line center due to saturation can not be seen in the spectra and does not significantly effect the resolved line shape provided that $\Delta\varsigma_D \ll$ resolution. If the equivalent width becomes significant with respect to the instrumental resolution we expect that spectral features will become broadened. As shown in the next section, increasing the width of a feature in the processed spectra can significantly degrade the precision of determining line positions. Since the equivalent width of a Doppler line W_D is limited to about ten times the Doppler width $\Delta\varsigma_D$, and since the Doppler width is about 100 times smaller than the instrumental resolution, Doppler lines can be used over

altitude ranges spanning tens of kilometers for obtaining wind speeds without having to be concerned with significant increases in the Doppler equivalent width. On the other hand, the equivalent width of pressure broadened lines increases rapidly with increasing pressure and absorber amount u. Pressure broadened lines therefore have smaller ranges over which they can be useful for measuring Doppler shifts and lines used for measuring relative speeds need to be carefully chosen to avoid the effects of pressure broadening in the resolved spectra.

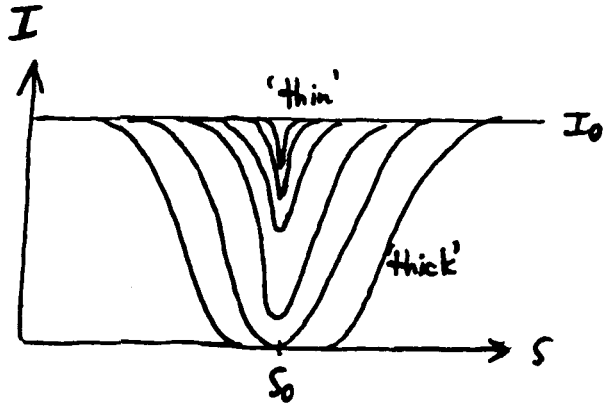

Figure 1.10.1 A sketch of line saturation as the optical depth changes from 'thin' ($\tau \ll 1$) to 'thick'. At saturation the line becomes opaque near the line center $ς_0$.

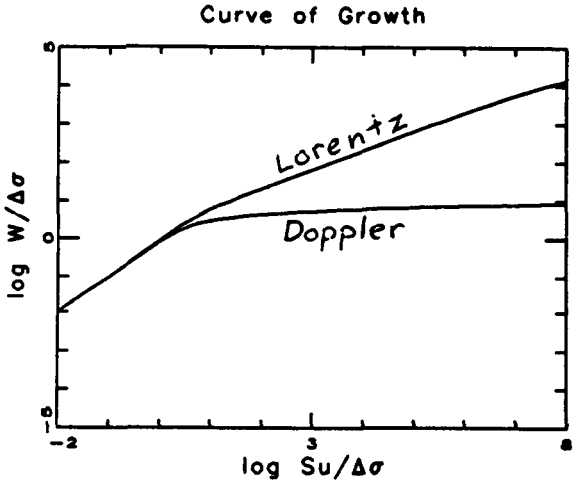

Figure 1.10.2 Curve of growth for Doppler and Lorentz lines computed from (1.156). The equivalent width W_D of the Doppler lines becomes almost 10 times its Doppler width $\Delta ς_D$ as the amount of absorber u increases. The equivalent width of the Lorenz lines W_C increases with u without limit relative to its collision broadened width $\Delta ς_C$.

I.11 Measurement Precision Theory

The purpose of this section is to examine how the measurement precision of the wavenumber of an absorption line is affected by the resolved shape of the line with a noisy background and digital frequency spacing. In the ATMOS spectra the noise level is about $\sigma(N) = 1\%$ of the background signal and the wavenumber spacing is 0.0075 cm^{-1}. For an absorption line with a typical resolved width of .015 cm^{-1} at half maximum, there are only 3 points to use to estimate the line position. The finite resolution of the spectra causes the lines to be "spread out" and the data used to obtain line positions correspond to the true spectra convolved with the (apodized) instrument function. Therefore the 'line shapes' present in the spectra are degraded by the instrumental resolution. In this section the 'width' of a line is the apparent or geometric width as it appears in the processed spectra. This instrumental width is limited by the resolution of the spectra.

Provided pressure saturation is not present, we can approximate the geometric shape of the a line in the convolved spectra by a parabola of the form

$$g(x) = \frac{2A_p}{w^2}x^2 \tag{1.165}$$

for $-w/2 \leq x \leq w/2$ where $x = 0$ corresponds to the line center, A_p is the geometric peak absorptance of the line and w the geometric width at half maximum. Figure 1.11.1 shows an example of this function. In order to test our ideas, we allow this function to describe the shape of the absorption line as it would be measured in the absence of noise. We can model the

actual observed data with this "clean" signal and a random distribution of noise added to each point. A random noise distribution $N(x)$ with a standard uncertainty $\sigma(N)$ is added to this "noiseless" signal $g(x)$ to produce an "observed signal" $g(x) + N(x)$.

Having obtained the data for this line suppose, for simplicity, that a trial function of the form

$$f(x) = (2A_p/w^2)(x - y)^2 \tag{1.166}$$

is to be fit to the observed signal $g(x) + N(x)$ by the least squares method. We wish to determine the best fit and hence the line position from this fit. We sample the signal $g(x) + N(x)$ at the n points x_j. The measured line center y_0 is the value of y which minimizes the least squares sum

$$M(y) = \sum_{j=1}^{n} \frac{[f(x_j) - (g(x_j) + N(x_j))]^2}{2\sigma^2(N)}. \tag{1.167}$$

The least squares sum M can be approximated by an integration over the range of sampled points

$$\begin{aligned} M &\approx \frac{1}{2\sigma^2(N)} \frac{n}{w} \int_{-w/2}^{w/2} dx \left[f(x) - (g(x) + N(x))^2 \right] \\ &= \frac{1}{2\sigma^2(N)} \frac{n}{w} \left[\int_{-w/2}^{w/2} dx \, (f(x) - g(x))^2 \right. \\ &- \left. 2 \int_{-w/2}^{w/2} dx N(x) (f(x) - g(x)) + \int_{-w/2}^{w/2} dx N^2(x) \right]. \end{aligned} \tag{1.168}$$

The second term on the right hand side is essentially zero since $N(x)$ is a random function with a mean of zero. The last term can be ignored since it is a constant which only depends on the noise distribution $\sigma(N)$. This gives

$$M \simeq \frac{1}{2\sigma^2(N)} \frac{n}{w} \int_{-w/2}^{w/2} dx \, (f(x) - g(x))^2 . \tag{1.169}$$

The value y_0 is chosen which minimizes M by the condition

$$\left.\frac{\partial M}{\partial y}\right|_{y_0} = 0. \tag{1.170}$$

At the stationary point y_0 the precision is given from elementary statistics [Bevington, 1969] by

$$\sigma^2(y_0) = \left.\left(\frac{\partial^2 M}{\partial y^2}\right)^{-1}\right|_{y_0}. \tag{1.171}$$

For our model functions

$$f(x) - g(x) = -\frac{2A_p}{w^2}\left(2xy + y^2\right) \tag{1.172}$$

so that

$$M = \frac{2nA_p^2}{\sigma^2(N)w^4}(y^4 + \frac{1}{3}w^2y^2). \tag{1.173}$$

The minimum occurs at $y_0 = 0$ which gives

$$\sigma(y_0) = \sqrt{\frac{3}{4n}}\frac{\sigma(N)w}{A_p}. \tag{1.174}$$

This relates the measurement precision to the geometric line width w, the noise-to-signal ratio $\sigma(N)$, the number of points sampled n, and the geometric peak absorptance of the line A_p.

The result for $\sigma(y_0)$ which comes from the integral approximation can be tested against a more direct calculation to estimate the uncertainties from the least squares fit. Once again introduce the least squares sum

$$M = \sum_{j=-m}^{m} \frac{[f(x_j) - (g(x_j) + N(x_j))]^2}{2\sigma^2(N)} \tag{1.175}$$

where this is related to the previous example by $n = 2m + 1$ and $x_j = (j/m)(w/2)$ for $-m \leq j \leq m$. Using the same functional forms $f(x) =$

$(2A_p/w^2)(x-y)^2$ and $g(x) = (2A_p/w^2)x^2$, the least squares sum can be expressed, after discarding terms involving the random function $N(x)$ for the same reasons given above, as

$$M = \frac{1}{2\sigma^2(N)} \sum_{j=-m}^{m} \left(\frac{2A_p}{w^2}(x_j - y)^2 - \left(\frac{2A_p}{w^2} x_j^2 + N(x_j) \right) \right)^2 \tag{1.176}$$

$$\approx \frac{2A_p^2 y^2}{m^2 \sigma^2(N) w^4} \sum_{j=-m}^{m} \left(m^2 y^2 - 2jmwy + jw^2 \right) \tag{1.177}$$

The sum (1.177) can be shown to be

$$M = \frac{(12m^2 + 6m)y^4 + (4m^2 + 6m + 2)w^2 y^2}{3m} \frac{A_p^2}{\sigma^2(N) w^4}. \tag{1.178}$$

Once again the measurement uncertainty can be estimated from (1.165) with $y_0 = 0$ which gives

$$\sigma(y_0) = \sqrt{\frac{3m}{8m^2 + 12m + 4}} \frac{\sigma(N) w}{A_p}. \tag{1.179}$$

The result of this calculation shows the same dependence on the parameters $\sigma(N)$, w, and A_p as the result from the integral approximation except for a multiplicative form factor f_n which only depends on the number of points n

$$\sigma(y_0) = f_n \frac{\sigma(N) w}{A_p}. \tag{1.180}$$

Table 1.11.1 shows how these form factors are related for various values of m. The values listed show that the integral approximation is higher by as much as 20% for small n than the direct sum calculation with better agreement as n increases.

This method of determining line positions is similar to the procedure which is followed by the line-finder program [Norton, 1986] which determines

the line positions from the ATMOS spectra. The model for the absorption line shapes is somewhat simplified and it is of interest to see how this parabola-parabola least squares fit compares to a fit of a parabola to a gaussian absorption. This pair of functions is chosen since the true absorption lines 'taper off' at wavenumbers away from the line center similar to a gaussian shape. Figure 1.11.2 shows such a sample gaussian described by

$$g(x) = A_p(1 - e^{-4\ln 2(x/w)^2}). \tag{1.181}$$

Again A_p represents the geometric peak absorptance and w is the geometric width at half maximum.

Although the gaussian line shape is chosen rather arbitrarily the dependence of the measurement precision to the geometric width w, the peak absorptance A_p and the noise amplitude $\sigma(N)$ remains the same as for the parabola-parabola fit. To see this, we fit

$$f(x) = (2A_p/w^2)(x - y)^2 \tag{1.182}$$

to $g(x)$ for $-w/2 \leq x \leq w/2$ by both the integration approximation and the direct sum methods. To solve for the measurement uncertainty we again followed the procedure above (1.169-71). The rather involved calculations were performed using the symbolic manipulation program MACSYMA at the VAX-8600 facility in the Physics Department at the Ohio State University. It was found that, by closely following the procedure (1.169-71), the result using the integration approximation is

$$\sigma(y_0) = \sqrt{\frac{\ln 2}{2n(\sqrt{\pi \ln 2}\,\mathrm{erf}(\sqrt{\ln 2}) - \ln 2)}}\frac{\sigma(N)w}{A_p}$$

$$= \sqrt{\frac{1.155}{n}} \frac{\sigma(N)w}{A_p}. \tag{1.183}$$

Once again the result is a form factor multiplied by the product $\sigma(N)wA_p^{-1}$. For the direct sum calculation the resulting measurement uncertainty following a procedure identical to (1.175-79), also evaluated by MACSYMA, is given by

$$\sigma(y_0) = \sqrt{\frac{1}{2}\left[4\sum_{j=0}^{m}\left(\frac{1}{2}\right)^{j^2/m^2} - (2m+1) + m^{-1}\right]^{-1}} \tag{1.184}$$

$$\times \frac{\sigma(N)W}{A_p} \tag{1.185}$$

The form factors are shown in Table 1.11.2. Again the integration approximation introduces larger uncertainties than the direct sum method, however, even more interesting is that the values for the parabola-parabola and parabola-gaussian direct sum methods give approximately the same answer. The former case has slightly smaller form factors. These results suggests that the measurement precision may not be very sensitive to the details of the geometric line shapes which can be seen by comparison of the direct sum methods which are more accurate.

The calculations above suggest that the measurement precision is proportional to the noise level $\sigma(N)$, the geometric line width W, and inversely proportional to the peak absorptance A_p. The signal to noise ratio (SNR) in the ATMOS spectra is approximately 100 in the ν_3 CO_2 region near 2350 cm^{-1} which corresponds to $\sigma(N) = 0.01$. For the apodized spectra the width at half maximum peak absorptance is about 0.015 cm^{-1}, which can be attributed to the instrumental resolution and can be seen from a few sample

line shown in Figures 1.11.3-4. (The ATMOS spectra is digitally processed at intervals of 0.0075 cm^{-1} and due to a "smoothing" procedure written by Norton the drawings of the absorption lines appear as curves.) The width of the line is approximately twice the digital spacing which gives $n = 3$. Table 1.11.3 shows estimated measurement uncertainties using these parameters for lines with various values of A_p.

From this information we can estimate the precisions by which Doppler shifts can be measured. From I.2 the uncertainty in measuring relative speeds v can be determined

$$\sigma(v) = \sigma(\Delta\varsigma)/\varsigma \cdot c. \tag{1.186}$$

The measurement error per line is dependent both on the precision by which line positions can be obtained $\sigma(\varsigma)$ and the central wavenumber ς. The measurement precision $\sigma(\varsigma)$ is frequency independent. Therefore, for lower wavenumber regions the error in measuring the relative speed $\sigma(v)$ increases. Using the data presented in Table 1.11.3 we see that, as an example, for lines with a peak absorptance of about 30 % and central wavenumber ς ~2000 cm^{-1} the precision of measuring relative speeds is about 25 ms^{-1} per line. Therefore a set of 25 lines can bring the mean precision to 25 $ms^{-1}/\sqrt{5}$ =5 ms^{-1}. This measurement precision theory predicts that precisions of obtaining 5 ms^{-1} are within the capabilities of the interferometer. Using higher frequency regions and stronger lines it is feasible to improve these statistics. However, due to the broadening effects discussed previously which may limit the altitude ranges for using atmospheric lines to obtain Doppler shifts, a wind speed measurements with precisions of 5 ms^{-1} was determined to be within the capabilities of the ATMOS instrument.

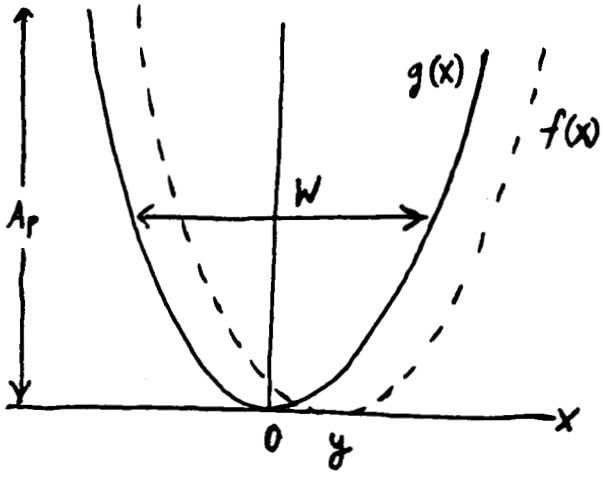

Figure 1.11.1 Function $g(x) = (2A_p/W^2)x^2$ and fitting function $f(x) = (2A_p/W^2)(x-y)^2$ to describe line profiles.

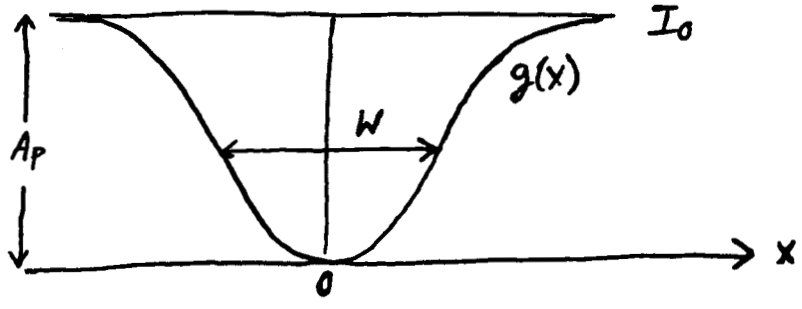

Figure 1.11.2 Function $g(x) = A_p(1 - e^{-4\ln 2(x/W)^2})$ to describe gaussian line profile.

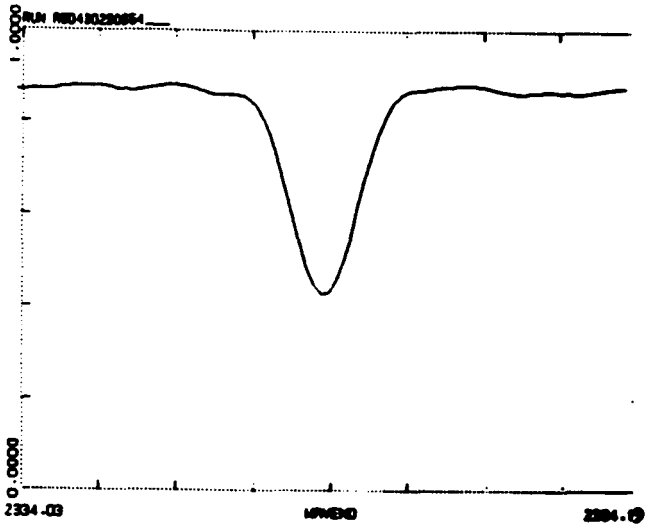

Figure 1.11.3 A CO_2 absorption line taken from ATMOS spectra.

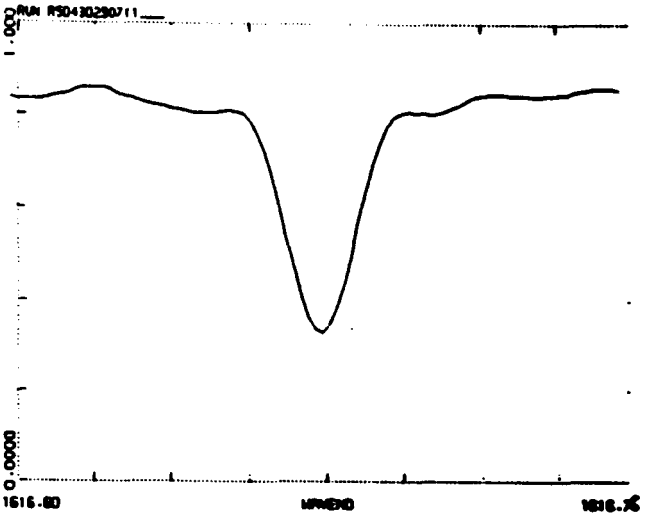

Figure 1.11.4 An H_2O absorption line taken from ATMOS spectra.

Table 1.11.1 Form factors for parabola-parabola least squares fit for various values of m.

m	$n = 2m + 1$	Integral	Direct Sum
1	3	0.50000	0.35355
2	5	0.38723	0.31623
3	7	0.32733	0.28347
4	9	0.28868	0.25820
5	11	0.26112	0.23837

Table 1.11.2 Form factors for parabola-gaussian least squares fit for various values of m.

m	$n = 2m + 1$	Integral	Direct sum
1	3	0.62051	0.35355
2	5	0.48065	0.32063
3	7	0.40622	0.28924
4	9	0.35825	0.26440
5	11	0.32405	0.24464

Table 1.11.3 Estimated measurement uncertainty from parabola-gaussian least squares fit using direct sum.

A_p	$\sigma(y_0)(\times 10^{-4}\text{cm}^{-1})$	A_p	$\sigma(y_0)(\times 10^{-4}\text{cm}^{-1})$
0.1	5.30	0.5	1.06
0.2	2.65	0.6	0.88
0.3	1.77	0.7	0.76
0.4	1.33	0.8	0.66

CHAPTER II

EXPERIMENTAL METHOD

II.1 Instrumental Calibration

CALIBRATION MODEL

To get useful wind speed measurements we must be able to measure Doppler shifts precisely for each spectrum and must be able to intercompare the spectra. The comparison of relative speeds determined from a series of spectra is limited by the calibration stability of the interferometer. As well as noise in the spectra, there is the possibility that the calibration contains random offsets due to errors in locating ZPD in each interferogram §I.1. An estimate of the magnitude of this *scale uncertainty* provides information about the precision of the ZPD locator program as well as setting limits of the accuracy of relative speed measurements. Sets of spectra may also have slowly changing calibration offsets caused by variations in the environment of the interferometer as well as "man-made" calibration offsets introduced

during the processing stage [Norton, 1986]. In order to obtain accurate measurements of Doppler shifts it is necessary to calibrate the spectra accurately.

Of the four spectral filters used with the interferometer only Filter 3, which covers the region 1600-3200 cm^{-1}, provided spectra with lines due to gases trapped or around the instrument by which the calibration stability could be analyzed. The strongest lines of the ν_3 CO_2 and ν_2 H_2O vibration bands from 2300 to 2380 cm^{-1} and 1600 to 2000 cm^{-1} respectively appeared in spectra taken at tangent heights far above the atmosphere. These lines appeared to be related to the environment of the instrument and were due to residual gas trapped in the instrument as well as gas floating in space with the orbiter. These lines were called *instrumental lines* and it was found that they provided a tool for directly measuring the behavior of the calibration system. Figures 2.1.1-2 show some of these absorption lines as they appeared in the ATMOS spectra. In Figure 2.1.1 the ν_3 CO_2 band is shown as well as the $v = 0 \rightarrow 1$ band head of solar CO. In Figure 2.1.2 some strong lines of ν_2 H_2O band are shown together with other weak lines of solar CO.

In order to test the accuracy of the instrumental calibration the measured positions from a set of instrumental lines ς_j^k of each line j in each spectrum k were assumed to be related to accepted standard positions $\hat{\varsigma}_j$ by the model

$$\varsigma_j^k = \hat{\varsigma}_j(1+\alpha) + e_j^k + \epsilon^k. \tag{2.1}$$

Here, α is an offset which is used to model any wavenumber errors in the calibration of the interferometer. This *global offset* is assumed to vary slowly over large wavenumber regions of the spectra and we will consider it be relatively constant over regions of several hundred cm^{-1}. The source of this kind

of offset is assumed to be related to environmental effects or arbitrarily introduced data processing artifacts [Norton, 1986]. The calibration noise due to phase errors in the processing stage is given by ϵ^k, a frequency independent scale error for the spectrum k, and e_j^k, the measurement error of the line j in the spectrum k. It was shown in §I.1 that the calibration uncertainties due to phase errors should be negligible but they are still included here. It is assumed that all of these errors are independent of each other. The position ς_j^k of each spectral line j in a given spectrum k is measured by a line-finder program developed by Norton (1986) which estimates the positions of absorption lines from the spectral data and its precision of $\mathcal{O}(10^{-4}\text{cm}^{-1})$ is discussed in §I.11. The measurement uncertainty $\sigma(e_j)$ and scale uncertainty $\sigma(\epsilon)$ both contribute to the position uncertainty $\sigma(\varsigma_j)$ and it is necessary to estimate the magnitudes of each of these.

DRIFT PARAMETER δ

Before proceeding along these lines it is important to check the calibration stability in each set of spectra for each occultation. A reference spectrum r was arbitrarily chosen, in this case at the highest tangent height, and a check for a calibration drift factor δ was made. It is assumed that there exists the possibility that

$$\varsigma_j^k = (1+\delta)\varsigma_j^r \tag{2.2}$$

where k are the other spectra in the set and δ may change between spectra in an occultation, a sort of calibration "drift" factor. Stability will be inferred if there are no statistically significant deviations away from $\delta = 0$. The

measured positions of each of the CO_2 and H_2O lines j in each spectrum k were compared to their corresponding positions in the reference spectrum r and a value for δ_j^k determined by

$$\delta_j^k \equiv \frac{\varsigma_j^k}{\varsigma_j^r} - 1. \tag{2.3}$$

An average value

$$\delta^k \equiv \langle \delta_j^k \rangle_j \tag{2.4}$$

and the uncertainty $\sigma(\delta^k)$ for each spectrum was determined. The brackets stand for an average over the subscript j - i.e. all of the lines used in spectrum k.

Estimated values of δ^k for the five occultations are shown in Figures 2.1.3-4 for CO_2 and H_2O instrumental lines respectively. The figures show the distribution of the drift factor of each spectrum as a function of tangent height. The values for δ have a scatter of about 5×10^{-8} and about 8×10^{-8} for the CO_2 and H_2O lines respectively. There does not appear to be any 'trend' to the data and no apparent calibration drift. Figures 2.1.5-6 show the respective uncertainties $\sigma(\delta^k)$. The uncertainties are of the order as the scatter of the δ. This indicates that the scatter of the drift factors δ are due to noise in the data and are not caused by any real drift. Tables 2.1.1-2 list

$$\delta = \langle \delta^k \rangle_k, \tag{2.5}$$

the average over all spectra k and the standard error $\sigma(\delta)$ for CO_2 and H_2O lines respectively for the five occultations. From these results there is no evidence of a measureable drift of the frequency calibration during an occultation since the average values of δ found are of the same order as

the measurement uncertainty in all of the spectra k. This indicates that the calibration does not "drift" between spectra during an occultation. The fractional change of a line position predicted in Table 1.11.3 is of the same order as these fluctuations. As an example, a line with a peak absorptance of 40 % at a frequency of 2330 cm^{-1} can be predicted to have a fractional measurement error of $1.33 \times 10^{-4}/2330 = 5 \times 10^{-8}$. This corresponds to wind speed errors of about 15 ms^{-1} per line.

GLOBAL CALIBRATION OFFSET α

It is useful to compare the instrumental line positions to a set of accepted standards in order to estimate α for each occultation. Assume that such a set of standards $\hat{\varsigma}_j$ exist. Sets of CO_2 and H_2O standards recommended by Brown (1986) were used and are listed in Tables 2.1.3-4 respectively. From (2.1) we can write

$$\alpha = \varsigma_j^k / \hat{\varsigma}_j^k - 1 + \text{error}. \tag{2.6}$$

For each line j in each spectrum k a value

$$\alpha_j^k = \varsigma_j^k / \hat{\varsigma}_j - 1 \tag{2.7}$$

is computed. The average value over all lines

$$\alpha^k = \langle \alpha_j^k \rangle_j \tag{2.8}$$

was determined for each spectrum and is displayed in Figures 2.1.7-11 for all five occultations using CO_2 and H_2O instrumental lines. The data show a variation from spectrum to spectrum of about 5×10^{-8}. Notice that there

does seem to be a significant offset on the average between the values of α computed for the CO_2 and H_2O lines. Figures 2.1.12-13 show $\bar{\sigma}(\alpha^k)$ for the CO_2 and H_2O lines respectively. The uncertainties for the CO_2 lines are about 2-3$\times 10^{-8}$ which is of the order of the average fluctuations of α^k. For H_2O the values for $\bar{\sigma}(\alpha^k)$ are about 4×10^{-8} and they are significantly larger than the CO_2 values but are also consistent with the average fluctuations of α^k. This information indicates that the fluctuations of measured values of α^k are due noise in the spectra rather than calibration fluctuations. The null result above for the calibration drift factor δ also confirms this.

Since α^k was found to vary randomly due to instrumental noise we determined the mean value for α in each occultation

$$\alpha = \langle \alpha^k \rangle_k. \tag{2.9}$$

The mean values α and mean standard error $\bar{\sigma}(\alpha)$ are given in Table 2.1.5-6 for the five occultations as computed from the ν_3 CO_2 and ν_2 H_2O bands respectively. Table 2.1.7 lists the differences between the two sets and it is evident, since the offset is larger than the mean errors, that the difference in their offsets $\Delta\alpha = \alpha_{CO_2} - \alpha_{H_2O}$ are statistically significant. Figure 2.1.14 shows the differences $\Delta\alpha^k$ for all occultations. The general trend of the difference of the offsets $\Delta\alpha^k$ appears to be between about 3-5$\times 10^{-8}$. The average difference between the instrumental global offsets α is $+1.38 \pm 0.41 \times 10^{-8}$. This indicates that the discrepancy between the positions determined from the instrumental lines and the standards is significant. Since, according to Brown (1986), the CO_2 standards are "good" (accurate to 10^{-4} cm^{-1}) the H_2O standard frequencies may be too low by this factor. This also suggests

that our assumption that the "instrumental" lines are at rest with respect to the interferometer may not be correct. This question of whether or not the "instrumental" lines are at rest is examined in §II.10.

Comparing the differences in $\Delta\alpha$ of the instrumental lines to the standard positions is like 'comparing apples and oranges'. Either set of standards may be 'correct' but there is no way of determining it from the data. However, we do have insight into the magnitudes of the discrepancies. It is shown in §II.5 that any *absolute* calibration offsets do not affect the accuracy in which Doppler shifts can be determined, provided they are consistent from spectrum to spectrum and that a set of instrumental 'absolute' standards are available, such as the instrumental CO_2 and H_2O lines.

The systematic relative velocity Δv shift caused by the global offset α for the two sets of instrumental lines is listed in Tables 2.1.5-6. The velocity shift is given by $\Delta v = \alpha\, c$ where $c = 299\,792\,458$ ms^{-1} is the speed of light. The mean errors in the relative velocity shift $\bar{\sigma}(\Delta v) = c\,\bar{\sigma}(\alpha)$ are between 1 and 3 ms^{-1}. The mean values Δv are an order of magnitude or more larger than these uncertainties and therefore there were statistically significant calibration offsets between occultations. The sunset occultation SS09 was found to have a particularly large offset of about 80 ms^{-1} compared to the other occultations. These offsets were probably introduced during the processing of the spectra and are artificial in origin [Norton, 1986] - specifically, the calibration scales were multiplied by certain factors during testing of the spectra. It is evident that the wavenumber calibration of the spectra need corrections, to agree with calibration standards as well as consistency between occultations, for wind speeds to be measured. When

instrumental lines are present in the spectra this calibration can be achieved since the instrumental lines mark the rest frame positions.

The frequency scales of all subsequent spectra were shifted by the correction factor $1 - \alpha$ to compensate for these offsets for each occultation. The positions of the instrumental ν_3 CO_2 lines were thus forced to agree with the standards. We can say that the spectra were calibrated with respect to the CO_2 standards. The CO_2 correction factors used are given in Table 2.1.5. As discussed above, the absolute calibration of the instrument is only as good as the ν_3 line standards themselves. We accepted these standards as the 'best available' and calibrated the instrument relative to these. However, it is shown in §II.4 that the accuracy of the relative speeds is independent of the set of standards used provided that instrumental lines are available in the spectra for calibration.

After these correction factors were applied to the frequency calibration it was then possible to make new estimates of the CO_2 and H_2O standards from the instrumental lines. All of the instrumental lines from $n = 125$ spectra from the five occultations were used. Tables 2.1.8-9 list the new positions from the ATMOS instrumental lines as compared to Brown's values, $\Delta\varsigma = \varsigma_{\text{inst}} - \varsigma_{\text{Brown}}$ for both regions. After calibration, α_{H_2O} was determined and the instrumental positions of the H_2O lines differ from Brown's standards by a factor $\alpha = -1.25 \pm 0.36 \times 10^{-8}$ which agrees with the estimate given previously. This can be seen by the multitude of minus signs in the differences column in Table 2.1.9. The average global offset for the CO_2 lines vanishes as required.

Also listed in Tables 2.1.8-9 are the precisions of the new positions. It

is worth noting that Brown's standards are known to 10^{-4} cm^{-1} accuracy while the precisions of the ATMOS values are almost an order of magnitude smaller than this. This suggests that there is an improvement of a factor of almost five in the line position precisions, particularly in the ν_3 CO_2 lines. However, most of the differences between the instrumental lines and Brown's standards are within 10^{-4} cm^{-1}. Hence, this agreement suggests that the ATMOS interferometer can be used for determining precise relative positions for other lines based on Brown's ν_3 CO_2 values.

From this analysis we found that the instrumental frequency calibration remains stable during the course of each occultation. Provided that scale errors do not exist, and we show in the next section that this appears to be true, we can rely on the frequency calibration of the interferometer to measure Doppler shifts and positions of lines relative to the overall calibration of the instrument. Measurement of the fluctuations in α^k and δ^k also hint that the measurement precision theory may be reliable and a more quantitative treatment is given in §II.11. After calibrating the spectra is was found that the measured positions of the instrumental CO_2 and H_2O lines were significantly improved over the precisions of the standards. Typical precision of 2-3$\times 10^{-5}$ cm^{-1} were found. This indicates that the differences between the values determined from ATMOS and the standard positions provided by Brown are statistically significant.

The absolute error in estimating Doppler shifts can now be estimated since instrumental lines were available in the spectra for calibration. The rest frame positions $\hat{\varsigma}$ of these lines were determined from the spectra to precisions of about 3×10^{-5} cm^{-1}. For 20 of these lines and using an average

frequency of about 2350 cm^{-1} the absolute uncertainty in relative velocity v is determined by

$$\text{absolute uncertainty} = \frac{3 \times 10^{-5}}{2350} \frac{c}{\sqrt{20}} < 1\,ms^{-1}. \qquad (2.10)$$

The instrumental lines allow us to calibrate the instrument to obtain absolute Doppler shifts to $< 1\ ms^{-1}$ provided the number of spectra n and the number of lines N are large enough so that the factor $\sqrt{nN}$ is large enough to reduce the mean uncertainties.

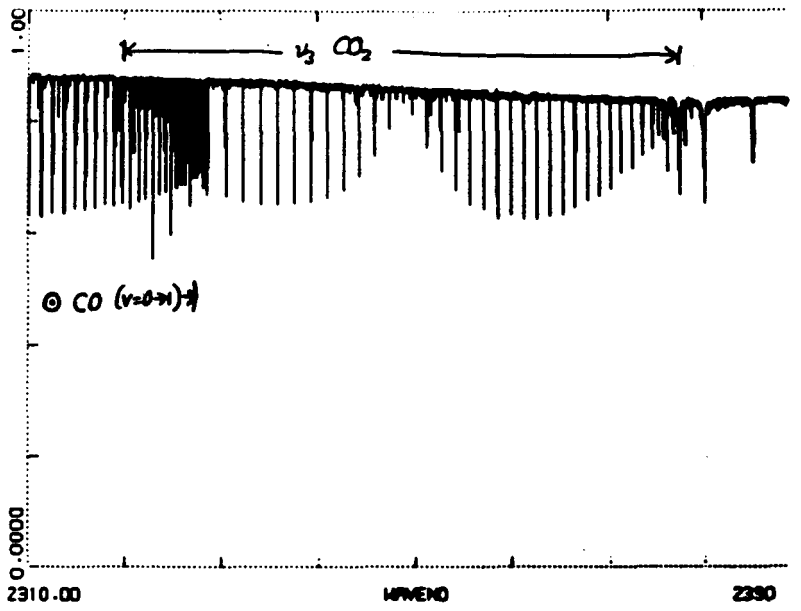

Figure 2.1.1 Instrumental ν_3 CO_2 absorption lines and ⊙ CO $v = 0 \rightarrow 1$ band head observed in solar spectra. The ν_3 CO_2 instrumental absorption lines are used for calibration. The ⊙ CO lines tend to interfere with atmospheric and instrumental lines causing unwanted line distortions.

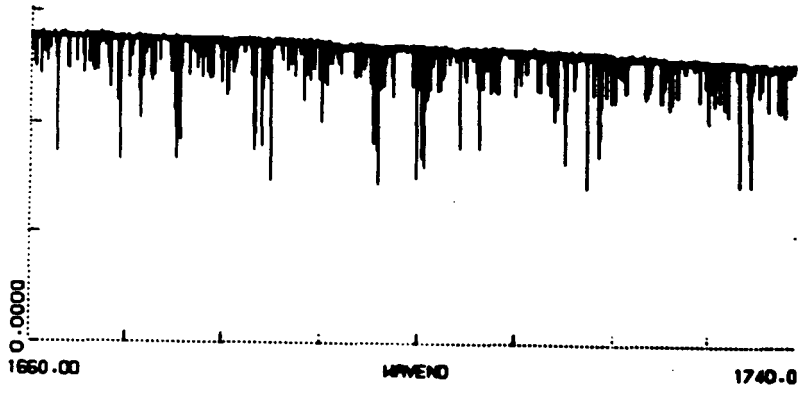

Figure 2.1.2 Instrumental ν_2 H_2O absorption lines intermixed ⊙ CO lines observed in solar spectra. The stronger lines as well as some weaker lines correspond to the instrumental lines. The water molecule is not linear and its spectra does not display evenly spaced rotational levels like CO_2. Water lines must be carefully checked for possible interferences with ⊙ CO lines.

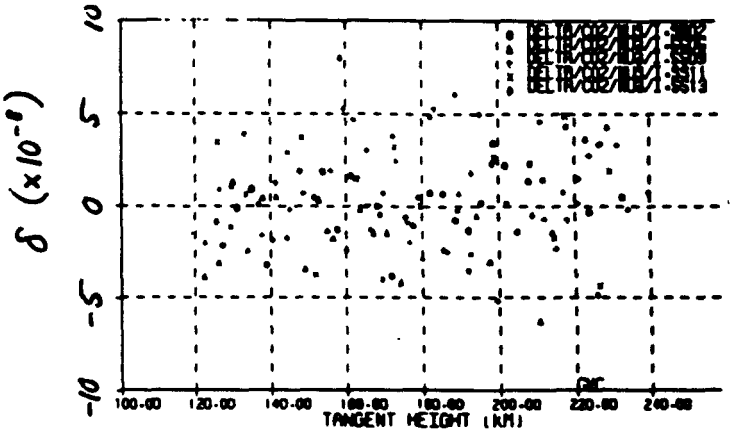

Figure 2.1.3 The test for calibration drift δ^k using ν_3 CO_2 instrumental lines for the five occultations. The data points appear to be randomly scattered about the origin with a variance of about 5×10^{-8} and this is due to measurement error associated with locating line positions.

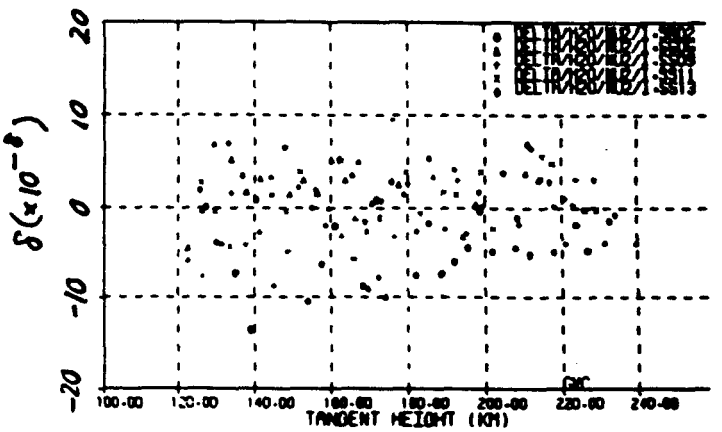

Figure 2.1.4 The test for alibration drift δ^k using ν_2 H_2O instrumental lines for the five occultations. The data points appear to be randomly scattered about the origin with a variance of about 8×10^{-8} and this is due to measurement error associated with locating line positions.

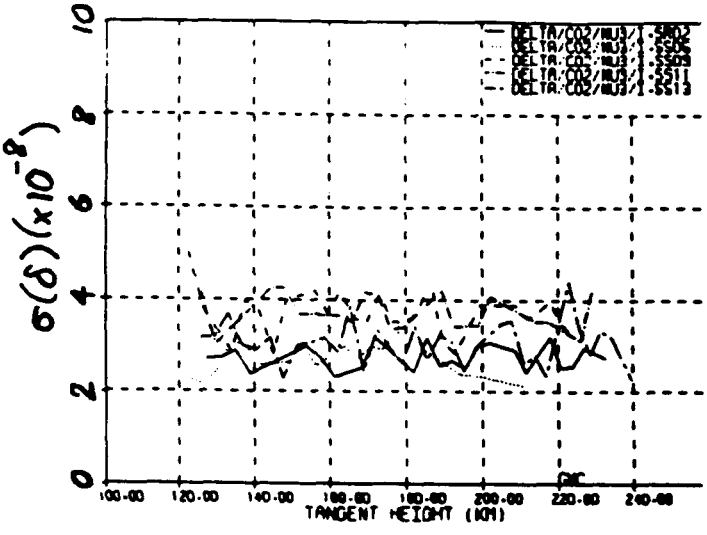

Figure 2.1.5 Measurement errors $\sigma(\delta^k)$ of the δ^k values in Fig. 2.1.3 using ν_3 CO_2 instrumental lines for the five occultations. The scatter per measurement is of the same order of magnitude as the scatter of values in 2.1.3. The scatter of points in 2.1.3 are due to random errosr in the line positions.

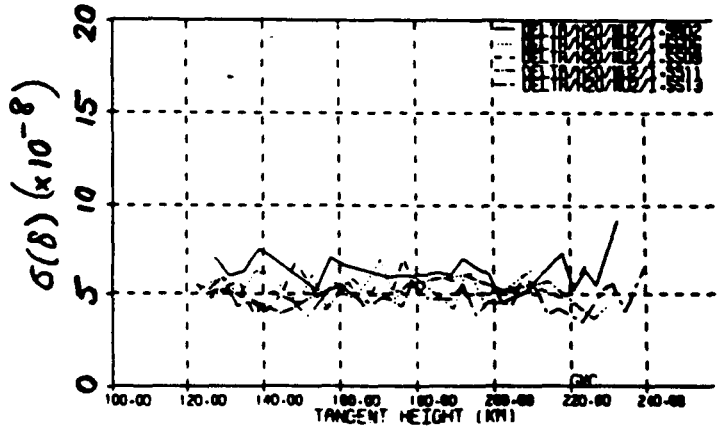

Figure 2.1.6 Measurement errors $\sigma(\delta^k)$ of the δ^k values in Fig. 2.1.4 using ν_2 H_2O instrumental lines for the five occultations. The scatter per measurement is of the same order of magnitude as the scatter of values in 2.1.4. The scatter of points in 2.1.3 are due to random errors in the line positions.

Table 2.1.1 Check for instrumental drift for the five occultations obtained from ν_3 CO_2 lines.

Occultation	$\delta(\times 10^{-8})$	$\sigma(\delta)(\times 10^{-8})$	Ref. Spectrum
SR02	−0.72	1.96	A50430113052
SS06	−0.62	2.15	A50430230523
SS09	−0.88	2.30	A50501172502
SS11	+0.58	3.01	A50501202822
SS13	−0.29	3.11	A50501233132

Table 2.1.2 Check for instrumental drift for the five occultations obtained from ν_2 H_2O lines.

Occultation	$\delta(\times 10^{-8})$	$\sigma(\delta)(\times 10^{-8})$	Ref. Spectrum
SR02	−4.70	3.55	A50430113052
SS06	+0.80	3.95	A50430230523
SS09	−1.02	4.12	A50501172502
SS11	+1.20	3.57	A50501202822
SS13	+1.14	3.94	A50501233132

Table 2.1.3 ν_3 CO_2 standards given by Brown (1986) used in primary instrumental calibration.

No.	Position (cm^{-1})	Rot	No.	Position (cm^{-1})	Rot
1	2330.5571	P22	16	2364.1053	R20
2	2334.1563	P18	17	2365.3876	R22
3	2335.9140	P16	18	2366.6451	R24
4	2337.6580	P14	19	2369.0853	R28
5	2339.3722	P12	20	2370.2679	R30
6	2341.0620	P10	21	2371.4255	R32
7	2342.7272	P 8	22	2372.5581	R34
8	2345.9841	P 4	23	2373.6656	R36
9	2354.4333	R 6	24	2374.7481	R38
10	2355.8894	R 8	25	2375.8055	R40
11	2357.3207	R10	26	2376.8377	R42
12	2358.7272	R12	27	2377.8448	R44
13	2360.1089	R14	28	2378.8268	R46
14	2361.4659	R16	29	2379.7836	R48
15	2362.7980	R18			

Table 2.1.4 ν_2 H_2O standards given by Brown (1986) used in primary instrumental calibration.

No.	Position (cm^{-1})	Vib-Rot	No.	Position (cm^{-1})	Vib-Rot
1	1616.7116	110 101	12	1756.8188	716 625
2	1627.8275	202 111	13	1771.2875	331 220
3	1647.4041	422 413	14	1775.6341	726 615
4	1669.1683	413 322	15	1790.9518	827 716
5	1669.3929	313 202	16	1799.6156	431 322
6	1688.3785	725 716	17	1802.4797	918 827
7	1704.4534	432 423	18	1825.2016	634 523
8	1714.0337	625 616	19	1844.1806	441 330
9	1715.1551	606 515	20	1867.8527	542 431
10	1718.6117	322 211	21	1889.5694	643 532
11	1730.0550	615 524	22	1942.5161	652 541

Table 2.1.5 Estimated global offsets α for the five occultations from ν_3 CO_2 lines. Lines 1-20 were used for this analysis.

Occultation	$\alpha(\times 10^{-8})$	$\bar{\sigma}(\alpha)(\times 10^{-8})$	Δv (m/s)	$\bar{\sigma}(\Delta v)$ (m/s)
SR02	+2.66	0.39	+7.97	1.17
SS06	−0.55	0.48	−1.65	1.42
SS09	−27.30	0.43	−81.84	1.29
SS11	−7.13	0.63	−21.38	1.89
SS13	−2.96	0.52	−8.87	1.56

Table 2.1.6 Estimated global offsets α for the five occultations from ν_2 H_2O lines.

Occultation	$\alpha(\times 10^{-8})$	$\bar{\sigma}(\alpha)(\times 10^{-8})$	Δv (m/s)	$\bar{\sigma}(\Delta v)$ (m/s)
SR02	−0.53	0.74	−1.59	2.22
SS06	−2.88	0.88	−8.63	2.64
SS09	−26.32	0.78	−78.91	2.34
SS11	−8.56	0.77	−25.66	2.31
SS13	−3.87	0.67	−11.60	2.01

Table 2.1.7 Differences between global offsets α for the five occultations.

Occultation	$\Delta\alpha(\times 10^{-8})$	$\bar{\sigma}(\Delta\alpha)(\times 10^{-8})$
SR02	+3.19	0.84
SS06	+2.33	1.00
SS09	−0.98	0.89
SS11	+1.43	0.99
SS13	+0.91	0.85

Table 2.1.8 ν_3 CO_2 standards given by Brown (1986) as compared to observed instrumental positions after primary calibration for $n = 125$ spectra. All frequencies in cm^{-1} where applicable.

No.	ς_{Brown}	ς_{inst}	$\Delta\varsigma$ $(\times 10^{-4})$	$\bar{\sigma}(\varsigma_{inst})$ $(\times 10^{-4})$
1	2330.5571	2330.55709	−0.1	0.20
2	2334.1563	2334.15633	+0.3	0.19
3	2335.9140	2335.91938	−0.2	0.18
4	2337.6580	2337.65799	−0.1	0.20
5	2339.3722	2339.37219	−0.3	0.21
6	2341.0620	2341.06197	−0.3	0.21
7	2342.7272	2342.72719	−0.1	0.24
8	2345.9841	2345.98410	0.0	0.34
9	2354.4333	2354.43342	+1.2	0.26
10	2355.8894	2355.88941	+1.0	0.22
11	2357.3207	2357.32067	−0.3	0.22
12	2358.7272	2358.72723	+0.3	0.19
13	2360.1089	2360.10892	+0.2	0.18
14	2361.4659	2361.46586	−0.4	0.17
15	2362.7980	2362.79803	+0.3	0.19
16	2364.1053	2364.10525	−0.5	0.20
17	2365.3876	2365.38761	+0.1	0.20
18	2366.6451	2366.64511	+0.1	0.20
19	2369.0853	2369.08528	−0.2	0.25
20	2370.2679	2370.26791	+0.1	0.29
21	2371.4255	2371.42548	−0.2	0.31

Table 2.1.9 ν_2 H_2O standards given by Brown (1986) as compared to observed instrumental positions after primary calibration for $n = 125$ spectra. All frequencies in cm^{-1} where applicable.

No.	ς_{Brown}	ς_{inst}	$\Delta\varsigma$ $(\times 10^{-4})$	$\bar{\sigma}(\varsigma_{inst})$ $(\times 10^{-4})$
1	1616.7116	1616.71148	−1.2	0.20
2	1627.8275	1627.82747	−0.3	0.26
3	1647.4041	1647.40405	−0.5	0.24
4	1669.1683	1669.16834	+0.4	0.34
5	1669.3929	1669.39287	−0.3	0.21
6	1688.3785	1688.37845	−0.5	0.38
7	1704.4534	1704.45341	+0.1	0.21
8	1714.0337	1714.03360	−1.0	0.30
9	1715.1551	1715.15508	−0.2	0.21
10	1718.6117	1718.61159	−1.1	0.22
11	1730.0550	1730.05499	−0.1	0.34
12	1756.8188	1756.81878	−0.2	0.24
13	1771.2875	1771.28742	−0.8	0.25
14	1775.6341	1775.63409	−0.1	0.42
15	1790.9518	1790.95184	+0.4	0.31
16	1799.6156	1799.61557	−0.3	0.30
17	1802.4797	1802.47976	+0.6	0.44
18	1825.2016	1825.20154	−0.6	0.23
19	1844.1806	1844.18061	+0.1	0.18
20	1867.8527	1867.85279	+0.9	0.33
21	1889.5694	1889.56936	−0.4	0.27
22	1942.5161	1942.51614	+0.4	0.36

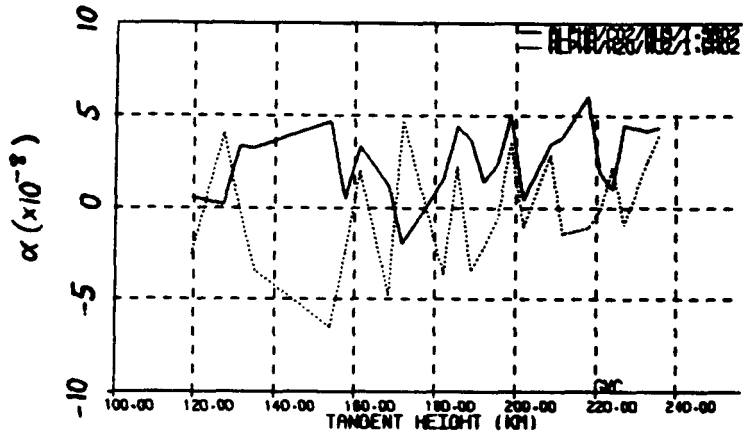

Figure 2.1.7 α^k determined from CO_2 (solid line) and H_2O (dotted line) instrumental lines for occultation SR02. The α^k values for CO_2 are generally greater than the H_2O values.

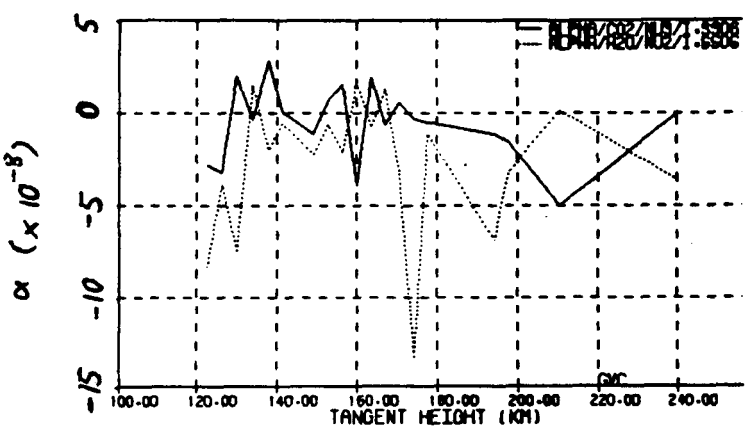

Figure 2.1.8 α^k determined from CO_2 (solid line) and H_2O (dotted line) instrumental lines for occultation SS06. The α^k values for CO_2 are generally greater than the H_2O values.

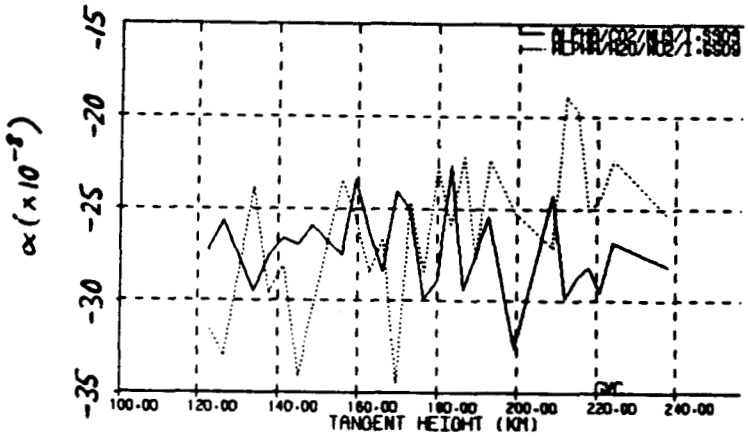

Figure 2.1.9 α^k determined from CO_2 (solid line) and H_2O (dotted line) instrumental lines for occultation SS09. The α^k values for CO_2 are generally greater than the H_2O values.

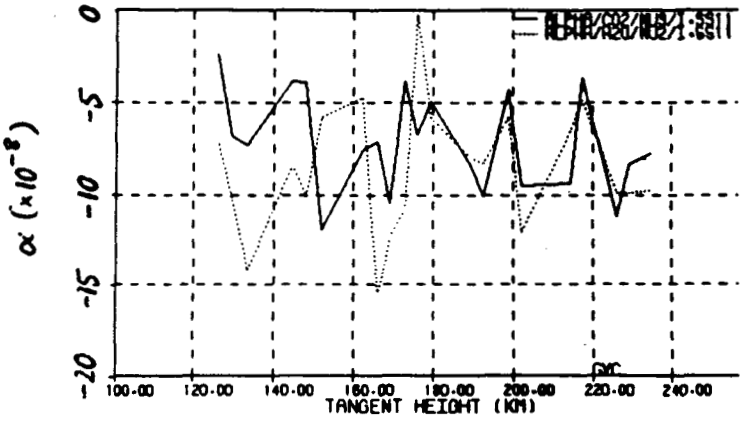

Figure 2.1.10 α^k determined from CO_2 (solid line) and H_2O (dotted line) instrumental lines for occultation SS11. The α^k values for CO_2 are generally greater than the H_2O values.

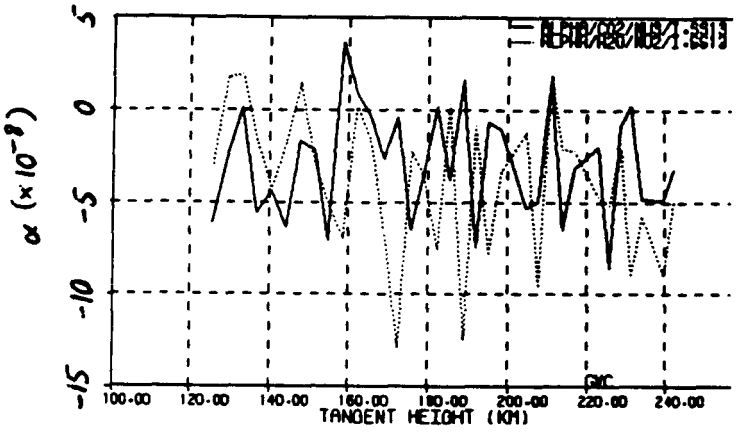

Figure 2.1.11 α^k determined from CO_2 (solid line) and H_2O (dotted line) instrumental lines for occultation SR13. The α^k values for CO_2 are generally greater than the H_2O values.

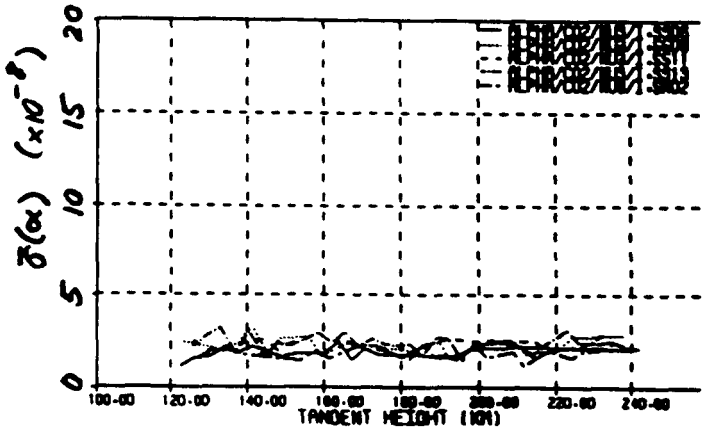

Figure 2.1.12 $\tilde{\sigma}(\alpha^k)$ from CO_2 instrumental lines for the five occultations. The mean uncertainties are typically about 2×10^{-8} which is typically the magnitude of the fluctuations of the α^k in Figs. 2.1.9-13 for CO_2.

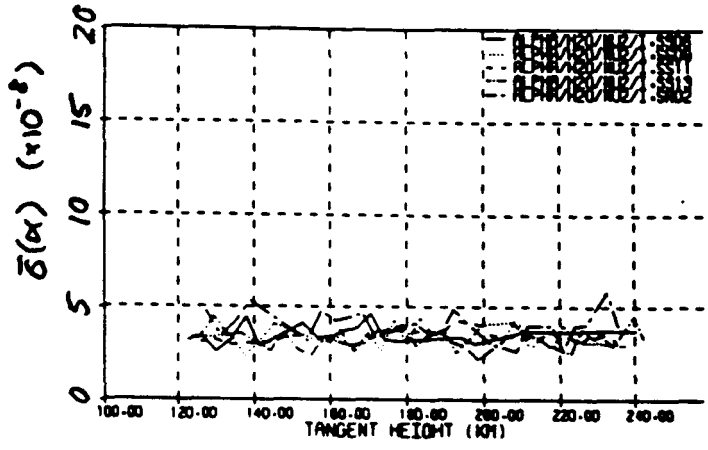

Figure 2.1.13 $\bar{\sigma}(\alpha^k)$ from H_2O instrumental lines for the five occultations. The mean uncertainties are typically about 4×10^{-8} which is typically the magnitude of the fluctuations of the α^k in Figs. 2.1.9-13 for H_2O.

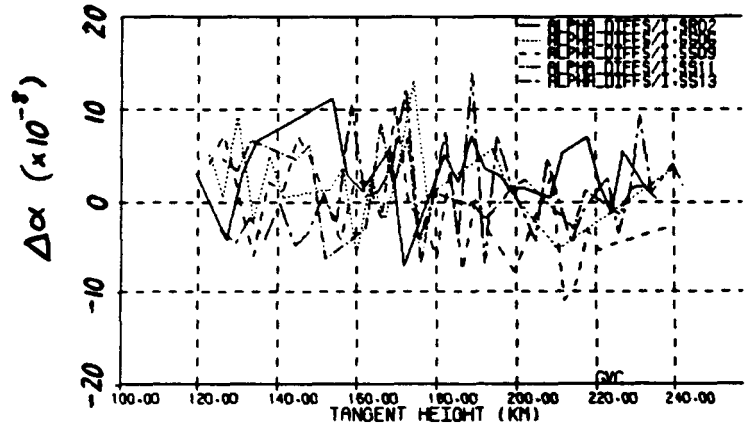

Figure 2.1.14 $\Delta(\alpha^k)$ between CO_2 and H_2O instrumental lines for the five occultations. The large fluctuations are due to measurement errors, however, the average of the differences tends to be larger than zero. The mean difference is $+1.38 \pm 0.41 \times 10^{-8}$ for all occultations.

II.2 Scale Uncertainty $\sigma(\epsilon)$

In the previous section we have calibrated the spectra using about 30 ν_3 instrumental lines of CO_2. Global calibration errors are not the only source of errors in the measurement of line positions. The scale uncertainty $\sigma(\epsilon)$ sets the ultimate limit to the precision by which wind speeds may be obtained. To estimate this scale uncertainty, consider (2.1) after correcting all spectra by the calibration factor $1 - \alpha$ §II.1. We have

$$\varsigma_j^k = \hat{\varsigma}_j + e_j^k + \epsilon^k. \tag{2.11}$$

which can be rearranged

$$\epsilon^k = \varsigma_j^k - \hat{\varsigma}_j - e_j^k. \tag{2.12}$$

Averaging this over all lines j in each spectrum k gives

$$\epsilon^k = \langle \varsigma_j^k - \hat{\varsigma}_j \rangle_j - \langle e_j^k \rangle_j. \tag{2.13}$$

For a sufficiently large sample size we expect that measurement errors due to noise vanish

$$\langle e_j^k \rangle_j \to 0. \tag{2.14}$$

If we impose this condition then (2.12) becomes

$$\epsilon^k \doteq \langle \varsigma_j^k - \hat{\varsigma}_j \rangle_j. \tag{2.15}$$

The CO_2 and H_2O line positions determined from the ATMOS spectra in Tables 2.1.8-9 were used for the standard positions $\hat{\varsigma}_j$ for both regions. In

Figures 2.2.1-2 values for ϵ^k from 125 spectra are plotted for both spectral regions respectively. The estimated values of the scale errors ϵ^k appear to scatter between 5 and 10×10^{-5} cm^{-1}. Also plotted is the mean uncertainties in measuring the scale error $\bar{\sigma}(\epsilon^k)$. We see that the error in the ϵ^k is approximately the same as their scatter between spectra. Values of the scale error can be determined by defining the average of the scale errors for each occultation

$$\epsilon \equiv \langle \epsilon^k \rangle_k \tag{2.16}$$

for each occultation. Tables 2.2.1-2 list ϵ and $\bar{\sigma}(\epsilon)$ for the CO_2 and H_2O lines respectively for each of the five occultations. It is evident that $|\epsilon| \leq \bar{\sigma}(\epsilon)$ in both regions. This indicates that the scale uncertainty is less than $5 \times 10^{-5} cm^{-1}$. It should also be noted that $\bar{\sigma}(\epsilon) \simeq \bar{\sigma}(\epsilon^k)$. This indicates that the measured values ϵ^k may in fact be due to noise instead of being due to a true scale uncertainty. More precisely stated, the approximation $\langle e_j^k \rangle_j$ may not vanish in each spectrum but may have a random fluctuation due to the finite sample size of about 20 lines. To test this we examined the correlations between the estimates for ϵ^k in each spectrum k for the H_2O and CO_2 regions. The correlations

$$C^k = \epsilon^k_{H_2O} \epsilon^k_{CO_2} \tag{2.17}$$

were determined in each spectrum and displayed in Figure 2.2.3 for all the spectra k. The correlations appear to be evenly distributed about zero. This suggests that there a correlation does not exist. The total correlation

$$C = \langle C^k \rangle_k \tag{2.18}$$

was then determined and values for C and $\bar{\sigma}(C)$ are listed in Table 2.2.3. The correlation overall correlation C is of $\mathcal{O}(3 \times 10^{-10})$ cm^{-2} and and the mean uncertainties $\bar{\sigma}(C)$ is also $\mathcal{O}(3 \times 10^{-10})$ cm^{-1}. The upper limit of the correlations is therefore determined by the uncertainties $\bar{\sigma}(C)$. Since the correlation is determined from the positions of two lines, the upper limit of the scale uncertainties is approximately determined by $\bar{\sigma}(C) \simeq 2\bar{\sigma}^2(\epsilon)$. Using the values of $\bar{\sigma}(C)$ in Table 2.2.3 this gives an upper limit of the scale fluctuations of about 1.3×10^{-5} cm^{-1}. This means that the frequencies obtained by the interferometer are good to at least 10^{-5} cm^{-1}. The results of the correlation analysis do not show any significant evidence of a calibration uncertainty. Since the correlations effectively vanish the values of ϵ^k plotted in Figures 2.2.1-2 are due to measurement errors e_j^k and not a true scale uncertainty. As previously stated, due to the number of lines sampled, $N = 20$, there may still be significant fluctuations in the average of the measurement errors of all the line positions obtained in spectrum k

$$e^k = \langle e_j^k \rangle_j \tag{2.19}$$

of the order

$$\sigma(e^k) = N^{-1/2}\sigma(e). \tag{2.20}$$

Using typical values for $\sigma(e)$ listed in Table 1.12.3, for example 2.65×10^{-4}cm^{-1} for peak absorptances of about 20% and using $N = 20$ we get an estimation for $\sigma(e^k) = 5.9 \times 10^{-4}$cm^{-1}. This agrees with the values estimated for $\bar{\sigma}(\epsilon^k)$ in Tables 2.2.1-2.

This suggests there is no evidence for the presence of a scale uncertainty. The estimate of the scale uncertainty in §I.1 predicted by the magnitude

of the phase errors is several orders of magnitude smaller that the estimates $\bar{\sigma}(\epsilon^k)$. From here on it is assumed that $\epsilon^k \equiv 0$ and that all fluctuations are due to measurement uncertainty. This result simplifies the analysis significantly. The scale uncertainty appears to be negligible and the relative accuracy of the wind speed measurements is not limited by this effect.

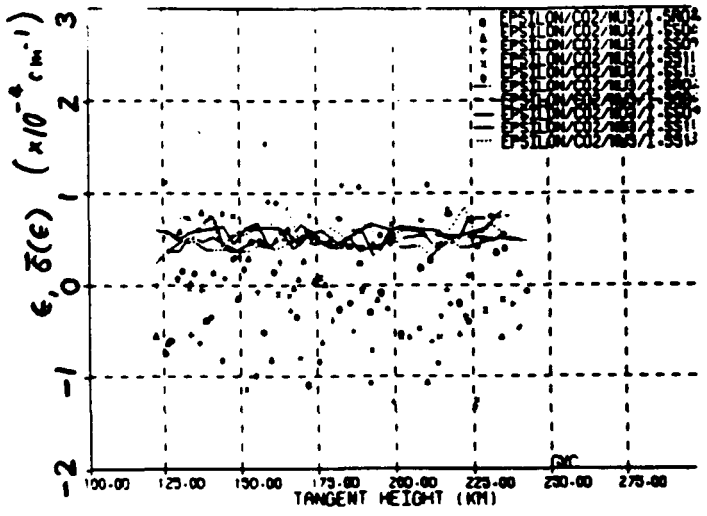

Figure 2.2.1 ϵ^k for the five occultations determined from CO_2 lines (points) and $\bar{\sigma}(\epsilon^k)$ (lines). The scatter of the data about zero is of the same order of magnitude of the mean uncertainties. This indicates that the scatter in points is probably due to noise instead of a true scale fluctuation.

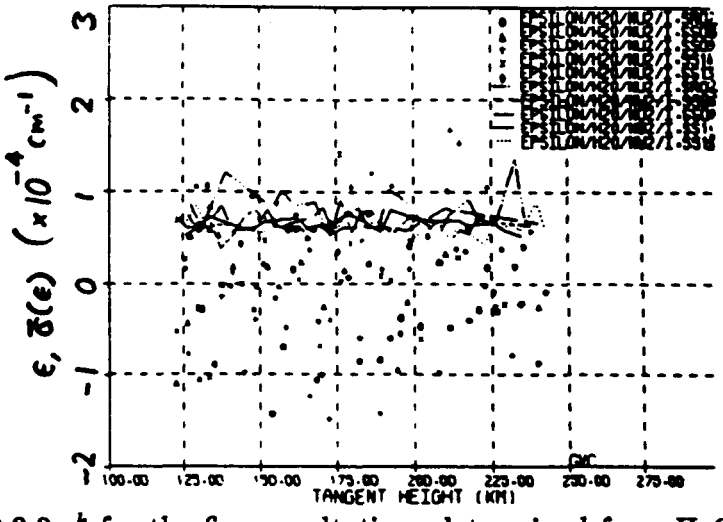

Figure 2.2.2 ϵ^k for the five occultations determined from H_2O lines (points) and $\bar{\sigma}(\epsilon^k)$ (lines). The scatter of the data about zero is of the same order of magnitude of the mean uncertainties. This indicates that the scatter in points is probably due to noise instead of a true scale fluctuation.

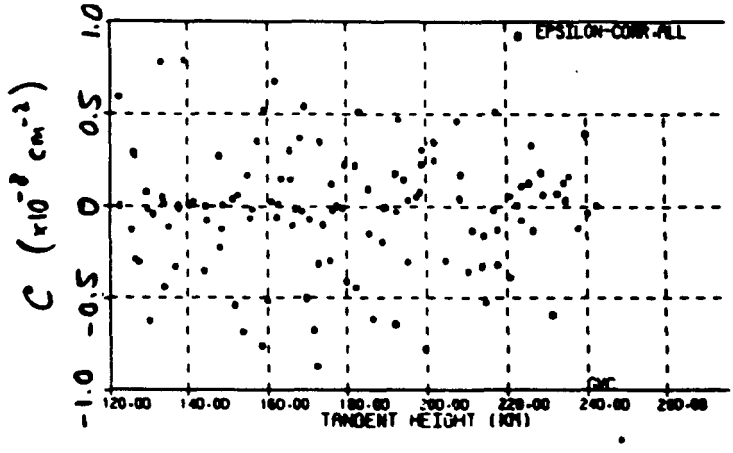

Figure 2.2.3 Correlation C^k of the CO_2 and H_2O ϵ^k determined from all five occultations. The scatter is within 0.5×10^{-8} cm^{-2}. The scatter of this correlation about zero means that the scale uncertainty $\sigma\epsilon$)is less than 2×10^{-5} cm^{-1}.

Table 2.2.1 ϵ determined from ν_3 CO_2 lines.

Occultation	$\epsilon(\times 10^{-5}\text{cm}^{-1})$	$\bar{\sigma}(\epsilon)(\times 10^{-5}\text{cm}^{-1})$
SR02	−0.083	4.533
SS06	−0.114	4.920
SS09	−0.090	5.269
SS11	−0.095	6.767
SS13	−0.094	7.184

Table 2.2.2 ϵ from ν_2 H_2O lines.

Occultation	$\epsilon(\times 10^{-5}\text{cm}^{-1})$	$\bar{\sigma}(\epsilon)(\times 10^{-5}\text{cm}^{-1})$
SR02	−3.356	6.521
SS06	−1.766	6.820
SS09	+3.964	7.096
SS11	−0.258	6.125
SS13	+0.599	6.721

Table 2.2.3 Correlations of ϵ^k between H_2O and CO_2 regions.

Occultation	$C(\times 10^{-10}\text{cm}^{-2})$	$\bar{\sigma}(C)(\times 10^{-10}\text{cm}^{-2})$
SR02	+0.838	6.507
SS06	−2.168	6.074
SS09	−12.62	7.267
SS11	+7.728	5.809
SS13	−6.488	8.475
all	−3.362	3.346

II.3 Solar and Ratioed Spectra

Figure 2.3.1 shows a condensed full Filter-3 solar spectrum collected at tangent heights above 120 km where there is not any significant atmospheric absorption. The spectral features are condensed due to the large range of wavenumbers $1600 < \varsigma < 3200$ cm^{-1} shown in a small space on the page. Many spectral features are evident, particularly the solar '$\odot$' CO fundamental ($\Delta v = 1$), - e.g. $v = 0 \rightarrow v = 1$, $v = 1 \rightarrow v = 2$, etc. - rotation-vibration bands with wavenumbers less than 2330 cm^{-1}. Figure 2.3.2 shows a 'magnification' of the $\odot$ CO band heads near 2300 cm^{-1} along with the ν_3 CO_2 instrumental lines. Instrumental water lines protrude below 2000 cm^{-1}. The lines in the spectrum above the ν_3 CO_2 region $\varsigma > 2380$ cm^{-1} are other solar lines. The $\odot$ CO bands can distort other spectral features which may be of interest. The instrumental CO_2 lines cannot be used for calibration in the region where the ν_3 CO_2 lines overlap with the $\odot$ CO lines since interferences distort the line shapes. Distortions can cause systematic errors in determining their positions ς. The lines used in this report were carefully selected to avoid these problems.

The spectral regions where the absorption bands used to obtain wind speeds in the atmosphere are located in Figure 2.3.1. All of the lines in the solar spectra appear to be superimposed on a 'background signal' S. The background signal appears to vary with wavenumber ς. This happens because the detector sensitivity and the filter transmittance vary with the wavenumber [Shaw, 1989]. The background signal as well as the instrumental

and solar lines superimposed on it serve as the input radiation intensity $I_\varsigma(0)$ described in §I.9 (1.144). The solar features are present in all of the ATMOS spectra, with or without atmospheric absorption.

The positions and shapes of the solar features and instrumental lines remained essentially unchanged during each occultation. It was desirable to 'factor out' these lines since they distort atmospheric features. The solar features serve as the background $I_\varsigma(0)$ in (1.144) for the atmospheric absorption $\exp[-k_\varsigma u]$ as described in §I.9. The signal $I_\varsigma(0)$ was estimated by averaging all of the solar spectra taken above the atmosphere for each occultation [Norton, 1986]. This produced solar spectra $I_\varsigma(0)$ with a very high SNR $\sim$ 500:1 [Norton, 1986]. The atmospheric absorption was then estimated by taking the ratio of the spectra containing atmospheric features I_ς to the solar average $I_\varsigma(0)$. These were termed 'ratioed' spectra and from (1.144) they are defined to be

$$R_\varsigma \equiv \frac{I_\varsigma}{I_\varsigma(0)}. \tag{2.21}$$

The ratioed spectra made by Norton (1986) were used for the majority of the atmospheric studies conducted by the ATMOS team.

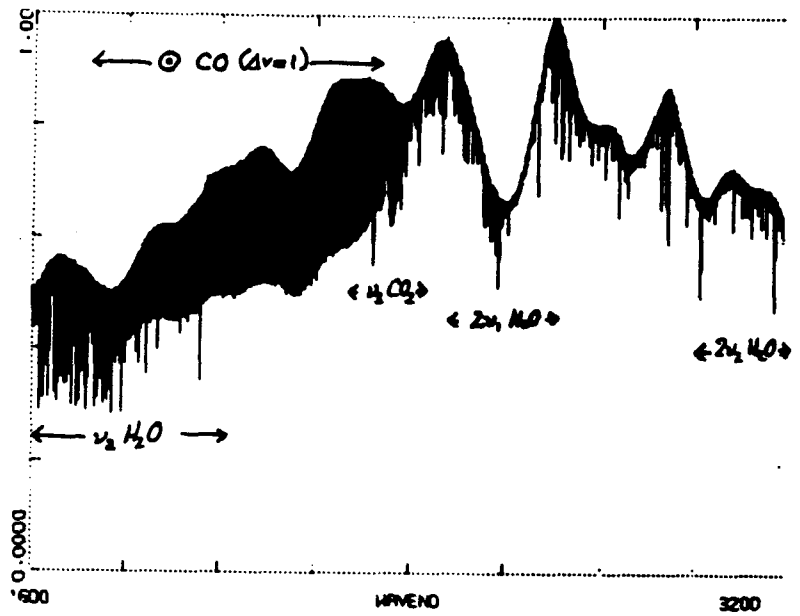

Figure 2.3.1 A complete Filter-3 solar spectrum. Instrumental lines of CO_2 and H_2O are superimposed on background solar spectra. Solar CO lines are present below ~ 2300 cm^{-1} and the variable output of the detector is evident.

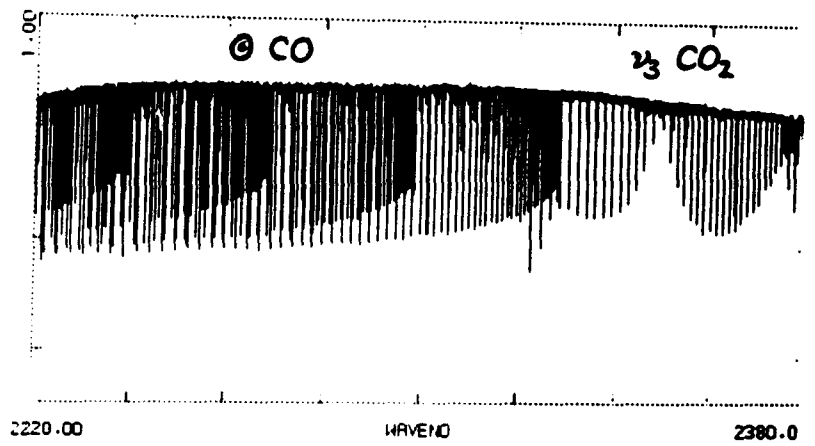

Figure 2.3.2 $\Delta v = 1$ $\odot$ CO band heads and instrumental ν_3 CO_2 lines observed in the solar spectra. This covers a slighly large wavenumber range than Figure 2.1.1.

II.4 Estimating the Noise Level

The interferograms included noise in the instrumental signals caused by fluctuations of the light source, photon noise caused by random arrival of photons from the source, thermal fluctuations in the detector, and external vibrations of the instrument [Norton, 1986; Thorne, 1988]. The noise in the interferograms $I(x)$ is transferred into noise in the spectra $I'(\varsigma)$ through the transform (1.9). In §I.11 it was shown how this noise affects the precision by which the positions of the absorption lines can be measured.

The ratioing process does not affect the signal to noise ratio SNR_ς of the spectra significantly. In the non-ratioed spectra the noise $\mathcal{N}_\varsigma$ in the signal $I_\varsigma(0)$ has random fluctuations $\sigma(\mathcal{N}_\varsigma)$. The ratioing process produces a constant background signal of unity by definition (2.20). The noise N_ς in the ratioed spectra R_ς then has fluctuations

$$\sigma(N_\varsigma) = \frac{\sigma(\mathcal{N}_\varsigma)}{I_\varsigma(0)}. \tag{2.22}$$

In regions where solar absorption features are not present the background signal S_ς and solar signal $I_\varsigma(0)$ are the same. The SNR of the ratioed spectra is dependent on the background signal in the denominator of (2.21). In regions where solar absorption features are strong the denominator of (2.21) may become large and the noise increases. To get the best results in measuring line positions in the ratioed spectra R_ς it is desirable to avoid spectral regions where the noise level caused by solar features is high. An estimate of the SNR_ς of the ratioed spectra R_ς can be determined by examining ratioed

spectra above tangent heights where atmospheric absorption is significant. Figure 2.4.1 shows one such spectra. We see that between 1600 and 2000 cm^{-1}, for example, the SNR is lower than near 2400 cm^{-1}. By visually comparing the wavenumber variations in fluctuations of the ratioed spectrum in Figure 2.4.1 to the wavenumber variations of the background signal in the unratioed solar spectrum in Figure 2.3.1 the correlation between the two is evident. This is predicted by (2.21).

Since scale errors ϵ^k are negligible, measurement uncertainties of the line j in the spectrum k can be determined from (2.10)

$$e_j^k = \varsigma_j^k - \hat{\varsigma}_j. \tag{2.23}$$

By using these values, from the theory §I.11

$$A_{pj}\sigma(e_j) \approx \sigma(\langle A_{pj}^k e_j^k \rangle_k) \doteq f_n \sigma(N) w, \tag{2.24}$$

where $\sigma(N) = 1/\mathrm{SNR}_\varsigma$ is the noise to signal ratio and is described by (2.21) in the ratioed spectra R_ς. By measuring the positions of instrumental lines of H_2O and CO_2 in the unratioed spectra we can estimate the signal to noise ratios for both regions in the ratioed spectra by using (2.23). We expect the relation (2.21) to hold true. From examination of Figure 2.3.1 the SNR of the H_2O region should be almost a factor of two smaller than the CO_2 region.

The *line noise* will be defined here to be $f_n\sigma(N)w$, f_n being the form factor, $\sigma(N) = 1/\mathrm{SNR}$ the signal fluctuations and w the geometric width of the line as described in §I.11. For a given spectral region the signal fluctuations $\sigma(N)$ are approximately a constant and since f_n and w are the same for similar lines, the line noise defined in (2.23) is approximately a constant. The line noise over all lines j in each region were determined using

(2.23) and are listed in Tables 2.4.1-2 for each occultation individually and all collectively for the CO_2 and H_2O instrumental lines respectively. The line noise for the CO_2 region is almost a factor of two larger than that the H_2O regions in agreement with (2.21). For the CO_2 instrumental lines the line noise of about 0.47×10^{-5} cm^{-1} is in close agreement with the estimate (2.23) predicted with rough estimates of the line parameters $f_n = 0.35355$, $\sigma(N) = 0.01$, and $W = 0.015$ cm^{-1} of 0.54×10^{-4} cm^{-1}. It appears that the measurement uncertainty theory can be used to describe the precision of the line-finder program quite accurately.

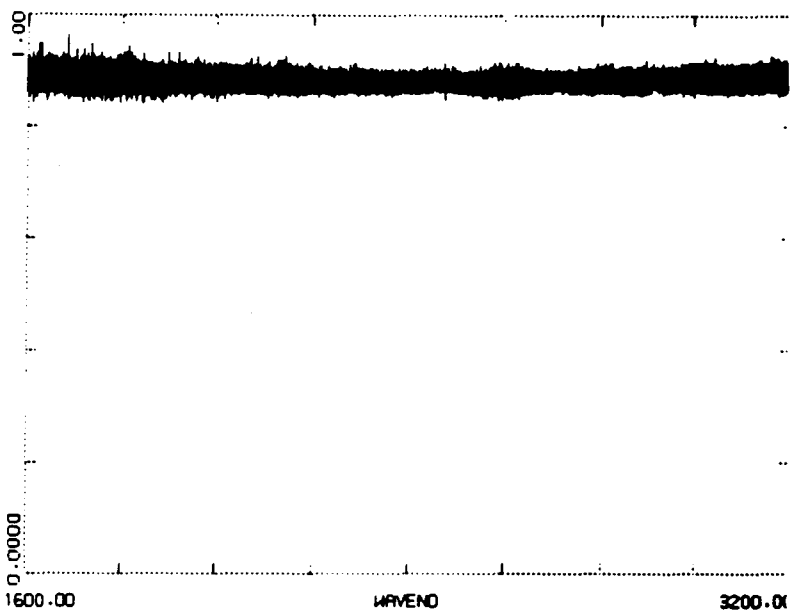

Figure 2.4.1 The noise level in the spectra after the ratioing process. This spectrum was taken at a tangent height where atmospheric absorption is absent. This represents the background noise level of the spectra. Note the variations in the spread of the noise with wavenumber.

Table 2.4.1 Estimates of noise level from CO_2 instrumental lines.

Occultation	mean ($\times 10^{-5} cm^{-1}$)
SR02	4.94
SS06	4.55
SS09	4.42
SS11	4.67
SS13	4.79
all	4.67

Table 2.4.2 Estimates of noise level from H_2O instrumental lines.

Occultation	mean ($\times 10^{-5} cm^{-1}$)
SR02	8.30
SS06	8.01
SS09	7.79
SS11	8.10
SS13	8.09
all	8.10

II.5 Estimating Relative Speeds Along the Line of Sight

The method of estimating individual line positions and the calibration stability of better than 2×10^{-5} cm^{-1} determined in §II.3 imply that wind speeds can be obtained to a precision of 5 ms^{-1} or better. It was also pointed out by Shaw (1985) that these kinds of precisions could be achieved using Filter 3 spectra provided that the SNR was large enough. From the data in Table 1.12.3 we can estimate the sample size needed to attain the precision of 5 ms^{-1} or better. From (1.186) the uncertainty per line j of the velocity is given by

$$\sigma(v_j) = \sigma(\varsigma_j)\frac{c}{\hat{\varsigma}_j}. \tag{2.25}$$

From the measurement theory (1.180) the uncertainty is proportional to A_p^{-1}. For a line with a peak absorptance $A_p \simeq 20\%$ and a position of $\hat{\varsigma}_j \simeq 2350\text{cm}^{-1}$ we see that $\sigma(v_j) \simeq 35$ ms^{-1}. Using N lines the precision of the relative velocity is then 35 ms$^{-1}/\sqrt{N}$ so we need about 50 lines to attain 5 ms^{-1}. However, for stronger lines, using a peak absorptance $A_p \simeq 70\%$ for example, this sample size can be considerably smaller. By using a value of $\sigma(\varsigma_j) \simeq 0.76 \times 10^{-4}\text{cm}^{-1}$ we find that $\sigma(v_j) \simeq 10$ ms^{-1} which requires a sample of size of only 4 lines to attain the desired precision. In practice the peak absorptances of the lines used are primarily in the 20-70% range and a sample size between 20 and 30 lines is usually available. Therefore we can predict that relative speeds can be determined to at least 5 ms^{-1} and most likely

better using single bands of atmospheric lines.

The accuracy by which line Doppler shifts can be determined is independent of any wavenumber dependent calibration errors, provided that line positions in the rest frame can be measured by the instrument. To see this, the wavenumbers measured by the instrument ς_{inst} can in principal be shifted from the "true" wavenumber ς_{true} by a small amount and this offset can be represented by

$$\varsigma_{inst} = (1 + \alpha)\, \varsigma_{true} \tag{2.26}$$

where α is may be regarded as constant over small spectral regions. Note that this α is not the same factor defined in §II.1. If the "true" rest frame position is given by $\hat{\varsigma}_{true}$ then the corresponding position as measured by the instrument will be at $\hat{\varsigma}_{inst} = (1 + \alpha)\, \hat{\varsigma}_{true}$. For Doppler shifted lines then

$$\begin{aligned} \varsigma_{inst} &= (1 + \alpha)\varsigma_{true} = (1 + \alpha)\left(1 + \frac{v}{c}\right)\hat{\varsigma}_{true} \\ &= \left(1 + \frac{v}{c}\right)\hat{\varsigma}_{inst} \end{aligned} \tag{2.27}$$

which is independent of the shift α. This is because the form $1+\alpha$ is the same for both the rest frame and moving frame positions. This result indicates that accurate relative speed measurements can be made provided that the rest frame positions $\hat{\varsigma}_{inst}$ are known and that the calibration of the ATMOS interferometer remains stable throughout the course of observation.

There are typically about 30 lines of the ν_3 CO_2 band which are visible in the spectra and can used to measure Doppler shifts. Relative speeds can be obtained to 5 ms^{-1} with these lines provided that the lines are not too weak or saturated. From (2.24) we see that the uncertainty of measuring Doppler shifts is wavenumber dependent. As an example, for the ν_2 CO_2 band near

667 cm^{-1}, many more lines are needed. For a wavenumber of about 1/4 of the ν_3 lines the uncertainty $\sigma(v_j)$ will be about 4 times as large. We would need 16 times as many lines. From a practical point of view, relative speed measurements should be confined to the higher wavenumber regions of the spectra.

II.6 Relative Speed Measurements Using ν_3 CO_2 Lines Between 2330 and 2372 cm^{-1}

The ATMOS instrument was found to have a stable frequency calibration as well as an excellent SNR of about 100:1. This enables precise relative speeds to be obtained from a small number of lines in the mid-infrared regions [Shaw, 1985]. Below about 120 km atmospheric absorption lines of the ν_3 CO_2 absorption band become visible in the spectra between 2330 and 2370 cm^{-1}. Figure 2.6.1 shows several of these lines along with their instrumental counterparts taken from an unratioed spectrum for illustration. These atmospheric lines were used to measure relative speeds from tangent heights of about 120 km to about 80 km where overlapping with other CO_2 bands and line saturations occur. A typical overlap of CO_2 lines from different bands taken in successive spectra is shown in Figure 2.6.2. As the tangent height decreased the lines begin to interfere with each other. The spectra are displaced vertically for clarity. The ν_3 lines used in this study were chosen to

be those lines which displayed minimal interferences. These were considered to be "good" lines. Another criterion used was that the peak absorptances range from 10-70% because resolved line weaker than these became distorted by the background noise while stronger lines become saturated. This caused the curvature of the line near the line center to become flat which increased the measurement error (the *geometrical* or *spectral* width w of the line increases dramatically).

With the above criteria for choosing absorption lines, the instrumental lines given in Table 2.1.8 were used as the standards $\hat{\varsigma}_j$ in (2.26). The relative speed for v_j^k for each spectrum k and line j was measured using (1.1)

$$v_j^k = \left(\frac{\varsigma_j^k}{\hat{\varsigma}_j} - 1 \right) c. \tag{2.28}$$

From this the relative speed v^k for each spectrum k was determined

$$v^k = \langle v_j^k \rangle_j \tag{2.29}$$

and its corresponding mean deviation $\bar{\sigma}(v^k)$ determined. This was performed for each of the occultations and the resulting relative speed profiles were determined. Figures 2.6.3-4 show the relative speed versus ray tangent height using the ν_3 CO_2 atmospheric lines for the sunrise and sunset occultations respectively. The relative speed profiles are typically of the order of 6000 ms^{-1}. This is due to the orbital motion of the satellite and and this motion is estimated and subtraced from the profiles to obtain zonal wind in the atmosphere around the tangent point §II.12.

The relative speed profiles show a variability with tangent height. The 'wavelike' structure of the relative speed profiles is immediately recognized,

particularly in Figure 2.6.4 where the four sunset profiles demonstrate a remarkable similarity with regards to altitudes of peaks and valleys. Large shears, especially between 105 and 120 km are apparent. The sunrise profile in Figure 2.6.3 demonstrates similar features. Figure 2.6.5 displays the mean error $\bar{\sigma}(v^k)$ for all of these occultations. Note that $\bar{\sigma}(v^k)$ increases at large heights because the lines become very weak. At the lowest tangent heights the increase in $\bar{\sigma}(v^k)$ is due to overlapping of lines and saturation. The curves all follow the same general trend and, as proposed above, precisions of 5 ms^{-1} are indeed found. Between 80 and 110 km these lines achieved a maximum precision of $\sim$2.5 ms^{-1}. Since the calibration of the instrument is stable these precisions indicate that the features observed are real. Also evident in Figure 2.6.4 are relative differences of over 100 ms^{-1} between SS06 and the rest of the sunset profiles. The relative speed profiles for SS09, SS11, and SS13 showed a trend of increasing relative speed with respect to the SS06 profile as the mission progressed. This is due to the changing geometrical orbit of the instrument and its component of velocity along the line of sight.

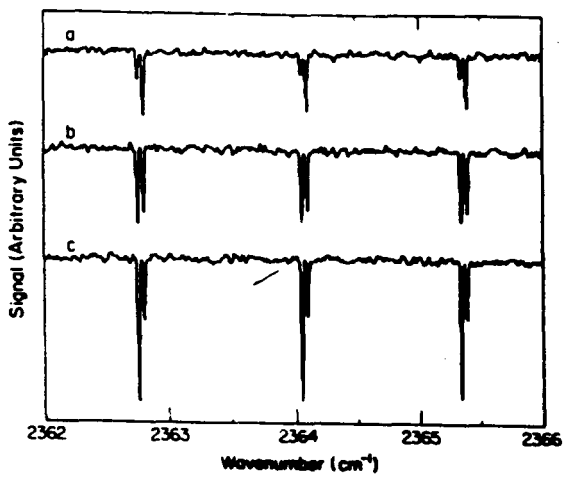

Figure 2.6.1 Pairs of instrumental and atmospheric lines. The atmospheric lines are red-shifted (towards the left) from the instrumental lines as the tangent height decreases from 112 (a) to 90 km (c) in a sunset occultation. The spectra are displaced for clarity. Note the increasing peak absorptions of the atmospheric lines as the tangent heights decreases.

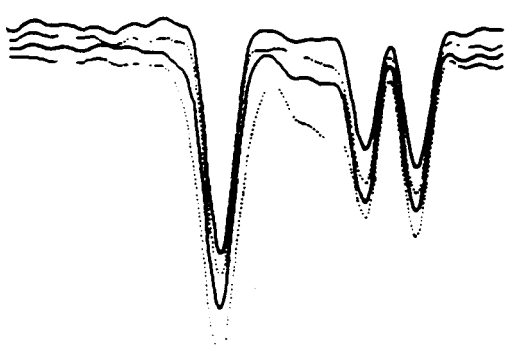

Figure 2.6.2 Overlapping of lines from ATMOS spectra. Notice how the line shapes become distorted by other spectral features as the tangent height decreases. Lines must be examined for interferences before including them in wind measurements. The spectra have been slightly displaced vertically for clarity.

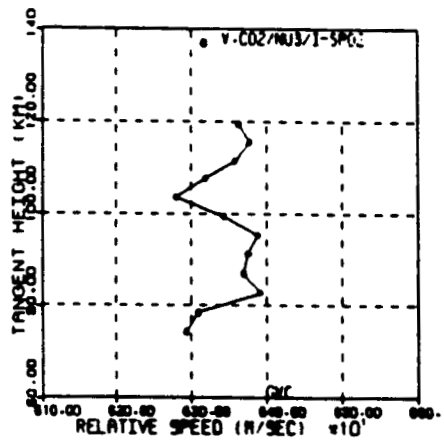

Figure 2.6.3 Relative speed profile determined using ν_3 CO_2 atmospheric lines for the sunrise occultation. There appear to be rather large shifts in the relative speeds near 80 and 105 km.

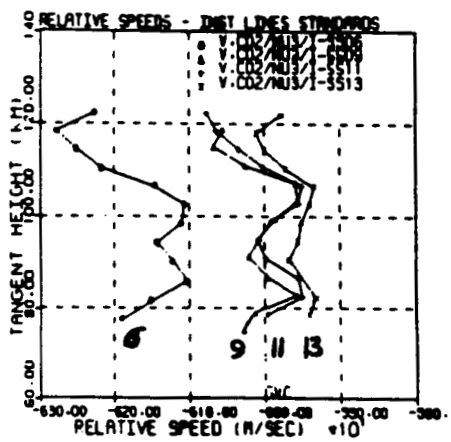

Figure 2.6.4 Relative speed profile determined using ν_3 CO_2 atmospheric lines for the sunset occultations. The four occultations (6) SS06 - (9) SS09 - (11) SS11 - (13) SS13 are displaced due to changes in the orbital motion §II.12. The appear to have similar relative speed shears near 80 and 105 km as well as 'minima' near 95 km. These are due to variations in the upper atmospheric wind speeds.

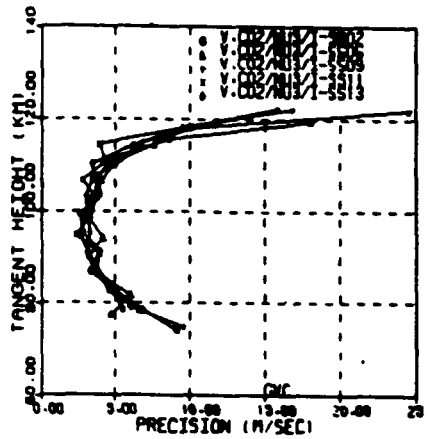

Figure 2.6.5 Measurement uncertainty $\bar{\sigma}(v^h)$ for all occultations using ν_3 CO_2 atmospheric lines. A precision of better than 5 ms^{-1} is achieved between 80 and 110 km. The increase outside of this region of high precision is due to the weakness of lines above 110 km and line saturation and interferences below 80 km.

II.7 Extending Relative Speed Measurements and the Determination of $\hat{\nu}_{\text{inst}}$

We now proceed to extend these measurements to lower altitudes using absorption lines in which no instrumental counterparts are available for determining the rest frame positions. The profiles in Figures 2.6.3-4 were determined by directly comparing the instrumental CO_2 lines to their atmospheric counterparts and thus directly measuring the Doppler shifts. In general, instrumental lines are not available for direct comparison at lower tangent heights. Fortunately there is a way of getting around this problem. We know that the calibration of the instrument is stable, we have determined relative speeds using the calibrated instrumental lines, and there are more lines entering into the spectra as the tangent height decreases. We must use these new atmospheric lines that are entering into the spectra, however we need to know $\hat{\varsigma}_{\text{inst}}$ for each of these lines.

Consider a set of new atmospheric lines which have entered the spectra. Their positions are Doppler shifted by (1.1). It should now be understood that we are referring our wavenumbers to the calibration system of the instrument and are no longer referring to 'absolute standards' which were used to calibrate the ν_3 CO_2 region. As shown in the previous section (2.26) absolute standards are no longer needed to measure absolute relative wind speeds. Let us suppose that the relative speeds v^k for a set of spectra k have been determined to a reasonable degree of precision (5 m/s or better). Then we can invert (2.26) to obtain an estimate of the rest frame positions of each

of the new lines which have appeared in the spectra for which v^k had been estimated

$$\hat{\varsigma}_j^k = \frac{\varsigma_j^k}{1 + v^k/c} \simeq \left(1 - \frac{v^k}{c}\right) \varsigma_j^k \tag{2.30}$$

from the observed atmospheric line position ς_k^j for each new line j in each spectrum k. We can estimate the rest frame position from the average

$$\hat{\varsigma}_j = \langle \hat{\varsigma}_j^k \rangle_k \tag{2.31}$$

as well as its mean error $\bar{\sigma}(\hat{\varsigma}_j)$. Having determined these rest frame positions the new lines may be used to extend the wind below the current minimum tangent height.

One problem with this technique as it is presently stated is that the line positions $\hat{\varsigma}_j$ determined are only as precise as the relative speed profiles v^k from which they were obtained. On the other hand, if the rest frame positions have a degrading precision then the relative speeds themselves will become less precise. An iterative scheme proved to be useful in dealing with this problem. Specifically, an initial set of relative speeds $v^{k,(0)}$ was determined from an initial set of rest frame positions $\hat{\varsigma}_j^{(0)}$ over an altitude range for all of the occultations. From these initial relative speeds $v^{k,(0)}$ an updated list of line positions was determined

$$\hat{\varsigma}_j^{k,(i)} = \frac{\varsigma_j^k}{1 + v^{k,(i-1)}/c}, \tag{2.32}$$

$$\hat{\varsigma}_j^{(i)} = \langle \hat{\varsigma}_j^{k,(i)} \rangle_k. \tag{2.33}$$

Then an updated relative speed profile was determined

$$v_j^{k,(i)} = \left(\frac{\varsigma_j^k}{\hat{\varsigma}^{k,(i)}} - 1\right) c, \tag{2.34}$$

$$v^{k,(i)} = \langle v_j^{k,(i)} \rangle_j. \tag{2.35}$$

This procedure was then repeated until a desired level of convergence in the mean uncertainties of the relative speeds $\bar{\sigma}(v^k)$ and the line positions $\bar{\sigma}(\hat{\varsigma}_j)$ were both obtained. I chose value of 0.1 ms^{-1} and 10^{-6} cm^{-1} respectively.

The relative speed profiles shown in Figures 2.6.3-4 were recomputed along with the rest frame positions of the atmospheric lines by using the above procedure for the lines specified in Table 2.1.8. The precisions in lines positions $\bar{\sigma}(\hat{\varsigma}_j)$ were found to converge to less than 10^{-6} cm^{-1} in usually three or four iterations with a simultaneous convergence of $\bar{\sigma}(v^k)$ less than 0.1 ms^{-1}. Figure 2.7.1 shows the precisions of the positions determined from measuring instrumental lines (bold line) and those positions computed from the atmospheric lines using the iteration procedure (points). The precisions determined using the atmospheric lines are more uniformly distributed with a value near 0.28×10^{-4} cm^{-1} than the positions determined from the instrumental lines. The apparent degradation of the precision is actually due to the smaller sample size of atmospheric spectra used (about 60) compared to the number of high altitude spectra used (about 125). However, the results do show that by using the velocity profiles to determine line positions, we can obtain satisfactory results, particularly in the case where only a few atmospheric lines are originally present for initial line position estimates. Figure 2.7.2 shows the precisions obtained using instrumental lines (bold lines) and atmospheric lines (points). The slight improvement below 100 km is not significant.

At wavenumbers between 2372 and 2380 cm^{-1} eight ν_3 CO_2 lines become reasonably strong ($A_p > 15\%$) at about 100 km and are useful for extending the relative speed profiles. Their positions $\hat{\varsigma}_j^{(0)}$ were estimated from (2.27-

8) using the relative speed profiles in Figures 2.6.3-4 above 80 km. The line positions were then used to extend the relative speed profiles to lower tangent heights. The iteration procedure was used for the lines between about 70 and 100 km. Figure 2.7.3 shows the improvements in the lines precisions between the first estimate (solid line) and the converged result (points). An improvement of about $5 \times 10^{-6} \mathrm{cm}^{-1}$, although small, is evident. The precisions in the relative speeds are shown in Figure 2.7.4 and there does not appear to be a significant difference before and after the iteration. Since the range of altitudes where these CO_2 lines appear overlap the relative speeds in Figures 2.6.3-4 is large (30 km) the sample size of lines for the new rest positions is large enough to ensure fairly precise initial estimates $\hat{\varsigma}_j^{(0)}$ of about 3×10^{-5} cm^{-1}. This is not the case in general, however.

The above results show that the initial relative speed profiles can be used to determine the unknown rest frame positions of atmospheric lines. In turn, these rest frame positions can then be used to determine relative speeds at extended tangent height ranges. Since the line positions and relative speeds are determined simultaneously, the precisions of the initial relative speed profiles are maintained. This indicates that by using the calibration stability of the instrument, relative speeds with precisions and accuracies similar to those determined by using the positions measured from the instrumental lines can be determined from other atmospheric lines. We used this procedure to extend relative speed profiles to 25 km by using N_2O, CO_2 and H_2O lines §II.9.

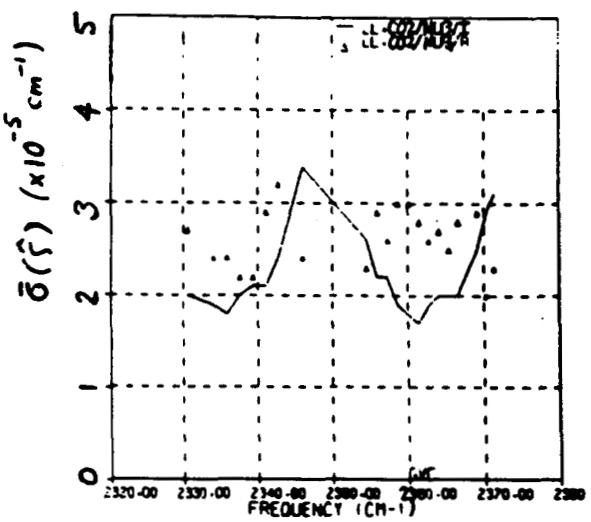

Figure 2.7.1 Precisions of ν_3 CO_2 rest frame positions determined from atmospheric lines ($\hat{\nu} < 2372$ cm^{-1}) before (line) and after (points) iteration procedure. The improvement in line positions is slight.

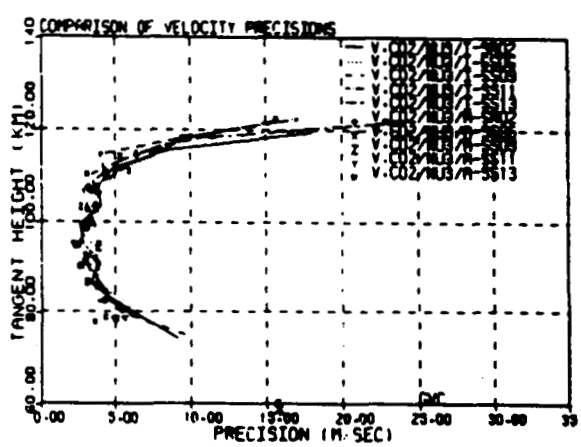

Figure 2.7.2 Precisions of relative speeds determined from ν_3 CO_2 atmospheric lines ($\hat{\nu} < 2372$ cm^{-1}) before (line) and after (points) iteration procedure. There is only a slight improvement in precisions from using the measured instrumental line positions.

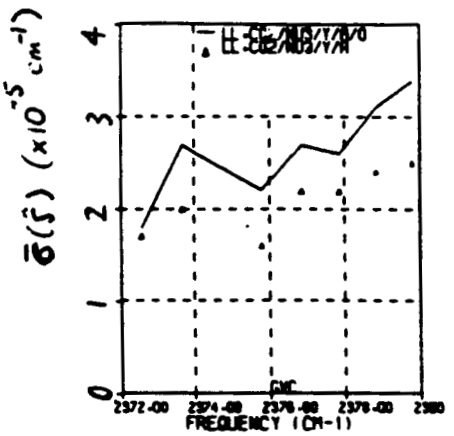

Figure 2.7.3 Precisions of ν_3 CO_2 rest frame positions determined from atmospheric lines ($\hat{\nu} > 2372$ cm^{-1}) before (line) and after (points) iteration procedure. There are improvements of up to 1×1'0^{-5} cm^{-1} in the line positions.

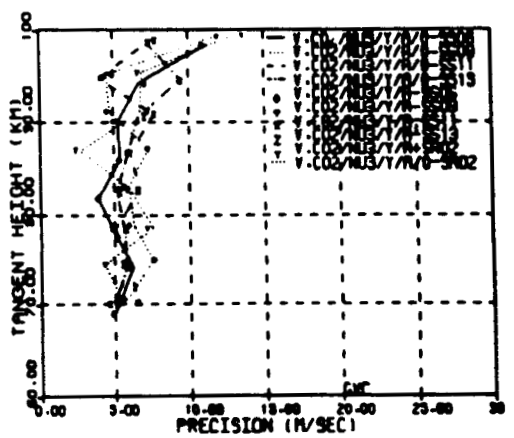

Figure 2.7.4 Precisions of relative speeds determined from ν_3 CO_2 atmospheric lines ($\hat{\nu} > 2372$ cm^{-1}) before (line) and after (points) iteration procedure. The improvement in the precisions is very small. Note that the precision of 5 ms^{-1} has been maintained to 70 km usingthese lines. The precision degreades above 90 km due to the weaknesses of the lines.

II.8 Weighted Averages of Relative Speed Profiles

We have obtained relative speed profiles from different sets of lines and we wish to combine the results to obtain the best profile. The speed profiles can be combined by calculating a weighted average. This takes into account the varying precisions of the relative speeds with height. Let us assume we have several profiles l for each spectrum k given by v_l^k with a mean uncertainty $\bar{\sigma}(v_l^k)$. Then the weighted average is

$$v^k = \sum_l w_l^k v_l^k \tag{2.36}$$

where the weights w_l^k are given by [Bevington, 1969]

$$w_l^k = \frac{1/\bar{\sigma}^2(v_l^k)}{\sum_{l'} 1/\bar{\sigma}^2(v_{l'}^k)}. \tag{2.37}$$

The weighted uncertainty is then determined by [Bevington, 1969]

$$\frac{1}{\bar{\sigma}^2(v^k)} = \sum_l \frac{1}{\bar{\sigma}^2(v_l^k)}. \tag{2.38}$$

Profiles combined in this method are called "extended" or "merged" relative speed profiles and are then used to determine initial estimates of line positions for further extension to lower tangent heights. Figures 2.8.1 and 2.8.2 show the extended relative speeds v^k (for sunsets) and their weighted precisions $\bar{\sigma}(v^k)$ determined using this method. It can be seen in Figure 2.8.2 that a 5 ms^{-1} precision or better is maintained to about 70 km. In the region of overlap between the two sets of ν_3 CO_2 lines between 80 and 100 km described in the previous two sections we have approximately 30 total

lines. The average peak absorptance is about 50% over this range. Using a noise level of $f_n\sigma(N)w = 5 \times 10^{-5}$ cm^{-1} from Table 2.4.1 the predicted measurement uncertainty per line from (1.180) is

$$\text{uncertainty} = \frac{5 \times 10^{-5}\text{cm}^{-1}}{.50} = 10^{-4}\text{cm}^{-1}. \tag{2.39}$$

For a central frequency of about 2350 cm^{-1} for 30 CO_2 lines the predicted uncertainty in the relative speeds is

$$\bar{\sigma}(v^k) = \frac{10^{-4}}{2350}\frac{c}{\sqrt{30}} \simeq 2.5 \text{ ms}^{-1}. \tag{2.40}$$

This is consistent with the observed precisions shown in §II.7.

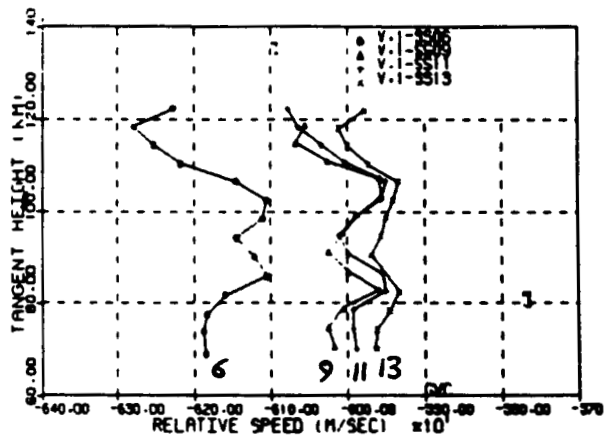

Figure 2.8.1 First extended relative speed profiles v^k for the four sunset occultations. The speed profiles using ν_3 CO_2 absorption lines which did not have instrumental counterparts have been combined with the sunset speed profiles in Figure 2.6.4. Notation is the same as in Figure 2.6.4.

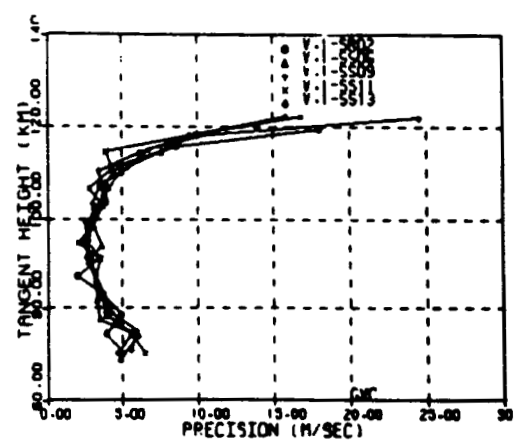

Figure 2.8.2 Precisions of first extended relative speed profiles $\bar{\sigma}(v^k)$ for all occultations. The precision of 5 ms^{-1} is maintained from 70 to 110 km.

II.9 Extensions to Lower Tangent Heights by Using H_2O and N_2O

In the spirit of the last two sections the profiles were extended by using three more bands. Between 40 and 80 km the ν_2 H_2O atmospheric counterparts to the H_2O instrumental lines given in Table 2.1.9 were used for an extension. Between 30 and 65 km lines of the $2\nu_2$ H_2O band near 3150 cm^{-1} was used and finally between 20 and 40 km lines of the $2\nu_1$ N_2O near 2550 cm^{-1} was used to complete the profiles.

The iterative technique was chosen to estimate the positions of the ν_2 water lines instead of relying on the instrumental positions as was done for the ν_3 CO_2 lines for a reason which will made clear shortly. In fact, we would like to compare the positions retrieved for both sets of lines and this is done in the following section. The initial positions $\hat{\varsigma}_j^{(0)}$ were determined from the spectra between 50 and 80 km and the relative speed profiles in Figure 2.8.1. The precisions $\bar{\sigma}(\hat{\varsigma}_j^{(0)})$ are shown by the bold line in Figure 2.9.1. The iterative scheme was then carried out and the precisions of the line positions are given by the points in Figure 2.9.1. There is an improvement in the mean uncertainties to better than 8×10^{-5} cm^{-1}. Figure 2.9.2 shows the initial (connected points) mean uncertainties for the estimated relative speeds between 40 and 80 km using these lines and the improved mean uncertainties (points). Between 45 and 60 km there is an improvement of up to 3 or 4 ms^{-1}. The resultant profiles were then merged with those given in Figure 2.9.1 and these are shown in Figures 2.9.3. The weighted mean uncertainties

are shown in Figure 2.9.4. The mean uncertainty $\bar{\sigma}(v^k)$ is 5 m/s or better between 50 and 110 km. The relative speeds appear to "flatten out" below 75 km and do not appear to show the rapid variations with height which are noticeable above this level.

The extension method at this point is fairly straightforward. The next set of lines which were found to be useful is the $2\nu_2$ H_2O vibration band which is approximately at twice the frequency as its ν_2 counterpart. However, the sample of nine lines chosen in the overlap regions between 30 and 65 km is much smaller than the ν_2 sample size of more than 20. This does not cause significant problems since the higher frequency of these lines helps the statistics (2.25). Figure 2.9.5 shows the initial estimates and final estimates in the line position precisions (line and points respectively). In every case there is a marked improvement. Figure 2.9.6 shows the initial and final mean uncertainties in the relative speeds and below 40 km there is an improvement of several ms^{-1} for most occultations. Finally the resultant relative speed profiles were merged with Figure 2.9.3 and are shown in Figure 2.9.7. The mean uncertainties are shown in Figure 2.9.8. Precisions are now about 5 m/s in most cases from about 35 to 110 km.

The final set of lines which were found to be useful is the $2\nu_1$ N_2O vibration band. There were 61 lines available in the overlap regions between 30 and 40 km. Even though lines were relatively weak in these regions ($A_p \simeq 10\%$) the large sample size improved the statistics. Figure 2.9.9 shows the initial estimates and final estimates in the line position precisions (line and points respectively). In every case there is again a significant improvement to less than 10^{-4} cm^{-1}. Figure 2.9.10 shows the initial and final mean uncertainties

in the relative speeds and below 30 km there is an improvement of several ms^{-1} for most occultations. Finally the resultant relative speed profiles were merged with Figure 2.9.8 and are shown in Figure 2.9.11-12 for the sunsets and sunrise respectively. The mean uncertainties are shown in Figure 2.9.13. Precisions are now between 2 and 5 ms^{-1} in most cases from about 25 to 110 km.

From these results we see that relative speeds precisions of better than 5 ms^{-1} can be obtained by measuring rest frame positions from the atmospheric lines. The calibration stability of the instrument is adequate to maintain these precisions throughout the middle atmosphere. The accuracy of the profiles is determined by using the CO_2 instrumental lines to calibrate the wavenumber scale. The iteration method of extending the relative speeds to lower tangent heights and using new atmospheric bands as they appear in the spectra does not degrade the precisions of obtaining line positions and speeds.

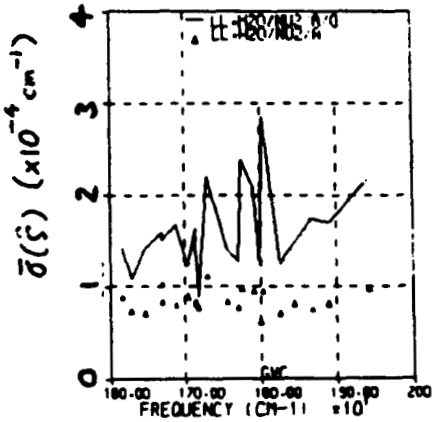

Figure 2.9.1 Precisions of ν_2 H_2O rest frame positions determined from atmospheric lines before (line) and after (points) iteration procedure. There is a noticable improvement in the line positions of up to 10^{-4} cm^{-1}.

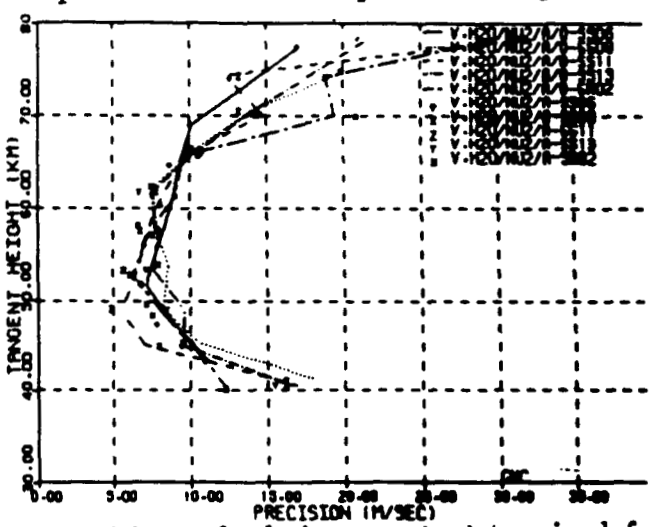

Figure 2.9.2 Precisions of relative speeds determined from ν_2 H_2O atmospheric lines before (lines) and after (points) iteration procedure. The improvement in precisions is small but up to 1 ms^{-1} in some cases. The relative speed precision between 5 ms^{-1} and 10 ms^{-1} is maintained between 45 and 65 km. This degradation in the precision is due to the small sample of atmospheric ν_2 H_2O lines available for initial position estimates.

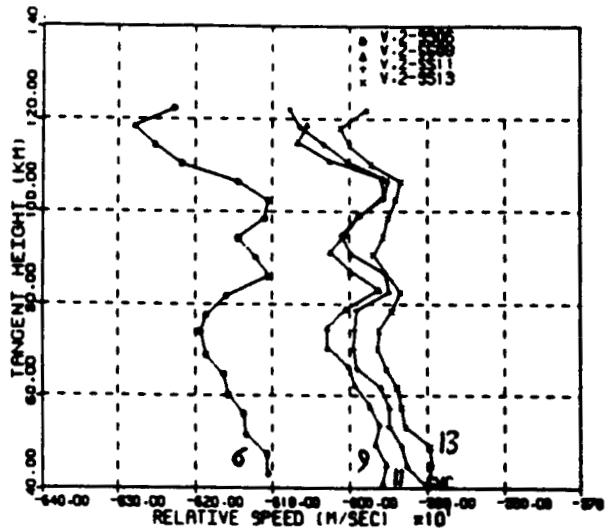

Figure 2.9.3 Second extended relative speed profiles v^k for the sunset occultations. This is obtained by combining the speed profiles determined with the atmospheric ν_2 H_2O lines with the profiles determined using the ν_3 CO_2 atmospheric lines. Rapid wind variations do not appear to occur below 70 km. The separation of the profiles due to changes in the orbital speed is evident.

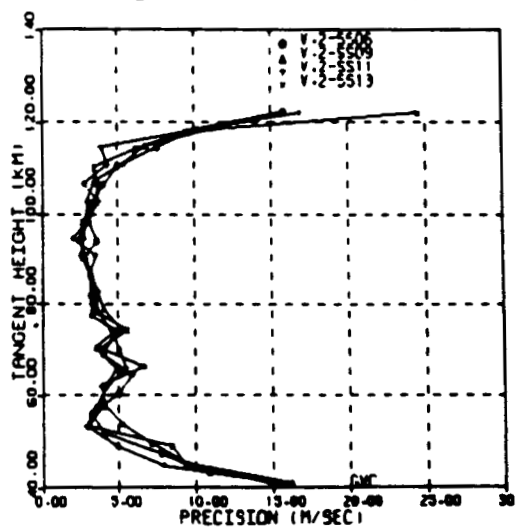

Figure 2.9.4 Precisions of second extended relative speed profiles $\tilde{\sigma}(v^k)$ described above for all occultations. A precision of 5 ms^{-1} is maintained above 50 km.

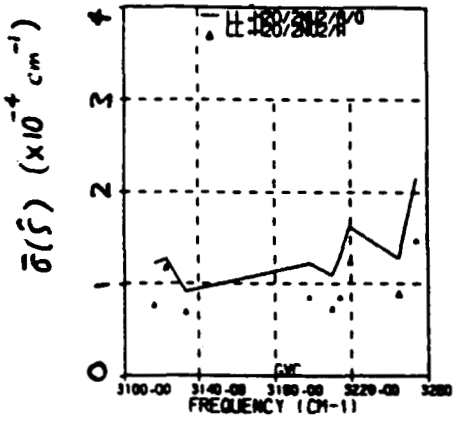

Figure 2.9.5 Precisions of $2\nu_2$ H_2O rest frame positions determined from atmospheric lines before (line) and after (points) iteration procedure. Precisions are improved from initial estimates by up to 0.5×10^{-4} cm^{-1}.

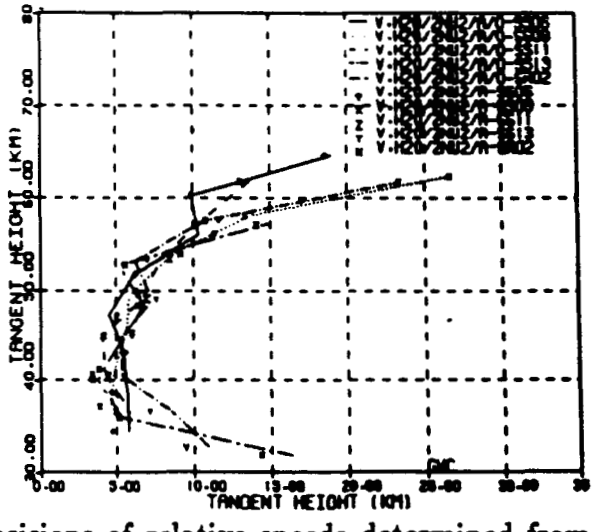

Figure 2.9.6 Precisions of relative speeds determined from $2\nu_2$ H_2O atmospheric lines before (lines) and after (points) iteration procedure. Precision of about 5 ms^{-1} are maintained betyween 35 and 50 km. Increases above that are due to the weaknesses of the lines. Relative speed precisions do not improve signifgicantly before and after the iteration procedure.

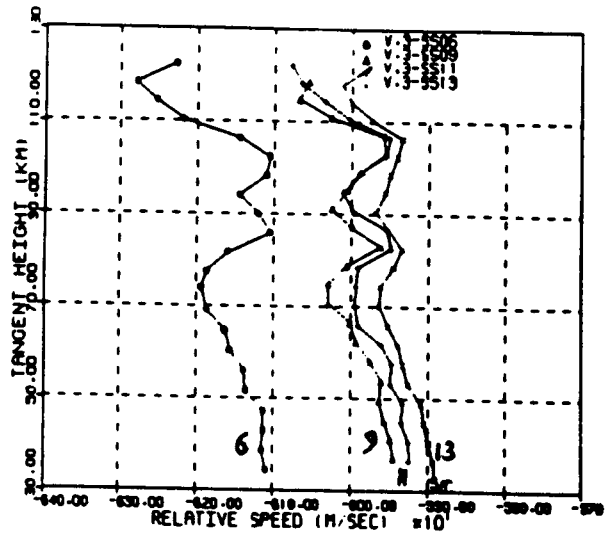

Figure 2.9.7 Third extended relative speed profiles v^k for the sunset occultations. This is obtained by combining the speed profiles determined with the atmospheric $2\nu_2$ H_2O lines with the profiles determined using the ν_3 CO_2 and ν_2 H_2O atmospheric lines.

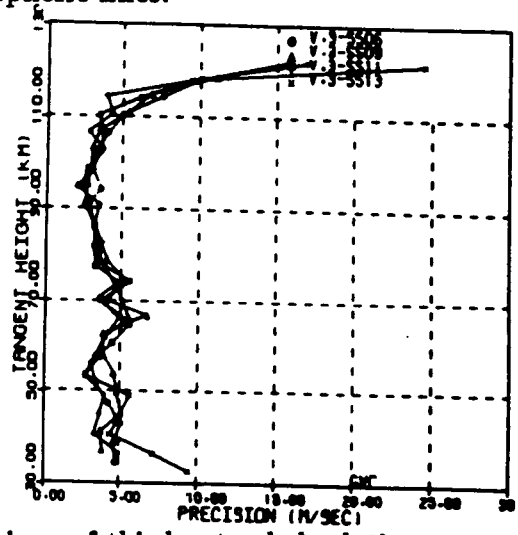

Figure 2.9.8 Precisions of third extended relative speed profiles $\bar{\sigma}(v^k)$ for all occultations which corresponds to the speed profiles above. A precision of 5 ms^{-1} is mainted between about 35 and 110 km.

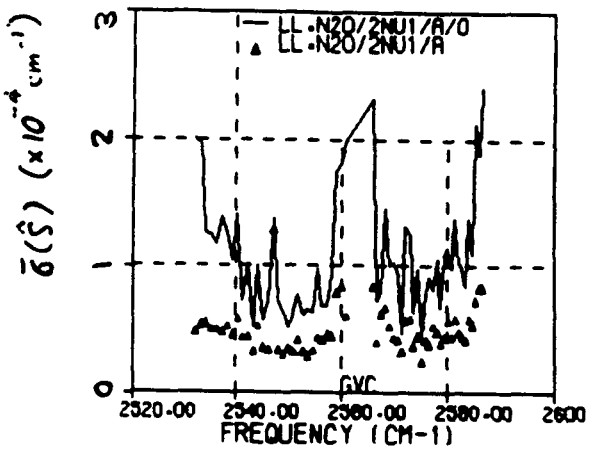

Figure 2.9.9 Precisions of $2\nu_1$ N_2O rest frame positions determined from atmospheric lines before (line) and after (points) iteration procedure. Improvements in precision of more than 1×10^{-4} cm^{-1} between the initial and final estimates is evident, particularly near the band origin near 2560 cm^{-1} and the high J lines.

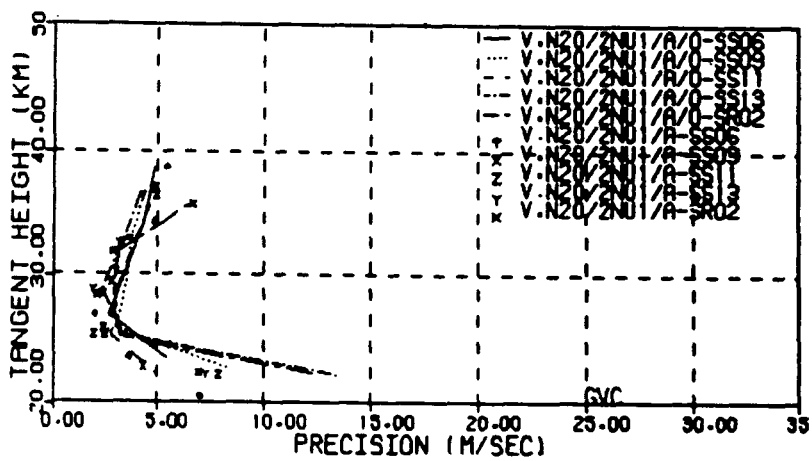

Figure 2.9.10 Precisions of relative speeds determined from $2\nu_1$ N_2O atmospheric lines before (lines) and after (points) iteration procedure. A precision of 5 ms^{-1} is maintained between about 5 and 38 km. Below 25 km line saturation due to pressure broadening degrades the precisions.

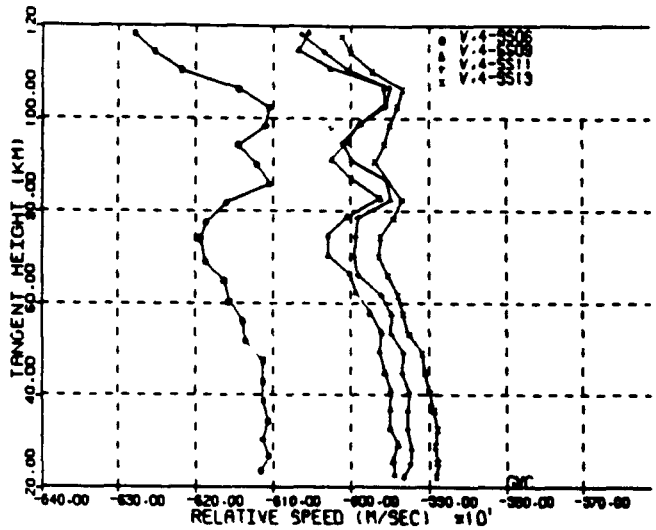

Figure 2.9.11 Fourth extended relative speed profiles v^k for the sunset occultations obtained from combining speed profiles determined using the $2\nu_1$ N_2O absorption lines to the profiles using the ν_3 CO_2, ν_2 $H)_2O$ and $2\nu_2$ H_2O atmosphwewric absorption lines. The gentle variation in relative speed with height below 60 km is evident as well as rapid variations with height above 70 km. The similarities in the variations with height in the profiles is evident. The separations between occultations is due to changes in the orbital geometry §II.12.

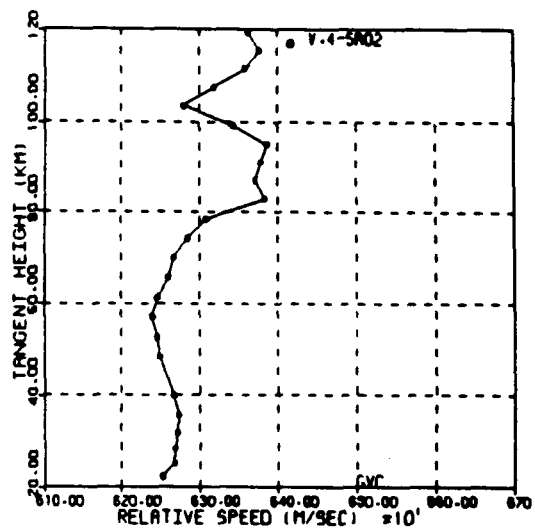

Figure 2.9.12 Same as in Figure 2.9.11 except for the sunrise occultation.

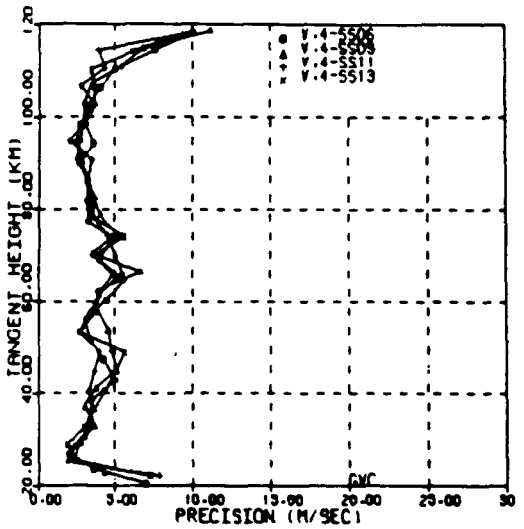

Figure 2.9.13 Precisions of the fourth extended relative speed profiles $\bar{\sigma}(v^k)$ for all occultations described in Figures 2.9.11-2. A precision of 5 ms^{-1} or better is maintained between 25 and 110 km for all occultations.

II.10 Line Positions Obtained and Calibration Standards

COMPARING RETRIEVED AND STANDARD LINE POSITIONS

It has been shown that the line positions determined from the wind retrieval method are precise to $\mathcal{O}(10^{-5}\ \mathrm{cm}^{-1})$ and accurate to $10^{-4}\ \mathrm{cm}^{-1}$. These were compared to a set of standard for the CO_2, H_2O and N_2O line positions compiled in the ATMOS line listing by Brown (1986). The differences between retrieved values $\hat{\varsigma}_{\mathrm{inst}}$ and the standards recommended by Brown $\hat{\varsigma}_{\mathrm{Brown}}$ or in the ATMOS line list $\hat{\varsigma}_{\mathrm{ATMOS}}$ are shown in Figure 2.10.1. For the ν_2 H_2O lines there does appear to be a difference between the positions determined from the atmospheric lines and the ATMOS standards positions of about $10^{-4}\ \mathrm{cm}^{-1}$ for most of the lines. The other bands appear to be distributed more or less about zero. Some of the N_2O lines have significant shifts of up to $5 \times 10^{-4}\ \mathrm{cm}^{-1}$. Since the precisions of $\mathcal{O}(10^{-5}\ \mathrm{cm}^{-1})$ we obtain are of an order of magnitude better than this the ATMOS instrument can be useful for improving rotation-vibration line wavenumbers and B values §I.6. For example, the $2\nu_2$ H_2O lines were only initially known to about $10^{-3}\ \mathrm{cm}^{-1}$ accuracy [Brown, 1986] and the precisions we obtain of $5 \times 10^{-4}\ \mathrm{cm}^{-1}$ is almost two orders of magnitude better than this. The low precision of the ATMOS line list for these lines is reflected in the large overall variation in the differences for these lines near $3200\ \mathrm{cm}^{-1}$.

We can estimate the offset α_{ab} between separate line lists 'a' and 'b'

$$\hat{\varsigma}_j^a = (1 + \alpha_{ab})\hat{\varsigma}_j^b \tag{2.41}$$

where 'a' and 'b' are two different sets of line positions for the same set of absorption lines. Table 2.10.1 gives values of α_{ab} between various linelists. The line positions determined from the interferometer are compared to accepted standards. For the CO_2 and ν_2 H_2O lines comparisons are also made between the instrumental lines and the positions determined from the atmospheric lines.

We see from the data that the CO_2 line positions agree within the uncertainty of about 3×10^{-5} cm^{-1} for the standards and positions determined using ATMOS. This is to be expected since we forced the instrumental line positions to agree with the standards during the wavenumber calibration. Similarly, positions determined using the atmospheric lines agree with the positions of the instrumental lines since these positions were derived from Doppler shifts, which in turn were derived initially from the instrumental positions. The measured positions of the $2\nu_2$ H_2O lines were also found to agree with the ATMOS linelisting standards. However, since they are only accurate to $\sim 10^{-3}$ cm^{-1}, this indicates only that we are obtaining at least that order of accuracy. The average positions of the $2\nu_1$ N_2O lines were found to agree with the ATMOS linelisting and a comparison between the positions determined using the atmospheric lines and the standards is given in Figure 2.10.2.

THE H_2O LINE POSITION PROBLEM

In the case of the ν_2 H_2O lines curious discrepancies are apparent. First of all, we see that, from comparing the instrumental lines to the standards provided by Brown, the difference may be significant but is of the order of the measurement erros. Secondly, and most importantly, there is a significant discrepancy between the positions determined from the atmospheric H_2O lines and the instrumental H_2O lines. From the data in Table 2.10.1 we see that this shift corresponds to a Doppler shift of almost $+15$ ms^{-1} between the standards where

$$\hat{\varsigma}_{\text{inst}} < \hat{\varsigma}_{\text{atm}}. \tag{2.42}$$

Due to this discrepancy and the marginal agreement with Brown's standards there is thirdly a significant offset between the atmospheric standards and Brown's standards. This discrepancy poses and interesting problem. If we calibrated the instrument with respect to the water lines instead of the carbon dioxide lines then the positions of the water lines determined from the atmospheric lines would be in agreement with the instrumental lines, since these positions would have been used to determine the Doppler shifts. This would cause a shift of -15 ms^{-1} in the recovered speed profiles. This, when determining the positions of the CO_2 lines from the atmospheric lines would cause them to be shifted -15 ms^{-1} from their instrumental counterparts

$$\hat{\varsigma}_{\text{inst}} > \hat{\varsigma}_{\text{atm}}. \tag{2.43}$$

Which calibration is the right one to use? Since the offset is significant it implies one of the two components of the gas, namely the CO_2 or H_2O, is *moving* with respect to the instrument. In the first case when we have calibrated relative to the CO_2 standards we find that the H_2O instrumental

frequencies are lower than those determined from the H_2O atmospheric lines - or synonomously with the CO_2 calibration via Doppler shifts. If we accept the accuracy of the positions determined from the H_2O atmospheric lines then the negative shift in the H_2O instrumental lines indicates that they are moving *away* from the instrument. On the other hand, if we calibrate relative to the H_2O standards the CO_2 instrumental lines will have a positive shift relative to the CO_2 atmospheric line positions. This means that the carbon dioxide lines are moving *toward* the instrument. The first implies a source of H_2O diffusing into space at a bulk velocity of 15 ms^{-1}. The second implies CO_2 sources converging on the instrument. There is no reasonable explanation for this latter kind of source. Therefore we should accept the former. This outgassing, or leakage of a trace amount of H_2O vapor from the shuttle itself, is the diffusion of a trace cloud of water vapor into space. The source of this outgassing may be due to water vapor desorbing from the outer shell of the shuttle itself. Shaw (1988) pointed out that this may be due to the high level of humidity present at the launch site. This also suggests that H_2O absorption lines may not be useful for absolute line position calibration.

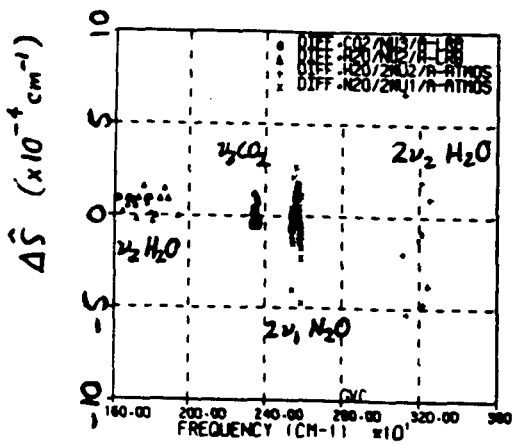

Figure 2.10.1 Differences between standard line positions (Brown's or ATMOS) and retrieved line positions for ν_3 CO_2, ν_2 H_2O, $2\nu_2$ H_2O and $2\nu_1$ N_2O from atmospheric lines.

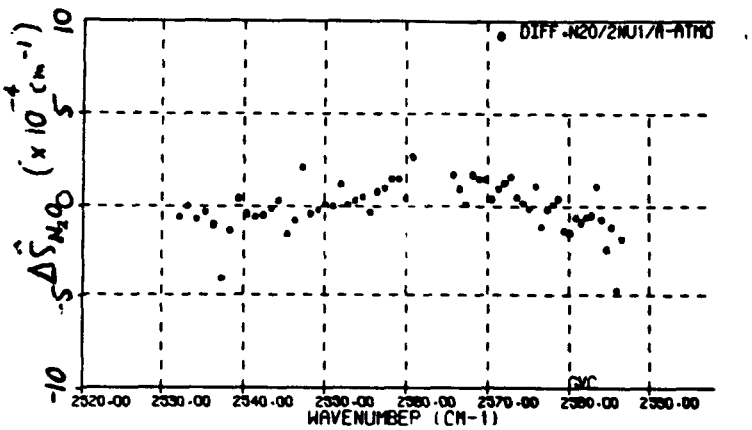

Figure 2.10.2 Differences between standard line positions (Brown's or ATMOS) and retrieved line positions for the $2\nu_1$ N_2O from atmospheric lines. This is the same data shown in Figure 2.10.1 but magnified for clarity. Notice that the differences in the position appear to systematically vary between the band center and the high J lines. These improvements in positions may be significant.

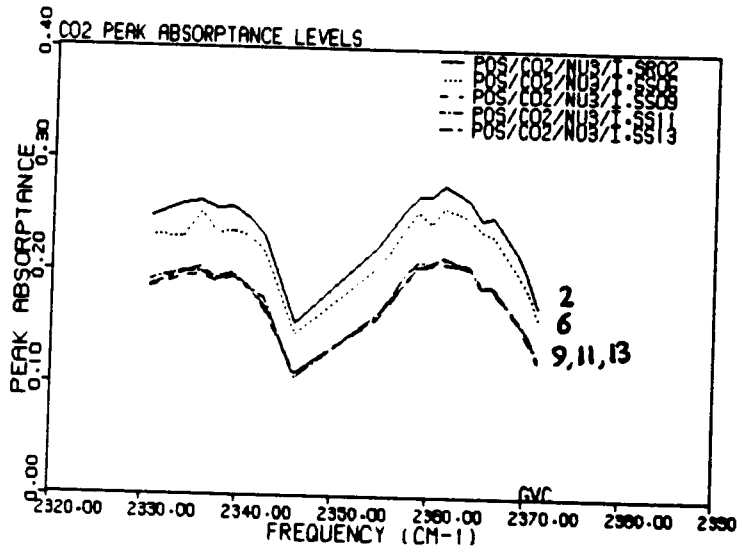

Figure 2.10.3 Peak absorptances of instrumental ν_3 CO_2 lines as observed in all five occultations - (2) SR02; (6) SS06; (9) SS09; (11) SS11; (13) SS13. The peak absorptances are initially decreasing with time and appear level off during SS09.

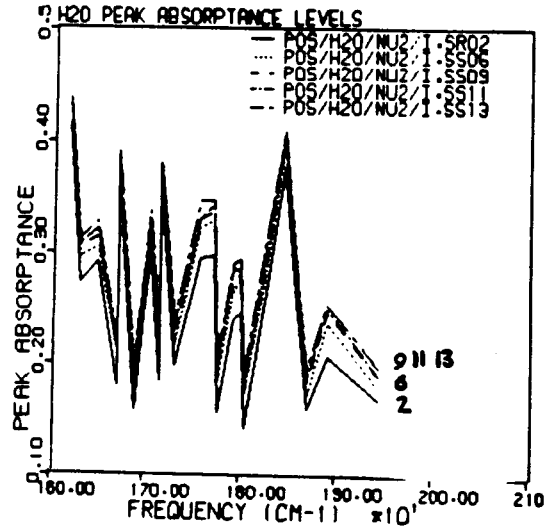

Figure 2.10.4 Peak absorptances of instrumental ν_2 H_2O lines as observed in all five occultations using the same labeling in Figure 2.10.3. The peak absorptances appear to slightly increase during time and this may be related to outgassing of water vapor from orbiter.

Table 2.10.1 Offsets between various line lists 'a' and 'b'. A - Positions determined from atmospheric lines. I - Positions determined from instrumental lines. LRB - Positions recommended by Brown (1986) for instrumental calibration. ATMOS - Positions archived in the ATMOS line listing.

Band	Linelist 'a'	Linelist 'b'	α_{ab} ($\times 10^{-8}$)	$\bar{\sigma}(\alpha_{ab})$ ($\times 10^{-8}$)	
ν_3 CO_2	A	LRB	−0.08	0.49	
	I	LRB	+0.04	0.33	
	A	I	−0.12	0.50	
$2\nu_2$ H_2O	A	ATMOS	−2.83	3.95	
$2\nu_1$ N_2O	A	ATMOS	−0.12	0.65	
ν_2 H_2O	I	LRB	−0.90	0.71	←
	A	I	+4.63	0.90	←
	A	LRB	+3.73	0.61	←

II.11 Testing the Measurement Theory

In §I.11 a theory was developed to predict the uncertainties in the measurement of line positions attainable using the ATMOS spectra. It was shown that the measurement uncertainties behave as

$$\sigma(\varsigma) = f\,\frac{\sigma(N)\,W}{A_p} \tag{2.44}$$

where f is a form factor which depends on the geometrical shapes of the lines and the sampling process, w is the width of the line at half maximum, A_p is the peak absorptance and $\sigma(N)$ is the background noise level. The atmospheric lines were used to test this theory.

After the relative speeds v^k were determined with the methods discussed previously, each atmospheric line position ς_j^k was shifted to a rest frame position $\hat{\varsigma}_j^k$ using

$$\hat{\varsigma}_j^k = \left(1 - \frac{v^k}{c}\right)\varsigma_j^k. \tag{2.45}$$

Then the difference between this value and the rest frame position estimated by (2.29) was calculated for each line

$$\Delta\hat{\varsigma}_j^k = \hat{\varsigma}_j^k - \hat{\varsigma}_j. \tag{2.46}$$

These values were then plotted versus A_{pj}^k. If the measurement theory is a realistic one then we would expect the spread of the distribution of $\Delta\hat{\varsigma}_j^k$ to have an envelope width proportional to A_p^{-1}. Figures 2.11.1-4 show this kind of behavior for the four bands used in the analysis - ν_3 CO_2, ν_2 H_2O, $2\nu_2$ H_2O, and $2\nu_1$ N_2O respectively. Indeed, the uncertainty of $\Delta\hat{\varsigma}_j^k$ does decrease

with increasing A_p. Since f, $\sigma(N)$ and W are approximately constant for each band we use (2.43)

$$A_p\sigma(\nu) = f\sigma(N)\,W. \qquad (2.47)$$

If we plot the distribution $A_{pj}^k \cdot \Delta\hat{\nu}_j^k$ versus A_{pj}^k we would expect to see a distribution whose width is independent of the peak absorptance. Figures 2.11.5-8 show these distributions for the four atmospheric bands used in the analysis. Table 2.11.1 list the distribution deviation $\bar{\sigma}(\Delta\nu\, A_p)$ for each of the bands. We see that the CO_2 lines have the smallest line noise §II.4 followed by the N_2O band and then the H_2O bands. This is in agreement with the ordering of the total background signal discussed in §II.4. We can also see upon comparing the ν_3 CO_2 and ν_2 H_2O noise levels computed from the atmospheric lines to those computed from the instrumental lines that the atmospheric values are higher. This may be caused by an increase in the line noise due to the ratio process. The ratio of the noise levels determined from the atmospheric ν_3 CO_2 lines to the ν_2 H_2O lines is about 1.6 from Table 2.11.1. A similar ratio determined from the values in Tables 2.3.1-2 is about 1.7. These two values are approximately the same which again suggests that the measurement precision theory of §I.11 can be used to describe the measurement uncertainties of line positions from the spectra.

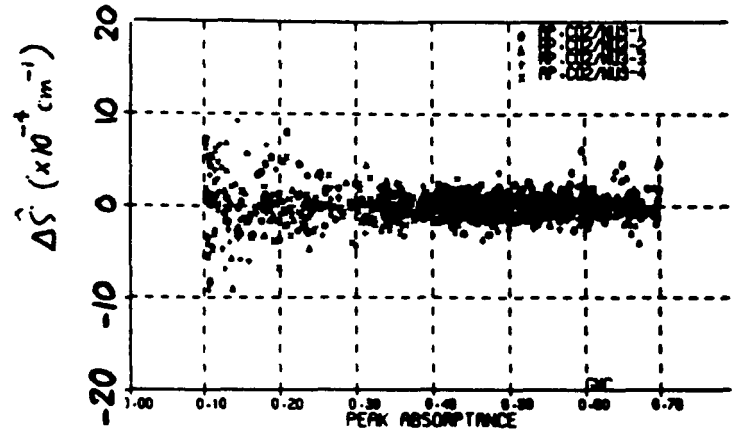

Figure 2.11.1 $\Delta\hat{\varsigma}$ for the ν_3 CO_2 atmospheric lines as a function of the measured peak absorptance A_p. The spread of the data is larger for small peak absorptances and becomes smaller as the peak absorptance increases.

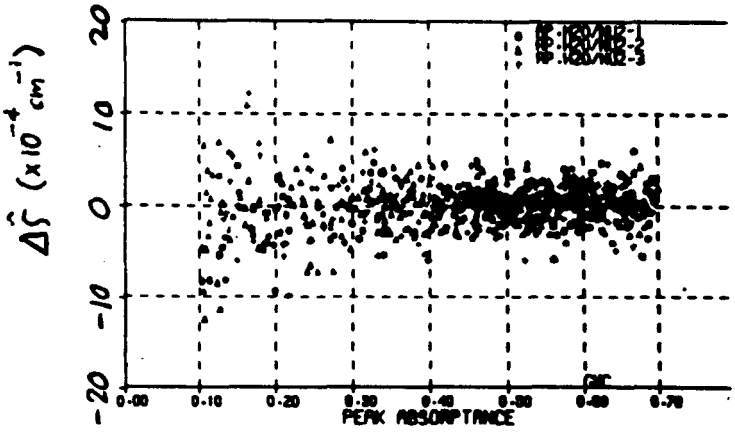

Figure 2.11.2 $\Delta\hat{\varsigma}$ for the ν_2 H_2O atmospheric lines as a function of the measured peak absorptance A_p. The spread of the data is larger for small peak absorptances and becomes smaller as the peak absorptance increases.

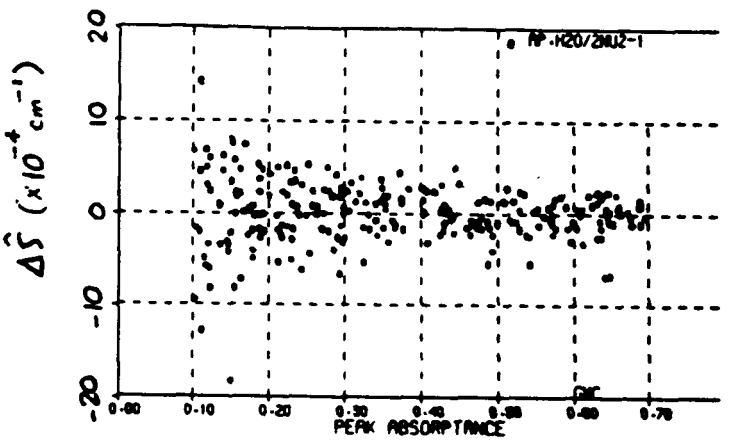

Figure 2.11.3 $\Delta\hat{\varsigma}$ for the $2\nu_2$ H_2O atmospheric lines as a function of the measured peak absorptance A_p. The spread of the data is larger for small peak absorptances and becomes smaller as the peak absorptance increases.

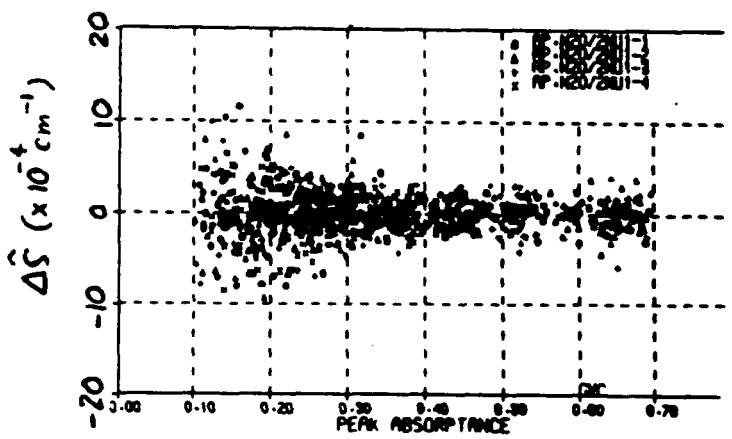

Figure 2.11.4 $\Delta\hat{\varsigma}$ for the $2\nu_1$ N_2O atmospheric lines as a function of the measured peak absorptance A_p. The spread of the data is larger for small peak absorptances and becomes smaller as the peak absorptance increases.

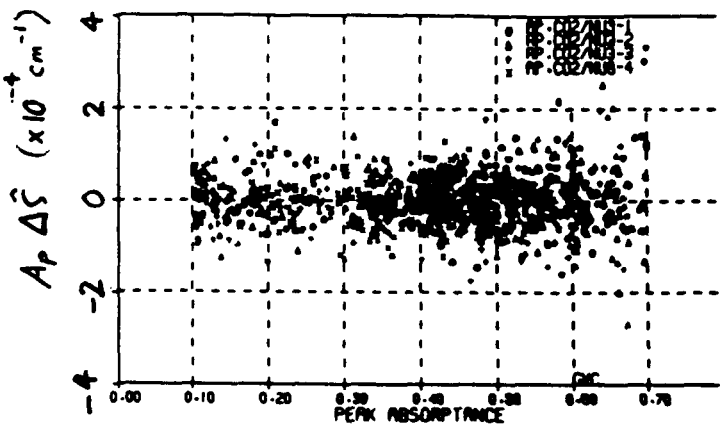

Figure 2.11.5 $A_p\Delta\hat{\varsigma}$ for the ν_3 CO_2 atmospheric lines as a function of the measured peak absorptance A_p. The spread of the data appears to remain constant as a function of the peak absorptance in agreement with the measurement precision theory.

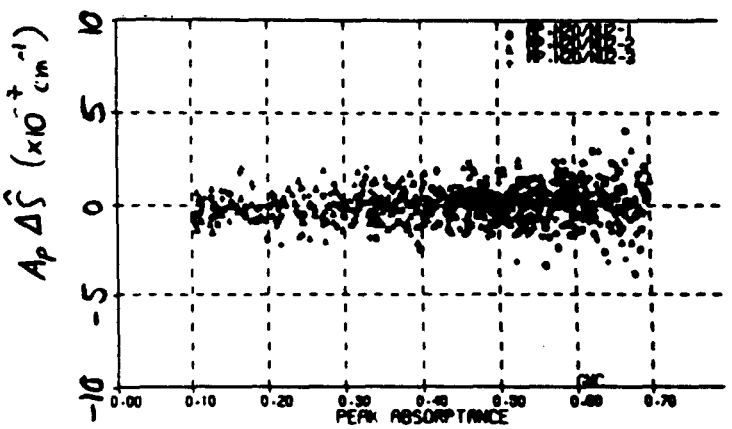

Figure 2.11.6 $A_p\Delta\hat{\varsigma}$ for the ν_2 H_2O atmospheric lines. The spread of the data appears to remain constant as a function of the peak absorptance.

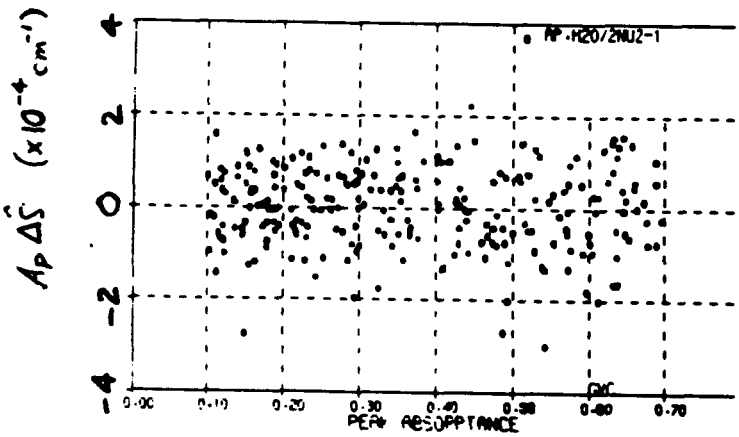

Figure 2.11.7 $A_p\Delta\hat{\varsigma}$ for the $2\nu_2$ H_2O atmospheric lines. The spread of the data appears to remain constant as a function of the peak absorptance.

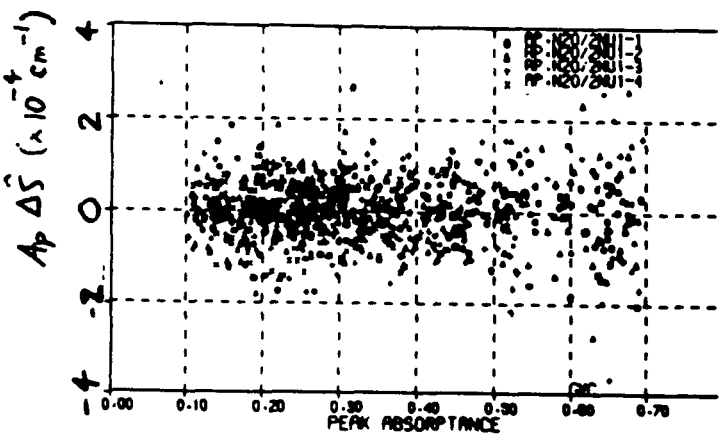

Figure 2.11.8 $A_p\Delta\hat{\varsigma}$ for the $2\nu_1$ N_2O atmospheric lines. The spread of the data appears to remain constant as a function of the peak absorptance.

Table 2.11.1 Estimates of *line noise* determined from atmospheric lines.

Band	mean ($\times 10^{-5}$cm^{-1})
ν_3 CO_2	6.1
ν_2 H_2O	9.8
$2\nu_2$ H_2O	9.5
$2\nu_1 N_2O$	7.5

II.12 Estimating the Doppler Shift due to Orbital Motion and the Earth's Rotation

THE EPHEMERAL DATA

The relative speed profiles presented in Figures 2.9.11-12 contain three independent Doppler shifts, the projection of the orbital velocity of the shuttle along the line of sight, the rotational speed of the earth along the line of sight, and the atmospheric winds along the line of sight. We wish to compute the effects due to the first two and then to subtract these from the relative speeds profiles to obtain residual wind speed profiles along the line of sight. The positions of the orbiter with respect to the earth were provided by Goddard Space Flight Center and were tabulated in terms of geocentric distance r, longitude ϕ, and latitude θ. Positions were evaluated at times t at six second intervals for each occultation. The orbital data are given in terms of the coordinate system of the earth rotating with the angular speed

$$\Omega = \frac{2\pi}{T_s} \tag{2.48}$$

where T_s is the sidereal day of 23h 56m. In order to examine the data in terms of a stationary frame it was necessary to translate the longitudes appropriately. This stationary frame can be arbitrarily chosen for the purposes of computing the relative motions of the orbiter with respect to the tangent point. I chose an initial time t^0 = 120d00 : 00 : 00 GMT. The sampled times t_i for each point i were converted to an elapsed time

$$\tau_i = t_i - t^0. \tag{2.49}$$

The longitudes ϕ_i were also translated to the reference frame at t^0 by

$$\phi_i' = \phi_i + \Omega\tau_i \tag{2.50}$$

so that a longitude ϕ_i given at the elapsed time τ_i corresponds to the longitude ϕ_i' at the time t^0. The positions are given in terms of this geocentric stationary coordinate system. It is useful to transform this spherical coordinate system into a Cartesian system via

$$x_i = r_i \cos\theta_i \cos\phi_i', \tag{2.51}$$

$$y_i = r_i \cos\theta_i \sin\phi_i', \tag{2.52}$$

$$z_i = r_i \sin\theta_i. \tag{2.53}$$

These positions were computed for all of the occultations and are presented in Figures 2.12.1-2 for x-y and x-z planar projections respectively. The figures show that the part of the orbit tabulated in the Goddard ephemeris closely follow a circular orbit, however there are notable changes in the orbit. Figures 2.12.3-4 are close up diagrams of the x-y planar projections for the sunset and sunrise occultations respectively. There is evidently a regular drift in the orbit. This drift is responsible for the shifts in the relative speeds for the sunset occultations shown in Figure 2.9.11. The gap between the profiles for SS06 and SS09 in Figure 2.9.11, for example, is related the change in position of the orbit between these two occultations which is evident in Figure 2.12.4.

The ephemeris data also give positions of the tangent points in the same terms as for the orbital data. Again the longitudes ϕ_i^{tang} are translated by

$$\phi_i'^{\text{tang}} = \phi_i^{\text{tang}} + \Omega\tau_i \tag{2.54}$$

and the Cartesian coordinates are given by

$$x_i^{\rm tang} = r^{\rm tang} \cos\theta^{\rm tang} \cos\phi_i'^{\rm tang}, \quad (2.55)$$

$$y_i^{\rm tang} = r^{\rm tang} \cos\theta^{\rm tang} \sin\phi_i'^{\rm tang}, \quad (2.56)$$

$$z_i^{\rm tang} = r^{\rm tang} \sin\theta^{\rm tang}. \quad (2.57)$$

The x-y planar projections of the tangent points as well as orbital data for the four sunset occultations is shown in Figure 2.12.5. The orbital drift is evident. It is useful to note that the ephemeris data are collected at time intervals $\Delta t \sim 6$s. The occultation takes about 5 min which gives us $n = \sim 300\text{s} / 6\text{s} = 50$ data points to use for the analysis below.

LEAST SQUARES METHOD

To get the Doppler shift from the positions of the orbiter and tangent points in terms of the Cartesian coordinate system we need to compute the rates of change of these positions. We wish to determine $\mathbf{v} = d\mathbf{r}/d\tau$ where $\mathbf{r} = \mathbf{r}(\tau)$ is a function to be determined from the data $\mathbf{r}_i$, τ_i. It was found that errors in the positions of the orbiter and tangent point caused uncertainties in the velocity of over 20 ms^{-1} between points using simple finite differences for the time derivative of the positions. A least squares method was used to determine the smooth trajectories of the orbiter and the tangent point as a function of elapsed time τ. A polynomial of order m was fit to the observed data of the form

$$x_i = \xi_0 + \xi_1\tau_i + \xi_2\tau_i^2 + \ldots + \xi_m\tau_i^m, \quad (2.58)$$

$$y_i = \eta_0 + \eta_1\tau_i + \eta_2\tau_i^2 + \ldots + \eta_m\tau_i^m, \quad (2.59)$$

$$z_i = \zeta_0 + \zeta_1\tau_i + \zeta_2\tau_i^2 + \ldots + \zeta_m\tau_i^m. \quad (2.60)$$

These are three independent sets of equations. If we consider the set of equations for the x_i and that there are n independent data points, we can write

$$\mathbf{x} = \mathbf{T}\boldsymbol{\xi} + \boldsymbol{\epsilon} \tag{2.61}$$

where

$$\mathbf{x} = \begin{bmatrix} x_1 \\ x_2 \\ \vdots \\ x_n \end{bmatrix}, \quad \mathbf{T} = \begin{bmatrix} 1 & \tau_1 & \tau_1^2 & \cdots & \tau_1^m \\ 1 & \tau_2 & \tau_2^2 & \cdots & \tau_2^m \\ \vdots & \vdots & \vdots & & \vdots \\ 1 & \tau_n & \tau_n^{r2} & \cdots & \tau_n^{rm} \end{bmatrix}, \quad \boldsymbol{\xi} = \begin{bmatrix} \xi_0 \\ \xi_1 \\ \xi_2 \\ \vdots \\ \xi_m \end{bmatrix} \tag{2.62}$$

and the column of model errors is given by

$$\boldsymbol{\epsilon} = \begin{bmatrix} \epsilon_1 \\ \epsilon_2 \\ \vdots \\ \epsilon_n \end{bmatrix}. \tag{2.63}$$

In order to get the best set of parameters ξ_j which best fit the measured positions x_i in a least squares sense we need to find the least squares estimator $\boldsymbol{\xi}^*$ for the coefficients $\boldsymbol{\xi}$ that satisfies

$$\frac{\partial}{\partial \boldsymbol{\xi}^*}\left[(\mathbf{x} - \mathbf{T}\boldsymbol{\xi}^*)^T (\mathbf{x} - \mathbf{T}\boldsymbol{\xi}^*)\right] = \mathbf{0}. \tag{2.64}$$

Here, $(\mathbf{x} - \mathbf{T}\boldsymbol{\xi}^*)^T (\mathbf{x} - \mathbf{T}\boldsymbol{\xi}^*)$ is the residual sum of squares. By differentiating (2.63) it can be shown that

$$(\mathbf{T}^T\mathbf{T})\boldsymbol{\xi}^* = \mathbf{T}^T\mathbf{x}. \tag{2.65}$$

So solving for $\boldsymbol{\xi}^*$,

$$\boldsymbol{\xi}^* = (\mathbf{T}^T\mathbf{T})^{-1}\mathbf{T}^T\mathbf{x}. \tag{2.66}$$

The matrix $\mathbf{T}^T\mathbf{T}$ is an $(m+1) \times (m+1)$ symmetric matrix.

The assumptions for the least squares method are that the errors ϵ_i arise from distributions which have a mean of zero

$$E(\boldsymbol{\epsilon}) = \mathbf{0} \tag{2.67}$$

and have a common unknown variance variance σ^2, but zero covariance

$$E(\boldsymbol{\epsilon}\boldsymbol{\epsilon}^T) = \sigma^2\mathbf{I}. \tag{2.68}$$

Under these conditions $\boldsymbol{\xi}^*$ is an unbiased estimator for $\boldsymbol{\xi}$ [Myers, 1986] since $E(\mathbf{x}) = \mathbf{T}\boldsymbol{\xi}$ and it can be shown that

$$E(\boldsymbol{\xi}^*) = \boldsymbol{\xi}. \tag{2.69}$$

The estimator $\boldsymbol{\xi}^*$ also has the minimum variance [Koerts, Abrahamse, 1969].

The parameters $\boldsymbol{\xi}^*$ have been estimated by (2.65) and we wish to estimate the errors $\boldsymbol{\epsilon}^*$. By using (2.60)

$$\boldsymbol{\epsilon}^* = \mathbf{x} - \mathbf{T}\boldsymbol{\xi}^* = \mathbf{N}\mathbf{x} \tag{2.70}$$

where

$$\mathbf{N} = \mathbf{I} - \mathbf{T}(\mathbf{T}^T\mathbf{T})^{-1}\mathbf{T}^T. \tag{2.71}$$

The $n \times n$ matrix $\mathbf{N}$ has the following properties [Graybill, 1976]

$$\mathbf{N} = \mathbf{N}^T, \tag{2.72}$$

$$\mathbf{N}\mathbf{T} = \mathbf{0}, \tag{2.73}$$

$$\mathbf{N} = \mathbf{NN} = \mathbf{N}^T\mathbf{N} = \mathbf{NN}^T, \tag{2.74}$$

$$\text{trace}\,\mathbf{N} = n - (m+1) = n - m - 1. \tag{2.75}$$

The last property can be proven since if $\mathbf{A}$ and $\mathbf{B}$ are square matrices of the same order then $\text{trace}(\mathbf{A}+\mathbf{B}) = \text{trace}\,\mathbf{A} + \text{trace}\,\mathbf{B}$ and $\text{trace}\,(\mathbf{AB}) = \text{trace}\,(\mathbf{BA})$. Then

$$\begin{aligned} \text{trace}\,\mathbf{N} &= \text{trace}\left[\mathbf{I} - \mathbf{T}(\mathbf{T}^T\mathbf{T})^{-1}\mathbf{T}^T\right] \\ &= \text{trace}\,\mathbf{I} - \text{trace}\left[\mathbf{T}(\mathbf{T}^T\mathbf{T})^{-1}\mathbf{T}^T\right] \\ &= \text{trace}\,\mathbf{I} - \text{trace}\left[(\mathbf{T}^T\mathbf{T})^{-1}(\mathbf{T}^T\mathbf{T})\right] \\ &= n - (m+1) \end{aligned} \tag{2.76}$$

since $\mathbf{T}^T\mathbf{T}$ is an $(m+1)\times(m+1)$ matrix.

We can now find an estimate s^2 for the unknown variance σ^2 of the errors. One way is to estimate it by the mean square of the residuals

$$s^2 = n^{-1}\epsilon^{*T}\epsilon^* = n^{-1}(\mathbf{Nx})^T\mathbf{Nx} = n^{-1}\mathbf{x}^T\mathbf{N}^T\mathbf{Nx} = n^{-1}\mathbf{x}^T\mathbf{Nx}. \tag{2.77}$$

This estimate is biased [Myers, 1986] since $E(s^2) \neq \sigma^2$

$$E(s^2) = n^{-1}E[\mathbf{x}^T\mathbf{Nx}] = n^{-1}E[\epsilon^T\mathbf{N}\epsilon] \tag{2.78}$$

using (2.60) and (2.72). At this point we make use of a theorem [Graybill, 1976] on the expected value of a quadratic form characterized by a matrix $\mathbf{Q}$. Given a random vector ϵ with a mean $E(\epsilon) = \mu$ and $E(\epsilon\epsilon^T) = \sigma^2\mathbf{I}$ then

$$E(\epsilon^T\mathbf{Q}\epsilon) = \sigma^2\,\text{trace}\,\mathbf{Q} + \mu^T\mathbf{Q}\mu. \tag{2.79}$$

In (2.77) we identify $\mu \to \mathbf{0}$ and $\mathbf{Q} \to \mathbf{N}$ so that

$$E(s^2) = \sigma^2 n^{-1}\,\text{trace}\,\mathbf{N} = (n-m-1)n^{-1}\sigma^2. \tag{2.80}$$

We see then that even though s^2 is a biased estimate the quantity $\sigma^{*2} \equiv s^2 n/(n-m-1)$ is an unbiased estimate. Therefore

$$\sigma^{*2} = (n-m-1)^{-1} [\mathbf{x} - \mathbf{T}\boldsymbol{\xi}^*]^T [\mathbf{x} - \mathbf{T}\boldsymbol{\xi}^*] \tag{2.81}$$

is an unbiased estimate of the variance. Now the variance-covariance matrix $\mathbf{X}$ for $\boldsymbol{\xi}^*$ can be evaluated by computing $\mathbf{X} \equiv E\{(\boldsymbol{\xi} - \boldsymbol{\xi}^*)(\boldsymbol{\xi} - \boldsymbol{\xi}^*)^T\}$ and it has been shown [Myers, 1986] that

$$\mathbf{X} \equiv E\{(\boldsymbol{\xi} - \boldsymbol{\xi}^*)(\boldsymbol{\xi} - \boldsymbol{\xi}^*)^T\} = \sigma^{*2}(\mathbf{T}^T\mathbf{T})^{-1}. \tag{2.82}$$

Having estimated the coefficients ξ_j we wish determine the velocity vectors from the least squares fit. We estimate the position $x(\tau)$ by the function

$$x^*(\tau) = \sum_{j=0}^{m} \xi_j^* \tau^j. \tag{2.83}$$

If we define the vector

$$\boldsymbol{\tau} = \begin{bmatrix} 1 \\ \tau \\ \tau^2 \\ \vdots \\ \tau^m \end{bmatrix} \tag{2.84}$$

then the variance is given by [Myers, 1986]

$$\bar{\sigma}^2(x^*) = \boldsymbol{\tau}^T \mathbf{X} \boldsymbol{\tau}. \tag{2.85}$$

The velocity can be estimated from (2.79) by

$$v_x^*(\tau) = \frac{dx^*(\tau)}{d\tau} = \sum_{j=0}^{m} j \xi_j^* \tau^{j-1}. \tag{2.86}$$

If we define the vector

$$\dot{\tau} = \frac{d\tau}{d\tau} \tag{2.87}$$

then the variance is estimated by

$$\bar{\sigma}^2(v_x^*) = \dot{\tau}^T \mathbf{X} \dot{\tau}. \tag{2.88}$$

The least squares method is similarly applied to the y and z variables as well for both the orbiter and tangent point.

CORRECTION FOR THE EARTH'S ROTATION

Finally we account for the rotational motion of the earth. At the equator the tangential velocity of the earth rotation is 467 ms^{-1} and causes significant Doppler shifts. The velocity vector of the rotation at the tangent point $\mathbf{r}^{tang}$ is given by

$$\mathbf{v}^{tang} = \boldsymbol{\Omega} \times \mathbf{r}^{tang} \tag{2.89}$$

where $\boldsymbol{\Omega}$ is the angular velocity of the earth's rotation. When the vector functions $\mathbf{r}^{*tang}(\tau)$ and $\mathbf{r}^{*orb}(\tau)$ have been respectively computed and their respective velocities $\mathbf{v}^{*tang}$ and $\mathbf{v}^{*orb}(\tau)$ determined the relative speed along the line of sight can then be estimated. The total contribution to the relative speed profiles caused by orbital motion and the earth's rotation is given by

$$\Delta \mathbf{v}^* = \mathbf{v}^{*orb} - \mathbf{v}^{*tang}. \tag{2.90}$$

The unit vector between the orbiter and the tangent is calculated by

$$\hat{\mathbf{n}} = (\mathbf{r}^{*orb} - \mathbf{r}^{*tang})/r^{*orb-tang} \tag{2.91}$$

where $r^{*orb-tang}$ is the distance between the orbiter and the tangent point. Finally the velocity along the line of sight is given by

$$\Delta v^* = \Delta \mathbf{v}^* \cdot \hat{\mathbf{n}}. \tag{2.92}$$

The quantity Δv^* must be subtracted from the relative speed profiles determined in §II.9 to obtain residual wind speeds along the line of sight. The variance of Δv^* can be estimated by expanding (2.91)

$$\Delta v^* = \Delta v_x^* \hat{n}_x + \Delta v_y^* \hat{n}_y + \Delta v_z^* \hat{n}_z. \tag{2.93}$$

Since the error in $\hat{n}$ is negligible and the Δv_i^* are uncorrelated then

$$\bar{\sigma}^2(\Delta v^*) = \bar{\sigma}^2(v_x^*)\,\hat{n}_x^2 + \bar{\sigma}^2(v_y^*)\,\hat{n}_y^2 + \bar{\sigma}^2(v_z^*)\,\hat{n}_z^2 \tag{2.94}$$

where the variances in the components are determined by (2.87).

These calculations were carried out for the ephemeris data described in Figures 2.12.1-2 for data corresponding to tangent heights from −40 to 300 km. In each occultation the elapsed time τ was determined relative to the time when the tangent height was nearest 30 km. This allowed us to obtain the best fit for the orbital/rotational speeds with tangent heights between 30 and 110 km since this altitude range represents the region where the 'origin' of the polynomial fit is located and the fit is better in this region than at the ends near 300 km and -40 km. In Figure 2.12.6-7 the relative speed profiles §II.9 together with their orbital/rotational motion contributions are plotted for the sunset and sunrise occultations respectively. The slopes of the orbital/rotational motion curves follow the trends of the relative speed profiles determined from the atmospheric lines. Figure 2.12.8 shows the uncertainty $\bar{\sigma}(\Delta v^*)$ from the least squares analysis using (2.90) for all five occultations. The uncertainties in the orbital/rotational speeds were about 3 ms^{-1} near 60 km tangent height. SS11 and SS13 have precisions by as much as 5 ms^{-1} worse than the other three occultations above 120 km since there are not as

many ephemeris data available for these two occultations. However, these precisions are still better than 5 ms^{-1} below 100 km.

PRECISION OF RESIDUAL SPEED PROFILES

The residual speed along the line of sight, which is the wind motion, is computed by subtracting the orbital-rotational motion from the relative speed profiles. The residual speeds for the four sunset and the sunrise occultations are plotted in Figures 2.12.9-10 respectively. We immediately see the striking similarity between the sunset profiles. The measurement precision is determined from the precision displayed in Figures 2.12.8 and 2.9.13

$$\bar{\sigma}^2(\text{residual}) = \bar{\sigma}^2(\text{relative}) + \bar{\sigma}^2(\text{orbit} - \text{rotation}). \qquad (2.95)$$

The precisions for the residual speed profiles are shown in Figure 2.12.11 This final result shows a total measurement uncertainty of about 5 m/s between 25 and 110 km for the five occultations. Since the amount of absorber of CO_2 above 110 km rapidly falls off and the orbital-rotational uncertainties becomes large with increasing tangent height the uncertainties in the residual wind speeds becomes large. Below 20 km the uncertainties becomes large due to the saturations of N_2O lines as well as orbital-rotation uncertainties. Between these regions we have obtained the desired total measurement precision of 5 ms^{-1}.

THE LINE OF SIGHT ORIENTATION

The orientation of the line of sight relative to the earth's surface was also determined. This calculation was performed by measuring the angle between the vector $\hat{\mathbf{n}}$ and the east-west unit vector $\hat{\boldsymbol{\phi}}$ using standard trigonometry. In Figures 2.12.12-13 this angle is plotted as a function of tangent height

for the sunset and sunrise occultations respectively. From these data we can see the line of sight is inclined to the zonal direction by about 17-18° and 21-23° for the sunsets and sunrise respectively. Therefore we can conclude that residual speeds measured are very nearly the zonal component of the wind speeds. In Figure 2.12.9 a positive residual speed is eastward for the sunsets while a negative residual speed in Figure 2.12.10 is eastward for the sunset. We see that in both figures an eastward prevailing wind of 25 and 50 m/sec between tangent heights of 20 and 70 km are present in the sunsets and sunrise respectively. Above 80 km rapid variations of the zonal wind with height are present. The similarity of zonal wind speed with height between the various sunset wind speed profiles in Figure 2.12.9 is particularly interesting and various possible causes of the observed wind speed features is discussed in §§III.

The Doppler shifts introduced by the orbital motion of the instrument as well as the rotation of the earth have been estimated to 5 ms^{-1} or better between tangent heights of 20 and 120 km from the ephemeris data. The ephemeris data can be used to determine absolute zonal wind speeds from the relative speed profiles determined in §II.9 without a significant degradation of the total precision from 5 ms^{-1} over the tangent height range.

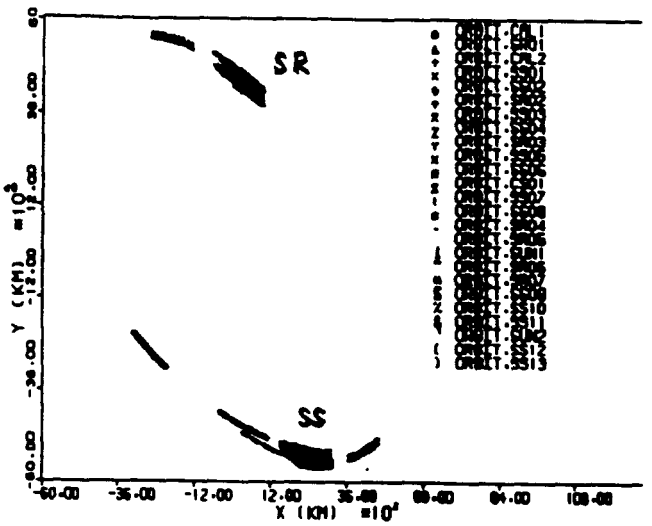

Figure 2.12.1 $x-y$ planar projection of orbital positions computed using the ephemeris data showing both sunset (SS) and sunrise (SR) positions for all of the occultations. The orientation of the coordinate system was arbitrarily chosen, however, the circular shape of the orbit can be seen. The identification of points is not important in this illustration. There are variations in the orbital path.

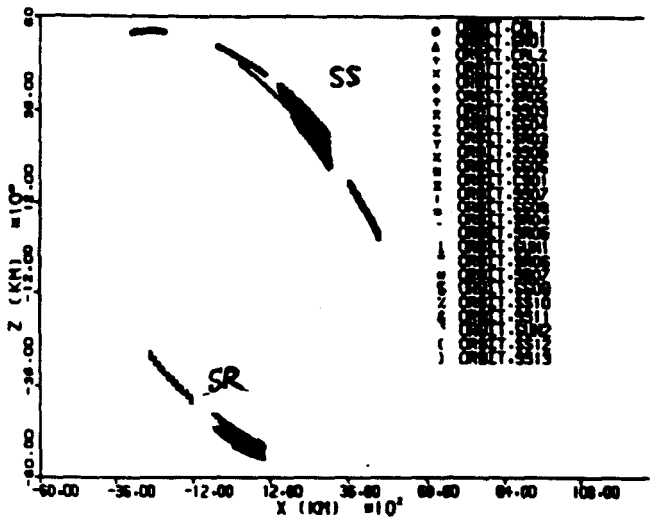

Figure 2.12.2 Same as in Figure 2.12.2 except for the $x-z$ planar projection.

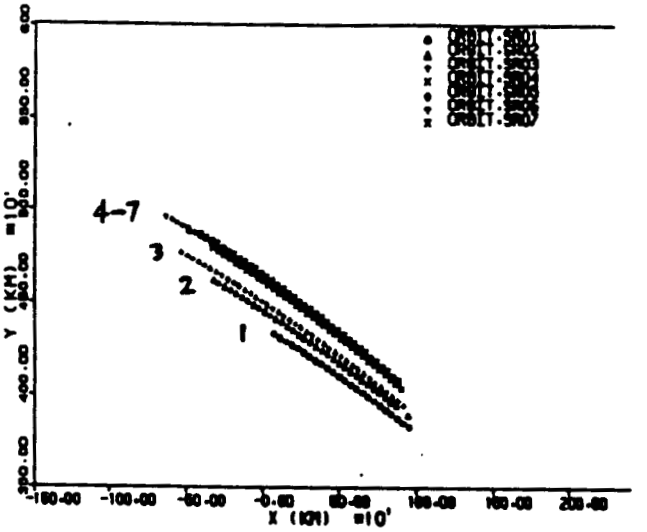

Figure 2.12.3 Close up $x - y$ planar projection of orbital positions for the sunrise occultations. There is a noticable changing of the orbit between occultation (1) SR01 through (7) SR07.

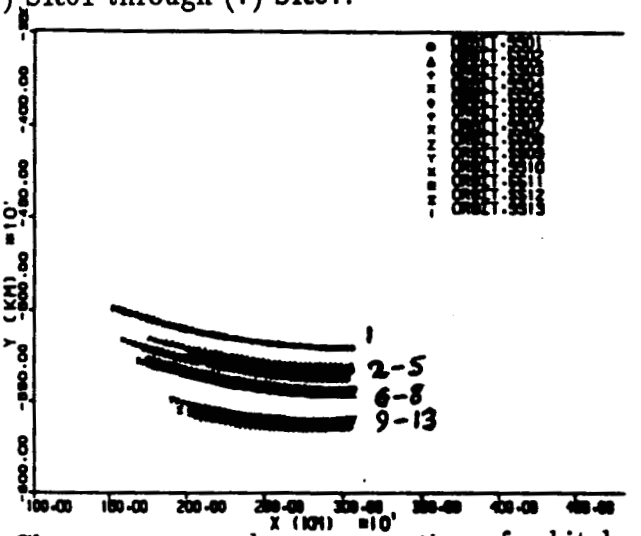

Figure 2.12.4 Close up $x - y$ planar projection of orbital positions for the sunset occultations. There is a noticable changing of the orbit between occultations (1) SS01 through (13) SS13. This changing of the orbital geometry causes the shifts between the relative speed profiles of up to 200 ms^{-1} in Figure 2.9.11.

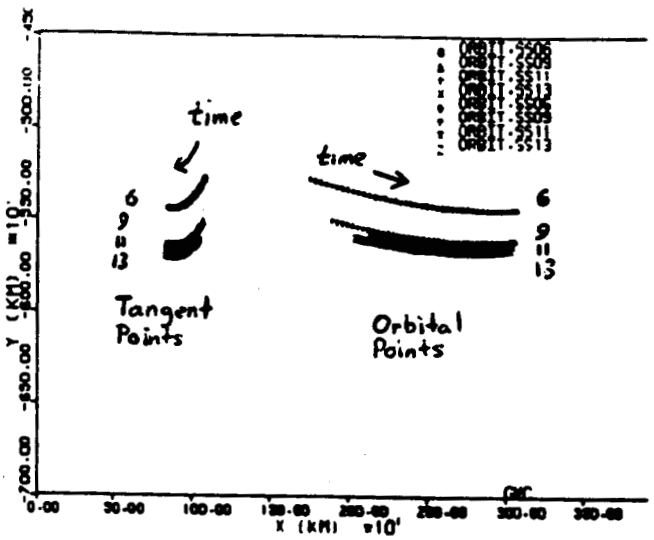

Figure 2.12.5 Close up x-y planar projection of orbital and tangent point positions for the four sunset occultations - (6) SS06 - (9) SS09 - (11) SS11 - (13) SS13. The progression of points as time increases during the occultation is indicated. This changing of the line of sight geometry causes the shifts between the relative speed profiles of up to 200 ms^{-1} in Figure 2.9.11.

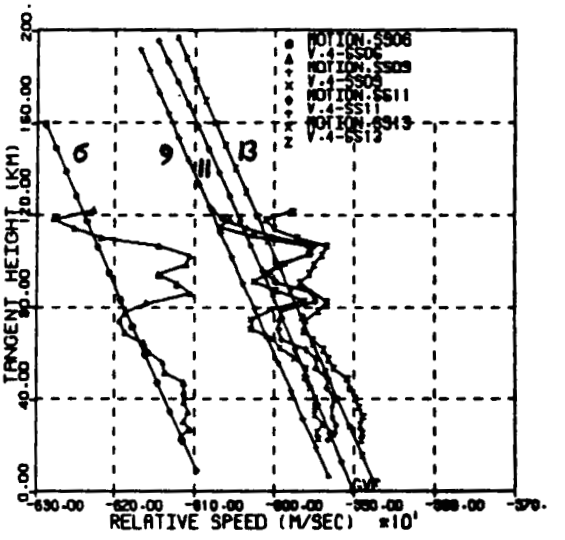

Figure 2.12.6 Orbital-rotational motion plotted with relative speed profiles for the sunset occultations - (6) SS06 - (9) SS09 - (11) SS11 - (13) SS13. The points on the approximately 'straight' curve represent relative speeds due to the orbital-rotational motion. The separations of the orbital-rotational motion are in agreement with the separation of speed profiles obtained by measuring the Doppler shifts of atmospheric lines. The rapid variations above 70 km are due to upper atmospheric winds.

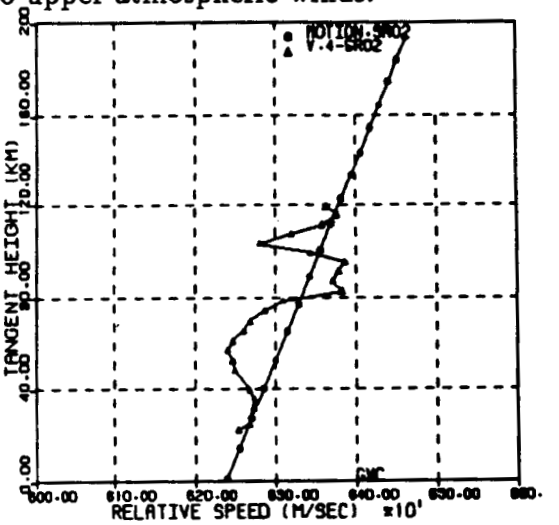

Figure 2.12.7 Same as above except for the sunrise occultation - (2) SR02.

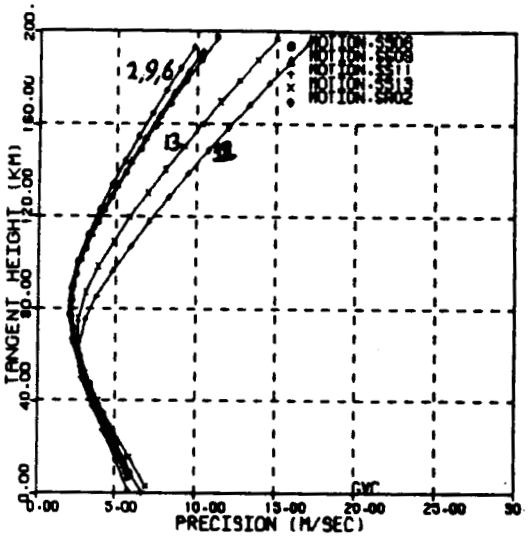

Figure 2.12.8 Uncertainty in least squares fit for orbital-rotational motion for all five occultations. The precision of 5 ms^{-1} or better is maintained between 20 and 100 km for all occultations.

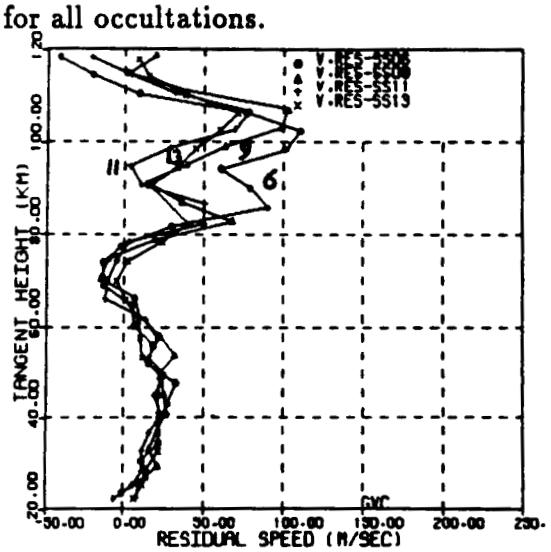

Figure 2.12.9 Residual speed profiles for the sunset occultations - (6) SS06 - (9) SS09 - (11) SS11 - (13) SS13.

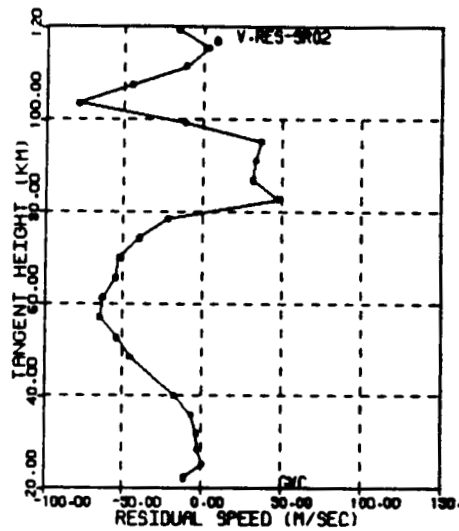

Figure 2.12.10 Residual speed profile for the sunrise occultation - (2) SR02.

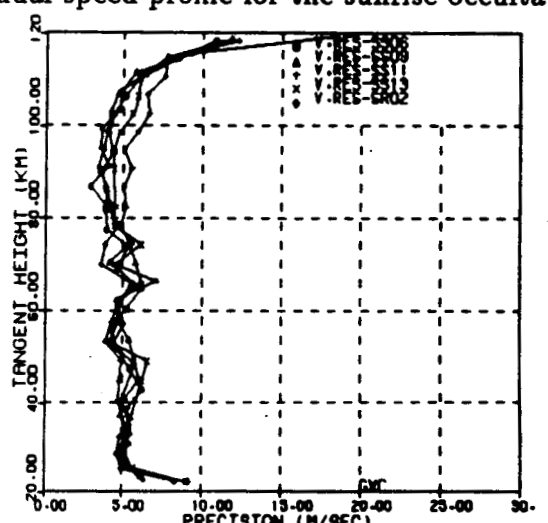

Figure 2.12.11 Combined uncertainty of residual speeds for all five occultations. A precision of about 5-6 ms^{-1} is maintained between 25 and 110 km.

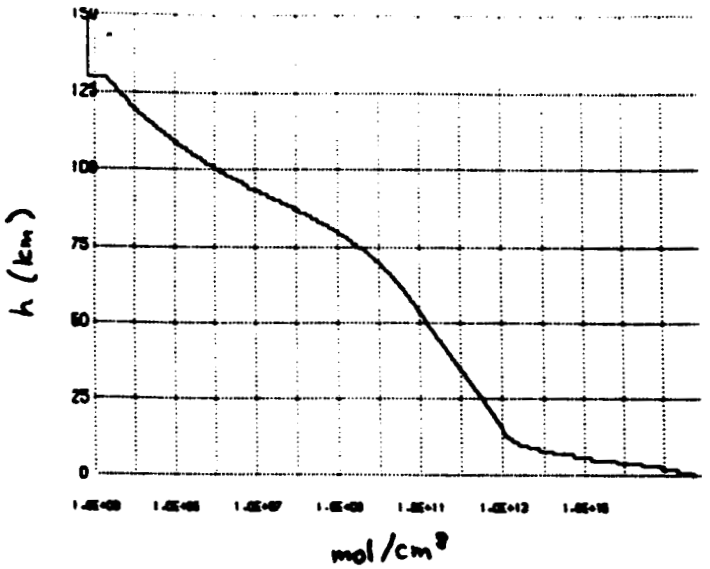

Figure 2.13.2 Concentration $c(h)$ for H_2O from ATMOS standard atmosphere.

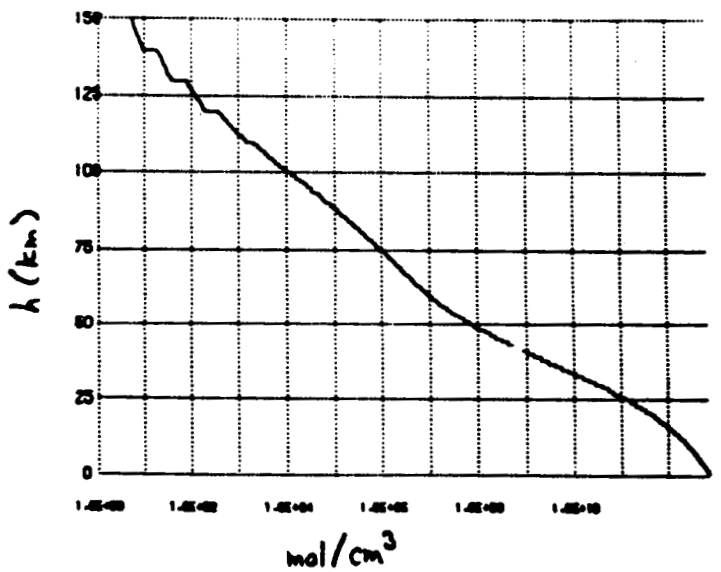

Figure 2.13.3 Concentration $c(h)$ for N_2O from ATMOS standard atmosphere.

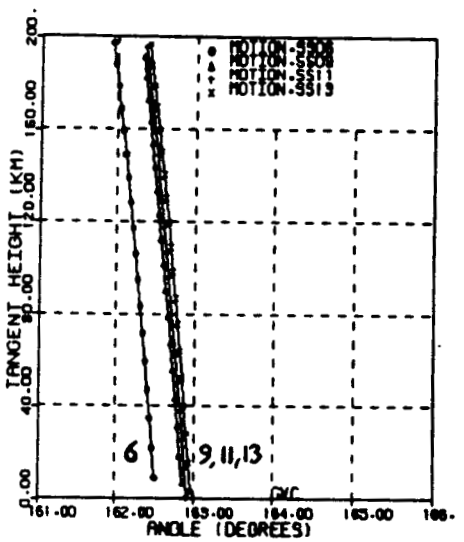

Figure 2.12.12 Angle between the line of sight and the zonal direction for the sunset occultations. The angle is approximately 17°.5 between the line of sight and the zonal direction indicating that the wind speeds are essentially the zonal component.

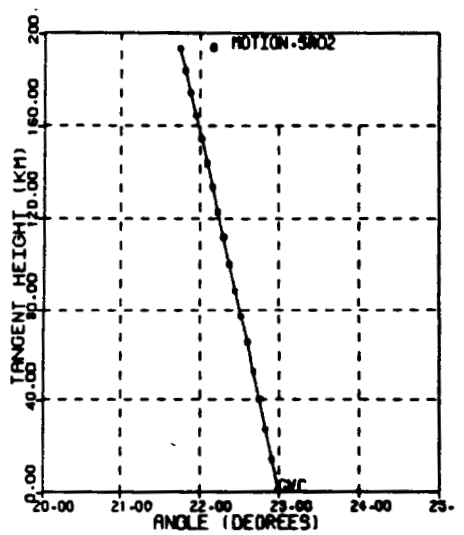

Figure 2.12.13 Angle between the line of sight and the zonal direction for the sunrise occultation. The angle is approximately 22° between the line of sight and the zonal direction indicating that the wind speeds are essentially the zonal component.

II.13 Density Weighted Residual Winds

The wind speeds determined in the previous section were computed under the assumption that the observations were made solely on gases at the tangent points. However, the line of sight penetrates all levels above the tangent height. We have seen that there are wind variations with height. If these variations are rapid enough, which may be the case for the zonal wind profiles determined in the previous section, they may cause a 'smearing' of the results and degrade the vertical resolution of the profiles. We wish to examine how this affects the vertical resolution of the results.

To begin with we can examine the number density of each gaseous component used to obtain wind speeds, namely CO_2, H_2O, and N_2O. Figures 2.13.1-3 show the concentrations as a function of height $c(h)$ as given in the ATMOS data base. We wish to determine the total fraction of absorber present as a function of distance about the tangent point. Figure 2.13.4 shows the typical geometry of a tangent ray. Refraction in the atmosphere is not taken into consideration since this model is only assumed to be a first approximation to begin with. The parameter x is the distance from the tangent point along the line of sight. Given the tangent height t and the distance x the altitude above the surface $h_t(x)$ is given by geometry

$$h_t(x) = \sqrt{(r_0 + t)^2 + x^2} - r_0. \tag{2.96}$$

Let the total path length through the atmosphere for a given tangent height

t be represented by

$$L_t = \sqrt{(r_0 + h_{\max})^2 - (r_0 + t)^2} \tag{2.97}$$

where $h_{\max}$ is "top" to the atmosphere and can usually be picked to be above the region where the wind measurements were carried out. This is a reasonable assumption since the amount of infrared absorber decreases rapidly as a function of height. We can then determine the number of molecules per unit area N_t along the line of sight

$$N_t \simeq \int_{-L_t}^{L_t} dx\, c(h_t(x)). \tag{2.98}$$

Having determined this we want to determine the total fraction $f_t(x)$ of absorber within a distance x to tangent point along the line of sight

$$f_t(x) = \frac{1}{N_t} \int_{-\infty}^{x} dx\, c(h_t(x)). \tag{2.99}$$

The integrated fraction was determined for the concentration profiles given in Figures 2.13.1-3. A maximum height of 150 km was assumed for $h_{\max}$. Figures 2.13.5-8 show the total fraction (2.98) as a function of x for various values of the tangent height t. It is found that 90% of each species is within 400 km of the tangent point, the remainder being distributed about the ray. For N_2O the 90% value threshhold is about 250 km.

It is of even more importance to estimate the range of altitudes which contain certain fractions of the total absorber along the line of sight. Figures 2.13.5-8 were transformed using (2.95) to examine how the integrated fraction is related the $h_t(x) - t$. For a given fraction of the total absorber along the line of sight a value of a "layer thickness" $h_t(x) - t$ can be determined. The

layer thickness for the three components are plotted in Figures 2.13.8-10 for various tangent heights t. We see that for CO_2 over the range of tangent heights where the atmospheric ν_3 lines are useful that 90% of the absorber is contained in the first 10 km or less of the above the tangent point. Since the spectra are sampled at approximately 4 km intervals, then 70 and 80% of the absorber is contained between a tangent height and the next highest sampling height. Between a tangent point and two sampling spectra more than 90% of the absorber is present. We therefore expect that the vertical resolution of the wind speed at a given tangent height is being degraded primarily by the next highest level.

Figure 2.13.11 is a diagram which defines a "layers" model. Basically, we can characterize the atmosphere for spectrum k at the tangent height t^k by the gas lying within $\pm R/2$ of the tangent height where R is the sampling resolution of approximately 4 km. We see from the diagram that the layer thickness for the tangent spectrum k is $R/2$ or about 2 km. The layer thickness for the next level $k+1$ is the full resolution R or about 4 km. From Figures 2.13.8-10 we see that approximately 60% of each absorber is contained within the first 2 km. This corresponds to the first dotted line above t^k in Figure 2.13.11. In the next layer between 2 and 6 km an additional 20 to 30 % of the absorber is present. In the next layer contains about 10% of the absorber, and so on. So we can assume, to a first approximation, that the winds measured from Doppler shifts in spectrum k are a weighted average of the "true" winds, the weights being the percentage of absorber each layer [Shaw, 1985].

The above argument suggests the following approximate weighting scheme.

Let each measure wind speed at the layer k be given by v^k and let the "true" speed be given by v'^k. Then by the above arguments we have that

$$v^k \simeq 0.6v'^k + 0.2v'^{k+1} + 0.1v'^{k+2} + \cdots \tag{2.100}$$

which is a set of equations for all the spectra k and this can be inverted. Figures 2.13.12-13 show the wind profiles predicted by this method. Comparing these figures to Figures 2.9.9-10 show that in the vicinity of large wind variations that the weighted profiles have an enhanced vertical resolution. The peaks are shifted slightly in altitude and the magnitudes are larger by up to 50 m/s near 105 km.

The layers model can be used to improve the vertical resolution since the ATMOS instrument has a limited sampling resolution of about 4 km between spectra. The interferences of lines in different layers in the spectra is caused by the rate by which the density changes with height and the curvature of the earth and is not related to the vertical sampling interval of about 4 km of the instrument. If the vertical sampling interval can be decreased in future missions it may be possible, however, to determine the contribution of each layer to the observed wind profiles.

Positive speeds in Figures 2.13.12-3 correspond to an eastward motion in the northern latitudes and a westward motion in the southern latitudes respectively. Figure 2.13.14 shows a zonal average from the four sunset occultations and Figure 2.13.15 shows the standard deviations about these mean values. Between 25 and 65 km there was an eastward wind of about 25 ms^{-1} which remained steady within the precision of 5 ms^{-1} over the period of observation and range of longitudes as indicated by the small standard

deviations in Figure 2.13.15. The consistency in the shapes of these profiles also confirms the stability of the instrument calibration. The wind motion reverses at 65 km and above 80 km. All of the sunset occultations show maxima near 85 and 105 km. The variations in these maximum speeds appear to be real. However, if the wind sheets are thin, the variations may be due in part to a lack of vertical resolution. These variations in maximum speeds may also be due to tides [Chapman and Lindzen, 1970] or breaking gravity waves [Fritts, 1984] (see §§III for the definitions of these terms). The minima near 90 km correspond to an eastward wind of about 25 ms^{-1}.

The sunrise occultation in Figure 2.13.13 shows a single eastward maximum of about 100 ms^{-1} near 105 km. From 80 to 95 km there is a westward motion of about 50 ms^{-1} which is opposite to the direction observed in the northern hemisphere. A wind shear of about 20 $ms^{-1}km^{-1}$ occurs between 84 and 78 km. From 30 to 75 km the eastward motion of about 50 ms^{-1} is nearly twice that observed in the northern hemisphere.

Because the observations were made over a 24 hour period we can conclude that there were vertically stratified zonal winds at sunset between 25 and 120 km altitudes near 30°N over a wide range of longitudes. The single occultation available for the southern hemisphere also shows winds with magnitudes, directions, and shears which have similarities to the northern hemisphere profiles. The measurements were made near the vernal equinox and since the asymmetries of the mesospheric circulation between hemispheres may be dependent on the seasons it would be useful to have more measurements at other latitudes and seasons [Labitzke, 1985].

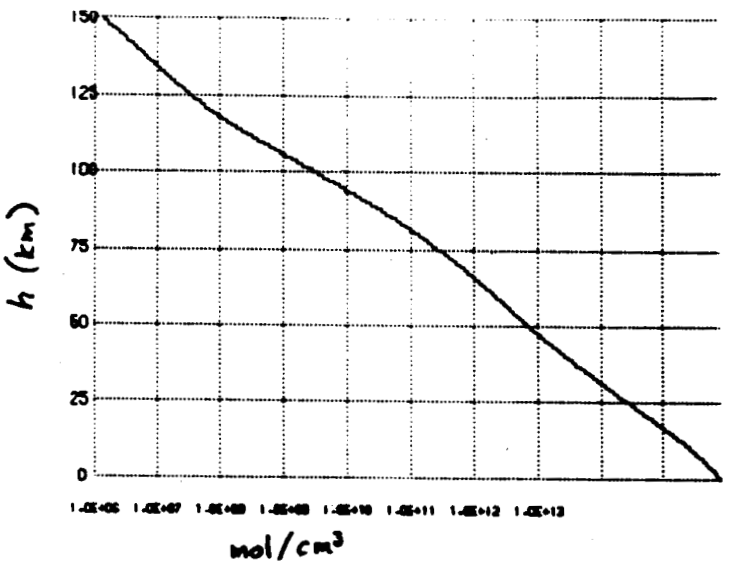

Figure 2.13.1 Concentration $c(h)$ for CO_2 from ATMOS standard atmosphere.

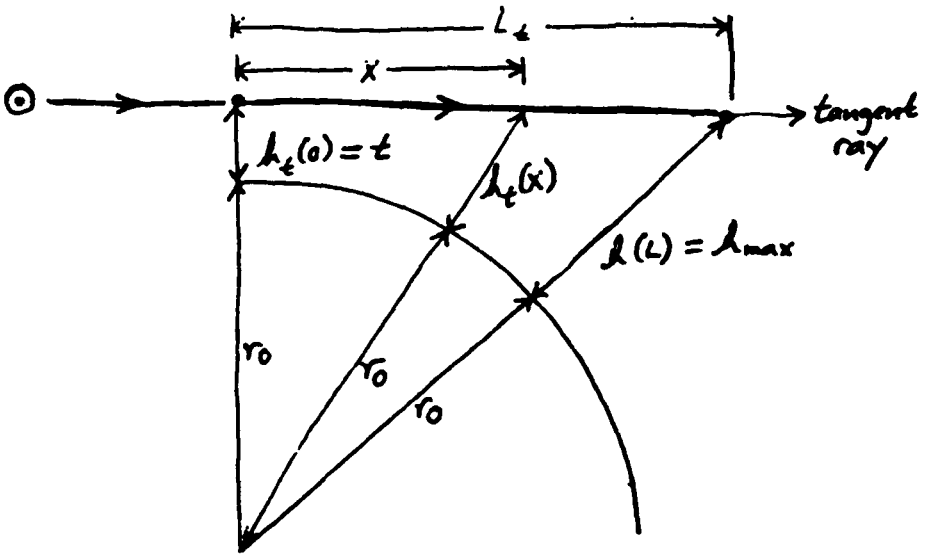

Figure 2.13.4 Tangent point geometry of the line of sight.

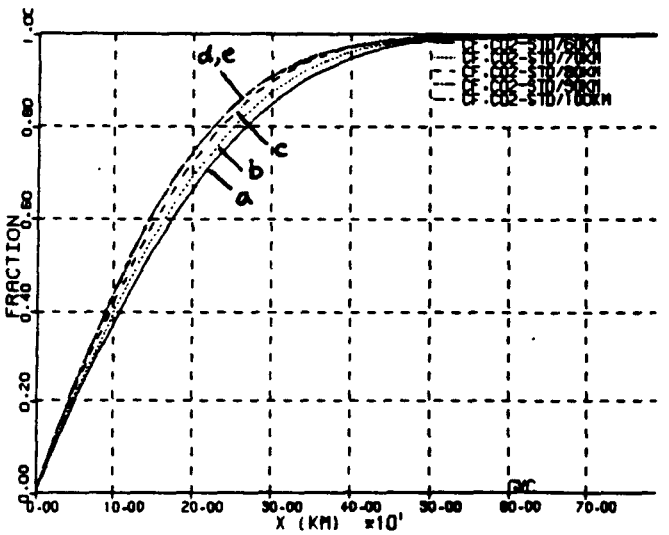

Figure 2.13.5 Concentration fraction as a function of x for CO_2 computed using data in Figure 2.13.1 for several tangent heights; (a) 60 km, (b) 70 km, (c) 80 km, (d) 90 km, (e) 100 km.

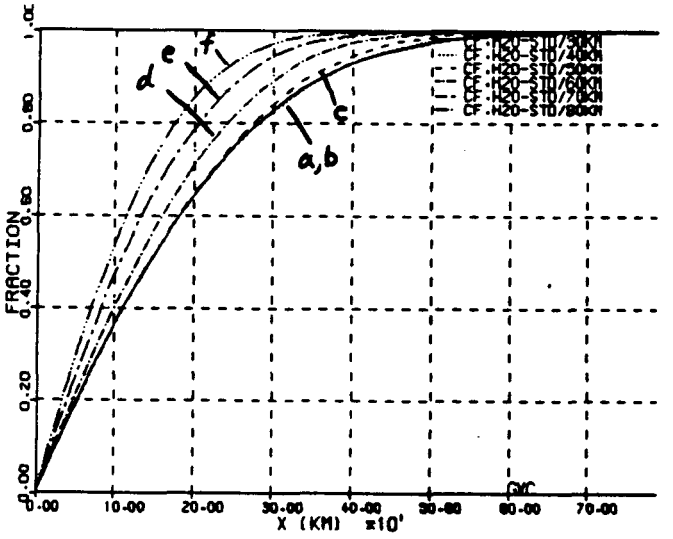

Figure 2.13.6 Concentration fraction as a function of x for H_2O at various tangent heights; (a) 30 km, (b) 40 km, (c) 50 km, (d) 60 km, (e) 70 km, (f) 80 km.

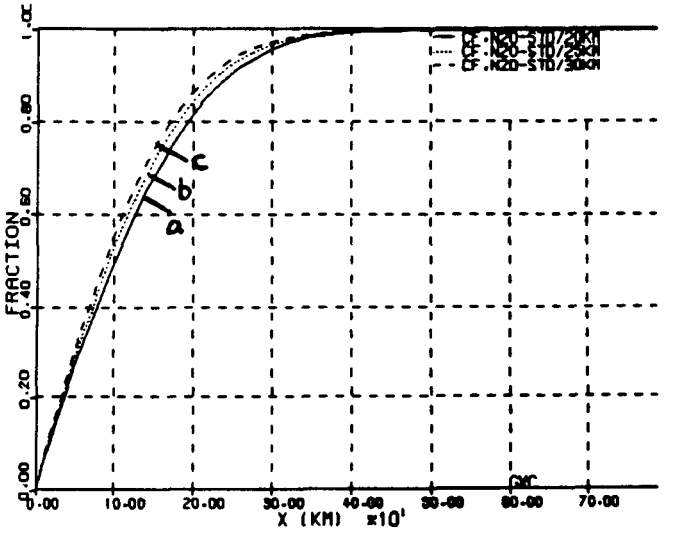

Figure 2.13.7 Concentration fraction as a function of x for N_2O at various tangent heights; (a) 20 km, (b) 25 km, (c) 30 km.

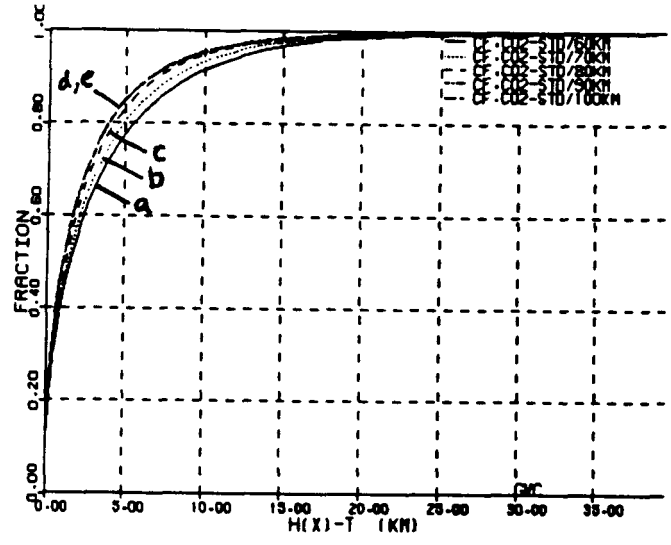

Figure 2.13.8 Concentration fraction as a function of layer thickness for CO_2 at various tangent heights; (a) 60 km, (b) 70 km, (c) 80 km, (d) 90 km, (e) 100 km.

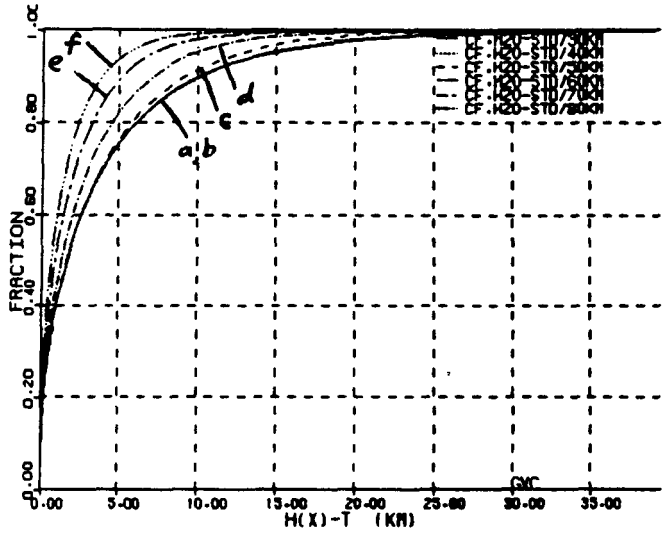

Figure 2.13.9 Concentration fraction as a function of layer thickness for H_2O at various tangent heights; (a) 30 km, (b) 40 km, (c) 50 km, (d) 60 km, (e) 70 km, (f) 80 km.

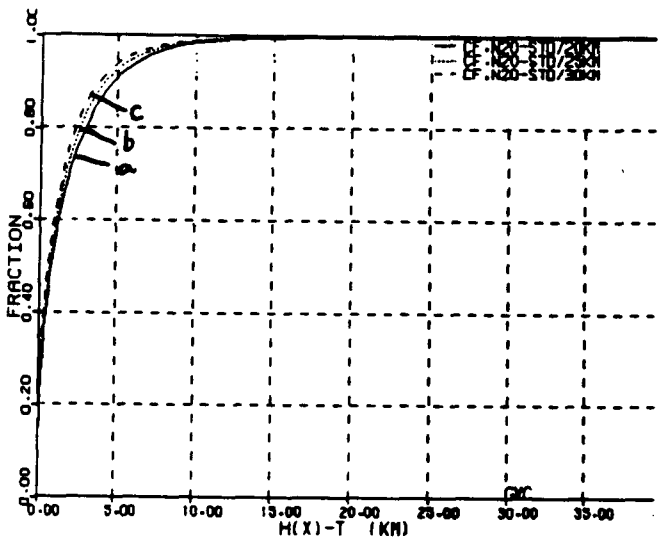

Figure 2.13.10 Concentration fraction as a function of layer thickness for N_2O at various tangent heights; (a) 20 km, (b) 25 km, (c) 30 km.

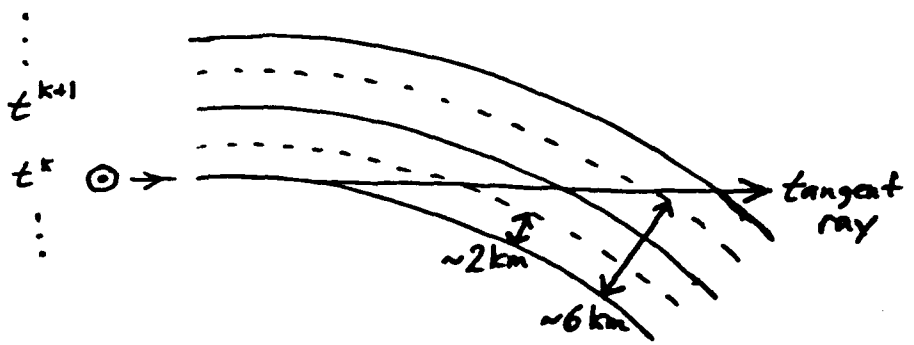

Figure 2.13.11 Illustration of layer thicknesses near the tangent point t^k.

C-3

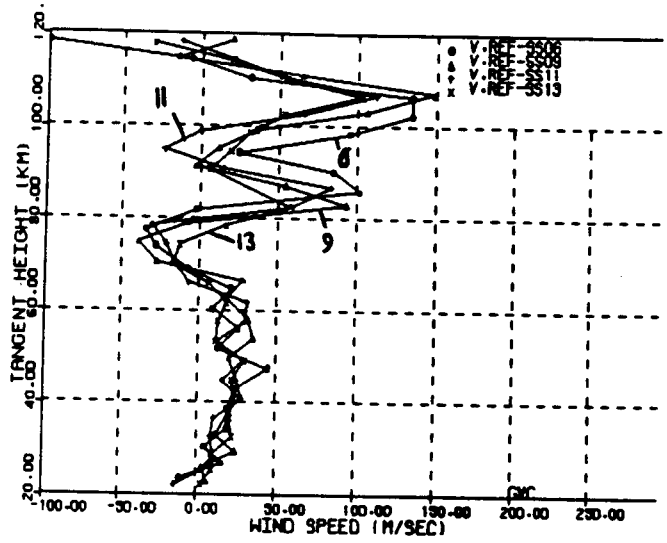

Figure 2.13.12 Density weighted zonal wind speed profiles for the sunset occultations. Positive speeds refer to an eastward flow; (6) SS06, (9) SS09, (11) SS11, (13) SS13.

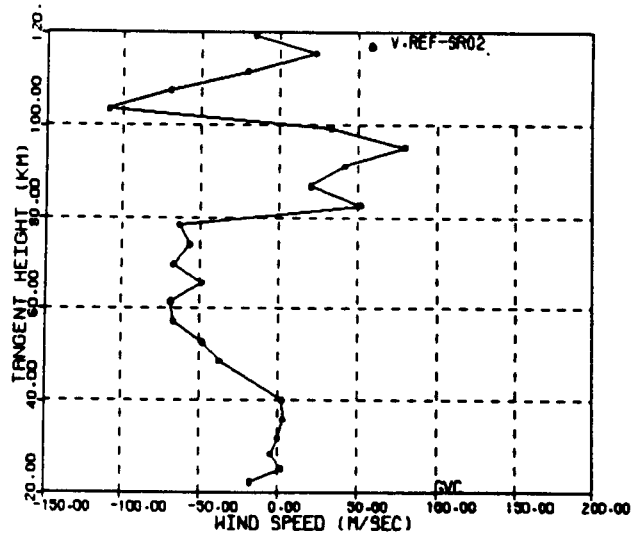

Figure 2.13.13 Density weighted zonal wind speed profiles for the sunrise occultation SR02. Negative speeds refer to an eastward flow.

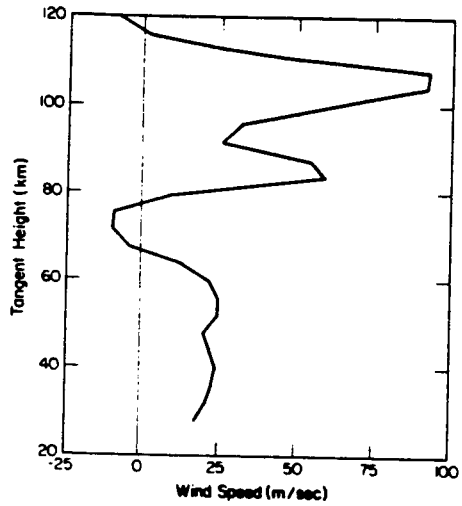

Figure 2.13.14 Zonal average of the wind speeds for the four sunset occultations near 30° N. A positive speed is eastward [van Cleef, Shaw, Farmer, 1987].

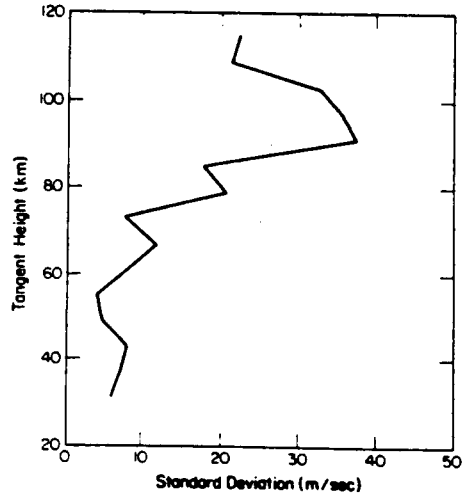

Figure 2.13.15 Standard deviations of the zonal average winds shown in Figure 2.13.14 [van Cleef, Shaw, Farmer, 1987].

II.14 Conclusion

Precisions of about 3×10^{-5} cm^{-1} for the assumed rest frame positions of the ν_3 CO_2 instrumental lines were sufficient to allow for stable frequency calibration and wind speeds to be accurate to better than 1 ms^{-1}. The calibration scale was found to be stable to better than 2×10^{-5} cm^{-1} and there were no indications of random calibration offsets between spectra. Thus Doppler shifts can be measured to accuracies of better than 5 ms^{-1}. Analysis of the orbital ephemeris data indicated that relative speeds between the orbiter and the earth with accuracies of 5 ms^{-1} or better could be obtained. We therefore successfully obtained zonal winds to precisions of 5 ms^{-1} between tangent heights of 25 and 120 km.

The relative positions of the lines used to obtain wind speeds were obtained to precisions of 5×10^{-5} cm^{-1} or better. There appeared to be significant improvements in the precisions of these line positions as compared to other sources [Brown, 1986]. The line positions were compared to other estimates of rest frame positions and were found to agree with them within the known accuracies of about 10^{-4} cm^{-1} (10^{-3} cm^{-1} for the $2\nu_2$ H_2O lines). The positions therefore agreed with the uncertainties of the standards. The accuracies of the rest frame positions, however, had no effect on the accuracy by which Doppler shifts could be measured since instrumental lines of CO_2 were available for absolute calibration.

The zonal wind speeds obtained by this method showed significant variations with height of up to the order of 100 ms^{-1}. The similarity in the sunset

wind profiles, taken at different longitudes but at similar latitudes and local times, indicate that the winds may be directly related to the atmospheric dynamics at sunset. Since there was only one sunrise occultation was available in the Filter 3 spectra similar conclusions cannot be made at this time.

CHAPTER III

LARGE SCALE DYNAMICS OF THE CIRCULATION OF THE EARTH'S ATMOSPHERE

In this chapter we examine several types of activity which are characteristic of the large scale circulation of the middle and upper atmosphere. This discussion is motivated to understand the 'oscillating' nature of the ATMOS wind profiles obtained from the spectral data. The different classifications of motion discussed in this chapter can be attributed to some of the observed features of the zonal winds shown in Figures 2.13-15. It was found that atmospheric tides, planetary scale oscillations produced by the daily or *diurnal* ultraviolet absorption and subsequent heating of the atmosphere by boundary layer water vapor and stratospheric ozone, are significantly large enough to produce the kind of wind speeds measured during the mission, particularly above stratospheric heights. In the stratosphere the wind motion is dominated by the thermal wind which can produce zonal wind motions of up to several tens of ms^{-1} and these appear in the ATMOS wind profiles at approximately the correct magnitude predicted [Salby, 1981] of several tens of ms^{-1}.

This chapter presents the linear theory of global scale atmospheric disturbances. The linearized theory predicts that the amplitudes of these disturbances, in terms of velocity, pressure and temperature perturbations from the mean state, will grow with height proportional to $\rho_b^{-1/2}$ where ρ_b is the mean background density. The exponential increase with height is due to energy transporting through the exponentially decreasing background density imposed by this linear theory [Kato, 1980]. The linear theory presented in this chapter includes *radiative damping* or *infrared cooling* [Andrews, Holton, Leovy, 1987] primarily due to the radiative properties of the 15 μm ν_2 CO_2 vibration band [Dickinson, 1984] but neglects dissipative mechanisms such as the kinematic viscosity which varies as $\rho_h^{-1/2}$ [Andrews, Holton, Leovy, 1987; Pedlosky, 1987].

In the previous chapter we showed how zonal wind speeds between 25 and 120 km were obtained with a precision of 5 ms^{-1} from the ATMOS spectra. The results indicated that there were variations of about 100 ms^{-1} in the wind speed over changes of only a few kilometers in the tangent height. The profiles in Figures 2.13.12-13 show that the amplitudes of the wind variations become larger with increasing height. The variations appear to begin at about 70 km with an amplitude of about 20 ms^{-1} and increase to almost 150 ms^{-1} at about 110 km. The sunset measurements occurred at a variety of longitudes at the same latitude and the wind structure appeared to be preserved between the occultations. This regularity of the wind patterns suggests that they are caused by global scale dynamics. Wind measurements by other researchers [Reed, 1969; Manson, Meek, 1986; Wallace, Tadd, 1974; Muraoka, Sugiyama, kawahira, 1988 - for example] indicate that the behavior observed by ATMOS

is typical of mesospheric and lower thermospheric dynamics.

The atmosphere heats and cools on a regular daily basis and this forces the upper atmospheric disturbances are periodic in nature. The *classical* or *linear* theory of atmospheric tides first described by Siebert (1961) and later by Chapman and Lindzen (1970) and Kato (1980) predicts atmospheric disturbances of pressure, density, temperature and wind due to atmospheric heating which propagate to thermospheric heights. The exponentially decreasing density of the atmosphere with height allows the amplitudes of pressure, density, temperature and velocity perturbations waves to grow with height [Fritts, 1984]. The classical theory of tides [Siebert, 1961; Chapman and Lindzen, 1970] predicts unlimited growth in wave amplitudes with height. This is due to the linearity of the theory. However, instabilities from the nonlinear terms in the fluid dynamical equations equations cause the waves to break which can lead to turbulence. Adiabatic instabilities due to large local potential temperature perturbations also may contribute to the breakdown of the tidal waves [Lindzen ,1981]. It is desirable to see if we can propose a theory which can 'explain' the nature of the wind speeds obtained by ATMOS.

In order to test the linear theory a model of atmospheric heating rates proposed by Groves (1982) was used as a periodic heating term and the response of the atmosphere is examined. The linear theory predicts that the leading diurnal tidal mode may be responsible for the regular structure observed in the ATMOS results. However, since the linear theory does not 'break', this response is overestimated.

III.1 The Atmospheric Temperature Distribution

The earth's atmosphere has an average altitude dependent temperature distribution similar to the one given in Figure 3.1.1 [from Andrews, Holton, Leovy, 1987]. Near the surface of the earth convection and adiabatic expansion of the atmosphere cause the temperature of the atmosphere to decrease with height [Kato, 1980]. The temperature minimum near 12 km is caused primarily by infrared emission of H_2O vapor. The region of the temperature decrease is known as the *troposphere* and the region where the minimum occurs is known as the *tropopause*. Above the tropopause the atmospheric temperature rises to a maximum near 50 km. The region between about 10 and 50 km where the temperature rises is known as the *stratosphere* and this is due mainly to the absorption of solar ultraviolet radiation by O_3 [Andrews, Holton, Leovy, 1987]. The maximum near 50 km is called the *stratopause* and occurs because the O_3 concentration decreases rapidly above this level and reduces the solar energy absorption. Above the stratosphere the temperature decreases again primarily due to infrared radiative cooling of CO_2 [Kato, 1980]. The temperature continues to decrease to a minimum near 85 km where the temperature again again begins to increase due to radiative solar heating by dissociation of molecular oxygen and by ionization of O [Kato, 1980]. The region between 50 and 85 km where the temperature decreases is known as the *mesosphere* and the region of the temperature minimum at about 85 km is known as the *mesopause*. The region above 85 km where the temperature increases is known as the *thermosphere*. Above the mesopause the amount of ionization of atomic species increases with height and the

atmosphere can conduct electricity and interact with magnetic fields. This region is known as the *ionosphere* and its electromagnetic interactions play a dominant role in the atmosphere above 150 km [Volland, Myers, 1977].

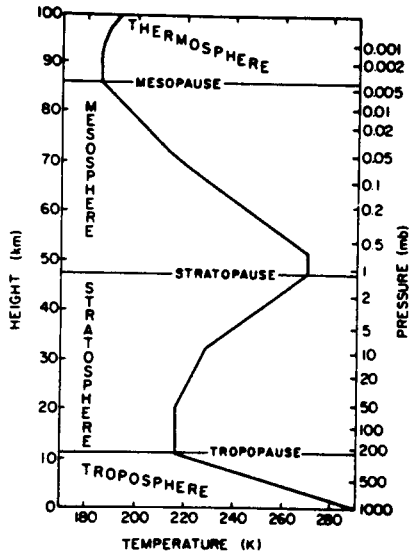

Figure 3.1.1 Midlatitude temperature profile based on *U.S. Standard Atmosphere* (1976) [from Andrews, Holton, Leovy, 1987].

III.2 Fluid Equations of Motion

The atmosphere's circulation is governed by the Navier-Stokes equation of fluid dynamics which can be expressed, as seen in a rotating coordinate frame, by [Pedlosky, 1987]

$$\rho\left[\frac{D\mathbf{u}}{Dt} + 2\boldsymbol{\Omega}\times\mathbf{u}\right] = -\nabla P + \rho\,\nabla\Phi + \mathcal{F} \tag{3.1}$$

where $\mathbf{u}$ is the velocity as observed in the rotating frame, the mass density of the fluid is defined by ρ, the pressure is given by P, the constant angular velocity of the earth's rotation is $\Omega = 7.272 \times 10^{-5}\mathrm{s}^{-1}$, the potential of conservative forces is Φ, and other non-conservative forces such as friction are represented by the term $\mathcal{F}$. The factor $2\boldsymbol{\Omega}\times\mathbf{u}$, the *Coriolis acceleration*, comes about from the coordinate transformation to the rotating frame of the earth. The total time derivative D/Dt is given by

$$\frac{D}{Dt} \equiv \frac{\partial}{\partial t} + \mathbf{u}\cdot\nabla \tag{3.2}$$

and represents the total time rate of change of any property following a fluid element. The conservation of mass is governed by the continuity equation and this is commonly expressed as [Pedlosky, 1987].

$$\frac{\partial\rho}{\partial t} + \nabla\cdot(\rho\mathbf{u}) = \frac{D\rho}{Dt} + \rho\,\nabla\cdot\mathbf{u} = 0. \tag{3.3}$$

For the atmosphere, the ideal gas law is used for the equation of state. This is given by the relation

$$P = \frac{\rho}{M} RT \tag{3.4}$$

where R is the gas constant, T is the kinetic temperature and M is the average molecular weight. The energy balance of the atmosphere is described by the thermodynamic equation [Pedlosky, 1987]

$$\frac{D\vartheta}{Dt} = \frac{M}{C_P}\frac{\vartheta}{T}\mathcal{H} \tag{3.5}$$

where the *potential* temperature ϑ is defined as

$$\vartheta \equiv T\left(\frac{P^0}{P}\right)^{R/C_P}. \tag{3.6}$$

Here P^0 is a constant reference pressure at temperature T^0 and $\mathcal{H}$ is the heating rate per unit mass. Since $C_P = R + C_V$ where C_V and C_P are the specific heats at constant volume and pressure respectively, then $\kappa \equiv R/C_P = 1 - \gamma^{-1}$ where $\gamma = C_P/C_V = 1.4$ is the ratio of specific heats [Pedlosky, 1987]. The five relations given in (3.1, 3, 5) and the equation of state (3.4) are used to describe atmospheric dynamics at all time and length scales.

The equations of motions (3.1, 3, 5) can be transformed into spherical coordinates representing the *height* z above the earth with radius a, *latitude* θ and *longitude* ϕ. We denote the *eastward* or *zonal* component of the velocity by u, the *northward* or *meridonial* component of the velocity by v, and the *upward* or *vertical* component of velocity by w. The zonal, meridonial and vertical momentum equations are [Pedlosky, 1987]

$$\frac{Du}{Dt} + \frac{wu}{a} - \frac{vu}{a}\tan\theta - 2\Omega\sin\theta\, v + 2\Omega\cos\theta\, w$$

$$= -\frac{1}{\rho a\cos\theta}\frac{\partial P}{\partial\phi} + \frac{\mathcal{F}_\phi}{\rho}, \tag{3.7}$$

$$\frac{Dv}{Dt} + \frac{wv}{a} + \frac{u^2}{a}\tan\theta + 2\Omega\sin\theta\, u = -\frac{1}{\rho a}\frac{\partial P}{\partial\theta} + \frac{\mathcal{F}_\theta}{\rho}, \tag{3.8}$$

$$\frac{Dw}{Dt} - \frac{u^2+v^2}{a} - 2\Omega\cos\theta\, u = -\frac{1}{\rho}\frac{\partial P}{\partial z} - g + \frac{\mathcal{F}_z}{\rho} \tag{3.9}$$

respectively where the gravitational acceleration is given in (3.1) by $\nabla\Phi = -g\hat{\mathbf{z}} \simeq -9.8\ \mathrm{ms}^{-1}\,\hat{\mathbf{z}}$. In this coordinate system the continuity equation (3.3) is

$$\frac{D\rho}{Dt} + \rho\left\{\frac{\partial w}{\partial z} + \frac{2w}{a} + \frac{1}{a\cos\theta}\left(\frac{\partial}{\partial\theta}(v\cos\theta) + \frac{\partial u}{\partial\phi}\right)\right\} = 0. \tag{3.10}$$

These equations (3.7-10) along with the thermodynamical relationship (3.5)

$$\frac{D\vartheta}{Dt} = \frac{M}{C_P}\frac{\vartheta}{T}\mathcal{H} \tag{3.11}$$

and the spherical coordinate representation of the time derivative operator (3.2)

$$\frac{D}{Dt} \equiv \frac{\partial}{\partial t} + w\frac{\partial}{\partial z} + \frac{v}{a}\frac{\partial}{\partial\theta} + \frac{u}{a\cos\theta}\frac{\partial}{\partial\phi} \tag{3.12}$$

are used to describe the dynamics in the spherical geometry of the earth.

III.3 Hydrostatic State and the Thermal Wind

The simplest static solution to the dynamical equations (3.7-11) is the time independent *hydrostatic* case where the atmospheric velocity vanishes everywhere $\mathbf{u} = \mathbf{0}$. This state can only occur if there are no horizontal temperature gradients. Assuming that this state represents the background is what is known as the *hydrostatic approximation.* If we assume that non-conservative forces vanish then from (3.7-11) the *conditions* for this solution are

$$\frac{\partial P_h}{\partial \phi} = 0, \tag{3.13}$$

$$\frac{\partial P_h}{\partial \theta} = 0, \tag{3.14}$$

$$\frac{\partial P_h}{\partial z} = -\rho_h g, \tag{3.15}$$

$$\mathcal{H} = 0. \tag{3.16}$$

The hydrostatic pressure field (denoted by the 'h' subscript) is independent of longitude ϕ and latitude θ. The height dependence of the hydrostatic with height z varies according to (3.15). By this relationship and the equation of state (3.4) the hydrostatic density and temperature (similar to Figure 3.1.1) must also only depend on the height z and the heating $\mathcal{H}$ must also vanish for the hydrostatic state to be realized.

The hydrostatic case is a highly idealized approximation to the true atmospheric state. Figure 3.3.1-2 show the zonal mean temperatures for altitudes of up to approximately 160 km respectively during equinox and solstice conditions [from Salby, 1981]. The average over latitudes is similar to the temperature profile in Figure 3.1.1 and there are variations between seasons

as well. From these data we see there are significant deviations of up to 10% in the temperature at a given height between different latitudes for each season and that the zonally averaged temperature background T_b is not independent of latitude θ. This temperature variation violates the conditions for the hydrostatic state which implies that the velocity field will not vanish and the horizontal temperature gradients induce a zonal velocity field. This is called the *thermal wind* and by assuming this to be the background state is known as the *thermal wind approximation.*

The simplest case for the thermal wind is a steady state ($\partial/\partial t = 0$) zonally symmetric solution ($\partial/\partial\phi = 0$) from the temperature data. The *zonal mean wind* can be derived from the latitudinal and vertical temperature gradients and assumes that the vertical and meridonial velocities vanish [Andrew, Holton, Leovy, 1987] $v = w = 0$. In the absence of dissipation, the dynamical equations become (3.7-11)

$$\frac{\partial P_b}{\partial \phi} = 0, \tag{3.17}$$

$$\frac{u_b^2}{a}\tan\theta + 2\Omega\sin\theta\, u_b = -\frac{1}{\rho_b a}\frac{\partial P_b}{\partial \theta}, \tag{3.18}$$

$$-\frac{u_b^2}{a} - 2\Omega\cos\theta\, u_b = -\frac{1}{\rho_b}\frac{\partial P_b}{\partial z} - g, \tag{3.19}$$

$$\frac{\partial u_b}{\partial \phi} = 0, \tag{3.20}$$

$$\mathcal{H} = 0. \tag{3.21}$$

These equations show that the fields are zonally symmetric and exist in the absence of heating. A differential equation which can describe the zonal velocity u_b in terms of the background temperature T_b can be derived from these equations. By combining (3.18-9) and using the equation of state it can

be shown [Kato, 1980] that to a first (linearized) approximation the zonal mean winds u_b can be derived from the zonal mean temperature T_b by the *thermal wind equation*

$$\frac{\partial u_b}{\partial z} - \frac{\partial}{\partial z}(\ln T_b)\, u_b = -\frac{g}{2\Omega \sin\theta\, a}\frac{\partial}{\partial \theta}(\ln T_b). \tag{3.22}$$

The differential equation which describes the relationship between the pressure and density can be determined by combining (3.18-9)

$$\frac{\partial P_b}{\partial z} + \frac{\cot\theta}{a}\frac{\partial P_b}{\partial \theta} = -\rho_b g. \tag{3.23}$$

The mean zonal wind determined from the mean temperature profiles in Figures 3.3.1-2 are given in 3.3.3-4 for equinox and solstice conditions respectively [after Salby, 1981]. Measurements of zonal mean temperatures are routinely conducted during the various month's of the year [see Barnett, Carney, 1985]. The zonal mean winds change as a function of height and latitude with the seasons. An eastward jet of about 50 ms^{-1} develops in the southern hemisphere during the equinox near 50° S around 9 scale heights or 60 km and continues to increase to about 80 ms^{-1} during the southern winter. The eastward maximum zonal wind of about 70 ms^{-1} between 40 and 80 km in sunrise zonal wind profile SR02 in Figure 2.13.13 determined from the ATMOS experiment can be explained by this jet near 50° S since the mission was flown about one month after the vernal equinox. The sunset wind speeds SS06, SS09, SS11 and SS13 in Figure 2.13.12 show an eastward flow of about 20 ms^{-1} near 50 km. This is about 10 ms^{-1} less than the value predicted for the equinox conditions of about 30 ms^{-1}. However, between the equinox and summer solstice the zonal wind speed will decrease with

time and changes direction which is evident by comparing the zonal winds in Figures 3.3.3-4 at 30° N.

The thermal wind due to latitudinal gradients of the zonal mean temperature can explain the eastward wind below 70 km which was observed observed in the ATMOS wind data. The consistency the zonal winds features of the sunset wind profiles in Figure 2.13.12 can be explained by the zonal symmetry of the thermal winds. Thermal wind features below 70 km can be expected in future ATMOS missions. Seasonal as well as latitudinal variability in the zonal winds should be expected [Barnett, Corney, 1985]. The ATMOS wind profiles confirm the steadiness of the zonal wind over a wide range of longitudes. The deviations of the averages of the four sunset profiles in Figure 2.13.15 are between 5 and 10 ms^{-1} below 60 km. This observation may be useful for calibrating spectra in which instrumental lines are not available for calibration §II.1 since bith observation and theory indicate that the zonal mean winds are very steady and predictable. By *assuming* that the thermal wind is steady, it may be useful in future missions to adjust the wavenumber calibration of the spectra to obtain the best mutual correlations with wind speeds below 60 km.

The temperature profiles T_b in Figures 3.3.1-2 and the corresponding zonal winds u_b in Figures 3.3.3-4 show that the atmospheric state is highly non-uniform with latitude and height. Above 13 scale heights or about 85 km the thermal wind vanishes since the zonal mean temperature in thermosphere effectively becomes independent of latitude [Salby, 1981] which can be seen in Figures 3.3.1-2. However, the ATMOS measurements indicate that there exist winds with zonal speeds of over 100 ms^{-1} and large wind shears. This

cannot be explained by the thermal wind. We can show that time dependent global waves play an important role in the circulation of the middle and upper atmosphere. From the perspective of modeling atmospheric circulation, the mean zonal-wind and temperature profiles can serve as a *background* upon which time dependent fluctuations occur [Lindzen, Hong, 1974; Waltersheid, Venkateswaran, 1979]. *Rossby waves*, which are homogeneous free atmospheric oscillations having periods on the order of days, can interact with the zonal-mean circulation and modify the zonal-mean winds predicted by the thermal wind equation (3.22) [Dickinson, 1969]. Atmospheric tides [Chapman and Lindzen, 1970], forced by the periodic heating and cooling of atmosphere by absorption of ultraviolet solar radiation by ozone and water vapor, have periods of a day and fractions thereof and interact with Rossby waves and the zonal mean flow to produce net accelerations as well [Teitelbaum, Vial, 1981; Zurek, 1986]. The mean zonal winds conversely affect the structure of the planetary waves and tides [see Lindzen and Hong, 1974; Waltersheid, Venkateswaran, 1976] and these types of atmospheric activity may be highly interdependent.

This section has shown that the eastward winds of about 30 ms^{-1} and 70 ms^{-1} in the northern and southern hemisphere ATMOS wind profiles below about 70 km can be described by the regular thermal wind associated with latitudinal temperature gradients of the lower and middle atmosphere. However, these represent are slowly varying with a time scale of the order of the seasons. Other time dependent effects also occur the wave like character of the ATMOS wind profiles §II.13 may be caused by other dynamics. These are discussed in the next few sections.

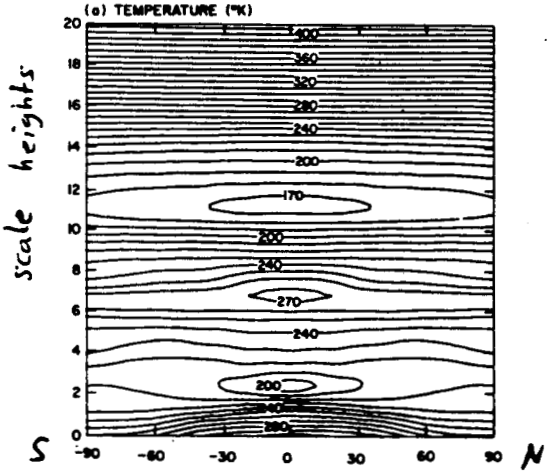

Figures 3.3.1 Zonal mean temperatures for equinox conditions [from Salby, 1981].

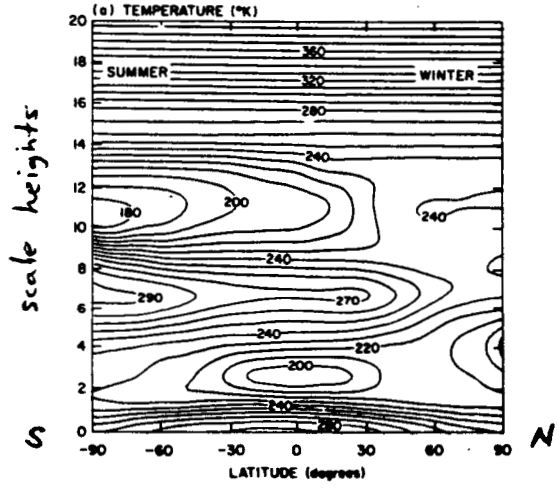

Figures 3.3.2 Zonal mean temperatures for winter soltice conditions [from Salby, 1981]. Summer soltice conditions are approximately the same with by interchanging N and S.

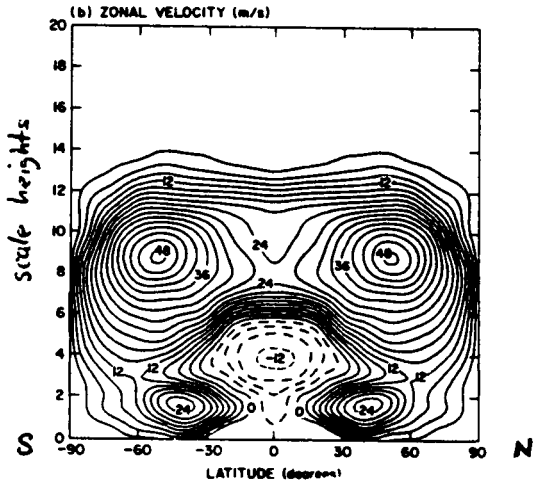

Figures 3.3.3 Zonal mean winds for equinox conditions. Solid contours are positive (eastward) speeds while dashed contours are negative (westward) speeds [from Salby, 1981].

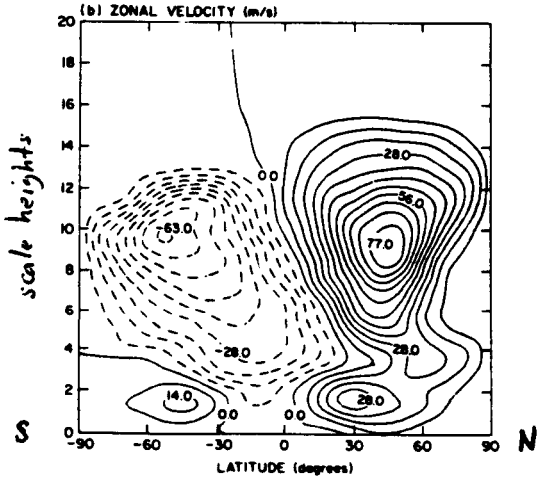

Figures 3.3.4 Zonal mean winds for winter soltice conditions. Solid contours are positive (eastward) speeds while dashed contours are negative (westward) speeds [from Salby, 1981]. Summer soltice conditions are approximately the same with by interchanging N and S.

III.4 Linear Waves on a Hydrostatic Spherical Atmosphere

We have seen that winds occur in the upper atmosphere. Indeed, the atmosphere can support a variety of free and forced wave motions. In the next few sections we briefly review the linear wave theory of global scale dynamics. The waves which have meteorological significance range from *acoustic gravity waves* [Kato, 1980] which are free oscillations with periods of several hours or less due to stratification of the background temperature, *atmospheric tides* [Chapman and Lindzen, 1970] with periods of a day or less and *planetary* or *Rossby waves* with periods of several days or more [Andrews, Holton, Leovy, 1987]. Of these three types of waves the latter two, atmospheric tides and Rossby waves, are significantly affected by the variation of Coriolis acceleration with latitude θ. I will not examine acoustic gravity waves in this report due their limited horizontal length scale [Gossard, Hooke, 1975; Kato, 1980]. However, they can be important in affecting the zonal mean circulations due to wave breaking [Fritts, 1986] and subsequent transfer of momentum due to turbulent eddy diffusion [Andrews, Holton, Leovy, 1987]. We will examine, therefore, waves which are of the greatest importance for the large scale circulation of the middle atmosphere since it is not possible to examine all waves in detail.

We shall only examine waves in an atmospheric background state which is vertically stratified without horizontal temperature gradients. This corresponds to the hydrostatic approximation. It was mentioned that the actual atmosphere is not in a hydrostatic state and possesses a mean thermal

wind. The presence of background winds can affects the way atmospheric waves propagate through the atmosphere [Lindzen, Hong, 1974; Waltersheid, Venkateswaran, 1979]. Although background winds tend to complicate linear wave calculations, qualitatively the results are similar to those obtained using the more tractable hydrostatic background approximation and can be found in the literature [Lindzen, Hong, 1974; Waltersheid, Venkateswaran, 1979].

The system of linear equations describing fluid motions on a sphere was originated by Laplace (1799, 1825) and is useful for understanding atmospheric tides and global modes (Rossby waves). The purpose of the following discussion is to examine some of the most important solutions.

The nonlinear equations which describe global scale dynamics are described in Appendix A. The final equations (A.61-7) are presented in *dimensionless* form and represent the behavior of the system in terms of the length and time scales for global scale disturbances. The scaling of the variables shows which terms in the dynamical equations are of primary and secondary importance. These derivations, although extensive, are the underlying basis for the linear wave theory of disturbances on a vertically stratified rotating spherical atmosphere. The description of linear wave theory which follows is based on the scaling derivations.

Linear atmospheric wave theory is derived from the equations of motion (A.61-7) by ignoring the nonlinear terms to a first approximation. The linear balance equations can then be written. The continuity equation (A.62)

becomes

$$\epsilon F \frac{\partial \rho}{\partial t} + \Lambda \frac{\partial w}{\partial x} - \left(\Lambda - \frac{d\Lambda}{dx} \right) w + \frac{\partial v'}{\partial \mu} + \frac{1}{1-\mu^2} \frac{\partial u'}{\partial \phi} = 0. \tag{3.24}$$

The horizontal momentum equations (A.63-4) are

$$\epsilon \frac{\partial u'}{\partial t} - \mu v' = -\frac{\partial P}{\partial \phi}, \tag{3.25}$$

$$\epsilon \frac{\partial v'}{\partial t} + \mu u' = -\left(1-\mu^2\right) \frac{\partial P}{\partial \mu}, \tag{3.26}$$

the vertical momentum equation (A.65) is

$$\rho = \left(\Lambda - \frac{d\Lambda}{dx} \right) P - \Lambda \frac{\partial P}{\partial x}, \tag{3.27}$$

the thermodynamical relation (A.66) is

$$\epsilon F \frac{\partial \vartheta}{\partial t} + \mathcal{N}^2 w = \mathcal{H}, \tag{3.28}$$

and the relationship between the potential temperature, pressure and density perturbations (A.67) is

$$\vartheta = \frac{1}{\gamma} \Lambda P - \rho. \tag{3.29}$$

The derivation of these equations is described in Appendix A. Basically, in dimensionless format, the zonal, meridonial and vertical velocity components are represented by u', v', and w respectively while the pressure, density and potential temperature perturbations about the hydrostatic state are represented by P, ρ and ϑ respectively. The vertical coordinate x defined in (A.54) represents the number of atmospheric e-folding scale heights above the surface, and a latitude coordinate has been introduced $\mu = \sin\theta$. The hydrostatic temperature distribution is contained in the function Λ (A.22)

and the dimensionless local bouyancy frequency $\mathcal{N}$ (A.49; see Appendix B). Time dependent external heating is represented by the dimensionless function $\mathcal{H}$ (A.52). This linearized approximation is used to describe atmospheric dynamics provided that the (dimensionless) variables have magnitudes much smaller than unity.

The standard procedure [Siebert, 1961; Chapman, Lindzen, 1970; Salby, 1979; Kato, 1980; Andrews, Holton, Leovy, 1987] for determining the solutions to the set of equations (3.24-9) is to pose the form

$$(u',\, v',\, P,\, w,\, \rho,\, \mathcal{H}) = \Re\{[u'(\theta,x),\, v'(\theta,x),\, P(\theta,x),\, w'(\theta,x),\, \rho(\theta,x), \mathcal{H}(\theta,x)] \times \exp[i(\sigma t + s\phi)]\}\,. \tag{3.30}$$

The zonal wave number s must be an integral value due to the periodicity of the azimuthal coordinate ϕ. The time t is the dimensionless representation described in the Appendix A, the rotational period of the earth being 2π in this representation. The (dimensionless) frequency number σ is continuous in general.

We define the number $f \equiv \sigma\epsilon = \sigma/2$ for convenience. The periodic horizontal momentum equations (3.25-6) are then

$$if u' - \mu v' = -isP, \tag{3.31}$$

$$if v' + \mu u' = -\left(1-\mu^2\right)\frac{\partial P}{\partial \mu}. \tag{3.32}$$

By using these equations the horizontal velocity field (u', v') can be determined in terms of the pressure P

$$u' = \frac{1}{f^2-\mu^2}\left[\mu\left(1-\mu^2\right)\frac{\partial P}{\partial \mu} - sfP\right], \tag{3.33}$$

$$v' = \frac{i}{f^2-\mu^2}\left[f\left(1-\mu^2\right)\frac{\partial P}{\partial \mu} - s\mu P\right]. \tag{3.34}$$

It is important to note that for $f \leq 1$ which corresponds to atmospheric tidal distrubances [Chapman, Lindzen, 1970] there are two latitudes where $\mu = \pm f$ and this causes the denominators in (3.33) and (3.34) to vanish. The latitudes, which depend on the frequency of the wavesthrough f, where this occurs are called the *critical latitudes.* Brilluon (1932) first showed that the numerators in (3.33-4) also vanish at these latitudes and they do not impose any theoretical difficulties. For the diurnal tide §III.6 the critical latitude is at 30° N and S.

Following Siebert (1961) we define the dimensionless divergence

$$X \equiv \nabla \cdot \mathbf{u} = \Lambda\frac{\partial w}{\partial x} + \frac{\partial v'}{\partial \mu} + \frac{is}{1-\mu^2}u'. \tag{3.35}$$

Since u' and v' depend on the pressure P the horizontal part X_h of the divergence (3.35) is

$$X_h \equiv \frac{\partial v'}{\partial \mu} + \frac{is}{1-\mu^2}u' = if\mathcal{L}P \tag{3.36}$$

where the operator $\mathcal{L}$ is defined as

$$\mathcal{L} \equiv \frac{\partial}{\partial \mu}\left(\frac{1-\mu^2}{f^2-\mu^2}\frac{\partial}{\partial \mu}\right) - \frac{1}{f^2-\mu^2}\left(\frac{s}{f}\frac{f^2+\mu^2}{f^2-\mu^2} + \frac{s^2}{1-\mu^2}\right) \tag{3.37}$$

by substituting (3.33-4) into (3.36). The relationship (3.35) can be written as

$$X - \Lambda\frac{\partial w}{\partial x} = if\mathcal{L}P. \tag{3.38}$$

The remaining three relations, namely the vertical momentum (3.27), continuity (3.24), and thermodynamical (3.28) equations become

$$\rho = \left(\Lambda - \frac{d\Lambda}{dx}\right)P - \Lambda\frac{\partial P}{\partial x}, \tag{3.39}$$

$$ifF\rho - \left(\Lambda - \frac{d\Lambda}{dx}\right) w + X = 0, \tag{3.40}$$

and

$$ifF\vartheta + \mathcal{N}^2 w = \mathcal{H} \tag{3.41}$$

respectively. From (3.29) we can solve for the density ρ and substitute into (3.39-40) to obtain the vertical momentum and continuity equations

$$\vartheta = -\mathcal{N}^2 P + \Lambda \frac{\partial P}{\partial x}, \tag{3.42}$$

$$\frac{1}{\gamma} ifF\Lambda P - ifF\vartheta - \left(\Lambda - \frac{d\Lambda}{dx}\right) w + X = 0. \tag{3.43}$$

The continuity equation (3.43) and thermodynamic equation (3.41) can be added to yield

$$ifFP = w - \frac{\gamma}{\Lambda}(X - \mathcal{H}). \tag{3.44}$$

This equation can be differentiated with respect to z (A.54) to give

$$\Lambda \frac{\partial w}{\partial x} = ifF\Lambda \frac{\partial P}{\partial x} + \gamma \left[\frac{\partial}{\partial x} - \frac{1}{\Lambda}\frac{d\Lambda}{dx}\right](X - \mathcal{H}). \tag{3.45}$$

The vertical momentum equation (3.42) can be rearranged

$$\Lambda \frac{\partial P}{\partial x} = \vartheta + \mathcal{N}^2 P. \tag{3.46}$$

We now solve for ϑ in (3.41) and substitute this and (3.44) into (3.46) to show

$$ifF\Lambda \frac{\partial P}{\partial x} = -\frac{\gamma}{\Lambda}\mathcal{N}^2 X + \left(1 + \frac{\gamma}{\Lambda}\mathcal{N}^2\right)\mathcal{H}. \tag{3.47}$$

This result can then be substituted into (3.45) to give

$$\Lambda \frac{\partial w}{\partial x} = \gamma \left[\frac{\partial X}{\partial x} - \kappa X - \left(\frac{\partial \mathcal{H}}{\partial x} - \mathcal{H}\right)\right]. \tag{3.48}$$

Differentiating this result with respect to z gives

$$\Lambda\frac{\partial}{\partial x}\Lambda\frac{\partial w}{\partial x} = \gamma\Lambda\left[\frac{\partial^2 X}{\partial x^2} - \kappa\frac{\partial X}{\partial x} - \left(\frac{\partial^2 \mathcal{H}}{\partial x^2} - \frac{\partial \mathcal{H}}{\partial x}\right)\right]. \tag{3.49}$$

If we now differentiate (3.38) with respect to z

$$\Lambda\frac{\partial X}{\partial x} - \Lambda\frac{\partial}{\partial x}\Lambda\frac{\partial w}{\partial x} = if\mathcal{L}\Lambda\frac{\partial P}{\partial x}. \tag{3.50}$$

We now substitute (3.47) and (3.49) into this equation to obtain the following differential equation for the dimensionless divergence X

$$\frac{\partial^2 X}{\partial x^2} - \frac{\partial X}{\partial x} - \left(\frac{\partial^2 \mathcal{H}}{\partial x^2} - \frac{\partial \mathcal{H}}{\partial x}\right) = \frac{1}{F\Lambda^2}\mathcal{L}\left[\mathcal{N}^2 X - \left(\Lambda - \frac{d\Lambda}{dx}\right)\mathcal{H}\right]. \tag{3.51}$$

This equation can be further simplified by introducing an auxiliary function y, which we will also term the *vertical structure function*, as

$$X \equiv ye^{x/2} + \mathcal{H} \tag{3.52}$$

Equation (3.51) then transforms to

$$\frac{\partial^2 y}{\partial x^2} - \frac{1}{4}y = \frac{1}{F\Lambda^2}\mathcal{L}\left[\mathcal{N}^2 y - \frac{1}{\gamma}\Lambda\mathcal{H}e^{-x/2}\right]. \tag{3.53}$$

This equation can be solved by using the method of separation of variables as described by Siebert (1961) and Chapman and Lindzen (1970). Consider a set of functions $\{\Theta_n^{\sigma s}(\mu)\}$ for $n = 0, 1, \ldots$ which is assumed to be complete over the interval $-1 \leq \mu \leq 1$ for each chosen pair σ, s. Then the vertical structure function y and heating $\mathcal{H}$ can be expanded on this complete set by

$$y = \sum_n y_n(x)\,\Theta_n^{\sigma s}(\mu), \tag{3.54}$$

$$\mathcal{H} = \sum_n \mathcal{H}_n(x)\,\Theta_n^{\sigma s}(\mu). \tag{3.55}$$

By calling the separation constant $-\lambda_n^{\sigma s}$ for each n component the following pair of equations can be derived

$$\mathcal{L}\Theta_n^{\sigma s} + \lambda_n^{\sigma s}\,\Theta_n^{\sigma s} = 0, \tag{3.56}$$

$$\frac{d^2 y_n}{dx^2} + \left[\frac{\lambda_n^{\sigma s}}{F\Lambda^2}\mathcal{N}^2 - \frac{1}{4}\right] y_n = \frac{1}{\gamma}\frac{\lambda_n^{\sigma s}}{F\Lambda}\mathcal{H}_n^{\sigma s} e^{-z/2}. \tag{3.57}$$

The eigenvalue problem for the operator $\mathcal{L}$ in (3.56) is known as *Laplace's Tidal Equation* [Longuett-Higgins, 1968; Chapman and Lindzen, 1970] since it was originally derived by Laplace (1799, 1825) to describe the free oscillations of an ocean. The eigenfunctions $\Theta_n^{\sigma s}$, commonly called *Hough functions* (after Hough, 1898), form a complete orthogonal set for each set σ, s. A method for computing the eigenfunctions and eigenvalues described in Appendix C is based on a method similar to one described by Longuett-Higgins (1968). The orthogonality of the Hough functions is also proved. The equation (3.57) is called the *vertical structure equation* [Siebert, 1961]. The solution for y_n is determined by the eigenvalue $\lambda_n^{\sigma s}$ and the heating term $\mathcal{H}_n^{\sigma s}$ together with appropriate boundary conditions.

The eigenvalues of (3.56) are related to the frequency of the mode through σ and, for each azimuthal mode number s, a relationship between the eigenvalues λ and σ can be determined. This relationship for the values of $-1 \leq s \leq +2$, as computed by Longuett-Higgins (1968), is shown in Figures 3.4.1-4. The modes where $s > 0$ ($s < 0$) are called *westward* (*eastward*) migrating modes since the longitude ϕ of constant phase decrease (increase) as time t increases. Negative values of the eigenvalue λ exist only for modes with $\sigma < 1$ [Longuett-Higgins, 1968; Andrews, Leovy, Holton, 1987].

Once the vertical structure equation (3.57) has been solved for each eigenmode n we can determine the physical fields. In terms of the Hough function expansion, equation (3.38) can be written

$$X_n - \Lambda \frac{dw_n}{dx} = -if\lambda_n^{\sigma s} P_n \tag{3.58}$$

and from equation (3.48)

$$\Lambda \frac{dw_n}{dx} = \gamma \left[\frac{dX_n}{dx} - \kappa X_n - \left(\frac{d\mathcal{H}_n}{dx} - \mathcal{H}_n \right) \right]. \tag{3.59}$$

By using (3.52) these can be combined to give the pressure in terms of the vertical structure function y_n

$$P_n = \frac{\gamma}{if\lambda_n^{\sigma s}} e^{x/2} \left[\frac{dy_n}{dx} - \frac{1}{2} y_n \right]. \tag{3.60}$$

With this result and equation (3.44) the vertical velocity becomes

$$w_n = \frac{\gamma F}{\lambda_n^{\sigma s}} e^{x/2} \left[\frac{dy_n}{dx} + \left(\frac{\lambda_n^{\sigma s}}{F\Lambda} - \frac{1}{2} \right) y_n \right]. \tag{3.61}$$

Combining (3.60) with (3.59) the density is

$$\rho_n = -\frac{\gamma}{if\lambda_n^{\sigma s}} \Lambda e^{x/2}$$

$$\times \left[\frac{d^2 y_n}{dx^2} - \left(1 - \frac{1}{\Lambda} \frac{d\Lambda}{dx} \right) \frac{dy_n}{dx} + \left(\frac{1}{4} - \frac{1}{2\Lambda} \frac{d\Lambda}{dx} \right) y_n \right]. \tag{3.62}$$

The velocity fields u' and v' are determined from equations (3.33-4)

$$u'_n = P_n(x)\, U'(\mu), \tag{3.63}$$

$$v'_n = iP_n(\dot{x})\, V'(\mu), \tag{3.64}$$

where

$$U_n^{\prime\sigma} \equiv \frac{1}{f^2-\mu^2}\left[\mu\left(1-\mu^2\right)\frac{d}{d\mu} - sf\right]\Theta_n^{\sigma s}, \tag{3.65}$$

$$V_n^{\prime\sigma s} \equiv \frac{1}{f^2-\mu^2}\left[f\left(1-\mu^2\right)\frac{d}{d\mu} - s\mu\right]\Theta_n^{\sigma s}. \tag{3.66}$$

The vertical components of the physical fields (3.60-4) along with the Hough eigenmodes Θ_n and the horizontal velocity modes U_n' and V_n' describe the time and space solutions of the linear wave equations for fluid motion on a spherical atmosphere.

The linear theory serves as tool by which periodic atmospheric disturbances may be studied. In the sections that follow we will show that both homogeneous solutions and nonhomogenous solutions of the vertical structure equation (3.57) exist and that planetary waves and atmospheric tides are representative of these kinds of solutions respectively. It will be shown that the homogeneous solutions, the planetary waves, are not likely to be responsible for the upper atmospheric winds observed using the ATMOS instrument. However, the nonhomogeneous solutions give rise to perturbations from the mean state large enough to account for the global extent and the magnitudes of the winds observed above 70 km by ATMOS.

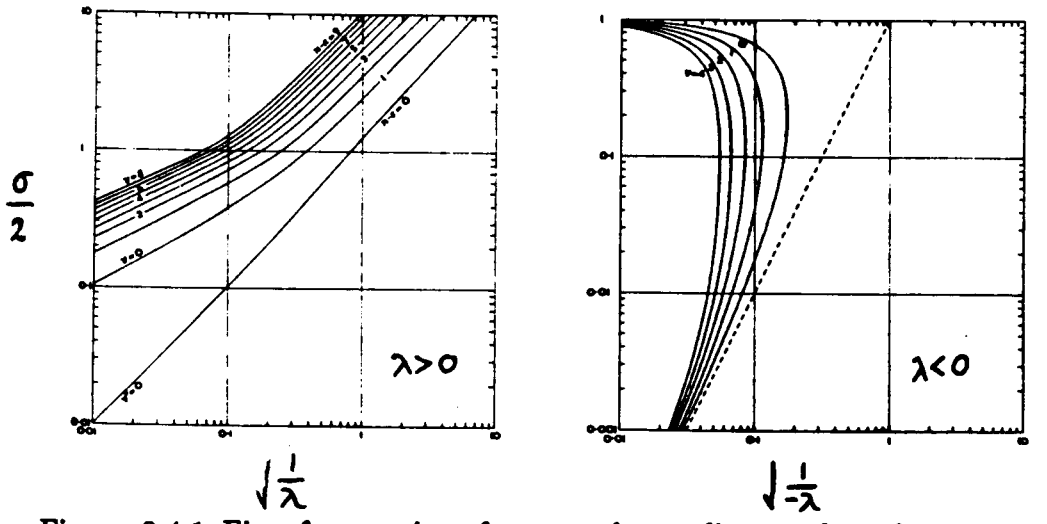

Figure 3.4.1 Eigenfrequencies of eastward traveling modes when $s = -1$ [adapted from Longuet-Higgins, 1968]. The frequency number σ (the number of oscillations per day) is plotted against the eigenvalue λ for various modes.

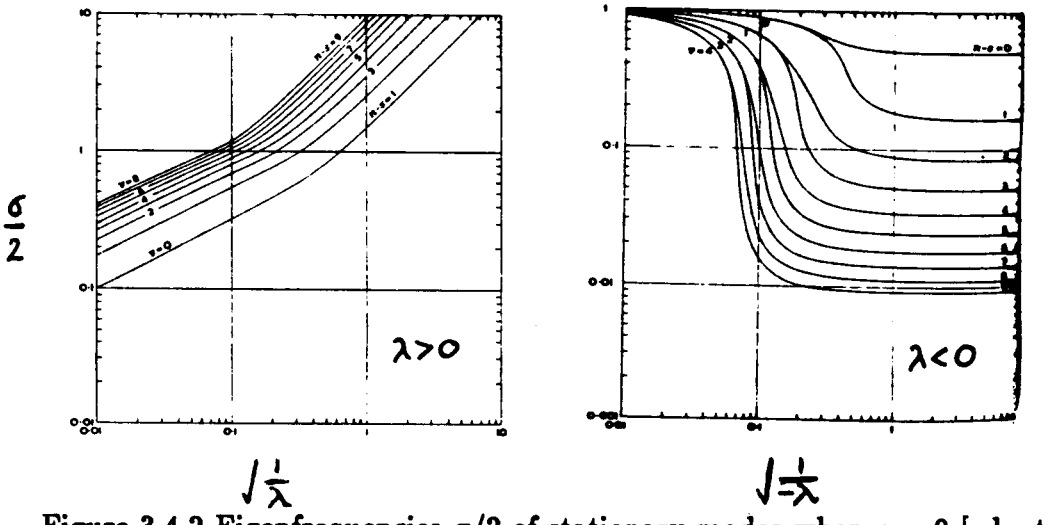

Figure 3.4.2 Eigenfrequencies $\sigma/2$ of stationary modes when $s = 0$ [adapted from Longuet-Higgins, 1968]. The frequency number σ (the number of oscillations per day) is plotted against the eigenvalue λ for various modes.

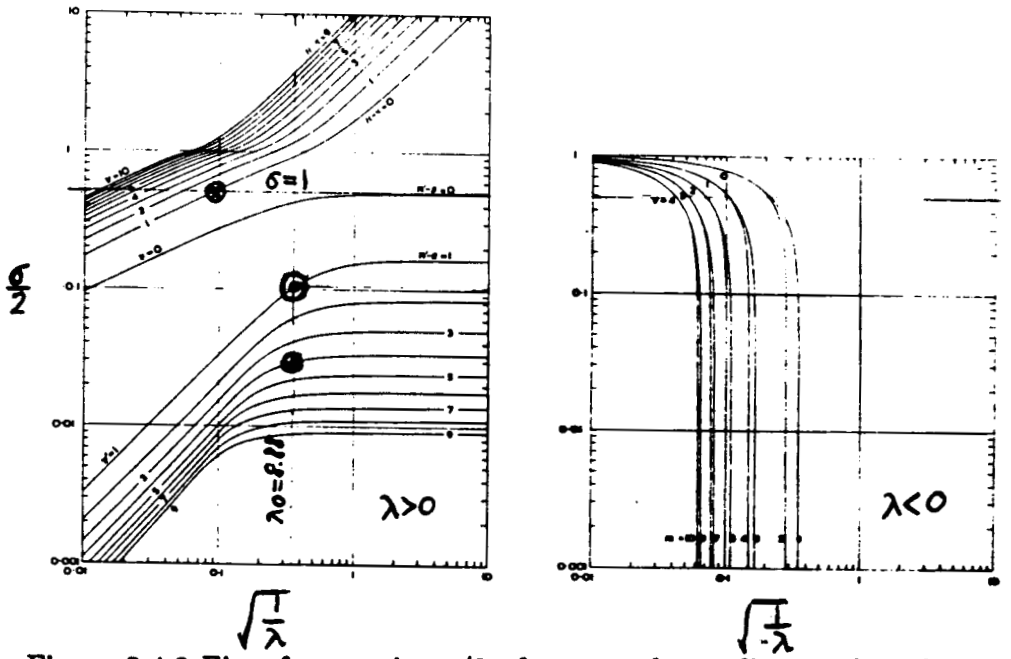

Figure 3.4.3 Eigenfrequencies $\sigma/2$ of westward traveling modes when $s = 1$ [adapted from Longuet-Higgins, 1968]. The frequency number σ (the number of oscillations per day) is plotted against the eigenvalue λ for various modes. The horizontal line at $\sigma = 2$ intercepts the dispersion curves which gives the diurnal eigenvalues λ_n. The Rossby 5-day wave $\odot$ and 16-day wave $\oplus$ are marked on the intersection of the dispersion curves with the atmosphere eigenvalue $\lambda_0 = 8.88$ giving the dimensionless frequencies σ of oscillation.

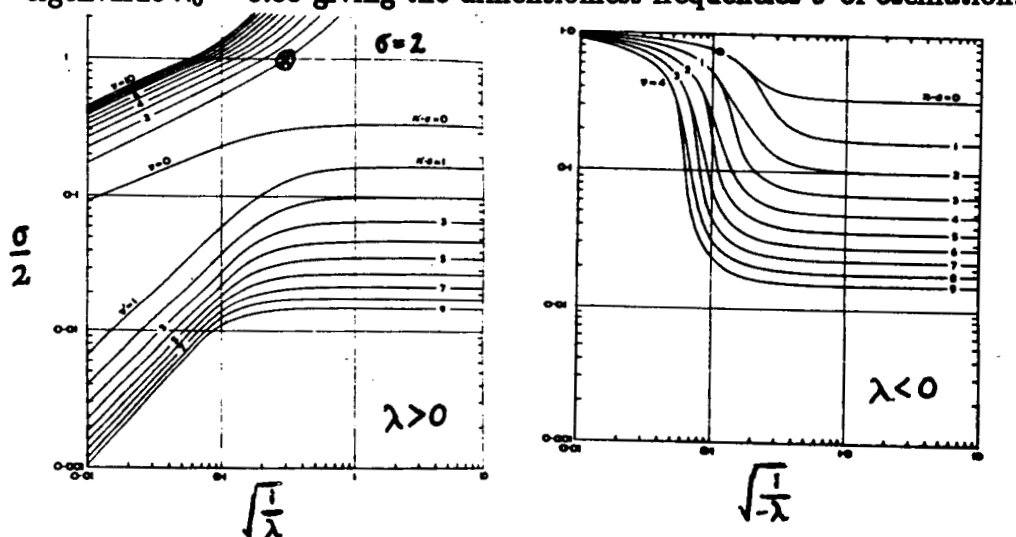

Figure 3.4.4 Eigenfrequencies $\sigma/2$ of westward traveling modes when $s = 2$ [adapted from Longuet-Higgins, 1968]. The frequency number σ (the number of oscillations per day) is plotted against the eigenvalue λ for various modes. The horizontal line at $\sigma = 2$ intercepts the dispersion curves which gives the semi-diurnal eigenvalues λ_n. The leading Hough mode is marked $\otimes$.

III.5 Free Planetary Waves - The Homogeneous Solutions to the Linear Wave Equations

The linear wave theory described in the previous section is used to describe both free and forced oscillations of the atmosphere. One set of solutions to the linear wave equations (3.24-9) is the homogeneous solution in which the atmosphere undergoes free oscillations. These kinds of waves, also known as *free traveling planetary waves* or *Rossby waves*[Andrews, Leovy, Holton, 1987], can exist throughout the lower and middle atmosphere in the absence of external forcing and have been well-documented. They appear in surface pressure data [Madden, 1978], upper tropospheric radio-sonde data [Madden, Labitzke, 1979; Venne, Stanford, 1979] and in stratospheric satellite data [Rodgers, 1976; Hartmann, 1976].

The most prominent of all of the atmospheric free oscillations is the westward traveling 5-day period wave with zonal wavenumber $s = 1$. Other traveling modes have also been observed, among them are the $s = 1$, 16-day wave [Madden, 1978; Madden, Labitzke, 1981; Madden, 1983] and the $s = 3$, 2-day wave [Salby, 1981; Rodgers, Prata, 1981]. Figure 3.5.1 shows the latitude variations of the temperature perturbations from the mean state for the 5-day component determined by Rodgers (1976). There are amplitude maxima of about 0.5 K near 50° N/S. Figure 3.5.2 shows a five day component of the pressure variation as observed in the stratosphere over the surface of the earth [Hirota, Hirooka, 1984]. The patterns show the $s = 1$ character of the waves with westward traveling surfaces of constant phase. The wave structure is symmetric about the equator and has amplitude maxima near

50° N/S latitude in agreement with Rodgers (1976).

The existence of a wave with a period of 5 days and zonal wavenumber $s = 1$ in the earth's atmosphere is in agreement with the theory of free planetary modes [Salby, 1979] and is a homogeneous solution of the linear wave theory §III.4. To determine the nature of the solutions, we solve (3.57) in the absence of heating $\mathcal{H} = 0$ [Salby, 1979]

$$\frac{d^2y}{dx^2} + \left[\omega\lambda - \frac{1}{4}\right] y = 0 \tag{3.67}$$

after defining the auxiliary function

$$\omega \equiv \frac{\mathcal{N}^2}{F\Lambda^2}. \tag{3.68}$$

The homogeneous equation (3.67) is considered to be an eigenvalue problem for the parameter λ [Salby, 1979; Andrews, Leovy, Holton, 1987] subject to appropriate boundary conditions. The value(s) of λ depends on the vertical temperature structure through the function ω. The frequency number σ which corresponds to the eigenvalue λ for each given s are then computed from the dispersion relations portrayed in Figures 3.4.1-7. This method provides the frequency for the free oscillations. The latitudinal Hough functions $\Theta_n^{\sigma s}$ are then determined using the method in Appendix C. In Figure 3.5.1 the Hough function for the 5-day wave is plotted along with the observed temperature fluctuation amplitude [Rodgers, 1976] and the similarity between the peaks near 50° N/S and the minimum at the equator is striking.

A single value of eigenvalue λ for free oscillations of the atmosphere of about 8.88 was determined shown to exist for free atmospheric oscillations from the ATMOS standard temperature profile in Figure 3.5.3 by the method

described in Appendix D. The corresponding frequencies of oscillation can be determined from the graphs of the dispersion relations (see Figures 3.4.1-7). The value of the Lamb mode eigenvalue $\lambda = 8.88$ is plotted on the $s = 1$ dispersion relation in Figure 3.4.5. The point marked $\odot$ corresponds to the eigenfrequency of $\sigma = 0.099$ which corresponds to a period of about 5.1 days. Since this wave is solution to the homogeneous problem it can propogate without the need for external forcing. The 5-day wave is believed to be excited by random disturbances in the atmosphere and fluctuations of mean winds [Andrews, Leovy, Holton, 1987] and can persist for weeks at a time [Salby, 1979]. The 5-day mode as well as the other homogeneous planetary waves are 'simply the result of the hydrostatic distribution of mass in the atmosphere, the earth's rotation, and spherical geometry' [Salby, 1981].

We can study how free traveling planetary waves can influence observed wind speeds. The vertical structure equation (3.67) is homogeneous for free oscillations and its solutions are unique to a multiplicative constant. This multiplicative constant can be determined by adjusting the amplitudes of the surface pressure oscillations predicted by the theory to fit observed amplitudes. An analysis by Burpee (1976) indicates that the component of the surface pressure oscillation identified with the 5 day wave is slightly less than 1 mb near 10-20° N latitude and some of the surface pressure data in that study is shown in Figure 3.5.4. The five day oscillating component is evident in the figure. Using these observations, the amplitude of the computed pressure fluctuation from the linear wave theory §III.4 was adjusted to the experimental values to have an amplitude of 1 mb at 15° N. The fractional deviation of the pressure from the hydrostatic value (given by $P'/P_h = \epsilon F \Lambda P$

in Appendix A) as function of the number of scale heights x and μ ($= \sin\theta$, θ = latitude) is shown in Figure 3.5.5. The amplitude P'/P_h remains below 10 % until about $x = 17$ which corresponds to about 120 km altitude. The corresponding zonal wind speed u is shown in Figure 3.5.6. The zonal winds are less than 1 ms^{-1} below $x = 17$ or 120 km altitude at all latitudes for the 5-day wave.

We therefore do not expect planetary waves to significantly influence the zonal wind speeds at mesospheric heights and below and conclude that this kind of atmospheric disturbance is not likely to be responsible for the large variations in winds measured during the ATMOS mission. We must therefore look for other effects. In the next section we show that the nonhomogenous solutions to the linear wave theory §III.4 which are driven by solar heating of the atmosphere can indeed influence the circulation of the atmosphere in a significant way and is likely to be responsible for the wave-like features observed consistently with the ATMOS instrument.

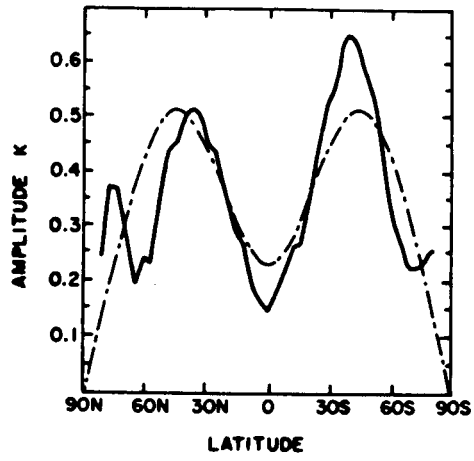

Figure 3.5.1 Solid curve: temperature amplitude of the 5-day wave as a function of latitude at about 42 km altitude for November 1973, as measured by the Selective Chopper Radiometer on the *Nimbus 5* satellite [after Rodgers, 1976]. Broken curve: latitudinal structure of the Hough function corresponding to the 5-day Rossby mode [from Andrews, Holton, Leovy, 1987].

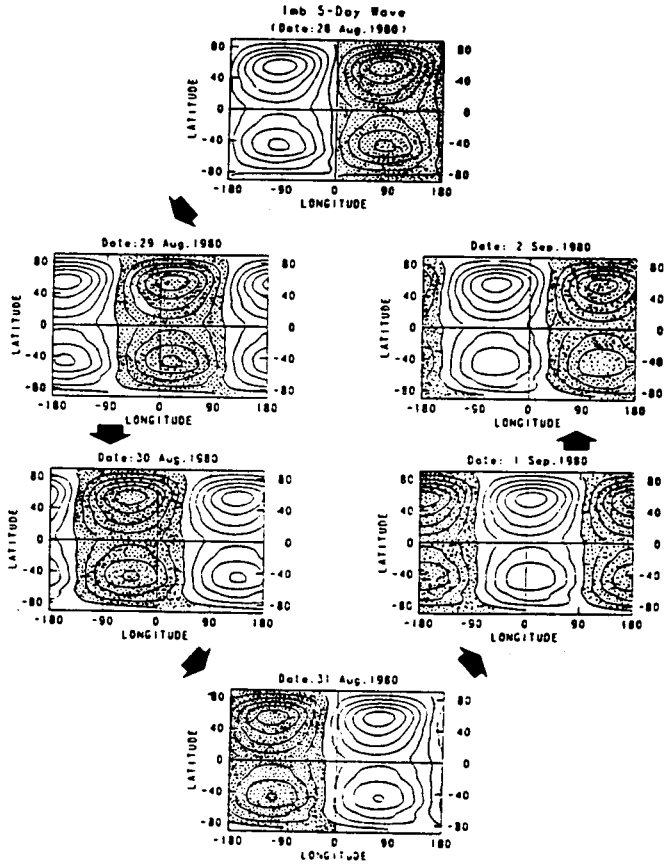

Figure 3.5.2 The 5-day wave at 1 mb or about 45 km as observed by the Stratospheric Sounding Unit on the *TIROS-N* satellite, for 6 successive days in August-September 1980 [Hirota, Hirooka, 1984]. The wave-number 1 Fourier component of the geopotential height anomaly (which can be directly related to pressure - see Houghton, 1987). The westward-travelling pattern except south of 50° S. Shaded areas denote negative anomalies; contour levels are 20 m [from Andrews, Holton, Leovy, 1987].

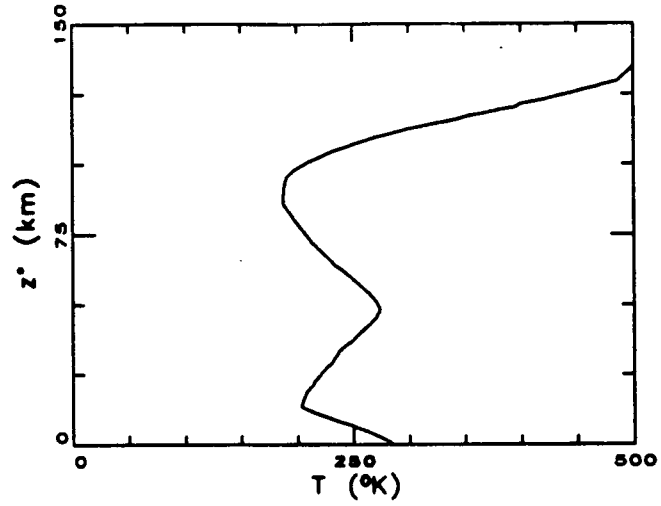

Figure 3.5.3 The ATMOS standard temperature profile used for the hydrostatic temperature background in the tidal calculations [from Norton, 1986].

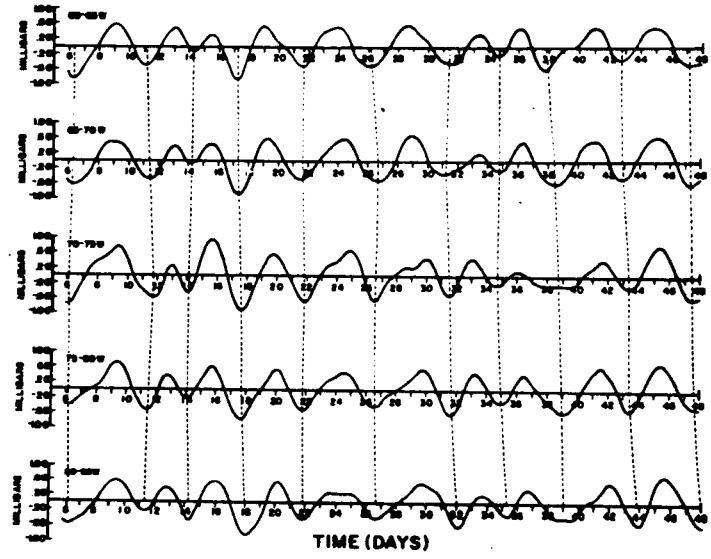

Figure 3.5.4 Time series of surface pressure averaged for groups of stations in 5° longitude bands from 10°-20° N in the Caribbean [from Burpee, 1976].

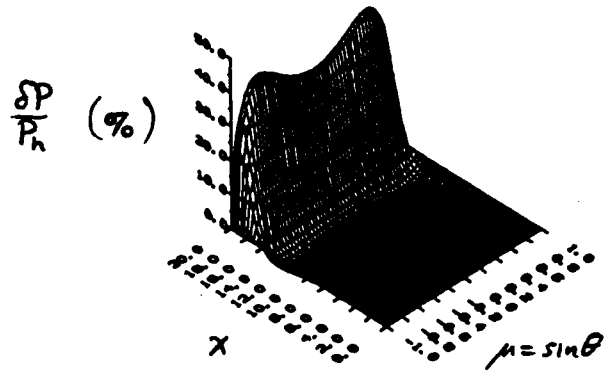

Figure 3.5.5 Fractional deviation of the pressure from the hydrostatic background pressure P_h as a function of number of scale heights x. Notice that the deviation remains below 10 % until $x \sim 14$ which corresponds to about 120 km. This type of oscillation does generate significant winds until great heights are reached (see Figure 3.5.6). Notice the two peaks at 50° N/S which agrees with the data presented in Figures 3.5.1-2.

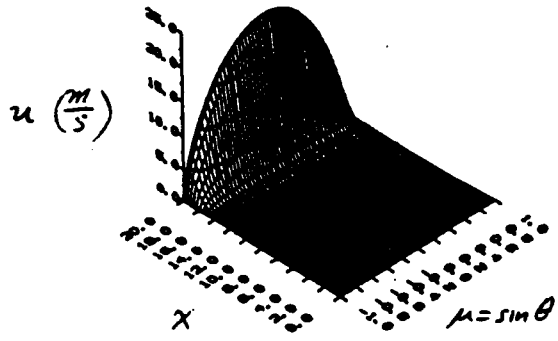

Figure 3.5.6 Computed zonal wind speeds as a fufction of number of scale heights x for the 5-day Rossby wave. Notice that the deviation remains below 5 ms^{-1} until $x \sim 18$ which corresponds to about 140 km.

III.6 Atmospheric Thermal Tides

In this section we show that forced tidal oscillations, due to the periodic heating and cooling of the atmosphere, can give rise to large perturbations of the pressure, density, temperature and velocity about the mean background state. Atmospheric thermal tides are forced global-scale daily oscillations. They are driven by the diurnally varying heating of the earth's atmosphere due to ultraviolet radiation absorption by water and ozone [Andrews, Leovy, Holton, 1987] between the surface and up to about 75 km [Chapman, Lindzen, 1970; Groves, 1982a-b].

The energy absorbed by the atmosphere is transformed into mechanical energy which is transported to great altitudes [Chapman and Lindzen, 1987]. Energy is also radiated away by infrared cooling (also known as radiative damping) primarily by the 15 μm band of CO_2, [Dickinson, 1984] which tends to restore the atmosphere to its undisturbed background temperature distribution [Chapman and Lindzen, 1970; Kato, 1980]. The first mechanism is usually incorporated into the boundary conditions of the vertical structure equation (3.57) described in Appendix D. Radiative damping is contained in the heating function $\mathcal{H}$ and its inclusion in the linear wave theory §III.4 is described in Appendix J.

The diurnal heating of the atmosphere with respect to local time can be represented by a distribution similar to Figure 3.6.1. The heating vanishes on the 'dark' side of the planet while it has a maximum near local noon and decreases to zero at local sunrise and sunset. A Fourier analysis of this distribution yields a steady component, a diurnal component (with a

24-hour period), a semidiurnal component (with a 12-hour period), and so on. In order to estimate the atmospheric response a knowledge of the Fourier components of the heating is necessary. The phase of the heating 'follows' the sun [Seibert, 1961; Chapman and Lindzen, 1970; Andrews, Leovy, Holton, 1987] and it is easily verified that the frequency number σ and the zonal number s in (3.30) are equal in this case. It can be verified that the phase of the heating and the linear response travels westward and hence the term *migrating tides* is used to describe this class of linear waves. The component $\sigma = s = 1$ is called the *diurnal tide* and the component $\sigma = s = 2$ is called the *semi-diurnal tide.* The dispersion relation for the eigenfunctions of Laplace's tidal equation are plotted for the diurnal and semi-diurnal modes in Figures 3.6.5-6 respectively.

For each tidal mode described by σ, a complete set of Hough eigenfunctions Θ_n and eigenvalues λ_n can be determined by the method in Appendix C. The corresponding vertical structure equation (3.57) can be solved and the local time, latitude and height dependence of the tidal modes can be determined §III.4 provided the Hough components of the heating term $\mathcal{H}$ are known.

In Figure 3.6.2 is shown theoretical northerly wind speeds [Lindzen, 1967] for a hydrostatic background model and rocket measurements [Reed, 1969] for the diurnal component. The amplitudes of these two sets of data are similar, however, the hours of maximum amplitude vary with altitude. The discrepancies between the phases with altitude are probably due to the neglect of mean winds, errors in the heating and perhaps atmospheric cooling in the theoretical model as pointed out by Lindzen and Hong's calculations

(1974) for the semi-diurnal components. In the lower atmosphere (below 60 km) the linear tidal theory can be used to describe wind speeds since the amplitudes of the waves are small (horizontal speeds < 10-20 ms^{-1}) and the linearization of (A.61-7) is a good approximation.

To further understand the tidal phenomena, we can calculate the solution to the linear theory using a model heating function and temperature profile. The ATMOS standard temperature profile in Figure 3.5.3 was used to model the hydrostatic background. The heating model given by Groves (1982a-b) was chosen since it includes results for diurnal and semi-diurnal heating components of both water vapor in the boundary layer and stratospheric ozone. The forcing model data describe the vertical structure of the heating $\mathcal{H}_n$ for each Hough component (see 3.55). The model also describes the heating components as function of the season. Since the ATMOS mission was flown near the vernal equinox the heating profiles corresponding to this time of the year was used. Figures 3.6.3 and 3.6.7 show the latitude and height dependences using (3.55) for the diurnal and semi-diurnal components respectively as given by the model [Groves, 1982-a-b].

The solutions to the linear theory §III.4 was applied to the diurnal and semi-diurnal modes using the heating rates by Groves (1982a-b). The calculated temerature and horizontal velocity components in Figures 3.6.4-6 and 3.6.8-10 for the diurnal and semidiurnal components respectively. These results show the exponential increase of the amplitudes of the physical fields with scale height x as described by (3.60-6). From these figures we see that above $x = 10$ or about 70 km the upper atmosphere is extremely active mechanically. Dissipative mechanisms such as molecular viscosity in the

lower thermosphere and infrared cooling by CO_2 [Dickinson, 1984] in the stratosphere and mesosphere along with non-linear wave breaking near the mesopause [Fritts, 1984] and subsequent generation of turbulence play a role in damping the amplitudes of these waves. Radiative damping using the Newtonian cooling approximation [Chapman and Lindzen, 1970; Andrews, Holton, Leovy, 1984] can be added to the linear wave theory §III.4 with little added complexity to the integration procedure (see Appendix J) and was used in my calculations. Lindzen and Hong (1974) have modeled mean winds as well as molecular viscosity and radiative damping effects in their calculations of semi-diurnal tidal perturbations and have found that velocity amplitudes reach a maximum value of about 100 ms^{-1} about 150 km.

Although the inclusion of radiative damping into the linear wave theory dampens the amplitudes by about 20 % [Chapman and Lindzen, 1970], it is not sufficient to prevent the growth of the waves with height. Other mechanisms become important. Large amplitudes of the potential temperature ϑ near 70 km [Andrews, Holton, Leovy, 1987] can cause local adiabatic instabilities since the static stability N^2 becomes negative and the local buoyancy frequency N becomes imaginary (see Appendix B). The atmosphere can then no longer support the wave and local turbulence and subsequent cascade of energy to smaller length and time scales occurs [Lindzen, 1981]. At about the same altitude where adiabatic instabilities set in, non-linearities also become significant [Andrews, Holton, Leovy, 1987]. When the horizontal velocity become of the order greater than 0.1 (in the dimensionless representation of Appendix A) or about 50 ms^{-1} then advective instabilities due to the $\mathbf{u} \cdot \nabla \mathbf{u}$ terms in the fluid equation §III.2 at wind shears become important [Wein-

stock, 1976]. The linearized approximation §III.4 which was used to compute the atmospheric response to the diurnal heating of the atmosphere is then no longer adequate for describing the dynamics.

From the results we conclude the linear theory calculations of the tidal response to diurnal atmospheric heating suggest that the zonal winds above 70 km observed during the ATMOS mission are caused primarily by the tidal waves propagating into the thermosphere. The waves in this region break due to non-linearities and static instabilities generated by tidal perturbations [Lindzen, 1981; Andrews, Holton, Leovy]. Non-linearities in the theory become important and make the problem complex and hence difficult to treat theoretically. I have currently reached this point in my study of atmospheric tides. My study of the ATMOS wind profiles is by no means completed and a more general method for incorporating the non-linear and adiabatic breaking of the tides needs to be developed.

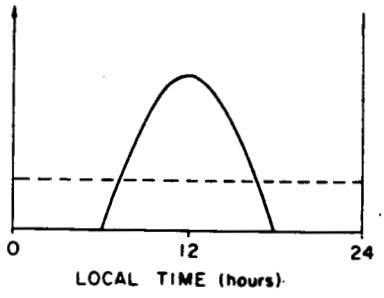

Figure 3.6.1 Variation of solar heating at a point in midlatitudes (heavy curve). The horizontal line represents the diurnal or zonal average of the heating. This is assumed to be balanced by a zonal-mean infrared cooling so that the net heating vanishes. The term H is represented by the departure of the heavy curve from the dashed curve [from Andrews, Holton, Leovy, 1987].

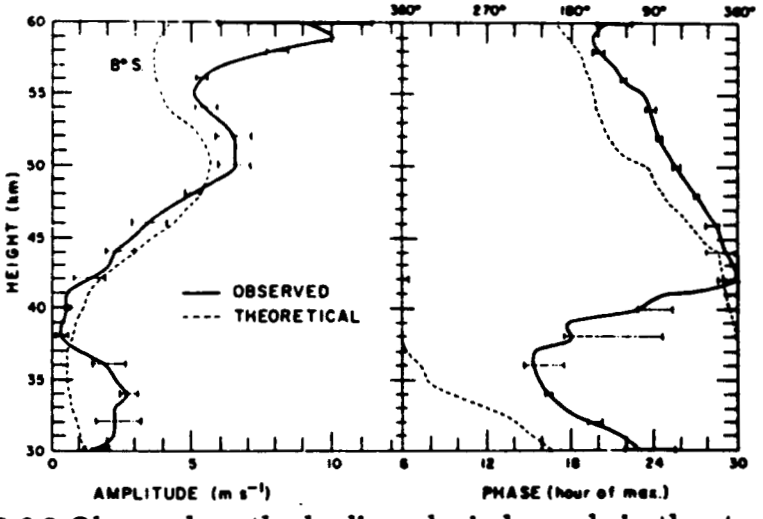

Figure 3.6.2 Observed northerly diurnal wind speeds in the stratosphere determined from rockets launched at Ascension Island (8°S) and theoretical calculations by Lindzen (1967) based on classical tidal theory [Reed, 1969].

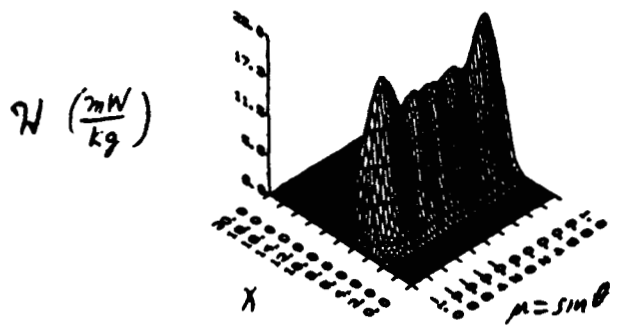

Figure 3.6.3 Diurnal heating rates per unit mass $\mathcal{H}$ as a function of scale heights x and latitude θ used as the driving term in the tidal model for equinox conditions [adapted from Groves, 1982a-b]. There is heating due of water vapor near the surface $x = 0$ and ozone in the stratosphere $4 < x < 12$.

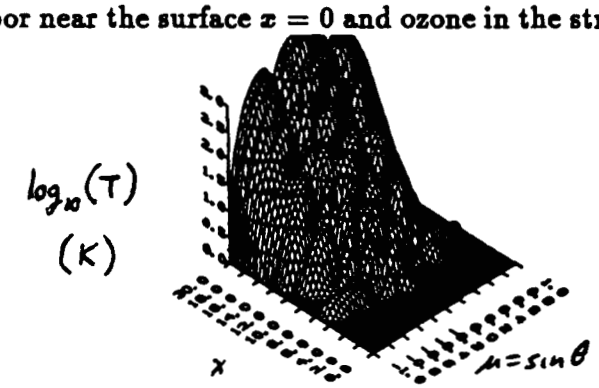

Figure 3.6.4 Amplitude of the diurnal temperature perturbation determined using the linear wave theory as a function of scale heights x and latitude θ. The exponentially increasing amplitude of the temperature perturbation with scale height x is evident.

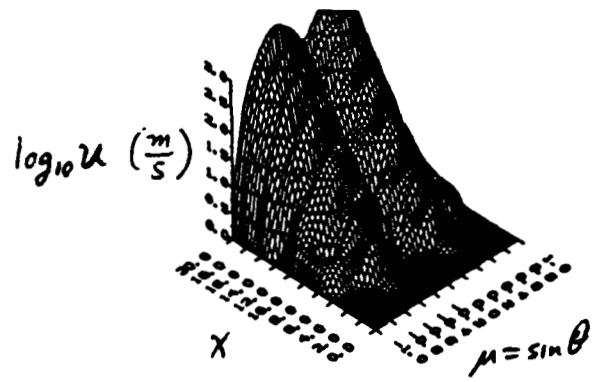

Figure 3.6.5 Amplitude of the diurnal zonal velocity perturbation determined using classical the linear wave theory as a function of scale heights x and latitude θ. This theory predicts that zonal winds can grow to great amplitudes > 100 ms^{-1} or more at mesospheric heights and propogate into the upper atmosphere. The great amplitudes determined here do not occur in the atmosphere, however, since nonlinear and adiabatic instabilities break the wave and prohibit its amplitude growth with scale height x.

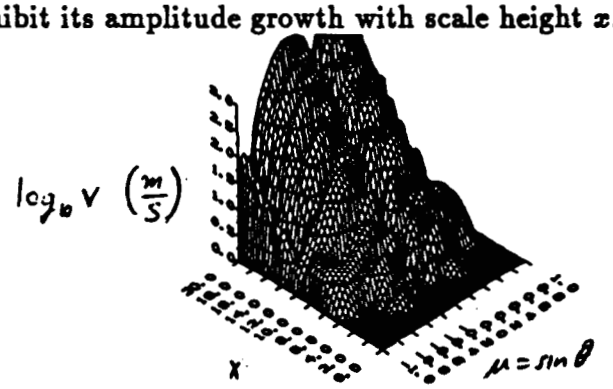

Figure 3.6.6 Amplitude of the diurnal meridonial velocity perturbation determined using classical the linear wave theory as a function of scale heights x and latitude θ.

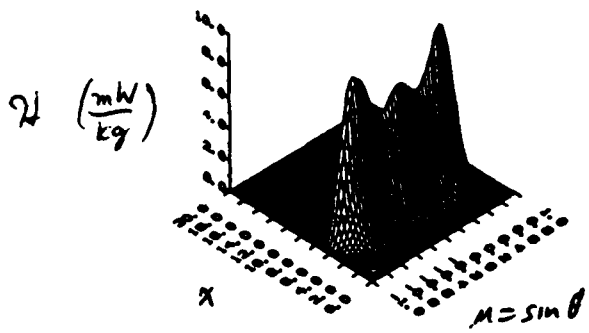

Figure 3.6.7 Semi-diurnal heating rates per unit mass $\mathcal{H}$ as a function of scale heights x and latitude θ used as the driving term in the tidal model for equinox conditions [adapted from Groves, 1982a-b]. There is heating due of water vapor near the surface $x = 0$ and ozone in the stratosphere $4 < x < 12$.

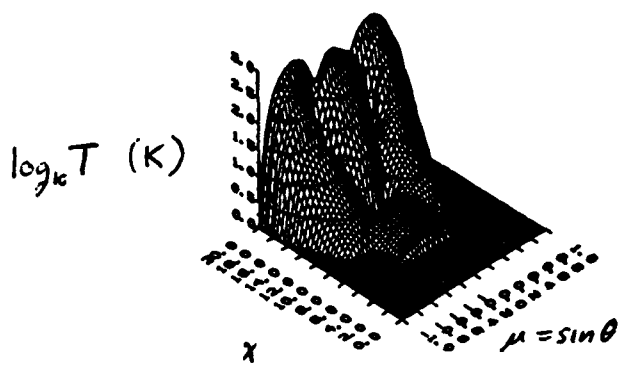

Figure 3.6.8 Amplitude of the Semi-diurnal temperature perturbation determined using the linear wave theory as a function of scale heights x and latitude θ. The exponentially increasing amplitude of the temperature perturbation with scale height x is evident.

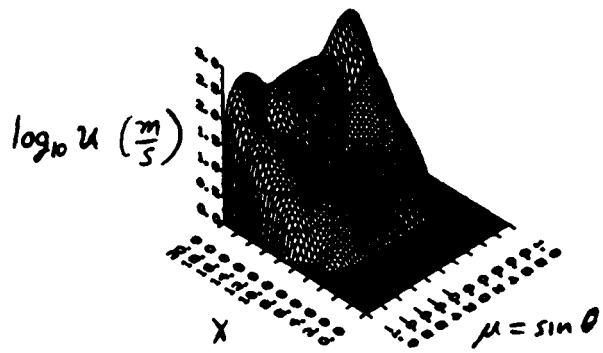

Figure 3.6.9 Amplitude of the semi-diurnal zonal velocity perturbation determined using classical the linear wave theory as a function of scale heights x and latitude θ. The semi-diurnal winds become large > 100 ms^{-1} at greater altitudes than the diurnal winds, however, the exponential growth of the wave will eventually force it to break and prohibits its amplitude growth with scale height x.

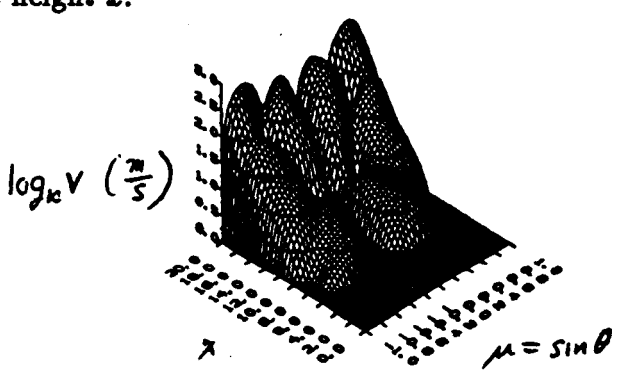

Figure 3.6.10 Amplitude of the semi-diurnal meridonial velocity perturbation determined using classical the linear wave theory as a function of scale heights x and latitude θ.

SUMMARY

I have presented many of the aspects of spectroscopy which were important for obtaining wind speeds in the upper earth's atmosphere. The primary objective was to determine whether or not such measurements were indeed possible considering the technical limitations of the ATMOS interferometer. These have been discussed in some detail, primarily as an instructive guide for future research with ATMOS or other similar instruments.

During the course of the research I have determined that the instrument is adequate for obtaining accurate wind speeds to precisions of 5 m/s. The technique described, however, is somewhat limited in its ability to obtain as much wind data as possible during the course of what may be a typical ATMOS mission due to other priorities. The lack of instrumental lines available for calibration in all but Filter 3 means that only a fraction of the total number of occultations are available to obtain wind data.

The calibration analysis indicated that the instrument was stable to better than 2×10^{-5} cm^{-1} from spectrum to spectrum and does not reveal significant fluctuations. This stability indicated that the instrument was providing consistent frequencies. Comparison between positions determined from atmospheric lines via the instrumental calibration indicated that the ATMOS data can be used to improveme accepted frequency standards, particularly those line positions where the accuracy and/or precision are not well known. The atmosphere itself provides a natural laboratory for spectroscopic measurements of trace gases, many species which are difficult to observe on

earth laboratories.

The instrumental lines which were present in the spectra indicated that the amount of CO_2 present tended to decrease in time. This information was consistent with the theory of outgassing by the instrument. The equivalent width of the H_2O lines appeared to remain relatively constantly throughout the mission. This information in addition to a Doppler shift of about +15 ms^{-1} away from the instrument suggests that the water vapor is outgassing from a source primarily external to the instrument while the CO_2 is primarily located in the instrument, since its concentration decreased with time and no Doppler shift was measured.

The winds obtained from the ATMOS spectra showed a similarity among the sunset occultations revealing consistent phase shifts and amplitudes. The source of this activity was studied from a theoretical point of view and the concept of the thermal wind and atmospheric tides was discussed. The study showed that models of the radiative transfer between the sun's radiation, ozone and water vapor drive upper atmospheric circulation in a manner which can be considered to be consistent with the results of the ATMOS experiment. The regularity of winds measured during the sunset occultation indicates that mesospheric winds might indeed be induced by the diurnal and semidiurnal tides. The theory presented was found to be inadequate in describing the detailed structure of the winds since the amplitudes of the waves predicted by the theory grow exponentially with height due to the exponential decrease of the hydrostatic background density. The presence of an adiabatic instability in the theoretical model was shown to occur at about twelve scale heights or about 85 km above the earth's surface.

The breakdown of the classical theory suggests that a more elaborate study into the nonlinear evolution of the tides at heights comparable to those studied by ATMOS is necessary. The response of the atmosphere to the heating of the ozone layer on a global scale suggests that upper atmospheric winds may contain much information regarding the latitudinal distribution of this species. A nonlinear theory of tides is probably need to better understand upper atmospheric wind patterns. The the vertical structure of atmospheric winds at each point in local time may contain information regarding the global distribution of the heating sources.

Appendix A. Scaling the Nonlinear Equations of Motion

The dynamical equations in §III.2 can be used for many meteorological problems. If we wish to use them to describe motion over an entire sphere the dynamical equations (3.7-12) are used. The horizontal length scale is assumed be of the order of the radius of the earth a while the vertical scale is of the order of 100 km. The time scale will be of the order of the rotation period. Due to the latitude dependence of the Coriolis force $\propto 2\Omega \sin\theta$, it can vary significantly over the horizontal scale.

Due to the complexity of the fluid equations in spherical coordinates it useful to introduce several changes of variables. The latitude θ can be transformed into the new coordinate

$$\mu \equiv \sin\theta \tag{A.1}$$

where $-1 < \mu < 1$. Then the derivatives

$$\frac{\partial}{\partial\theta} = \sqrt{1-\mu^2}\,\frac{\partial}{\partial\mu} \tag{A.2}$$

can be determined. It is also useful to redefine the horizontal velocity functions [Margules, 1893] as

$$u' = \sqrt{1-\mu^2}\,u, \tag{A.3}$$

$$v' = \sqrt{1-\mu^2}\,v. \tag{A.4}$$

By substituting these definitions into the total time derivative (3.12)

$$\frac{D}{Dt} = \frac{\partial}{\partial t} + w\frac{\partial}{\partial z} + \frac{1}{a}\left(v'\frac{\partial}{\partial \mu} + \frac{u'}{1-\mu^2}\frac{\partial}{\partial \phi}\right). \tag{A.5}$$

The continuity equation (3.10) becomes

$$\frac{D\rho}{Dt} + \rho\left\{\frac{\partial w}{\partial z} + \frac{2w}{a} + \frac{1}{a}\left(\frac{\partial v'}{\partial \mu} + \frac{1}{1-\mu^2}\frac{\partial u'}{\partial \phi}\right)\right\} = 0 \tag{A.6}$$

and the horizontal momentum equations (3.7-8) are

$$\frac{Du'}{Dt} + \frac{wu'}{a} - 2\Omega\mu\, v' + 2\Omega\mu\sqrt{1-\mu^2}\, w = -\frac{1}{\rho a}\frac{\partial P}{\partial \phi} + \sqrt{1-\mu^2}\,\frac{\mathcal{F}_\phi}{\rho}, \tag{A.7}$$

$$\frac{Dv'}{Dt} + \frac{wv'}{a} + \frac{1}{a}\frac{\mu}{1-\mu^2}\left(u'^2 + v'^2\right) + 2\Omega\mu\, u' = -\frac{1}{\rho a}(1-\mu^2)\frac{\partial P}{\partial \mu} + \sqrt{1-\mu^2}\,\frac{\mathcal{F}_\theta}{\rho}. \tag{A.8}$$

The vertical momentum equation (3.9) is

$$\frac{Dw}{Dt} - \frac{1}{a}\frac{1}{1-\mu^2}\left(u'^2 + v'^2\right) - 2\Omega u' = -\frac{1}{\rho}\frac{\partial P}{\partial z} - g + \frac{\mathcal{F}_r}{\rho}. \tag{A.9}$$

We now wish to examine dynamics on the scales appropriate for global scale disturbances. Atmospheric oscillations can be classified by the time scale and horizontal distance scale over which the motions vary. In the case of planetary and tidal waves, the characteristic horizontal distance is of the order of the radius of the earth a. Since the horizontal extent of these kind of atmospheric disturbances is as large as it is, the Coriolis acceleration will vary significantly over the range of latitudes in which these kinds of global disturbances propagate.

The problem is mathematically manageable by following a scaling technique similar to Pedlosky (1987). It is useful to introduce a change in notation. Dynamical fields will be represented in both dimensioned and non-dimensioned form, a " • " superfix representing the dimensional form. For

"Page missing from available version"

Here, u', v', w, z, and t are dimensionless variables. The condition that the dimensionless velocities are much less than $\mathcal{O}(1)$ will be used in many of the arguments. The r^* and t^* derivatives become

$$\frac{\partial}{\partial t^*} = \frac{U}{a}\frac{\partial}{\partial t} = \Omega\frac{\partial}{\partial t}, \tag{A.12}$$

$$\frac{\partial}{\partial r^*} = \frac{\partial}{\partial z^*} = \frac{1}{D}\frac{\partial}{\partial z}. \tag{A.13}$$

The total time derivative D/Dt^* scales as

$$\frac{D}{Dt^*} = \Omega\frac{D}{Dt} = \left(\frac{U}{a}\right)\frac{D}{Dt} \tag{A.14}$$

where

$$\frac{D}{Dt} \equiv \frac{\partial}{\partial t} + w\frac{\partial}{\partial z} + v'\frac{\partial}{\partial \mu} + \frac{u'}{1-\mu^2}\frac{\partial}{\partial \phi} \tag{A.15}$$

in terms of the dimensionless variables.

The dynamics are superimposed on a *hydrostatic* background state. Let the pressure $P_h(z)$ and density $\rho_h(z)$ represent this "standard" hydrostatic state and further assume that they depend on z^* alone. Since we are interested in the magnitudes of the variables the neglect of horizontal temperature gradients is unimportant in the scaling transformations. The hydrostatic condition requires that

$$\frac{dP_h}{dz^*} = -\rho_h g. \tag{A.16}$$

Let the background be characterized by a temperature $T_h(z)$ and a constant mean molecular weight $\bar{M}$. The background pressure and density are related by the ideal gas law (3.4) as

$$P_h(z) = \frac{\rho_h(z) R T_h(z)}{\bar{M}}. \tag{A.17}$$

Defining the *scale height* as

$$H(z) \equiv \frac{RT_{\rm h}(z)}{\bar{M}g} \tag{A.18}$$

then

$$P_{\rm h} = \rho_{\rm h} g H. \tag{A.19}$$

The hydrostatic condition (A.16) can then be written

$$\frac{dP_{\rm h}}{dz^*} = -\rho_{\rm h} g = -\frac{P_{\rm h}}{H}. \tag{A.20}$$

Integrating this equation gives the background pressure field in terms of the surface value $P_{\rm h}(0)$ and the scale height $H(z^*)$

$$P_{\rm h}(z^*) = P_{\rm h}(0) e^{-\int_0^{z^*} d\zeta^*/H(\zeta^*)}. \tag{A.21}$$

It is useful to introduce a dimensionless inverse scale height by

$$\Lambda(z) \equiv \frac{D}{H(z)}. \tag{A.22}$$

The hydrostatic pressure is then

$$P_{\rm h}(z) = P_{\rm h}(0) e^{-\int_0^z d\zeta\, \Lambda(\zeta)} \tag{A.23}$$

in dimensionless units. By using the ideal gas law the hydrostatic density becomes

$$\rho_{\rm h}(z) = \frac{P_{\rm h}(0)}{gD} \Lambda(z) e^{-\int_0^z d\zeta\, \Lambda(\zeta)}. \tag{A.24}$$

The pressure P^* and density ρ^* must now be scaled appropriately and the quasi-geostrophic scaling given by Pedlosky (1987) is useful. In this scaling

we define the total pressure and density as the sum of the hydrostatic value and a departure from this value given by "prime" notation

$$P^* = P_h(z) + P'(z,\theta,\phi,t), \tag{A.25}$$

$$\rho^* = \rho_h(z) + \rho'(z,\theta,\phi,t). \tag{A.26}$$

The condition of quasi-geostrophic balance requires that the horizontal pressure gradients should be of the same order of magnitude of the Coriolis force. This can be written as

$$\rho^* 2\Omega u^* = \mathcal{O}(2\Omega U \rho_h), \tag{A.27}$$

and this should be of the order P'/a. Then, $P' = \mathcal{O}(2\Omega U a \rho_h)$. So the natural scaling for P^* is

$$P^* = P_h + \rho_h \cdot 2\Omega U a P \tag{A.28}$$

where P is dimensionless. To scale the density the vertical pressure gradient associated with P' is

$$\frac{\partial P'}{\partial z^*} = \mathcal{O}\left(\frac{P'}{D}\right) = \mathcal{O}\left(\frac{2\Omega U a \rho_h}{D}\right) = \mathcal{O}\left(\rho' g\right). \tag{A.29}$$

This suggests that ρ' be scaled as

$$\rho' = \mathcal{O}\left(\frac{2\Omega U a \rho_h}{gD}\right).$$

Therefore we write

$$\rho^* = \rho_h \left(1 + \frac{2\Omega U a}{gD}\rho\right). \tag{A.30}$$

By defining the *Rossby number*

$$\epsilon \equiv \frac{U}{2\Omega a}, \tag{A.31}$$

which is $1/2$ since $U = \Omega a$ using this particular scaling, and by defining the parameter

$$F \equiv \frac{(2\Omega a)^2}{gD}, \tag{A.32}$$

the pressure and density can be written by using the hydrostatic condition (A.19) and (A.22) as

$$P^* = P_h(1 + \epsilon F \Lambda P), \tag{A.33}$$

$$\rho^* = \rho_h(1 + \epsilon F \rho). \tag{A.34}$$

With the scaling parameters used above $F \approx 0.9$.

By using these scaling laws the continuity equation (A.6) can be determined in terms of these dimensionless variables and the hydrostatic condition to be

$$\epsilon F \frac{D\rho}{Dt} + (1+\epsilon F\rho)\left\{\frac{1}{\rho_h}\frac{\partial}{\partial z}(\rho_h w) + 2\Delta w + \left(\frac{\partial v'}{\partial \mu} + \frac{1}{1-\mu^2}\frac{\partial u'}{\partial \phi}\right)\right\} = 0. \tag{A.35}$$

The horizontal momentum equations (A.7-8) become

$$\epsilon\left\{\frac{Du'}{Dt} + \Delta w u'\right\} - \mu v' + \Delta\mu\sqrt{1-\mu^2}\, w = -\frac{1}{1+\epsilon F\rho}\frac{\partial P}{\partial \phi} + \sqrt{1-\mu^2}\,\frac{\mathcal{F}_\phi^*}{2\Omega U \rho^*}, \tag{A.36}$$

$$\epsilon\left\{\frac{Dv'}{Dt} + \Delta w v' + \frac{\mu}{1-\mu^2}\left(u'^2 + v'^2\right)\right\} + \mu u' = -\frac{1}{1+\epsilon F\rho}(1-\mu^2)\frac{\partial P}{\partial \mu} + \sqrt{1-\mu^2}\,\frac{\mathcal{F}_\theta^*}{2\Omega U \rho^*}. \tag{A.37}$$

The vertical momentum equation (A.9) is

$$(1+\epsilon F\rho)\left\{\epsilon\Delta^2\frac{Dw}{Dt} - \epsilon\Delta\frac{1}{1-\mu^2}\left(u'^2 + v'^2\right) - \Delta u'\right\} = \Lambda P - \frac{1}{\Lambda}\frac{\partial}{\partial z}(\Lambda P) - \rho$$

$$+\frac{\Delta\mathcal{F}_r^*}{2\Omega U\rho_h}. \tag{A.38}$$

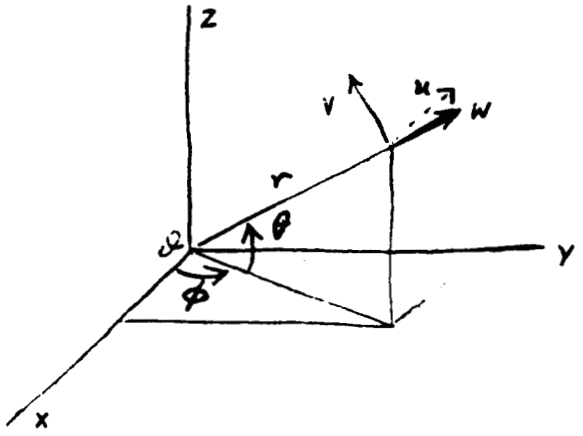

Figure A.1 Spherical coordinate system.

Equations (A.35-8) represent the continuity and momentum equations respectively. However, the system of equations cannot be solved without the thermodynamic relationship (3.11). This equation must be scaled in an appropriate manner consistent with (A.35-8). From (3.6) we have

$$\vartheta^* = \frac{MP_h(0)}{R\rho^*}\left(\frac{P^*}{P_h(0)}\right)^{\frac{1}{\gamma}}. \tag{A.39}$$

Then

$$\begin{aligned}\ln\vartheta^* &= \frac{1}{\gamma}\ln\left[\frac{P_h}{P_h(0)}(1+\epsilon F\Lambda P)\right] - \ln\left[\frac{R\rho_h}{MP_h(0)}(1+\epsilon F\rho)\right] \\ &= \ln\vartheta_h + \frac{1}{\gamma}\ln(1+\epsilon F\Lambda P) - \ln(1+\epsilon F\rho)\end{aligned}$$

$$\simeq \ln \vartheta_{\rm h} + \frac{1}{\gamma}\epsilon F \Lambda P - \epsilon F \rho$$

$$\simeq \ln \vartheta_{\rm h} + \ln\left(1 + \frac{1}{\gamma}\epsilon F \Lambda P - \epsilon F \rho\right). \tag{A.40}$$

By using the approximation $\ln(1+y) \simeq y$ we have

$$\vartheta^* = \vartheta_{\rm h}\left(1 + \frac{1}{\gamma}\epsilon F \Lambda P - \epsilon F \rho\right). \tag{A.41}$$

The fractional change of the potential temperature is

$$\frac{\delta\vartheta^*}{\vartheta_{\rm h}} = \epsilon F\left(\frac{1}{\gamma}\Lambda P - \rho\right). \tag{A.42}$$

If we define the dimensionless potential temperature perturbation

$$\vartheta \equiv \frac{1}{\gamma}\Lambda P - \rho \tag{A.43}$$

then the local potential temperature (A.41) becomes

$$\vartheta^* = \vartheta_{\rm h}(1 + \epsilon F \vartheta). \tag{A.44}$$

The buoyancy frequency, described in Appendix B, of the hydrostatic state can also be defined by

$$N_{\rm h}^2 \equiv \frac{g}{\vartheta_{\rm h}}\frac{d\vartheta_{\rm h}}{dz^*} \tag{A.45}$$

where the hydrostatic potential temperature is defined by using (3.6)

$$\vartheta_{\rm h} = \frac{M P_{\rm h}(0)}{\rho_{\rm h} R}\left(\frac{P_{\rm h}}{P_{\rm h}(0)}\right)^{1/\gamma}. \tag{A.46}$$

By combining the hydrostatic condition (A.19), (A.22) and the relationship

$$\frac{1}{\rho_{\rm h}}\frac{d\rho_{\rm h}}{dz^*} = -\frac{1}{D}\left(\Lambda - \frac{1}{\Lambda}\frac{d\Lambda}{dz}\right) \tag{A.47}$$

with (A.46) we obtain

$$N_h^2 = \frac{g}{D}\left(\kappa\Lambda - \frac{1}{\Lambda}\frac{d\Lambda}{dz}\right). \tag{A.48}$$

It is also useful to define dimensionless hydrostatic buoyancy term

$$\mathcal{N}^2 \equiv \kappa\Lambda - \frac{1}{\Lambda}\frac{d\Lambda}{dz} \tag{A.49}$$

so that

$$N_h^2 = \frac{g}{D}\mathcal{N}^2. \tag{A.50}$$

This relationship can be substituted into (3.11) and using the scaling laws in the previous two sections it can be shown that

$$\epsilon F\frac{D\vartheta}{Dt} + (1+\epsilon F\vartheta)\,\mathcal{N}^2 w = (1+\epsilon F\theta)\frac{\kappa\Lambda\mathcal{H}^*}{gD\Omega}. \tag{A.51}$$

If we define the dimensionless heating rate per unit mass

$$\mathcal{H} \equiv \frac{\kappa\Lambda\mathcal{H}^*}{gD\Omega} \tag{A.52}$$

and use the relationship (A.43) the thermodynamic relationship can be expressed in the form

$$\epsilon F\frac{D\vartheta}{Dt} + (1+\epsilon F\theta)\mathcal{N}^2\, w = (1+\epsilon F\vartheta)\mathcal{H}. \tag{A.53}$$

The fluid equations can be expressed in a still more fundamental form by a transformation of the vertical coordinate

$$x = \int_0^z d\zeta\ \Lambda(\zeta). \tag{A.54}$$

Then

$$\frac{\partial}{\partial z} = \frac{dx}{dz}\frac{\partial}{\partial x} = \Lambda\frac{\partial}{\partial x}. \tag{A.55}$$

This vertical coordinate allows us to express the hydrostatic background pressure (A.23) as

$$P_{\rm h}(x) = P_{\rm h}(0)\, e^{-x}. \tag{A.56}$$

The hydrostatic density (A.24) becomes

$$\rho_{\rm h}(x) = \frac{P_{\rm h}(0)}{gD}\Lambda(x)\, e^{-x}. \tag{A.57}$$

The hydrostatic condition is then

$$\frac{dP_{\rm h}}{dx} = -P_{\rm h}, \tag{A.58}$$

(A.47) becomes

$$\frac{\Lambda}{\rho_{\rm h}}\frac{d\rho_{\rm h}}{dx} = -\left(\Lambda - \frac{d\Lambda}{dx}\right), \tag{A.59}$$

and the dimensionless hydrostatic buoyancy frequency (A.49) is

$$\mathcal{N}^2 = \kappa\Lambda - \frac{d\Lambda}{dx}. \tag{A.60}$$

The dimensionless total time derivative (A.15) is

$$\frac{D}{Dt} = \frac{\partial}{\partial t} + \Lambda w\frac{\partial}{\partial x} + v'\frac{\partial}{\partial \mu} + \frac{u'}{1-\mu^2}\frac{\partial}{\partial \phi}. \tag{A.61}$$

We now have showed how the five dynamical equations behave under these scaling transformations. Since the scaling parameter $\Delta = D/a \sim 1/64$ is very small, terms involving it can be ignored to a first approximation. By ignoring terms of order Δ as well as frictional terms, the five non-linear equations (A.35-8, 51) become

$$\epsilon F\frac{D\rho}{Dt} + (1+\epsilon F\rho)\left\{\Lambda\frac{\partial w}{\partial x} - \left(\Lambda - \frac{d\Lambda}{dx}\right) w + \frac{\partial v'}{\partial \mu} + \frac{1}{1-\mu^2}\frac{\partial u'}{\partial \phi}\right\} = 0, \tag{A.62}$$

$$\epsilon\frac{Du'}{Dt} - \mu v' = -\frac{1}{1+\epsilon F\rho}\frac{\partial P}{\partial \phi}, \tag{A.63}$$

$$\epsilon\left\{\frac{Dv'}{Dt} + \frac{\mu}{1-\mu^2}\left(u'^2 + v'^2\right)\right\} + \mu u' = -\frac{1}{1+\epsilon F\rho}(1-\mu^2)\frac{\partial P}{\partial \mu}, \tag{A.64}$$

$$\Lambda P - \frac{\partial}{\partial x}(\Lambda P) - \rho = 0, \tag{A.65}$$

$$\epsilon F\frac{D\vartheta}{Dt} + (1+\epsilon F\theta)\,\mathcal{N}^2 w = (1+\epsilon F\theta)\,\mathcal{H} \tag{A.66}$$

respectively. These five equations, along with (A.43)

$$\vartheta \equiv \frac{1}{\gamma}\Lambda P - \rho \tag{A.67}$$

are the nonlinear equation which describe global scale disturbances.

Appendix B. The Atmospheric Buoyancy Frequency

The hydrostatic background temperature can sustain periodic free buoyancy oscillations, also known as 'gravity waves' [Houghton, 1986; Pedlosky, 1987]. Consider a fluid element A at the height z_A and another B at z_B where $z_B = z_A + dz$. Suppose the fluid element A is displaced upwards to the level z_B occupied by B. Let the displacement of fluid element A over the distance dz be slow enough that the pressure of the fluid element A continuously adjusts to its surrounding but rapid enough so that thermal dissipation and external heating of the fluid element is negligible. The fluid element is then undergoing an adiabatic displacement. Mathematically it can be stated that the potential temperature of the fluid element is preserved during the displacement. We can say that

$$d\vartheta = 0 \tag{B.1}$$

following the fluid element. From (3.23) this means that

$$\frac{1}{\gamma P} dP = \frac{1}{\rho} d\rho. \tag{B.2}$$

The change in density of the element A can then be determined

$$d\rho_A = \left(\frac{\partial \rho}{\partial z}\right)_{\text{adiabatic}} dz = \frac{1}{\gamma} \frac{\rho}{P} \frac{\partial P}{\partial z} dz. \tag{B.3}$$

Now the density of the fluid element B is

$$\rho_B = \rho_A + \left(\frac{\partial \rho}{\partial z}\right) dz. \tag{B.4}$$

The difference in density of the displaced fluid elements A and the background fluid elements B is

$$(\rho_A + d\rho_A) - \rho_B = \left(\frac{1}{\gamma}\frac{\rho}{P}\frac{\partial P}{\partial z} - \frac{\partial \rho}{\partial z}\right) dz. \tag{B.5}$$

The restoring force per unit mass caused by this density fluctuation is

$$\begin{aligned} \frac{g}{\rho}(\rho_A + d\rho_A - \rho_B) &= g\left(\frac{1}{\gamma P}\frac{\partial P}{\partial z} - \frac{1}{\rho}\frac{\partial \rho}{\partial z}\right) dz \\ &= \frac{g}{\vartheta}\frac{\partial \vartheta}{\partial z} dz. \end{aligned} \tag{B.6}$$

Since the restoring force is proportional to the displacement an oscillation with frequency N is implied

$$N^2 = \frac{g}{\vartheta}\frac{\partial \vartheta}{\partial z}. \tag{B.7}$$

N is called the Brunt-Väisälä frequency, also known as the buoyancy or gravity wave frequency, and represents the natural frequency of vertical oscillation in a density stratified fluid. If $N^2 > 0$ the atmosphere oscillates vertically about an equilibrium state and the atmosphere is adiabatically stable. However, if $N^2 < 0$ the displacements of the fluid elements continue to grow and the atmosphere is unstable.

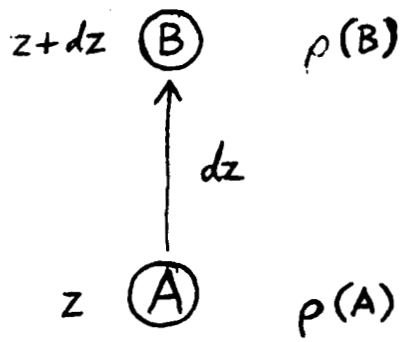

Figure 3.4.1 Fluid element A at z^* is slowly raised to $z^* + dz^*$.

Appendix C. Method for Determining the Eigenfunctions $\Theta_n^{\sigma s}(\mu)$

To determine the eigenfunctions of Laplace's tidal equation a decomposition described by Longuett-Higgins (1968) and Moura (1976) was found to be particularly useful for computational purposes. The streamline approach described by [Longuett-Higgins 1968; Moura, 1976] was found to be useful in determining the atmospheric tidal eigenfunctions and the implementation of this method is reviewed in this appendix.

For convenience, we define the differential operator

$$\mathcal{D} \equiv \left(1-\mu^2\right)\frac{d}{d\mu}. \tag{C.1}$$

Then (3.124-5) are written as the pair of equations

$$if u' - \mu v' = -isP, \tag{C.2}$$

$$if v' + \mu u' = -\mathcal{D}P. \tag{C.3}$$

Since

$$\begin{aligned} P &= \sum_n P_n \Theta_n, \\ u' &= \sum_n P_n U_n', \\ v' &= \sum_n i P_n V_n', \end{aligned} \tag{C.4}$$

and by omitting the σ, s superscripts since they are understood at this point of the development, then it can easily be shown that for each mode n

$$fU' - \mu V' = -s\Theta, \tag{C.5}$$

$$fV' - \mu U' = \mathcal{D}\Theta. \tag{C.6}$$

By taking

$$\frac{d}{d\mu}(\text{C.5}) + \frac{s}{1-\mu^2}(\text{C.6})$$

we get the relation

$$f\left(\frac{dU'}{d\mu} + \frac{s}{1-\mu^2}V'\right) - \mu\left(\frac{dV'}{d\mu} + \frac{s}{1-\mu^2}U'\right) - V' = 0. \tag{C.7}$$

By taking

$$\frac{d}{d\mu}(\text{A.6}) + \frac{s}{1-\mu^2}(\text{A.5})$$

we also find

$$f\left(\frac{dV'}{d\mu} + \frac{s}{1-\mu^2}U'\right) - \mu\left(\frac{dU'}{d\mu} + \frac{s}{1-\mu^2}V'\right) - U' = \nabla^2\Theta \tag{C.8}$$

after defining the horizontal Laplacian

$$\nabla^2 \equiv \frac{d}{d\mu}\left(1-\mu^2\right)\frac{d}{d\mu} - \frac{s^2}{1-\mu^2}. \tag{C.9}$$

At this point it is useful to introduce the velocity potential Φ and stream function Ψ [Longuett-Higgins, 1968] by the transformations

$$U' = -\mathcal{D}\Psi + s\Phi, \tag{C.10}$$

$$V' = -\mathcal{D}\Phi + s\Psi. \tag{C.11}$$

Substituting these transformations into (C.7) and (C.8) we obtain the pair of equations

$$\left(f\nabla^2 + s\right)\Psi - \left(\mu\nabla^2 + \mathcal{D}\right)\Phi = 0, \tag{C.12}$$

$$\left(f\nabla^2 + s\right)\Phi - \left(\mu\nabla^2 + \mathcal{D}\right)\Psi = -\nabla^2\Theta. \tag{C.13}$$

At this point we have two equations for the three unknown functions Φ, Ψ, and Θ. By using the expansions (C.4) and Laplace's tidal equation (3.149) in (3.129) it can be shown that

$$\frac{dV'}{d\mu} + \frac{s}{1-\mu^2}U' = -\lambda f \Theta \tag{C.14}$$

where it is understood that λ is the eigenvalue. However, by using the transformations (C.10-1)

$$\frac{dV'}{d\mu} + \frac{s}{1-\mu^2}U' = -\nabla^2\Phi. \tag{C.15}$$

Therefore

$$\nabla^2\Phi = \lambda f \Theta \tag{C.16}$$

and

$$\nabla^2\Theta = \frac{1}{\lambda f}\nabla^4\Phi. \tag{C.17}$$

When this is substituted into (C.13) we find

$$\left(\frac{1}{\lambda f}\nabla^4 + f\nabla^2 + s\right)\Phi - \left(\mu\nabla^2 + \mathcal{D}\right)\Psi = 0. \tag{C.18}$$

This equation together with (C.12) constitutes the eigenvalue problem and is equivalent to solving the eigenvalue problem (3.149).

In order to solve the system of differential equations (C.12) and (C.18) we expand the functions Φ and Ψ over an orthogonal set. The "standard" representation of the associated Legendre functions P_m^s satisfy the eigenvalue problem

$$\nabla^2 P_m^s = -m(m+1)P_m^s. \tag{C.19}$$

The "standard" representation is normalized as

$$\int_{-1}^{1} d\mu\, P_m^s P_{m'}^s = \frac{2}{2m+1}\frac{(m+s)!}{(m-s)!}\delta_{mm'} \tag{C.20}$$

and satisfies the recursion relations

$$\mu P_m^s = \frac{m+s}{2m+1} P_{m-1}^s + \frac{m-s+1}{2m+1} P_{m+1}^s, \tag{C.21}$$

$$\mathcal{D} P_m^s = \frac{(m+1)(m+s)}{2m+1} P_{m-1}^s - \frac{m(m-s+1)}{2m+1} P_{m+1}^s. \tag{C.22}$$

It can be shown from these recursion relations that

$$\left(\mu\nabla^2 + \mathcal{D}\right) P_m^s = -\frac{(m-1)(m+1)(m+s)}{2m+1} P_{m-1}^s - \frac{m(m+2)(m-s+1)}{2m+1} P_{m+1}^s. \tag{C.23}$$

We use the expansions

$$\Phi = \sum_{m \geq s} \Phi_m P_m^s, \tag{C.24}$$

$$\Psi = \sum_{m \geq s} \Psi_m P_m^s. \tag{C.25}$$

With this representation and the above recursion relations then after a series of algebraic manipulations that (C.12) and (C.18) become the system of equations

$$L_m \Psi_m + p_{m+1} \Phi_{m+1} + q_{m-1} \Phi_{m-1} = 0, \tag{C.26}$$

$$\left[-\frac{1}{\lambda} + L_m\right] \Phi_m + p_{m+1} \Psi_{m+1} + q_{m-1} \Psi_{m-1} = 0 \tag{C.27}$$

where

$$L_m = \frac{f^2}{m(m+1)} - \frac{fs}{m^2(m+1)^2}, \tag{C.28}$$

$$p_m = -\frac{f(m+1)(m+s)}{(m-1)m^2(2m+1)}, \tag{C.29}$$

$$q_m = -\frac{fm(m-s+1)}{(m+1)^2(m+2)(2m+1)}. \tag{C.30}$$

Solving for Ψ_m in (C.26) and substituting into (C.27) we get the equation

$$-\frac{1}{\lambda}\Phi_m - R_m\Phi_m - P_{m+2}\Phi_{m+2} - Q_{m-2}\Phi_{m-2} = 0 \qquad \text{(C.31)}$$

where the auxiliary symbols

$$R_m = -\left(L_m - \frac{p_{m+1}q_m}{L_{m+1}} - \frac{p_m q_{m-1}}{L_{m-1}}\right), \qquad \text{(C.32)}$$

$$Q_m = \frac{q_m q_{m+1}}{L_{m+1}}, \qquad \text{(C.33)}$$

$$P_m = \frac{p_m p_{m-1}}{L_{m-1}} \qquad \text{(C.34)}$$

are used. Then (C.31) becomes two sets of equations

$$\left[\left(-\frac{1}{\lambda}\right)\mathcal{I} - \begin{pmatrix} R_s & P_{s+2} & 0 & 0 & \\ Q_s & R_{s+2} & P_{s+4} & 0 & \cdots \\ 0 & Q_{s+2} & R_{s+4} & P_{s+6} & \\ 0 & 0 & Q_{s+4} & R_{s+6} & \\ & \vdots & & & \ddots \end{pmatrix}\right]\begin{pmatrix} \Phi_s \\ \Phi_{s+2} \\ \Phi_{s+4} \\ \Phi_{s+6} \\ \vdots \end{pmatrix} = 0, \qquad \text{(C.35)}$$

$$\left[\left(-\frac{1}{\lambda}\right)\mathcal{I} - \begin{pmatrix} R_{s+1} & P_{s+3} & 0 & 0 & \\ Q_{s+1} & R_{s+3} & P_{s+5} & 0 & \cdots \\ 0 & Q_{s+3} & R_{s+5} & P_{s+7} & \\ 0 & 0 & Q_{s+5} & R_{s+7} & \\ & \vdots & & & \ddots \end{pmatrix}\right]\begin{pmatrix} \Phi_{s+1} \\ \Phi_{s+3} \\ \Phi_{s+5} \\ \Phi_{s+7} \\ \vdots \end{pmatrix} = 0 \qquad \text{(C.36)}$$

for the symmetric and anti-symmetric solutions respectively. If a $\pm$ superscript denotes these two classes of solutions. Then (C.35-6) can be written as

$$\left[\epsilon^{\pm}\mathcal{I} - \mathcal{A}^{\pm}\right]\Phi^{\pm} = 0. \qquad \text{(C.37)}$$

This is an eigenvalue problem where $\lambda^{\pm} = -1/\epsilon^{\pm}$ and $\mathcal{A}^{\pm}$ is the matrix in brackets. The eigenvectors $\Phi^{\pm}$ are the expansion coefficients in terms of the standard representation of the associated Legendre functions. However, in the form (C.35-6) the matrix $\mathcal{A}^{\pm}$ is not symmetric. Therefore the eigenvectors will not be orthogonal. This is due to non-normalized form of the standard representation P_m^s. From (C.16) and by using an expansion

$$\Theta = \sum_{m \geq s} \Theta_m P_m^s \tag{C.38}$$

and by using (C.19) we have

$$\Theta_m^{\pm} = -\frac{m(m+1)}{\lambda^{\pm} f} \Phi_m^{\pm}. \tag{C.39}$$

This can be written more compactly in matrix form as

$$\Theta^{\pm} = -\frac{1}{\lambda^{\pm} f} \mathcal{M}^{\pm} \Phi^{\pm} \tag{C.40}$$

where $\mathcal{M}^{\pm}$ are the diagonal matrices

$$\mathcal{M}^{+} = \begin{pmatrix} M_s & 0 & 0 & \\ 0 & M_{s+2} & 0 & \cdots \\ 0 & 0 & M_{s+4} & \\ & \vdots & & \ddots \end{pmatrix}, \tag{C.41}$$

$$\mathcal{M}^{-} = \begin{pmatrix} M_{s+1} & 0 & 0 & \\ 0 & M_{s+3} & 0 & \cdots \\ 0 & 0 & M_{s+5} & \\ & \vdots & & \ddots \end{pmatrix}, \tag{C.42}$$

and the matrix elements are given by

$$M_m = m(m+1).$$

Then (C.37) can be transformed into

$$\left[\epsilon^{\pm}\mathcal{I} - \mathcal{M}^{\pm}\mathcal{A}^{\pm}\mathcal{M}^{\pm -1}\right]\Theta^{\pm} = 0. \tag{C.43}$$

In this form the matrix is still not symmetric because the standard representation is not normalized. Define the "normalized representation" $\bar{P}_m^s$ by

$$\bar{P}_m^s = \sqrt{\frac{2m+1}{2}\frac{(m-s)!}{(m+s)!}}\,P_m^s. \tag{C.44}$$

From (C.20) it is trivial to show that

$$\int_{-1}^{1} d\mu\, \bar{P}_m^s \bar{P}_{m'}^s = \delta_{mm'}. \tag{C.45}$$

The eigenfunctions Θ can also be expanded upon these

$$\Theta = \sum_{m \geq s} \bar{\Theta}_m \bar{P}_m^s \tag{C.46}$$

where the overbar refers to the normalized representation. Define the normalizing factor

$$N_m = \sqrt{\frac{2m+1}{2}\frac{(m-s)!}{(m+s)!}} \tag{C.47}$$

so that (C.44) becomes

$$\bar{P}_m^s = N_m P_m^s \tag{C.48}$$

and substitute into (C.46). Using (C.38) it becomes clear that the components in the standard and normalized representations are related by

$$\Theta_m^{\pm} = N_m \bar{\Theta}_m^{\pm}. \tag{C.49}$$

In matrix form

$$\Theta^{\pm} = \mathcal{N}^{\pm}\bar{\Theta}^{\pm} \tag{C.50}$$

where the matrices $\mathcal{N}^{\pm}$ are

$$\mathcal{N}^{+} = \begin{pmatrix} N_s & 0 & 0 & \\ 0 & N_{s+2} & 0 & \cdots \\ 0 & 0 & N_{s+4} & \\ & \vdots & & \ddots \end{pmatrix}, \tag{C.51}$$

$$\mathcal{N}^{-} = \begin{pmatrix} N_{s+1} & 0 & 0 & \\ 0 & N_{s+3} & 0 & \cdots \\ 0 & 0 & N_{s+5} & \\ & \vdots & & \ddots \end{pmatrix}. \tag{C.52}$$

Since diagonal matrices commute then in the normalized representation (C.43) becomes

$$\left[\epsilon^{\pm}\mathcal{I} - \left(\mathcal{N}^{\pm -1}\mathcal{M}^{\pm}\right)\mathcal{A}^{\pm}\left(\mathcal{N}^{\pm -1}\mathcal{M}^{\pm}\right)^{-1}\right]\bar{\Theta}^{\pm} = 0. \tag{C.53}$$

The matrix $\left(\mathcal{N}^{\pm -1}\mathcal{M}^{\pm}\right)\mathcal{A}^{\pm}\left(\mathcal{N}^{\pm -1}\mathcal{M}^{\pm}\right)^{-1}$ is symmetric. It can be shown that

$$\left(\mathcal{N}^{+ -1}\mathcal{M}^{+}\right)\mathcal{A}^{+}\left(\mathcal{N}^{+ -1}\mathcal{M}^{+}\right)^{-1} = \begin{pmatrix} R_s & T_s & 0 & 0 & \\ T_s & R_{s+2} & T_{s+2} & 0 & \\ 0 & T_{s+2} & R_{s+4} & T_{s+4} & \cdots \\ 0 & 0 & T_{s+4} & R_{s+6} & \\ & & \vdots & & \ddots \end{pmatrix}, \tag{C.54}$$

$$\left(\mathcal{N}^{--1}\mathcal{M}^{-}\right)\mathcal{A}^{+}\left(\mathcal{N}^{--1}\mathcal{M}^{-}\right)^{-1} = \begin{pmatrix} R_{s+1} & T_{s+1} & 0 & 0 & \\ T_{s+1} & R_{s+3} & T_{s+3} & 0 & \\ 0 & T_{s+3} & R_{s+5} & T_{s+5} & \cdots \\ 0 & 0 & T_{s+5} & R_{s+7} & \\ & & \vdots & & \ddots \end{pmatrix} \tag{C.55}$$

where

$$T_m = \frac{M_{m+2}}{M_m} Q_m \sqrt{\frac{2m+1}{2m+5}\frac{(m+s+1)(m+s+2)}{(m-s+1)(m-s+2)}}. \tag{C.56}$$

Since these matrices are real-symmetric then the eigenvectors $\bar{\Theta}^{\pm}$ are orthogonal with real eigenvalues $\epsilon^{\pm} = -1/\lambda^{\pm}$ [Mathews, Walker, 1970]. The eigenvectors are then normalized. The phases of the eigenvectors are chosen so that $\Theta^{+}(0) > 0$ and $d\Theta^{-}/d\mu(0) > 0$ for the symmetric and anti-symmetric eigenfunctions respectively.

Now that the eigenvectors $\bar{\Theta}^{\pm}$ in the normalized representation $\bar{P}_m^s$ have been determined we wish to compute $U'^{\pm}$ and $V'^{\pm}$. We use expansions over the standard associated Legendre functions

$$U'^{\pm} = \sum_{m \geq s} U_m'^{\pm} P_m^s, \tag{C.57}$$

$$V'^{\pm} = \sum_{m \geq s} V_m'^{\pm} P_m^s. \tag{C.58}$$

From (C.10-1) we see that U' and V' are determined from Φ and Ψ. Now

$$\Phi_m^{\pm} = N_m^{\pm} \bar{\Phi}_m^{\pm} \tag{C.59}$$

and since

$$\bar{\Phi}_m^{\pm} = -\lambda^{\pm} f \bar{\Theta}_m^{\pm} / M_m. \tag{C.60}$$

therefore

$$\Phi_m^{\pm} = -\lambda^{\pm} f \frac{N_m}{M_m} \bar{\Theta}_m^{\pm}. \tag{C.61}$$

The stream function Ψ can be determined from (C.26)

$$\Psi_m = -\frac{1}{L_m}\left(p_{m+1}\Phi_{m+1} + q_{m-1}\Phi_{m-1}\right). \tag{C.62}$$

After substituting the standard representations of U', V', Φ, and Ψ into (C.10-1) it can be shown that

$$U_m'^{\pm} = s\Phi_m^{\pm} - \Psi_{m+1}^{\pm}\frac{(m+2)(m+s+1)}{2m+3} + \Psi_{m-1}^{\pm}\frac{(m-1)(m-s)}{2m-1}, \tag{C.63}$$

$$V_m'^{\pm} = s\Psi_m^{\pm} - \Phi_{m+1}^{\pm}\frac{(m+2)(m+s+1)}{2m+3} + \Phi_{m-1}^{\pm}\frac{(m-1)(m-s)}{2m-1}. \tag{C.64}$$

The derivations in this section were used to obtain the Legendre function expansions for the eigenfunctions Θ and eigenvalues λ of Laplace's tidal equation. This technique can be used for arbitrary values of f and s. The differential operator $\mathcal{L}$ is represented by a matrix and the eigenvectors and eigenvalues are obtained by using algebraic methods. Once the expansion coefficients $\bar{\Theta}_m$ are determined the velocity eigenfunctions U' and V' are determined by using recursion relations.

This method presented in this appendix was used for the latitudinal structure of the linear wave theory §III.4 and susequent calculations §III.5-6.

Appendix D. Method for Solving the Homogeneous Vertical Structure Equation

In this appendix we present a method which is used to determine the eigenvalues and eigenfunctions of the homogeneous vertical structure equation (3.67) for the auxiliary temperature dependent function ω defined in (3.68). Equation (3.67) can be written in the form

$$\frac{d^2y}{dx^2} + k^2(\lambda; x)y = 0 \tag{D.1}$$

where

$$k^2(\lambda; x) = \omega\lambda - \frac{1}{4} \tag{D.2}$$

is a complicated expression and plays the role of the refractive index [Chapman and Lindzen, 1970; Salby, 1979]. In regions where $k^2 > 0$ we have oscillatory behavior of y while in regions where $k^2 < 0$ the behavior of y is evanescent and reflections can occur [Salby, 1979]. The homogeneous vertical structure equation (D.1) is solved with two boundary conditions. At the surface $x = 0$ we impose the condition that the vertical velocity w vanishes [Chapman and Lindzen, 1970; Salby, 1979]. Using (3.44) this is expressed

$$\left\{\frac{dy}{dx} + \left(\frac{\lambda}{F\Lambda} - \frac{1}{2}\right) y\right\}\Bigg|_{x=0} = 0. \tag{D.3}$$

The upper boundary condition must satisfy a radiation/finite energy condition [Chapman and Lindzen, 1970; Salby, 1979]. The radiation condition in the WKB approximation is discussed in Appendix E and we will use the

result for the upper boundary condition. From the WKB approximation, at some upper level x_{top} the solution y must satisfy the boundary condition

$$\left.\frac{dy}{dx}\right|_{x_{top}} = \left(ik - \frac{dk/dx}{2k}\right) y\Big|_{x_{top}} = 0. \tag{D.4}$$

This condition along with (D.3) are used to determine the eigenvalues λ of the system for the temperature profile described by ω.

To solve the eigenvalue problem we can use a finite difference approximation. We will divide the region $0 < x < x_{top}$ into $N+1$ levels with spacing Δ. The lower boundary is given by $x_0 = 0$ and the upper boundary $x_N = x_{top}$. In (D.1) the second derivative of y is approximated by

$$\left.\frac{d^2y}{dx^2}\right|_m \simeq \frac{y_{m+1} - 2y_m + y_{m-1}}{\Delta^2}. \tag{D.5}$$

The differential equation (D.1) can be expressed in terms of the difference equation for $1 \leq m \leq N-1$

$$y_{m-1} + (-2 + \Delta^2 k_m^2)\, y_m + y_{m+1} = 0. \tag{D.6}$$

Using the finite difference method the lower boundary condition (D.3) can be expressed in the form

$$\left[-1 + \Delta\left(\frac{\lambda}{F\Lambda_0} - \frac{1}{2}\right)\right] y_0 + y_1 = 0. \tag{D.7}$$

The upper boundary equation is derived from (D.4) and is

$$y_{N-1} + \left[-1 + \Delta\left(ik - \frac{dk/dx}{2k}\right)_N\right] y_N = 0. \tag{D.8}$$

The system of equations (D.6-8) can be cast into the form

$$\mathbf{My} = \mathbf{0} \tag{D.9}$$

where y is the column vector of y values

$$\mathbf{y} = \begin{bmatrix} y_0 \\ y_1 \\ \vdots \\ y_N \end{bmatrix} \tag{D.10}$$

and the matrix M is defined by the coefficients of the y_m in (D.6-8). The equation (D.9) has a non-trivial solution if

$$\det[\mathrm{M}] = 0. \tag{D.11}$$

The eigenvalues of the system are those values of λ in which (D.11) is true.

The eigenvalues λ of the system can be determined by a search method in which the parameter λ is varied and the magnitude of the determinant is evaluated. This technique was carried out for the ATMOS standard temperature profile described in §III.5. Trial values of λ were varied from -10 through 40 and $|\det[\mathrm{M}]|$ vs. λ with a spacing $\Delta\lambda$ of 0.2 is shown in Figure D.1. Two 'spikes' were found in the data at $\lambda \simeq 8.88$ and 13.18. These minima are magnified in Figures D.2-3. Increasing the resolution of $\Delta\lambda$ to 0.05 near $\lambda \sim 9$ increases the sharpness of the first peak. This indicates that an eigenvalue has been detected. Near the eigenvalue $\lambda \sim 13$ increasing the resolution of $\Delta\lambda$ was not found to increase the sharpness of the peak. Indicate that there is no true eigenvalue near $\lambda \sim 13$ and I will disregard it in this study.

We see that a solution to the homogeneous vertical structure equation exists with a unique eigenvalue $\lambda \sim 8.9$ and vertical structure function $y(x)$. Corresponding to this eigenvalue is a multitude of eigenfunctions to Laplace's

tidal equation (3.56) with various frequencies and azimuthal wave numbers for free oscillation.

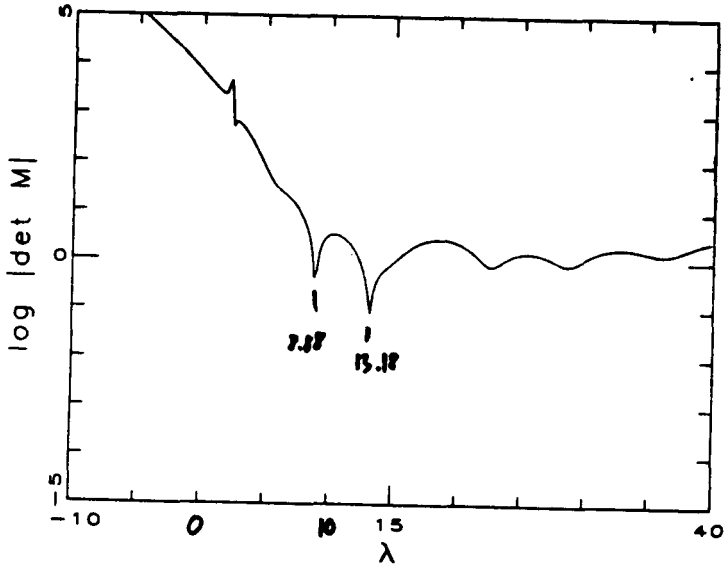

Figure D.1 Graph of values of det[M] as the parameter λ was varied between 10 and 40. There are two distinct 'spikes' in the data at 8.88 and 13.18 respectively. The first value corresponds to the free oscillating mode or *Lamb* mode. The second spike is 'approximately' an eigenvalue and it depends on the temperature profile [see Salby, 1979].

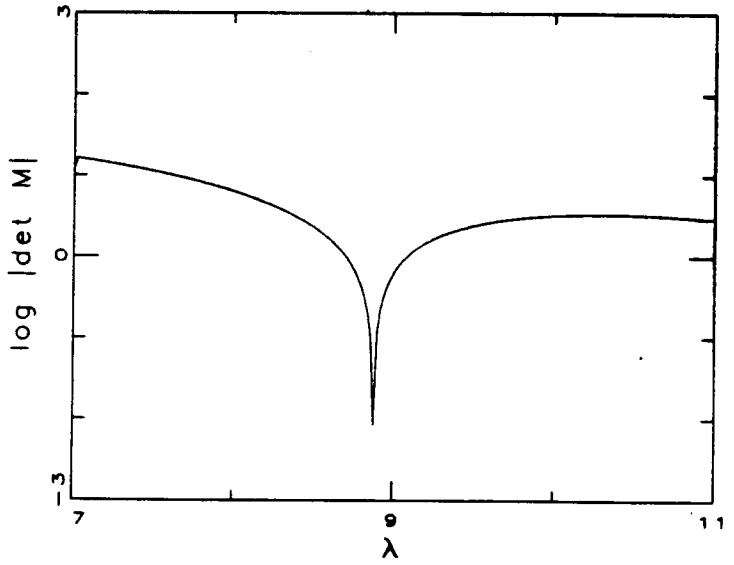

Figure D.2 Region around $\lambda \sim 9$ at higher resolution. The magnitude of the minimum increases by a factor of 40 compared with Figure D.1 as the search resolution $\Delta\lambda$ is improved. This suggests the presence of the eigenvalue.

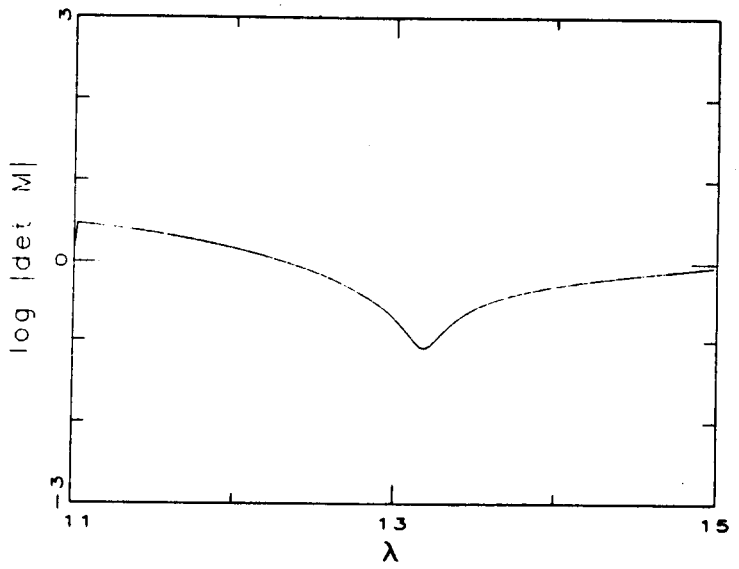

Figure D.3 Similar to Figure D.2 in the region around $\lambda \sim 13$ at higher resolution. In difference to Figure D.2, the magnitude of the minimum does not increase any further with increased search resolution $\Delta\lambda$. This suggests that the dip near 13.18 is an artifact of the calculation and probably does not correspond to a true eigenvalue of the atmosphere.

Appendix E. The WKB Approximation

One particularly useful approximation to the solution of equations of the form

$$\frac{d^2y}{dx^2} + k^2(x)\,y = 0 \tag{E.1}$$

is to use the WKB approximation [Richmond, 1971; Mathews, Walker, 1970]. This method is valid when $k(x)$ varies sufficiently slowly with x so that the change in k in one wavelength is smaller than k itself. The form of (E.1) suggests solutions of the form

$$y \propto e^{i\phi(x)}. \tag{E.2}$$

Then (E.1) becomes

$$-(\phi')^2 + i\phi'' + k^2 = 0. \tag{E.3}$$

If we assume ϕ'' is small then to a first approximation

$$\phi' \simeq \pm k \tag{E.4}$$

so that

$$\phi \simeq \pm \int dx\, k. \tag{E.5}$$

The "smallness" of ϕ'' requires that

$$|\phi''| \simeq |k'| \ll \left|k^2\right|. \tag{E.6}$$

A second approximation is determined by iteration.

$$\phi'' \simeq \pm k'. \tag{E.7}$$

This is substituted into (E.3) to yield

$$(\phi')^2 \simeq k^2 \pm ik'. \tag{E.8}$$

The condition (E.8) gives

$$\phi' \simeq \pm k + \frac{i}{2}\frac{k'}{k} \tag{E.9}$$

so that

$$\phi \simeq \pm \int dx\, k + \frac{i}{2} \ln k. \tag{E.10}$$

Then the two choices of sign yield two approximate solutions

$$y^{(\pm)} = \frac{c_\pm}{\sqrt{k}} e^{\pm i \int^x dx\, k} \tag{E.11}$$

the general solution being

$$y = \frac{1}{\sqrt{k}} \left[c_+ e^{i \int^x dx\, k} + c_- e^{-i \int^x dx\, k} \right]. \tag{E.12}$$

For the case where $k^2(x) > 0$ the solutions are oscillatory. In the case where $k^2 < 0$ the solutions will have an exponential behavior.

Appendix F. The Upper Boundary Conditions

The vertical structure equation (3.57) in the homogeneous region where $\mathcal{H} = 0$ is described by (3.67). At the upper boundary at x_{top} we can assume the solutions to be represented by the WKB approximation described in Appendix E. In this appendix we derive the relationship between dy/dx and y at the upper boundary appropriate to atmospheric gravity waves.

First consider the case where $k^2 > 0$ in the WKB approximation (E.1). In this case there is an oscillatory boundary condition. The analysis is further simplified if we impose a 'radiation condition' that the energy flow is vertically upwards out of the heating region $x < x_N$ [Wilkes, 1949; Siebert, 1961; Chapman and Lindzen, 1970]. The radiation condition is specified by choosing c_- to vanish. The reasons for this are discussed by Kato (1980) and he shows that for gravity waves, the energy propagation is opposite in direction of the phase velocity. If $c_- = 0$ we have downwards phase progression which gives outward energy flow. The radiation condition assumes that there exist no energy sources outside of the integration region and that the energy propagates toward $z = +\infty$ from the lower atmosphere. As pointed out by Chapman and Lindzen (1970) this approximation neglects reflection of waves at greater heights which can be a source of disturbance. If this condition is used then our solutions above the top layer N are of the form

$$y = \frac{c_+}{\sqrt{k}} e^{i\int_{x_N}^{x} dx\, k} \tag{F.1}$$

and

$$\frac{dy}{dx} = i\left[k + \frac{i}{2}\frac{k'}{k}\right] y. \tag{F.2}$$

For simplicity we define

$$K \equiv k + \frac{i}{2}\frac{k'}{k} \tag{F.3}$$

so that

$$\frac{dy}{dx} = iKy \tag{F.4}$$

represents the radiation condition.

In the case where $k^2 < 0$ we can write that $k = ik_i$ so that the WKB solution to (E.1) is given by

$$y = \frac{1}{\sqrt{k}}\left[c_+ e^{-\int_{z_N}^{z} dz\, k_i} + c_- e^{\int_{z_N}^{z} dz\, k_i}\right]. \tag{F.5}$$

The two solutions represent exponentially decaying and increasing amplitudes with height in addition to that predicted by (3.52). The exponential growth is assumed to be unrealistic in the context of this atmospheric model which demands $c_- = 0$ unless a source of further attenuation exists at higher altitudes. If the solution at the upper boundary is specified by

$$y = \frac{c_+}{\sqrt{k}} e^{-\int_{z_N}^{z} dz\, k_i} \tag{F.6}$$

then

$$\frac{dy}{dx} = -\left[k_i + \frac{1}{2}\frac{k_i'}{k_i}\right] y. \tag{F.7}$$

Again we define

$$K \equiv k_i + \frac{1}{2}\frac{k_i'}{k_i} \tag{F.8}$$

we gives

$$\frac{dy}{dx} = -Ky. \tag{F.9}$$

Appendix G. Integrating the Vertical Structure Equation

In this appendix we describe how the vertical structure equation (3.57) can be solved. A method of solving second order ordinary differential equations with boundary conditions at different points is used which follows the integration scheme proposed by Chapman and Lindzen (1970). Two boundary conditions are specified at the surface of the earth and at altitudes where the heating term is zero. At the surface we assume that the vertical velocity of the atmosphere vanishes. At the upper 'free' boundary we assume that energy propagates outwards with no reflections. This is known as the radiation condition.

The method described in the previous two appendices describes how to obtain eigenvalues $\lambda_n^{\sigma s}$ and eigenfunctions $\Theta_n^{\sigma s}$ of the horizontal structure equation (3.56), i.e.- Laplace's tidal equation. However, this is only half of the problem for understanding the three dimensional dynamics since the vertical structure must also be known for each eigen-mode $S_n^{\sigma s}$. The eigenvalue $\lambda_n^{\sigma s}$ provides this coupling. The driving terms in (3.57) are the Hough components of the heating distribution $\mathcal{H}_n^{\sigma s}(x)$.

A fairly technique for integrating second order ordinary differential equations introduced by Richtmyer (1957) and described by Chapman and Lindzen (1970) was used. Consider an equation of the form

$$F(x)\,\frac{d^2Y}{dx^2}(x) + G(x)\,\frac{dY}{dx}(x) + H(x)\,Y(x) = J(x). \qquad \text{(G.1)}$$

We wish to determine a numerical solution for $Y(x)$ given the other functions $F(x)$, $G(x)$, $H(x)$, and $J(x)$. Suppose we wish to integrate this solution over the range $x_0 < x < x_N$ and this range is divided into N equal subintervals of width Δ. Then the derivatives of Y at each point x_m can be approximated by

$$\left(\frac{dY}{dx}\right)_m \simeq \frac{Y_{m+1} - Y_{m-1}}{2\Delta}, \tag{G.2}$$

$$\left(\frac{d^2Y}{dx^2}\right)_m \simeq \frac{Y_{m+1} - 2Y_m + Y_{m-1}}{\Delta^2}. \tag{G.3}$$

Then the differential equation (G.1) can be cast into the finite difference form

$$A_m Y_{m+1} + B_m Y_m + C_m Y_{m-1} = D_m \tag{G.4}$$

where

$$A_m = F_m + \frac{1}{2}\Delta G_m, \tag{G.5}$$

$$B_m = -2F_m + \Delta^2 H_m, \tag{G.6}$$

$$C_m = F_m - \frac{1}{2}\Delta G_m, \tag{G.7}$$

$$D_m = \Delta^2 J_m. \tag{G.8}$$

If we introduce a change of variables

$$Y_m = \alpha_m Y_{m+1} + \beta_m. \tag{G.9}$$

then

$$Y_{m-1} = \alpha_{m-1} Y_m + \beta_{m-1}. \tag{G.10}$$

Thus the difference equation (G.4) can be put into the form

$$Y_m = -\frac{A_m}{B_m + \alpha_{m-1} C_m} Y_{m+1} + \frac{D_m - \beta_{m-1} C_m}{B_m + \alpha_{m-1} C_m}. \tag{G.11}$$

By comparing this to (G.9) we see that

$$\alpha_m = \frac{-A_m}{B_m + \alpha_{m-1}C_m}, \tag{G.12}$$

$$\beta_m = \frac{D_m - \beta_{m-1}C_m}{B_m + \alpha_{m-1}C_m}. \tag{G.13}$$

If α_0 and β_0 are known then all of the other α_m and β_m can be determined. The simplest lower boundary condition is usually chosen to represent a smooth spherical earth where the vertical velocity w vanishes at the surface $x = 0$ [Chapman and Lindzen, 1970]. From equation (3.61) this can be expressed as

$$\left.\frac{dy}{dx}\right|_{x=0} + \left(\frac{\lambda^{\sigma s}}{F\Lambda} - \frac{1}{2}\right) y\Big|_{x=0} = 0. \tag{G.14}$$

In terms of finite differences

$$\frac{y_1 - y_0}{\Delta} + \left(\frac{\lambda_n^{\sigma s}}{F\Lambda_0} - \frac{1}{2}\right) y_0 = 0 \tag{G.15}$$

and this can be rewritten

$$y_0 = \left[1 - \Delta\left(\frac{\lambda_n^{\sigma s}}{F\Lambda_0} - \frac{1}{2}\right)\right]^{-1} y_1. \tag{G.16}$$

Upon examination of (G.9) we can identify

$$\alpha_0 = \left[1 - \Delta\left(\frac{\lambda_n^{\sigma s}}{F\Lambda_0} - \frac{1}{2}\right)\right]^{-1}, \tag{G.17}$$

$$\beta_0 = 0. \tag{G.18}$$

From (G.12-3) all of the other α_m and β_m are determined.

After calculating all of the α_m and β_m the function Y can be determined from (G.10) provided that an upper value Y_N is given, since

$$Y_{N-1} = \alpha_{N-1}Y_N + \beta_{N-1},$$

$$\begin{aligned} Y_{N-2} &= \alpha_{N-2} Y_{N-1} + \beta_{N-2}, \\ &\vdots \\ Y_1 &= \alpha_1 Y_2 + \beta_1. \end{aligned} \tag{G.19}$$

The result (G.19) implies that we need to know the value for the upper boundary Y_N to complete the integration.

For the case in which the vertical structure equation is homogeneous (§III.5, Appendix D) the upper boundary value is arbitrary since there is a free constant of integration which can have any value. The upper boundary dynamics - i.e. radiation condition - is imposed on the solution during the determination of the eigenvalue λ. In the case of the inhomogeneous equation (3.57) the upper boundary dynamics are imposed during the integration procedure. We use the WKB approximation (F.4) or (F.9) depending on whether $k^2 > 0$ or $k^2 < 0$ at the upper boundary respectively.

For the case where $k^2 > 0$ we have a radiation boundary condition and apply (F.4) at the level N. Then (F.4) is approximately

$$\frac{y_N - y_{N-1}}{\Delta} \approx iK_N y_N. \tag{G.20}$$

Since, in this integration scheme,

$$y_{N-1} = \alpha_{N-1} y_N + \beta_{N-1}, \tag{G.21}$$

it can be shown that

$$y_N \approx \frac{\beta_{N-1}}{1 - \alpha_{N-1} - i\Delta K_N}. \tag{G.22}$$

This results then allows a full integration of the vertical structure equation below the top layer.

For the case where $k^2 < 0$ we have an evanescent boundary and apply (F.9) to the upper boundary level. Similar to the derivation of (G.15) we apply this condition at the level N so that

$$\frac{y_N - y_{N-1}}{\Delta} \approx -K_N y_N. \tag{G.23}$$

Again using (G.16) we find that

$$y_N \approx \frac{\beta_{N-1}}{1 - \alpha_{N-1} + \Delta K_N}. \tag{G.24}$$

This final boundary condition allows the vertical structure equation to be integrated.

From this appendix we can integrate the second order vertical structure equation (3.57) consistent with two boundary conditions specifying the behaviour of the atmosphere at great heights and at ground level. The upper boundary condition assumes that the heating of the atmosphere from below is eventually radiated outward by the tidal gravity waves (or, in the case of the homogeneous equation, any constant value will do). Although it does not assume sources of energy above the upper level, the inclusion of such sources can be built into theory by an appropriate adjustment of the upper boundary condition. The lower boundary is assumed to correspond to a flat surface which has no vertical component of motion and hence wind. Although this does not take into account features such as continents and possible tidal deformations of the oceans, they can be assumed to be negligable to at least $\mathcal{O}(\Delta)$ in the scale of the dynamics and of secondary importance.

Appendix H. Energy Transport in Linear Wave Theory

The linear wave theory presented in can be used to describe the physical structure of the velocity, pressure and density perturbations to the hydrostatic state generated due to homogeneous oscillations and inhomogeneous waves, particularly in the case of atmospheric thermal tides in which the periodic ozone and water water vapor heating of the atmosphere can drive upper atmospheric circulation. In this section we outline how these waves also transport energy through the atmosphere. In the absence of nonlinear turbulence and radiative dissipation the linear waves may transport the energy absorbed by the atmosphere outwards. In this section we examine the energy transport of these waves.

For notational simplicity we will temporarily omit the "*" superscript to denote dimensioned quantities. The energy flux per unit mass **S** is given by [Kato, 1980]

$$\mathbf{S} = P\mathbf{u}. \tag{H.1}$$

The divergence of the flux density is

$$\begin{aligned} \nabla \cdot \mathbf{S} &= \nabla \cdot P\mathbf{u} \\ &= \nabla P \cdot \mathbf{u} + P \nabla \cdot \mathbf{u}. \end{aligned} \tag{H.2}$$

By using the momentum equation (3.1) and continuity equation (3.2) we

have

$$\nabla \cdot \mathbf{S} = -\rho \left[\frac{D}{Dt} \left(\frac{|\mathbf{u}|^2}{2} \right) + \frac{P}{\rho^2} \frac{D\rho}{Dt} - \mathbf{g} \cdot \mathbf{u} \right]. \tag{H.3}$$

From the thermodynamic equation (3.11) it can be shown that

$$\frac{P}{\rho^2} \frac{D\rho}{Dt} = \frac{1}{\gamma - 1} \frac{D}{Dt} \left(\frac{P}{\rho} \right) - \mathcal{H}. \tag{H.4}$$

Then (H.3) can be shown to be

$$\frac{D}{Dt} \left(\frac{|\mathbf{u}|^2}{2} + \frac{1}{\gamma - 1} \frac{P}{\rho} \right) + \frac{1}{\rho} \nabla \cdot \mathbf{S} = \mathcal{H} + \mathbf{g} \cdot \mathbf{u}. \tag{H.5}$$

We see that the energy per unit mass E is given by

$$E = \frac{|\mathbf{u}|^2}{2} + \frac{1}{\gamma - 1} \frac{P}{\rho} \tag{H.6}$$

and (H.5) can be expressed

$$\rho \frac{DE}{Dt} + \nabla \cdot \mathbf{S} - \rho \mathbf{g} \cdot \mathbf{u} = \rho \mathcal{H}. \tag{H.7}$$

The energy equation (H.7) expresses how the energy of the wave is exchanged. Some of the heating is used to increase the energy density, some is transported, and some goes into doing work against gravity. Since the tides are periodic in time (and local time) we can average the energy equation over a sphere to obtain the average energy exchange as a function of altitude. Let us define the spherical average, which is also an average over one period, by

$$\langle \cdots \rangle \equiv \frac{1}{4\pi} \int_{-1}^{1} d\mu \int_{0}^{2\pi} d\phi \cdots . \tag{H.8}$$

The spherical average of (H.7) is then

$$\left\langle \rho \frac{DE}{Dt} \right\rangle + \langle \nabla \cdot \mathbf{S} \rangle - \langle \rho \mathbf{g} \cdot \mathbf{u} \rangle = \langle \rho \mathcal{H} \rangle . \tag{H.9}$$

The fields will be assumed to vary as §III.6

$$f = \sum_{\sigma=1}^{2} f^{\sigma\sigma}\, e^{i\sigma(\Omega t+\phi)}. \tag{H.10}$$

It is also understood that we use the real parts of the dynamical fields in (H.7) when taking these averages. If we denote the complex conjugate of a function f by $f^\dagger$ then

$$\Re f = \frac{1}{2}(f + f^\dagger). \tag{H.11}$$

Only products of non-conjugate and conjugate pairs will survive the averaging process.

If we write the pressure and density in the form §III.3

$$P = P_{\rm h}(1 + P'), \tag{H.12}$$

$$\rho = \rho_{\rm h}(1 + \rho') \tag{H.13}$$

then the energy flux divergence is

$$\begin{aligned} \nabla \cdot \mathbf{S} &= \nabla \cdot P\mathbf{u} = P\nabla \cdot \mathbf{u} + \mathbf{u} \cdot \nabla P \\ &= P_{\rm h}(1 + P')\nabla \cdot \mathbf{u} + \mathbf{u} \cdot \nabla P_{\rm h}(1 + P') \\ &= P_{\rm h}\left[(1 + P')\left(\nabla \cdot \mathbf{u} - \frac{w}{H}\right) + \mathbf{u} \cdot \nabla P'.\right] \end{aligned} \tag{H.14}$$

The spherical average of (H.14) is then (omitting "$\sigma\sigma$" superscripts)

$$\langle \nabla \cdot \mathbf{S} \rangle = P_{\rm h}\left\langle P'\left(\nabla \cdot \mathbf{u} - \frac{w}{H}\right) + \mathbf{u} \cdot \nabla P' \right\rangle. \tag{H.15}$$

Since the fields in (H.15) are the real parts of the solutions, in terms of the complex functions we have using (H.10-1)

$$\langle \nabla \cdot \mathbf{S} \rangle = \frac{P_{\rm h}}{8} \sum_{\sigma} \int_{-1}^{1} d\mu \left[P'\left(\frac{\partial w^\dagger}{\partial z} + \frac{2w^\dagger}{r} + \frac{1}{r}\frac{\partial v'^\dagger}{\partial \mu} - \frac{1}{r}\frac{i\sigma}{1-\mu^2}u'^\dagger\right)\right.$$

$$+P'^{\dagger}\left(\frac{\partial w}{\partial z}+\frac{2w}{r}+\frac{1}{r}\frac{\partial v'}{\partial \mu}+\frac{1}{r}\frac{i\sigma}{1-\mu^2}u'\right)-\frac{1}{H}(wP'^{\dagger}+w^{\dagger}P')$$
$$-\frac{1}{r}\frac{i\sigma}{1-\mu^2}u'P'^{\dagger}+\frac{1}{r}\frac{i\sigma}{1-\mu^2}u'^{\dagger}P'+\frac{v'}{r}\frac{\partial P'^{\dagger}}{\partial \mu}+\frac{v'^{\dagger}}{r}\frac{\partial P'}{\partial \mu}$$
$$+w\frac{\partial P'^{\dagger}}{\partial z}+w^{\dagger}\frac{\partial P'}{\partial z}\Big]. \qquad \text{(H.16)}$$

We now wish to express this in terms of the dimensionless variables. From §III.10

$$\begin{aligned} u' &= U\sum_n P_n U'_n, \\ v' &= U\sum_n iP_n V'_n, \\ w &= \Delta U\sum_n w_n\Theta_n, \\ P' &= \epsilon F\Lambda\sum_n P_n\Theta_n, \\ \rho' &= \epsilon F\sum_n \rho_n\Theta_n. \end{aligned} \qquad \text{(H.17)}$$

By using these transformations (H.16), the orthogonality of the Hough functions and (A.14)

$$\langle\nabla\cdot\mathbf{S}\rangle=\frac{P_{\rm h}(0)}{8}\frac{\epsilon FU}{r_0}\Lambda\sum_\sigma\sum_n\frac{d}{dx}\left[e^{-x}\Lambda(w_nP_n^{\dagger}+w_n^{\dagger}P_n)\right]+\mathcal{O}(\Delta). \qquad \text{(H.18)}$$

In a similar manner the power lost to gravity can be evaluated

$$\begin{aligned} \langle\rho gw\rangle &= \rho_{\rm h}g\epsilon F\langle\rho' w\rangle \\ &= \frac{P_{\rm h}(0)}{8}\frac{\epsilon FU}{r_0}\Lambda\sum_\sigma\sum_n e^{-x}(\rho_n^{\dagger}w_n+\rho_n w_n^{\dagger}). \end{aligned} \qquad \text{(H.19)}$$

The term on the right hand side of (H.7) represents the energy expended in heating density perturbations

$$\begin{aligned} \langle\rho\mathcal{H}\rangle &= \rho_{\rm h}\epsilon F\langle\rho'\mathcal{H}\rangle \\ &= \frac{P_{\rm h}(0)}{8}\frac{\epsilon FU}{r_0}\frac{1}{\kappa}\sum_\sigma\sum_n e^{-x}(\rho_n^{\dagger}\mathcal{H}_n+\rho_n\mathcal{H}_n^{\dagger}). \end{aligned} \qquad \text{(H.20)}$$

The total rate of change of energy following the fluid particles can be evaluated from (H.7)

$$\left\langle \rho \frac{DE}{Dt} \right\rangle = \langle \rho \mathcal{H} \rangle - \langle \rho g w \rangle - \langle \nabla \cdot \mathbf{S} \rangle . \tag{H.21}$$

The flux density can be computed from $\langle \mathbf{S} \cdot \mathbf{n} \rangle$ where $\mathbf{n}$ unit vector pointing outward from the spherical surface at level x.

$$\langle \mathbf{S} \cdot \mathbf{n} \rangle = \frac{P_h(0)}{8} \frac{\epsilon F U}{\tau_0} D \Lambda \sum_{\sigma} \sum_{n} e^{-x} (w_n P_n^{\dagger} + w_n^{\dagger} P_n). \tag{H.22}$$

The energy sources and sinks given by (H.18-20) can be used to compute the spherically averaged energy exchange of the linear wave solutions. The energy flow of the linear waves are given by (H.22). We see that due to the orthogonality of the Hough functions that the total energy terms are the sum of the various component terms. This allows us to examine each mode separately.

Appendix J. Including Radiative Damping into the Linear Wave Theory

The primary absorption processes of solar radiation in the atmosphere are the ultraviolet absorption of water near the surface and ozone in the stratosphere [Andrews, Holton, Leovy, 1987]. The 15-μm band of CO_2 is the primary source of infrared emission in the atmosphere and it provides the

medium by which the atmosphere radiates [Dickinson, 1984]. The hydrostatic temperature distribution can be assumed to be produced by a balance between radiative and non-radiative processes – see Andrews, Holton, Leovy (1987) for details. We will assume that any temperature perturbation will lead to an increase or decrease in infrared cooling which tends to restore the atmosphere to its original temperature [Chapman and Lindzen, 1970].

Including this type of dynamics into the linear wave theory §III.4 requires only a slight modification. We can substitute (3.6) into (3.5) to obtain

$$\frac{DT}{Dt} = \kappa \frac{T}{P} \frac{DP}{Dt} + \frac{M}{C_P} \mathcal{H}. \tag{J.1}$$

Since the infrared cooling opposes the growth in temperature, following Chapman and Lindzen (1970) we include a term into the right hand side

$$\frac{DT}{Dt} = \kappa \frac{T}{P} \frac{DP}{Dt} + \frac{M}{C_P} \mathcal{H} - a\, \delta T \tag{J.2}$$

where a is the infrared cooling coefficient and δT is the deviation of the temperature from the equilibrium temperature. This is known as the *Newtonian cooling approximation* [see Andrews, Holton, Leovy, 1987] and a is the *Newtonian cooling coefficient*. We can write (J.2) in the form

$$\frac{DT}{Dt} = \kappa \frac{T}{P} \frac{DP}{Dt} + \frac{M}{C_P} \hat{\mathcal{H}} \tag{J.3}$$

with the 'modified' heating

$$\hat{\mathcal{H}} \equiv \mathcal{H} - \frac{C_P}{M} a\, \delta T. \tag{J.4}$$

When we include a Newtonian cooling term, the linear wave theory §III.4 is still used with the replacement of $\mathcal{H} \rightarrow \hat{\mathcal{H}}$.

The vertical structure equation (3.57) requires that the heating be in the dimensionless representation of Appendix A. This is achieved with the transformation (A.52)

$$\hat{\mathcal{H}} = \frac{\kappa\Lambda\hat{\mathcal{H}}^*}{gD\Omega} \tag{J.5}$$

where now we have introduced the dimensional '*' notation (see Appendix A). The temperature perturbation, described in Appendix K, is then

$$\delta T = T_h \cdot \epsilon F T \tag{J.6}$$

where T_h is the background temperature and T is the temperature perturbation function. Using (J.4) in (J.5) it can be shown using the definition of Λ and the vertical depth κ described in Appendix A that the dimensionless heating is

$$\hat{\mathcal{H}} = \frac{\kappa\Lambda\mathcal{H}^*}{gD\Omega} - \alpha T \tag{J.7}$$

where the dimensionless Newtonian cooling coefficient is defined

$$\alpha \equiv \epsilon F \frac{a}{\Omega}. \tag{J.8}$$

Using (K.6) we can then write (J.7) in terms of the pressure and density perturbation functions P and ρ

$$\hat{\mathcal{H}} = \frac{\kappa\Lambda\mathcal{H}^*}{gD\Omega} - \alpha(\Lambda P - \rho). \tag{J.9}$$

The dimensionless heating $\hat{\mathcal{H}}_n$ can be shown to be related to the vertical structure function y_n for each Hough component of (J.9) using (3.60) and (3.62)

$$\hat{\mathcal{H}}_n = \mathcal{H}_n - \alpha \frac{\gamma\Lambda}{if\lambda_n} e^{x/2} \left[\frac{d^2 y_n}{dx^2} + \frac{1}{\Lambda}\frac{d\Lambda}{dx}\frac{dy_n}{dx} - \left(\frac{1}{4} + \frac{1}{2\Lambda}\frac{d\Lambda}{dx} \right) y_n \right]. \tag{J.10}$$

With this result, the vertical structure equation with Newtonian cooling can be derived. Substituting (J.10) for the heating function which drives (3.57) we obtain the following second order differential equation for the vertical structure function y_n

$$\left(1+\frac{\alpha}{ifF}\right)\frac{d^2y_n}{dx^2}+\frac{\alpha}{ifF}\frac{1}{\Lambda}\frac{d\Lambda}{dx}\frac{dy_n}{dx}+\left[\frac{\lambda_n^{\sigma s}}{F\Lambda^2}\mathcal{N}^2-\frac{1}{4}-\frac{\alpha}{ifF}\left(\frac{1}{4}+\frac{1}{2\Lambda}\frac{d\Lambda}{dx}\right)\right]y_n$$
$$=\frac{1}{\gamma}\frac{\lambda_n^{\sigma s}}{F\Lambda}\mathcal{H}^{\sigma s}e^{-z/2}. \qquad \text{(J.11)}$$

Appendix K. Linearized Temperature Perturbation

The ideal gas law (A.17) is a non-linear relationship between the pressure, density and the temperature. Using the notation of Appendix A for dimensional and nondimensional variables (A.33-4) describe the total pressure P^* and density ρ^* respectively in terms of the hydrostatic background P_h, ρ_h and perturbation functions P, ρ

$$P^* = P_h(1 + \epsilon F \Lambda P), \tag{K.1}$$

$$\rho^* = \rho_h(1 + \epsilon F \rho) \tag{K.2}$$

where ϵ and F are scaling factors and Λ contains information regarding the hydrostatic temperature distribution with height. For simplicity, we can define a dimensionless background temperature perturbation function T by

$$T^* = T_h(1 + \epsilon F T) \tag{K.3}$$

where T^* is the total temperature, T_h is the background temperature. Using the ideal gas law

$$P^* = \frac{\rho^* R T^*}{M} \tag{K.4}$$

and (A.17) for the background it can be verified that the dimensionless perturbation functions P, ρ and T are related to each other by

$$\Lambda P = \rho + T + \epsilon F \rho T. \tag{K.5}$$

Linearizing and rearranging we obtain

$$T = \Lambda P - \rho. \tag{K.6}$$

LIST OF REFERENCES

Aller, L. H., *Astrophysics - The Atmospheres of the Sun and Stars*, Ronald, New York, 1963.

Andrews, D. G., Holton, J. R., Leovy, C. B., *Middle Atmospheric Dynamics*, Academic, Orlando, 1987.

Barnet, J. J., Corney, M., Middle atmosphere reference model derived from sattelite data, *Handbook for MAP*, 16, 1985.

Berry, R. S., Rice, S. A., Ross, J., *The Structure of Matter, Physical Chemistry*, Wiley, New York, 1980.

Bevington, P. R., *Data Reduction and Error Analysis for the Physical Sciences*, McGraw-Hill, New York, 1969.

Breen, R. G., *Theories of Spectral Line Shape*, Wiley, New York, 1981.

Brilluon, M., Les latitudes critiques, *Compt. Rend. Acad. Sci. Paris*, 194, 801-4, 1932.

Brown, L. R., personal communication, 1986.

Burpee, R. W., Some features of global-scale 4 – 5 day waves, *J. Atmos. Sci.*, 33, 2292-2299.

Chapman, S., Lindzen, R. S., *Atmospheric Tides*, Reidel, Dortrecht, Holland, 1970.

Cohen-Tannoudji, C. C., Diu, B., Laloe, F., *Quantum Mechanics*, Wiley, New York, 1977.

Craig, R. A., *The Upper Atmosphere, Meteorology and Physics*, Academic Press,

New York, 1965.

Dickinson, R. E., Theory of planetary wave-zonal flow interaction, *J. Atmos. Sc.*, 26, 73-81, 1969.

Dickinson, R. E., Infrared radiative cooling in the mesosphere and lower thermosphere, *J. Atmos. Terr. Phys.*, 46, 995-1008, 1984.

Farmer, C. B., High resolution infrared spectroscopy of the sun and the earth's atmosphere from space, *Mikrochim. Acta*, III, 189-214, 1987.

Farmer, C. B., Raper, O., High resolution infrared spectroscopy from space: a preliminary report on the results of the Atmospheric Trace Molecule Spectroscopy (ATMOS) experiment on Spacelab 3, *NASA Conference Proceedings, Spacelab 3 Mission Review, CP-2429,* May 1986.

Fetter, A. L., Walecka, J. D., *Theoretical Mechanics of Particles and Continua*, McGraw-Hill, New York, 1980.

Flattery, T. W., Hough Functions, Technical Report, 21, Dept. of Geophysical Sciences, U. Chicago, 1967.

Forbes, J. M., Middle atmospheric tides, *J. Atmos. Terr. Phys.*, 46, 1049-1067, 1984.

Forbes, J. M., Garrett, H. B., Theoretical studies of atmospheric tides, *Rev. Geophys.*, 17. 1951-1981, 1979.

Fritts, D. C., Gravity wave saturation in the middle atmosphere: a review of theory and observation, *Rev. Geophys. Space Phys.*, 22, 275-308, 1984.

Gao, B. C., The retreival of atmospheric temperatures and gas volume mixing

ratios and column amounts from infrared solar absorption spectra, Ph. D. Thesis, The Ohio State University, Spring 1988.

Geisler, J. E., Dickinson, R. E., The five-day wave on a sphere with realistic zonal winds, *J. Atmos. Sc.*, 33, 632-641, 1976.

Goody, R. M., *Atmospheric Radiation - I Theoretical Basis*, Oxford U. Press, Glasgow, 1964.

Gossard, E. E., Hooke, W. H., *Waves in the Atmosphere*, Elsevier, New York, 1975.

Graybill, (statistics stuff)

Groves, G. V., Latitude and height dependence of solar atmospheric tides, *J. Br. interplanet. Soc.*, 28, 797-809, 1975.

Groves, G. V., Energy fluxes propogated by diurnal oscillations in the upper atmosphere, *J. Br. interplanet. Soc.*, 30, 32-36, 1977.

Groves, G. V., Hough components of ozone heating, *J. Atmos. Terr. Phys.*, 44, 111-121, 1982a.

Groves, G. V., Hough components of water vapour heating, *J. Atmos. Terr. Phys.*, 44, 281-290, 1982b.

Hartmann, D. L., The structure of the stratosphere in the Southern Hemisphere during late winter 1973 as observed by satellite, *J. Atmos. Sc.*, 36, 2016-2019, 1979.

Haurwitz, B., Cowley, D., Diurnal and semidiurnal barometric oscillations, *Pure Appl. Geophys.*, 102, 193-222, 1973.

Herzberg, G., *Molecular Spectra and Molecular Structure, II. Infrared and Raman Spectra of Polyatomic Molecules*, Van Nostrand Reinhold Co., New York, 1945.

Hirota, I., Hirooka, T., Normal mode Rossby waves observed in the upper stratosphere. Part I: First symmetric modes of zonal wavenumbers 1 and 2, *J. Atmos Sc.*, 41, 1253-1267, 1984.

Hough, S. S., The application of harmonic analysis to the dynamical theory of the tides, Part II. On the general integration of Laplace's dynamical equations, *Phil. Trans. Roy. Soc. London*, A191, 201-257, 1898.

Houghton, J. T., *The Physics of Atmospheres*, Cambridge University Press, Cambridge, 1986.

Jackson, J. D., *Classical Electrodynamics*, Weiley, New York, 1975.

Kato, S., *Dynamics of the Upper Atmosphere*, Center for Academic Publications, Tokyo, 1980.

Labitzke, K. (Ed.), Draft of a new references middle atmosphere, *Handbook for MAP*, 16, 1985.

Landau, L. D., Lifshitz, E. M., *Fluid Mechanics*, Pergamon, London, 1959.

Laplace, P. S., *Mecanique celeste*, Paris 2 (iv), 294-298, 1799.

Laplace, P. S., *Mecanique celeste*, Paris 5 (xiii), 145-167, 1825.

Layzer, D., Bedinger, J. F., Upper winds and their interpretation—II, Planet. Space Sci., 17, 1891-1911.

Levine, I. N., *Molecular Spectroscopy*, Wiley, New York, 1975.

Lindzen, R. S., Turbulence and stress owing to gravity wave and tidal breakdown, *J. Geophys. Res.*, 86, 9807-9714,1981.

Lindzen, R. S., Hong, S., Effects of mean winds and horizontal temperature gradients on solar and lunar semidiurnal tides in the atmosphere, *J. Atmos. Sci.*, 31, 1421-1446, 1974.

Longuet-Higgins, M. S., The eigenfunctions of Laplace's tidal equations over a sphere, *Phil. Trans. Roy. Soc.*, A269, 511-607, 1967.

Lorenz, E. N., Available potential energy and the maintenance of the general circulation, *Tellus*, 7, 157-167, 1955.

Lorenz, E. N., Deterministic nonperiodic flow, *J. Atmos. Sci.*, 20, 130-142, 1963.

Madden, R. A., Further evidence of traveling planetary waves, *J. Atmos. Sci.*, 35, 1605-1618, 1978.

Madden, R. A., Labitzke, K., A free Rossby wave in the troposphere and stratosphere during January 1979, . *J. Geophys. Res.*, 86, 1247-1254, 1981.

Madden, R. A., The effect of the interference of traveling and stationary waves on time variation of the large-scale circulation, J. Atmos. Sci., 40, 1110-1125, 1983.

Maeda, K., Kato, S. , Electrodymics of the ionosphere, *Space Phys. Rev.*, 5, 57-79, 1966.

Manson, A. H., Meek, C. E., Dynamics of the middle atmosphere at Saskatoon (52° N, 107° W): a spectral study during 1981, 1982, *J. Atmos. Terr.*

Physics, 48, 1039-1055, 1986.

Mathews, J., Walker, R., L., *Mathematical Methods of Physics*, Benjamin Cummings, Menlo Park Ca., 1970.

Meada, K., Matsumoto, H., *Rep. Ionosph. Space Res. Japan*, 16, 1-26, 1962.

Moura, A. D, The eigensolution of linearized balance equations over a sphere, *J. Atmos. Sc.*, 33, 877-907, 1976.

Muroaka, Y., Sugiyama, T., Kawahira, K., Cause of a monochromatic inertia-gravity wave breaking observed by the MU radar, *Geophys. Res. Lett.*, 15, 1349-1352, 1988.

Myers, R. H., *Classical and Modern Regression with Applications*, Duxbury, Boston, 1986.

Norton, R. H., Beer, R., New apodizing functions for Fourier spectroscopy, *J. Opt. Soc. Am.*, 66, n.3, 259-264, 1976.

Norton, R. H., personal communication, 1986.

Park, J. H., Effect of interferogram smearing on atmospheric limb sounding by Fourier transform spectroscopy, *Appl. Opt.*, 21, n.8,1356- ,1982.

Pedlosky, J., *Geophysical Fluid Dynamics*, Springer-Verlag, New York, 1987.

Pitteway, M. L. V., Hines, C. O., The reflection and ducting of atmospheric acoustic-gravity waves, *Can. J. Phys.*, 43, 2222-2243, 1965.

Rao, K. N. (Ed.), *Molecular Spectroscopy - Modern Research*, v. 3, Academic Press, Orlando, 1985.

Reed, R. J., Oard, M. J., Sieminski, M., A comparison of observed and theo-

retical diurnal motions between 30 and 60 km, *Mon. Weather Rev.*, 97, 456-459, 1969.

Reif, F., *Fundamentals of Statistical and Thermal Physics*, McGraw-Hill, New York, 1965.

Richmond, A. D., Tidal winds at ionospheric heights, *Radio Sc.*, 6, 175-189, 1971.

Rodgers, C. D., Evidence for the five-day wave in the upper stratosphere, *J. Atmos. Sc.*, 33, 710-711, 1976.

Rodgers, C. D., Prata, A. J., Evidence for a traveling two-day wave in the middle atmosphere, *J. Geophys. Res.*, 86, 9661-9664.

Rodgers, C. D., Walshaw, C. D., The computation of infrared cooling rates in planetary atmospheres, *Quart. J. Roy. Meteorol. Soc.*, 92, 67-92, 1966.

Rybicki, G. B., Lightman, A. P., *Radiative Processes in Astrophysics*, Wiley, New York, 1979.

Salby, M. L., On the solution of the homogeneous vertical structure problem for long-period oscillations, *J. Atmos Sc.*, 36, 2350-2359, 1979.

Salby, M. L., The 2-day wave in the middle atmosphere: observation and theory, *J. Geophys. Res.*, 86, 9654-9660, 1981.

Shaw, J. H., Atmospheric winds from occultation spectra, *Appl. Opt.*, 24, 2433-2436, 1985.

Shaw, J. H., personal communication, 1988.

Siebert, M., Atmospheric tides, *Adv. Geophys., 7*, Academic Press, New York,

105-182, 1961.

Steinfeld, J. I., *Molecules and Radiation*, MIT Press, Cambridge, 1985.

Stenning, R. J., A diurnal modulation of the lunar tide in the upper atmosphere, *Geophys. Res. Lett.*, 16, 307-310, 1989.

Thorne, A. P., *Spectrophysics*, Chapman and Hill, London, 1988.

Teitelbaum, H., Vial, F., Momentum transfer to the thermosphere by atmospheric tides, *J. Geophys. Res.*, 86, 9693-9697, 1981.

Volland, H., A theory of thermospheric dynamics-I, diurnal and solar cycle variation, *Planet. Space Sc.*, 17, 1581-1597, 1969.

Volland, H., A theory of thermospheric dynamics-II, geomagnetic activity effect, 27-Day variation and semiannual variation, *Planet. Space Sc.*, 17, 1709-1724, 1969.

van Cleef, G. W., Shaw, J. H., Farmer, C. B., Zonal winds between 25 and 120 km obtained from solar occultation spectra, *Geophys. Res. Let.*,14, 1266-1268, 1987.

Wallace, J. M., Tadd, R. F., Some further results concerning the vertical structure of atmospheric tidal motions within the lowest 30 km, *Mon. Weather Rev.*, 102, 795-803.

Walterscheid, R. L., Venkateswaran, S. V., Influence of mean zonal motion and meridonial temperature gradients on the solar semidiurnal atmospheric tide: a spectral study. Part I: Theory, *J. Atmos. Sc.*, 36, 1623-1635, 1979a.

Walterscheid, R. L., Venkateswaran, S. V., Influence of mean zonal motion and meridonial temperature gradients on the solar semidiurnal atmospheric tide: a spectral study. Part I: Numerical results, *J. Atmos. Sc.*, 36, 1636-1662, 1979b.

Weinstock , J., Nonlinear theory of acoustic-gravity waves - 1. Saturation and enhanced diffusion, *J. Geophys. Res.*, 81, 633-652, 1976.

Wilkes, M. V., *Oscillations of the Earth's Atmosphere*, Cambridge Univ. Press, Cambridge, 1949.

Zurek, R. W., Atmospheric tidal forcing of the zonal-mean circulation: The Martian dust atmosphere, *J. Atmos. Sc.*, 43, 652-670.